A Thesis Submitted for the Degree of PhD at the University of Warwick

Permanent WRAP URL:

http://wrap.warwick.ac.uk/160268

Organometallic Iridium and Rhodium Anticancer Complexes

A Thesis Submitted for the Degree of

Doctor of Philosophy

By

Wenying Zhang
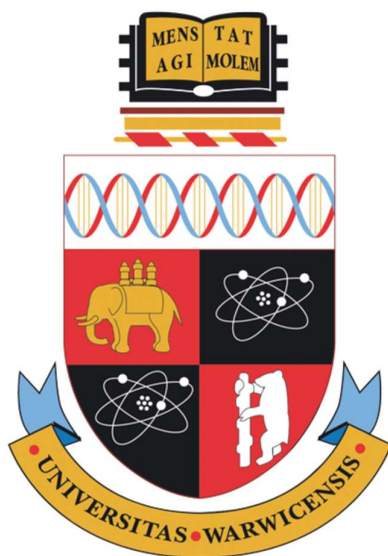
University of Warwick

Department of Chemistry

March 2020

Contents

Acknowledgements

Firstly, I would like to express my sincere gratitude to my supervisor Professor Peter Sadler for his invaluable guidance throughout my PhD study. Your patience, encouragements, and profound knowledge have inspired me deeply on the way of research. I am extremely thankful for all the precious opportunities you have provided for me during my time in the PJS group. I would also like to extend my sincere thanks to Tessa for your kind annual summer BBQ invitations and warm Christmas wishes.

Special thanks to University of Warwick for offering me a Chancellor's Scholarship for my PhD study. Many thanks to Professor Sébastien Perrier and Professor Tim Bugg as my advisory panel to give feedback at different stages.

Thanks also go to Dr. Lijiang Song, Mr. Philip Aston, and Mr. James Morrey for great help with mass spectrometry, LC-MS and ICP; Dr. Ivan Prokes for the NMR training and high-field spectra experiments; Dr. Guy Clarkson for the X-ray crystallography; Dr. Ben Breeze for the EPR experiments. Thank Hannah E. Bridgewater, Ji-Inn Song, Dr. James P. C. Coverdale, and Dr. Isolda Romero-Canelón for the assistance on the bio-experiments. Without the help from all of you, my projects cannot be finished in a timely manner.

I thank Dr. Abraha Habtemariam, Dr. Samya Banerjee, Dr. Cinzia Imberti, and Dr. Feng Chen, for stimulating discussions and instrumental or biological trainings. You are the best officemates! I cherish the nice and happy moments in our C411.

A big thanks to Dr. Huayun Shi, Dr. Huaiyi Huang and Dr. Pingyu Zhang for sharing experimental experiences and giving encouragements.

Declaration

I declare that this thesis is an original report of my research, and has not been submitted for any other degree, diploma or other qualification. I confirm that this thesis is composed by myself, except where specific reference has been made to the work of others. The data presented were collected and analysed by the author, except in the cases outline below.

Work in Chapter 3 has been accepted by *chemical science* as:
Ligand-Centred Redox Activation of Inert Organoiridium Anticancer Catalysts.
Wen-Ying Zhang, Samya Banerjee, George M. Hughes, Hannah E. Bridgewater, Ji-Inn Song, Ben Breeze, Guy J. Clarkson, James P. C. Coverdale, Carlos Sanchez-Cano, Fortuna Ponte, Emilia Sicilia, and Peter J. Sadler.
Preparation, hydrolysis studies by ^{1}H NMR, and the cytotoxicity determination of complexes **9** and **10** were performed by Dr. George Hughes, which were part of his PhD thesis. IC$_{50}$ values of other complexes were determined by Ji-Inn Song; ROS detection and cellular iridium quantification conducted by Hannah Bridgewater; zebrafish toxicity study conducted by Dr. James Coverdale and Hannah Bridgewater; EPR spectroscopy data provided by Dr. Ben Breeze; X-ray crystallographic data analysed by Dr. Guy Clarkson; DFT calculations carried out by Fortuna Ponte and Prof. Emilia Sicilia.

Work in Chapter 4 has been published as:
Ligand-Controlled Reactivity and Cytotoxicity of Cyclometalated Rhodium(III) Complexes. Wen-Ying Zhang, Hannah E. Bridgewater, Samya Banerjee, Guy J. Clarkson, Joan J. Soldevila-Barreda, Huayun Shi, Cinzia Imberti and Peter J. Sadler. *Eur. J. Inorg. Chem.*, DOI:10.1002/ejic.201901055.
The ROS detection and apoptosis assay were performed by Hannah Bridgewater and X-ray crystallographic data analysed by Dr. Guy Clarkson.

Work in Chapter 5 has been published as:
Strategies for Conjugating Iridium(III) Anticancer Complexes to Targeting Peptides via Copper-Free Click Chemistry. Wen-Ying Zhang, Samya Banerjee,

Cinzia Imberti, Guy J. Clarkson, Qian Wang, Qian Zhong, Lawrence S. Young, Isolda Romero-Canelón, Musheng Zeng, Abraha Habtemariam, and Peter J. Sadler. *Inorg. Chim. Acta*, 2020, **503**, 119396.
X-ray crystallographic data were analysed by Dr. Guy Clarkson.

Chapter **6**
X-ray crystallographic data were analysed by Dr. Guy Clarkson; confocal microscopy experiments carried out by Hannah E. Bridgewater; phototoxicity assays on the human nasopharyngeal carcinoma cell line performed by Dr. Huaiyi Huang.

Additionally, I have contributed to the following papers whose results are not presented in this thesis,

Endoplasmic Reticulum: Target for Next-Generation Cancer Therapy. S. Banerjee and Wen-Ying Zhang, *ChemBioChem*, 2018, **19**, 2341-2343.

Metallic Iron in Cornflakes. Frederik Lermyte,[‡] Wen-Ying Zhang,[‡] Jake Brooks, Steven Huband, Joanna F. Collingwood, Martin R. Lees, Margaret P. Rayman and Peter J. Sadler. *Food Funct*., DOI: 10.1039/c9fo02370d. ([‡]These authors contributed equally.)

Wenying Zhang
April 2020

Courses Attended

1. Transferable skills in science

2. RSC lectures

3. Weekly Chemical Biology cluster talks

4. The Sadler research group seminars

Conferences and Meetings Attended

1. *Department of Chemistry Postgraduate Symposium 2018*, University of Warwick, (April 2018). Poster presentation "Peptide-targeted Half-sandwich Iridium Anticancer Complexes" by <u>Wenying Zhang</u>, Abraha Habtemariam, Peter J Sadler.

2. *14th European Biological Inorganic Chemistry Conference,* Birmingham, UK (August 2018). Poster presentation "Activation of Potent Organometallic Iridium(III) Anticancer Complexes" by <u>Wenying Zhang</u>, George M. Hughes, Samya Banerjee, Isolda Romero-Canelón, Ji-Inn Song, Guy J. Clarkson, Fortuna Ponte, Emilia Sicilia, Peter J. Sadler.

3. *Department of Chemistry Postgraduate Symposium 2019*, University of Warwick, (May 2019). Oral presentation "Catalytic Iridium(III) Anticancer Complexes" by <u>Wenying Zhang</u>.

4. *19th International Conference on Biological Inorganic Chemistry*, Interlaken, Switzerland (August 2019). Poster presentation "Activation of Potent Organometallic Iridium(III) Anticancer Complexes" by <u>Wenying Zhang</u>, George M. Hughes, Samya Banerjee, Ji-Inn Song, Guy J. Clarkson, Fortuna Ponte, Emilia Sicilia, Peter J. Sadler.

Organometallic Iridium and Rhodium Anticancer Complexes

Abstract

The use of clinical drug cisplatin is hampered by the severe toxic side effects due to lack of tumor-specificity and the emergence of platinum resistance. Group 9 metal iridium/rhodium complexes with novel mechanisms of action are promising alternatives to cisplatin. This thesis is focused on the chemical and biological studies on half-sandwich organo-Ir^{III} and organo-Rh^{III} anticancer complexes of the type [(η^5-Cp^X)M(XY)Z] (Cp^X = pentamethylcyclopentadienyl Cp*, 1-phenyl-2,3,4,5-tetramethylcyclopentadienyl Cp^{xph}, 1-biphenyl-2,3,4,5-tetramethylcyclopentadienyl Cp^{xbiph}, M = Ir/Rh, Z = Cl/I/pyridine).

Eight iodido Ir^{III} complexes [(η^5-Cp^X)Ir(5-R$_2$-pyridylazo-4-R$_1$-phenyl)I]PF$_6$ featuring a strong π-acceptor azopyridine ligand (Cp^X = Cp* or Cp^{xph}; R$_1$ = Br, CF$_3$, or H; R$_2$ = OH, or H) have been synthesised and characterised. Six X-ray crystal structures showing a typical "piano-stool" configuration have been determined. Most iridium complexes exhibited higher antiproliferative activity than cisplatin against human A549 lung cancer cells with the most potent complex **3** (Cp*, R$_1$ = OH, R$_2$ = Br) approximately 10 times more active. Despite their inertness toward aquation, iodido complexes can undergo redox activation by attack of the abundant intracellular tripeptide glutathione (GSH) on the chelated azopyridine ligand to generate paramagnetic intermediates, and hydroxyl radicals, together with thiolate-bridged dinuclear iridium complexes and liberated reduced hydrazopyridine ligand. DFT calculations provided insight into the mechanism of this activation. GS$^-$ attack on the azo bond facilitates the substitution of iodide by GS$^-$, and leads to formation of GSSG and superoxide if O$_2$ is present as an electron-acceptor, in a largely exergonic pathway. Reaction of iodido complexes with GSH generates [(Cp*)Ir(azopyridine)SG] complexes, which are catalysts for GSH oxidation. The complexes promoted elevated levels of reactive oxygen species (ROS) in human lung cancer cells.

Six half-sandwich Rh^{III} cyclometalated complexes [(Cp^X)Rh(C^N)Z]$^{0/+}$ (where Cp^X = Cp*, Cp^{xph}, or Cp^{xbiph}, C^N = benzo[h]quinoline, and Z = Cl or pyridine) were synthesised and characterised. Three X-ray crystal structures show the expected "piano-stool" configurations. The chlorido complexes hydrolyze faster in aqueous solution, react with 9-ethylguanine to a large extent, and react much faster with

glutathione compared to their pyridine analogues. The chlorido complex [(Cp^{xbiph})Rh(benzo[h]quinoline)Cl] (**3a**) is the most efficient catalyst in oxidizing reduced coenzyme nicotinamide adenine dinucleotide (NADH) to NAD$^+$ and induces an elevated level of reactive oxygen species (ROS) in A549 human lung cancer cells. The pyridine complex [(Cp^{xbiph})Rh(benzo[h]quinoline)py]$^+$ (**3b**) is the most potent against human A549 lung and A2780 ovarian cancer cell lines, being 5-fold more active than cisplatin towards A549 cells, but acted as a ROS scavenger.

Three half-sandwich Ir^{III} complexes [(Cp*)Ir(4-methyl-4'-carboxy-2,2'-bipyridine)Cl]PF$_6$ (**Ir-I**), the product (**Ir-II**) from amide coupling of **Ir-I** to dibenzocyclooctyne-amine, and its conjugate (**Ir-CP**) with the cyclic nona-peptide c(CRWYDENAC) were synthesised and characterised. The 'piano-stool' configuration of complex **Ir-I** was confirmed by its X-ray structure. Significantly, copper-free click strategy were developed for site-specific conjugation of the parent complex **Ir-I** to the tumour targeting nona-cyclic peptide. Complex **Ir-I** was inactive towards human A2780 ovarian cancer cells, whist complex **Ir-II** exhibited moderate cytotoxic activity.

Classes of novel half-sandwich Ir^{III} complexes conjugated to a ferrocene group or a luminescent probe anthracene, BODIPY, or cyclometalated iridium were synthesised and characterised. The structure of half-sandwich complex **4** bearing one ferrocene group was determined by X-ray crystallography. The ferrocene/ferricenium couple becomes more difficult to oxidize in the iridium complexes compared to free ferrocene. The ferrocene-conjugated chlorido complexes also exhibited slightly lower antiproliferative activity than the analogues without ferrocene conjugation towards human A2780 ovarian cancer cells. Half-sandwich iridium complexes bearing a tridentate dipicolyamine ligand conjugated to an anthracene or a BODIPY group, are inert toward reactions with the biomolecules (GSH and 9-EtG), and show characteristic emissions of the conjugated anthracene or BODIPY fluorophore. Meanwhile, the BODIPY-containing complex [(Cp*)Ir(Bdp-Dpa)](NO$_3$)$_2$ (**10**) was found to localize mainly in the mitochondria of human ovarian A2780 cancer cells. Its photocytotoxicity is higher than that of anthracene-conjugated complex [(Cp*)Ir(An-Dpa)](PF$_6$)$_2$ (**7**), which makes it a superior phototherapeutic agent. Phototoxic half-sandwich iridium complex [(ppy)$_2$Ir(Ppy-Phen)(Cp*Ir)Cl]Cl (**12**) conjugated to a cyclometalated iridium unit, has more than 33-fold lower cytotoxicity in the dark than the cyclometalated complex [(ppy)$_2$Ir(Ppy-Phen)]Cl (**11**) towards

human A2780 ovarian cancer cells, suggesting a greater potential of **12** to kill cancer cells selectively under area-targeted light irradiation. Meanwhile, its photocatalytic turnover frequency (TOF) in catalyzing NADH oxidation is 2-3x higher than that of complex **11** or complex [(Cp*)Ir(ppy)Cl] (**13**).

Abbreviations

Å	Angstrom
Anal.	Combustion elemental analysis
azpy	2-(phenylazo)pyridine
BODIPY	Boron-dipyrromethene
ca.	Circa
calcd	Calculated
CDDP	Cisplatin
COSY	Correlation spectroscopy
CP	Cyclic peptide
Cp*	1,2,3,4,5-pentamethylcyclopentadienyl
Cp^{xph}	1-phenyl-2,3,4,5-tetramethylcyclopentadienyl
Cp^{xbiph}	1-biphenyl-2,3,4,5-tetramethylcyclopentadienyl
CV	Cyclic voltammetry
DCM	Dichloromethane
DEPMPO	5-diethoxyphosphoryl-5-methyl-1-pyrroline-N-oxide
DFT	Density functional theory
DMPO	5,5-Dimethyl-1-pyrroline N-oxide
DMSO	Dimethyl sulfoxide
DNA	Deoxyribonucleic acid
en	Ethylenediamine
9-EtG	9-Ethylguaine
equiv.	Equivalents
ESI-MS	Electrospray ionisation – mass spectrometry
EPR	Electron paramagnetic resonance
Fc	Ferrocene
Fc^+	Ferrocenium

5'-GMP	Guanosine-5'-monophosphate
GSH	Glutathione
GSSG	Glutathione disulfide
HPLC	High-performance liquid chromatography
HR-MS	High resolution mass spectrometry
i.e.	That is
IC_{50}	50% growth inhibition concentration
ICP-OES	Inductively coupled plasma-optical emission spectroscopy
ICP-MS	Inductively coupled plasma-mass spectrometry
J	Coupling constant
Log P	Partition coefficient
L-BSO	L-buthionine-sulfoximine
LC-MS	Liquid chromatography–mass spectrometry
m	Multiplet
MoA	Mechanism of action
mM	Millimolar
μM	Micromolar
mol equiv.	Molar equivalents
nM	Nanomolar
NAD^+	B-nicotinamide adenine dinucleotide (oxidised)
NADH	B-nicotinamide adenine dinucleotide (reduced)
NAC	N-acetyl-L-cysteine
NMR	Nuclear magnetic resonance
PB	Phosphate buffer
PBS	Phosphate buffered saline
phen	1,10-phenanthroline
PI	Propidium iodido/ phototoxicity index
ppy	2-phenylpyridine
Py	Pyridine
RF	Resistance factor

ROS	Reactive oxygen species
RPMI-1640	Rosswell park memorial institute medium 1640
s	Singlet
SD	Standard deviation
SRB	Sulforhodamine B
t	Triplet
TEA	Triethylamine
TFA	Trifluoroacetic acid
TON	Turnover number
TOF	Turnover frequency
TS	Transitional state
UV-vis	Ultraviolet-visible

Chapter 1

Introduction

This thesis is concerned with the synthesis, characterisation, chemical and biological activity of novel organometallic (Ir, Rh) complexes with antiproliferative activity. In this Chapter, the traits of cancer, cancer therapies, especially the transition metal chemotherapeutic agents with different mechanisms of action are summarized. Meanwhile, a new strategy of designing catalytic metal complexes as anticancer agents is introduced.

1.1 Cancer

Cancer as the second leading cause of worldwide death, was responsible for an estimated 9.6 million deaths in 2018.[1] Globally, about 1 in 6 deaths is due to cancer, and the two most common cases are lung and breast cancers, each of 2.09 million cases.[1] Meanwhile, lung cancer is the most common cause of cancer death (1.76 million deaths).[1] Cancer is defined as a condition where cells in a specific part of the body grow and reproduce uncontrollably, including the solid malignant (cancerous) tumours and blood cancers. The cancerous cells can invade nearby tissues in the body, including organs, which is also described as metastasis. Metastases are a major cause of death from cancer. Age, environmental carcinogens (e.g. sunburn, tabacco smoke), genetic mutations, lifestyle (e.g. smoking, drinking), etc., can increase the risk of developing cancer.

1.2 Hallmarks of Cancer

The process of the normal cells becoming cancerous arise from the mutations of various genes which control cell growth. In the course of normal cells evolving to a

neoplastic state, they acquire successively certain distinctive and complementary capabilities that enable tumour growth and metastasis. Over the past two decades, eight hallmarks have been summarized by Hanahan and Weinberg based on the remarkable progress of cancer research (Figure 1.1).
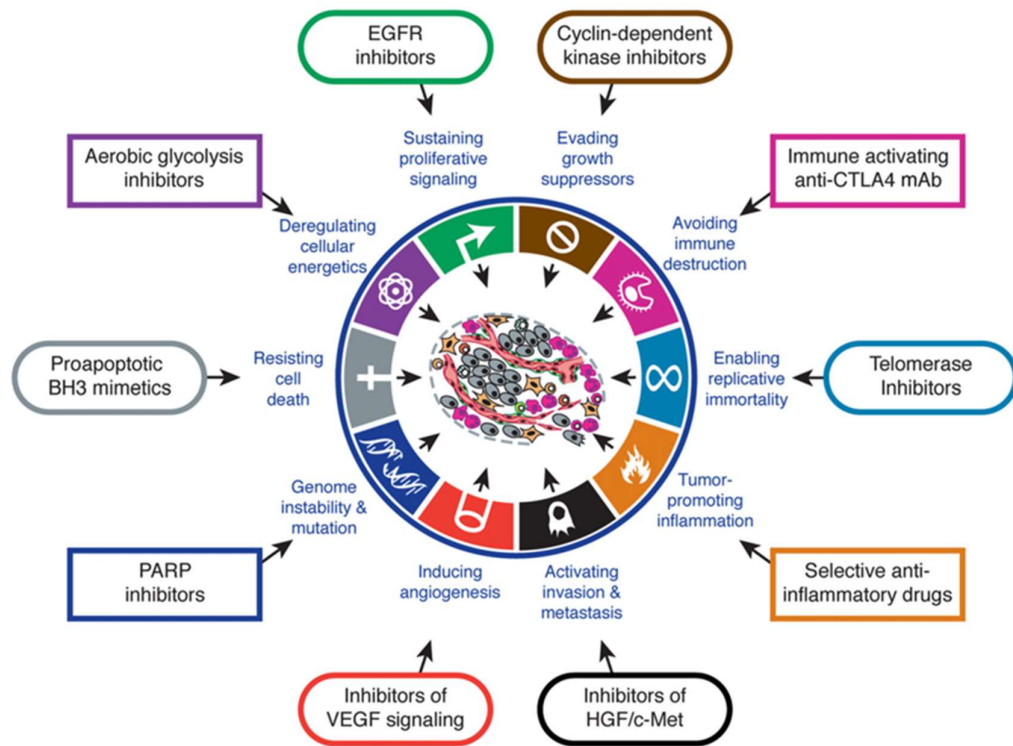
Figure 1.1. The hallmarks of cancer with the corresponding targeted therapeutics. Adapted from ref. 3.

They include sustaining proliferative signaling, evading growth suppressors, resisting cell death, enabling replicative immortality, inducing angiogenesis, activating invasion, metastasis, and the subsequent emerging two hallmarks of reprogramming of energy metabolism, and evading immune destruction.[2,3] These

hallmark traits have provided a solid foundation for understanding tumour biology, which will also affect the development of new cancer therapies. Drugs that interfere with each of the acquired capabilities necessary for tumour growth and progression have been developed (Figure 1.1) and are in clinical trials or in some cases approved for clinical use in treating certain forms of human cancer.

1.3 Cancer Therapies

Depending on the type and stages of cancer, patients are treated with either the most traditional and common types of therapies (chemotherapy, surgery and radiotherapy), or newer forms of treatment, such as hormone therapy, immunotherapy, gene therapy, stem cell and bone marrow transplants, photodynamic therapy (PDT), and targeted cancer drugs.[4]

In theory, surgery is an ideal localized treatment for non-hematological cancers, but it is generally used only when the cancer is localized. Radiation therapy uses the high-energy particles or waves, such as x-rays, gamma rays, electron-beams or protons to destroy the DNS of cancerous tissue leading to cellular death. Chemotherapy is an effective and widespread way of cancer treatment, which operates by blocking the unwanted proliferation of cancer cells. Because some chemotherapeutic drugs work better together than alone, so the most chemotherapy regimens are given in a combination.

1.4 Transition Metal-Based Anticancer Drugs

Metal-based compounds widely used in the treatment of diseases date back to the ancient time. For example, the ancient Assyrians, Egyptians and Chinese knew the use of cinnabar (mercury sulfide) in the treatment of ailments.[5] Arsenic trioxide was used by the traditional Chinese medical practitioners as an antiseptic and in the treatment of rheumatoid diseases, syphilis and psoriasis.[6] The history of chemotherapy can be traced back to the use of nitrogen mustard and antifolate drugs for cancer treatment in the 1940s.[7] Nevertheless, transition metal-based coordination compounds as anticancer drugs began with the discovery of the inhibitory activity of cisplatin on cell division by Barnett Rosenberg in 1967.[8] The unparalleled success of platinum drugs has inspired the development of a huge number of transition-metal compounds as anticancer agents, including coordination complexes and organometallic structures.[9,10] The d-block transition metal compounds offer a wide range of oxidation states, coordination numbers, and geometries, providing a vast structural and chemical space to explore. To date, the transition metals which have actively explored as anticancer agents are marked in Figure 1.2.

Figure 1.2. Compounds of the transition metals (with magenta background) having anticancer activity.

1.4.1 Platinum Anticancer Drugs

Platinum drugs are the mainstay of the chemotherapeutic agents in the treatment of cancer, which constitute approximately 50% of all cancer treatments.[11] One remarkable success of the platinum drugs is the fact that cure rates for testicular cancer have exceeded 95% since the introduction of cisplatin into the treatment regimen.[12] Despite the clinical success, there are currently only three platinum drugs in worldwide use as shown in Figure 1.3, namely cisplatin, carboplatin and oxaliplatin. Three additional platinum drugs: nedaplatin, heptaplatin and lobaplatin are used in Japan, South Korea and China, respectively, as shown in Figure 1.3.[13]

Cisplatin (1978)   Carboplatin (1989)   Oxaliplatin (2002)

Nedaplatin (1995)   Heptaplatin (1999)   Laboplatin (2010)
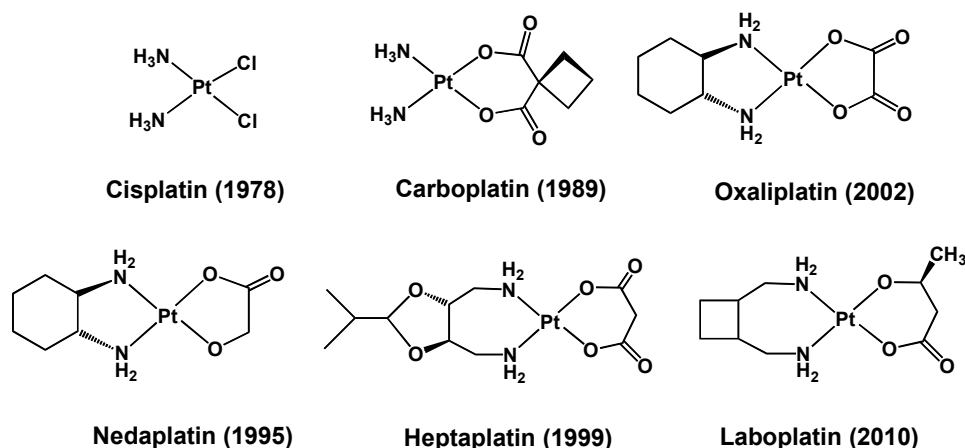
Figure 1.3. Chemical structures of platinum anticancer drugs in clinical use with the years in which they received regulatory approval in parentheses.[11]

Cisplatin and carboplatin operate by binding to nuclear DNA to inhibit the transcription and replication, thus triggering cell-death pathways.[14,15] In their structures, the ammine ligands are as "the non-leaving group" through the course of intracellular transformations, while the labile chlorido or dicarboxylato ligand as the

6

"leaving group".[16] Pathways through which cisplatin reaches the DNA target are shown in Figure 1.4.[13] First step is the entry into cells through passive diffusion or the active transport pathways involving the copper transporter[17] (CTR1) or organic cation transporter[18] (OCT1-3). In the cytoplasm, cisplatin is activated by hydrolysis of the chloride ligand favored by the lower chloride ion concentration in cytosol (10-20 mM) than in blood (0.1 M). The formed aquated cisplatin readily binds to the N7 atoms of the purine residue guanine and adenine on DNA to form intrastrand and interstrand DNA cross-links which have been confirmed by X-ray crystal or NMR structures.[14]
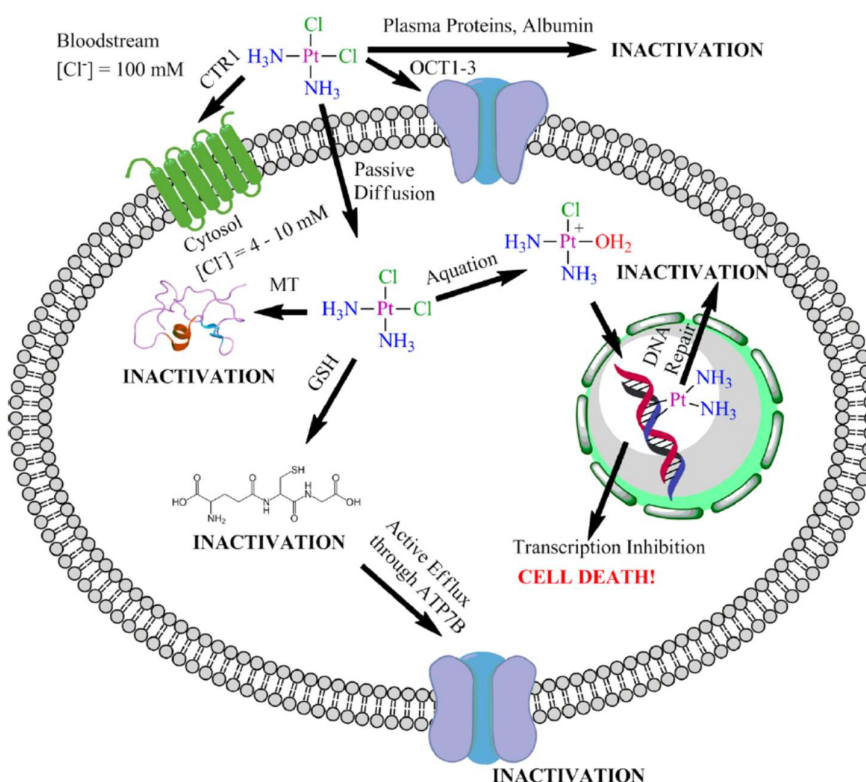
Figure 1.4. Extracellular and intracellular events that influence cisplatin activity. Reproduced from ref. 13.

In addition, the sulfur-containing nucleophiles, such as glutathione and metallothioneins existing inside cells as well as the human serum albumin containing a cysteine residue in the human bloodstream, readily bind with cisplatin to prevent it from reaching nucleus DNA.[19] Thus, to enhance the stability and reducing the unwanted side reactions, the subsequent approved clinical platinum drugs contain chelating dicarboxylato ligands. Meanwhile, compared to cisplatin, the more stable carboplatin is significantly less toxic on the body.[12] On the other hand, human cancer cells can also acquire resistance from genetic and/or epigenetic changes to reduce the drug sensitivity.[20] In order to overcome the toxicity and resistance associated with the "classical" platinum drugs, efforts to develop "non-classical" platinum drugs have been made, such as the exploration of polynuclear platinum(II) compounds, platinum(II) drugs tethered with tumour-targeting vectors, platinum(IV) prodrugs, and nanotechnology delivery of platinum drugs.[12,21]

1.4.2 Ruthenium Anticancer Drugs

Ruthenium has a range of accessible oxidation states (II, III, and IV) under physiologically relevant conditions.[22] Ruthenium compounds were developed as alternatives of platinum drugs, particularly on resistant tumours, or to reduce host toxicity at active doses, as they have similar kinetic spectrum of ligand substitution as the Pt(II) complexes in aqueous medium.

A breakthrough of ruthenium-based drug development is attributed to NAMI-A and KP1019 (Figure 1.5). NAMI-A: ([trans-Ru^{III}Cl4(S-dmso)(Im)] (ImH), Im = imidazole) developed by Mestroni, Alessio, *et al.* has reached phase-I/II trials in

combination with gemcitabine. However, the limited efficacy of NAMI-A in phase II clinical studies prevented its further clinical development.[23] Another Ru therapeutic KP1019 ((IndH)[$trans$-Ru^{III}Cl$_4$(Ind)$_2$], Ind = indazole) (Figure 1.5) developed by Keppler et $al.$ entered phase I clinical trials.[24] Due to solubility issues, it has been replaced with KP-1339 (Na[$trans$-RuCl$_4$(Ind)$_2$], the sodium salt of KP1019) which possesses greater aqueous solubility, and is currently in Phase I clinical trials.[25]

Although structurally related, NAMI-A and KP1019/1039 have a different cytotoxic profile toward the tumour cells. NAMI-A shows little activity against primary tumours but high activity against secondary tumours and inhibits metastases, while KP1039 behaves as a classic cytotoxic drug and is potent against primary cisplatin-resistant tumors. The modest cellular uptake of ruthenium by NAMI-A is also distinct from the significantly higher ruthenium concentration in the cytosol of the KP1019 treatment.[24] The biological effects of NAMI-A seem to derive from its anti-angiogenic properties, binding to collagens of the extracellular matrix and cell surface integrins, leading to increased cell adhesion and reduced invasiveness of cancer cells.[26] The strong interactions of KP1039 with cytosolic proteins leads to oxidative stress and ER stress to trigger apoptosis through a mitochondrial pathway.[27]

These Ru^{III} compounds are suggested to serve as prodrugs activated by reduction in $vivo$ to Ru^{II} to coordinate more rapidly to biomolecules.[28] The stability of Ru^{II} is also favored by the lower oxygen content and more acidic pH in tumours compared with normal tissues. Therefore, further studies on the anticancer activity of Ru^{II} complexes have been stimulated. For example, the octahedral Ru(II) polypyridyl complexes have emerged as promising anticancer agents for photodynamic therapy[29]

or photoactivated chemotherapy.[30] A significant example is the Ru(II)-based therapeutic TLD1433 (Figure 1.5), which is the first Ru(II)-based photosensitizer to enter a human clinical trial for non-muscle invasive bladder cancer treatment.[31]
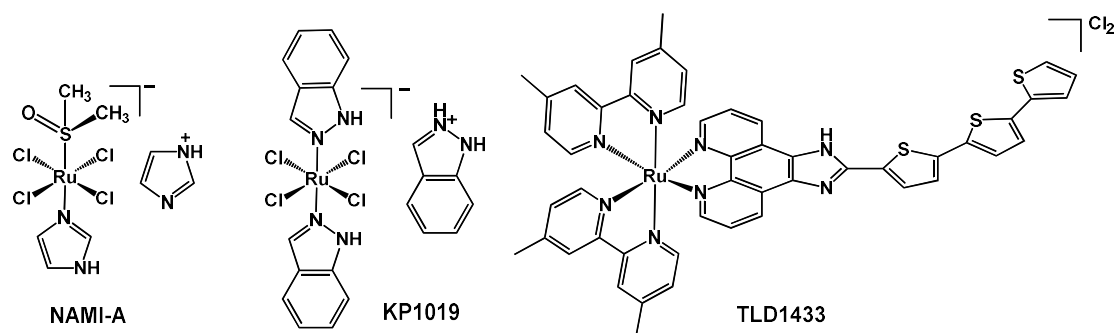
Figure 1.5. Chemical structures of Ru anticancer drugs (NAMI-A, KP1019, TLD1433) for clinical trials.

1.5 Organometallic Anticancer Complexes

Organometallic compounds defined as metal complexes containing at least one metal-carbon bond, own great structural variety, diverse stereochemistry, variable oxidation states, tunable kinetic properties by rational ligand design, and relative lipophilicity, which render them as a novel class of transition meatal-based drug candidates.[32]

The most well-studied organometallic anticancer compounds include metallocenes (titanocene and ferrocene), half-sandwich compounds of Ru, Os, Ir and Rh, metal-carbene and metal-carbonyl compounds and cyclometallated complexes. Titanocene dichloride – [Ti(η^5-C$_5$H$_5$)$_2$Cl$_2$] was first studied in 1979 by Köpf-Maier and Köpf, as a cytostatic (inhibition of cell growth) agent, which finally reached

10

Phase II clinical trials but did not progress due to lack of efficacy in patients.[33]

Nevertheless, it was the first organometallic compound to undergo clinical trials in 1993 as a chemotherapy drug. The early promising research on it has inspired the exploration of anticancer properties of organometallics.[34] Here several types of relevant organometallics are discussed.

1.5.1 Ferrocene

Ferrocene – $[Fe(\eta^5\text{-}C_5H_5)_2]$, in which the Fe^{II} is sandwiched between two π-bonded cyclopentadienyl (Cp) ligands in staggered conformation (shown in Figure 1.6a), is a groundbreaking discovery in organometallic chemistry. The stability of ferrocene in aqueous and aerobic media, the accessibility of various derivatives and most importantly, its reversible electrochemical properties have made ferrocenyl compounds popular as molecules for medicinal research. Ferrocene by itself is not a particularly toxic agent, but after a one-electron oxidation the yielding ferrocenium salts (Figure 1.6a) have antiproliferative effects on mice bearing the Ehrlich ascites tumour, reported by Köpf-Maier, Köpf and Neuse in 1984.[35]
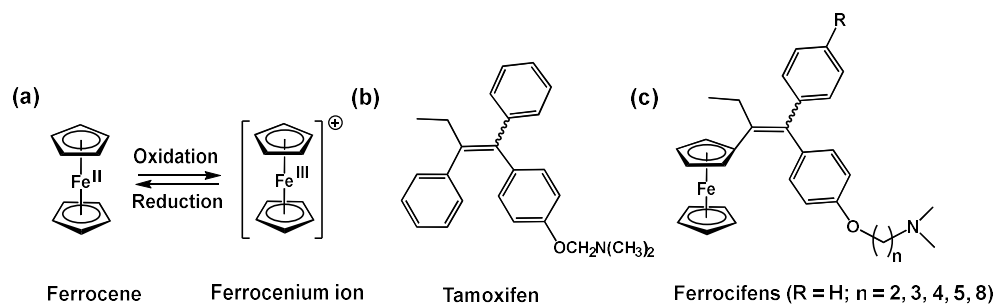
Figure 1.6. (a) Reversible oxidation of ferrocene to ferrocenium; and the chemical structure of (b) tamoxifen and (c) ferrocifens.

The anticancer potential of ferrocene derivatives was known in the late 1970s when Brynes and co-workers reported that ferrocenyl compounds bearing amine groups exhibit low but significant activity against lymphocytic leukemia P-388.[36] After that, numerous ferrocene derivatives have been tested for antiproliferative purposes.[37] Among them, the ferrocifens (Figure 1.6c) are the most widely studied, which substitutes one phenyl ring in tamoxifen (Figure 1.6b) by Jaouen and co-workers.[38] Tamoxifen, shown in Figure 1.6b, is an established chemotherapeutic drug for the treatment of breast cancer with the estrogen receptor (ER(+)), acting as estrogen receptor modulators to suppress estradiol-mediated DNA transcription in the tumour tissue.[39] Ferrocifens are believed to have a similar mechanism to tamoxifen, and are effective antiestrogens in ER(+) MCF-7 breast cancer cells. Surprisingly, the n = 4 ferrocifen compound (Figure 1.6c) is also active against the ER(-) MDA-MB231 tumor cell line, which is not susceptible to tamoxifen treatment.[40] Apart from the tamoxifen-like mechanism, Jaouen *et al.* subsequently proposed redox activation as the second mode of action of ferrocifens, in which after ferrocene is oxidized, a quinone methide intermediate is formed by proton abstraction, and is readily attacked by nucleophiles (Figure 1.7).[41]

1.5.2 Ruthenium Arene Complexes

Apart from the Ru-based coordination complexes, numerous organometallic Ru(II) complexes have been intensely investigated in the Sadler and Dyson research groups. The prototype complexes were Ru(II) arene ethylenediamine (en) derivatives $[(\eta^6\text{-}$arene)Ru(N,N-en)Cl]$^+$ (en = 1,2-ethylenediamine, Figure 1.8a) developed by Sadler

et al. and RAPTA derivatives [(η^6-*p*-MeC$_6$H$_4$Pr^i)Ru(P-pta)Cl$_2$] (pta = 1,3,5-triaza-7-phospha-tricyclo-[3.3.1.1]decane, Figure 1.8b) developed by Dyson *et al.*.
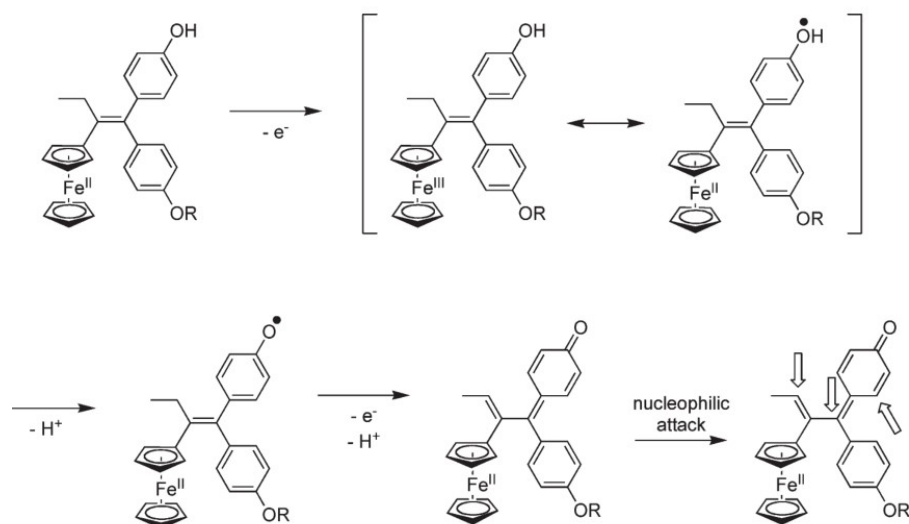
Figure 1.7. Redox activation of ferrocifens as proposed by Jaouen and coworkers. Adapted from ref. 41.
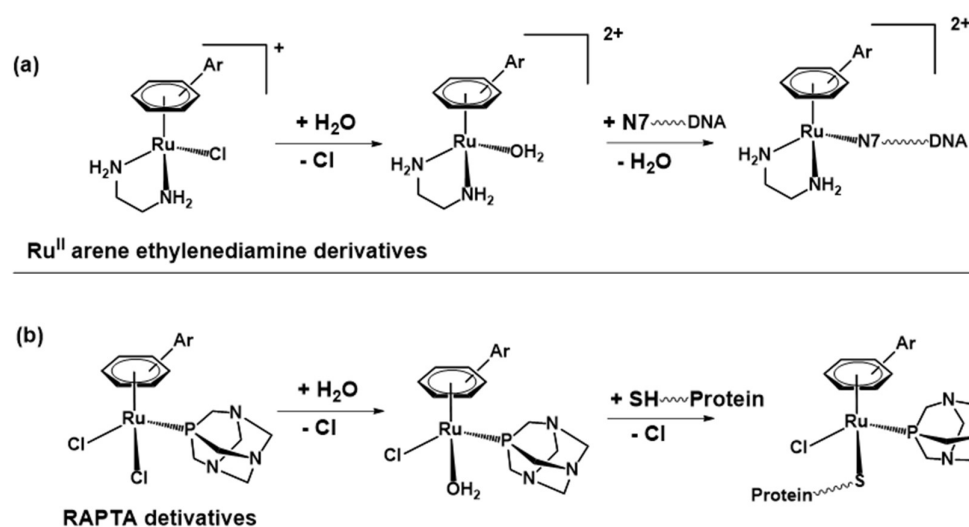
Figure 1.8. Brief illustration of the different mechanisms of action of Ru(II) arene (a) ethylenediamine derivatives and (b) RAPTA derivatives.

Despite structure similarity and hydrolysis lability, these two types of derivatives seem to act differently in cells. The mechanism of the ethylenediamine compounds is reminiscent of cisplatin which involves hydrolysis to aqua species and binding to the N7 atoms of guanine bases of DNA as shown in Figure 1.8a.[42,43] Since these derivatives were also active against cisplatin-resistant cell lines, they might have different detoxification mechanisms from that of cisplatin.[44] What is more, oxidation of the thiolato complex $[(\eta^6\text{-biphenyl})\text{Ru(en)SG}]$ to sulfenato complex $[(\eta^6\text{-biphenyl})\text{Ru(en)S(O)G}]$ in air through the reaction of Ru arene chlorido complex with GSH, has been demonstrated to provide a facile route for replacement of S-bound GSH with the N7 atom of the guanine base on the Ru centre, further indicating that GSH conjugation appears not to be a detoxification route for the Ru arene complexes unlike detoxification of cisplatin by GSH.[45]

By contrast, the RAPTA compounds do not bind to DNA, rather bind to the sulfur atom of cysteine residues of proteins (Figure 1.8b), particularly cathepsin B, which is a prognostic marker in the migration and invasive of tumors.[46-48] Computer docking has validated the stability of the corresponding stability of RAPTA/Cathepsin B adducts, which correlates well with the inhibition potency.[49] Although many RAPTA compounds are not cytotoxic and non-toxic to healthy cells, two RAPTC derivatives (RAPTA-C and RAPTA-T) can inhibit lung metastasis in CBA mice bearing the MCa mammary carcinoma by reducing the number and weight of metastases, while having only mild effect on the primary tumor, which makes them promising as treatment options for metastases based on removal of the primary tumor by surgery.[50]
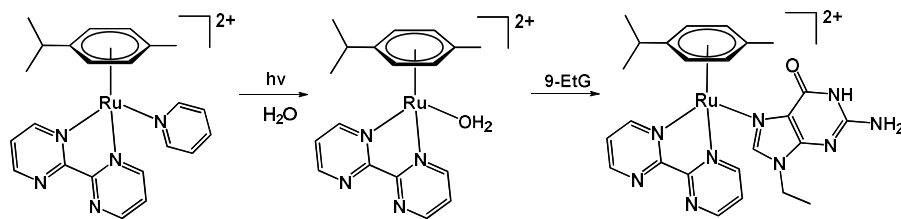
Figure 1.9. Photo-controlled nucleobase binding of the Ru(II) arene complex. Adapted from ref. 51.

The Sadler research group have also discovered that some Ru(II) arene complexes are photoactivable. For example, the pyridine Ru(II) complex in Figure 1.9 can be activated by visible light to hydrolyze into the aqua adducts which bind to DNA nucleobases.[51] Their DNA-targeting specificity can be improved by conjugation of cancer cell-targeting peptides.[52] The same group have discovered that Ru arene complexes can also act as radiosensitizer, enhancing the effect of radiation on colorectal cancer cells.[53]

1.5.3 Osmium Arene Complexes

Compared with the lighter congener ruthenium, osmium has been little explored as therapeutic agents due to its reputation of being relatively substitution inert and highly toxic. Extensive studies have shown that the fate of osmium arene complexes in cells is markedly dependent on the ligands surrounding the Os centre.[54] Sadler *et al.* have recently reported new classes of promising osmium(II) arene anticancer agents (Figure 1.10a-e).[54] For example, the osmium analogue of the active ethylenediamine (en) Ru(II) complex, $[(\eta^6$-biphenyl)Os(en)Cl]$^+$, Figure 1.10a, was

prepared to understand the effects of the metal on the activity and mode of action.[55] Notably, hydrolysis of this Os arene complex is 100 times slower than that of the Ru(II) analogue $[(\eta^6\text{-biphenyl})Ru(en)Cl]^+$, but it exhibits promising activity with IC$_{50}$ = 7-10 µM against the human ovarian cancer A2780 and lung A549 cancer cell lines. The replacement of neutral N^N en ligand with anionic O^O acetylacetonate (acac), Figure 1.10b, leads to low cytotoxicity, which can be attributed to the fast hydrolysis of the O^O complex generating the unreactive hydroxo-bridged osmium dimers.[56] Later, the osmium complex featuring N^O chelating picolinate (pico) ligand (Figure 1.10c) was prepared and were significantly stable in aqueous media with similar cytotoxicity as carboplatin against human ovarian cancer cells.[57,58] Meanwhile, the cellular uptake and binding to DNA was enhanced by conjugating the Os^{II}(picolinato) complex (Figure 1.10d) to cell-penetrating peptides, such as octaarginine (Arg8), without loss of the cytotoxicty.[59]
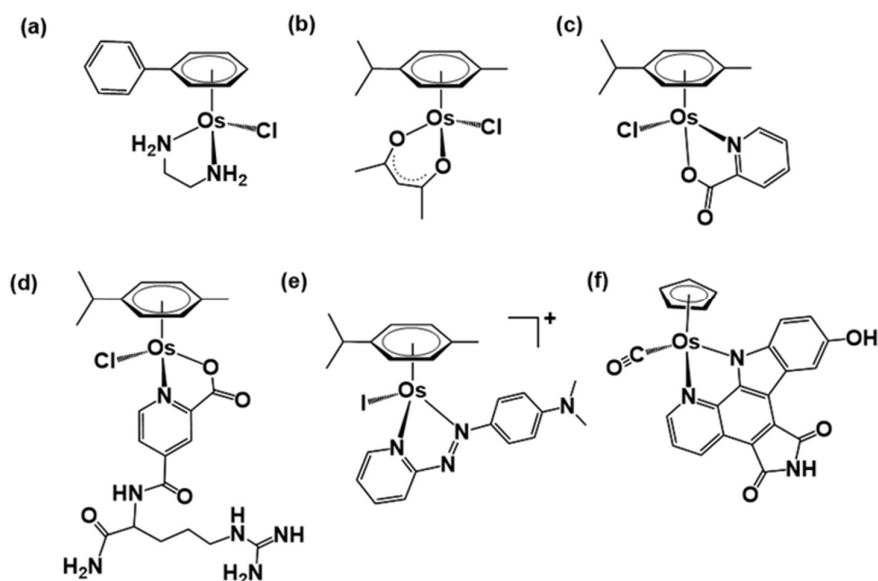
Figure 1.10. Structures of the osmium(II) arene complexes introduced here.

Notably, the Sadler group have also developed a library of Os(II) arene azopyridine complexes.[60] As shown in Figure 1.10e, complex $[(\eta^6\text{-}p\text{-}$Cymene)Os(Azpy-NMe$_2$)I]PF$_6$, namely, **FY026**, exhibits ten-fold higher potency than cisplatin against tested cancer cells and delays the growth of HCT-116 human colon cancer xenografts in mice with negligible toxicity.[61] Interestingly, such Os complexes bearing the iodide ligand undergo hydrolysis activation of forming Os-OH species through attack of GSH on the azopyridine ligand.[62,63] Their mechanism of action involves inducing bursts of reactive oxygen species, especially superoxide in cells. The synchrotron x-ray fluorescence nanoprobe data consistently suggests that the Os localizes in mitochondria and not in the nucleus.[64] A further synchrotron experiment has detected and quantified both Os^{II} and Os^{III} species distributes heterogeneously in different areas of the treated A2780 cells by FY026.[65]

Meggers *et al.* also designed the osmium arene complex shown in Figure 1.10f analogous to the known kinase inhibitor staurosporin, which inhibits kinases by competitively binding to the ATP-binding site of the enzyme.[66] The osmium was thought to have a purely structural function, as the osmium replacement of ruthenium led to the same antiproliferative activity and identical mode of action as protein kinase inhibitors.[66]

1.5.4 Half-sandwich Iridium Complexes

Discovered in 1803 as an impurity in platinum, iridium is one of the nine least abundant stable elements in the Earth's crust. As a relatively rare precious heavy metal, the global consumption of iridium was 6,180 kg in 2018.[67] Iridium compounds have

been notably successful catalysts in the chemoselective and enantioselective hydrogenation of C=N and C=C bonds, such as the prominent Crabtree's hydrogenation catalyst $[Ir^I(cod)(PCy_3)py]PF_6$ (cod = 1,5-cyclooctadiene, Cy = cyclohexyl) as one of the most active catalyst for the hydrogenation of hindered C=C bonds.[68] Half-sandwich pentamethylcyclopentadienyl (Cp^*) Ir^{III} complexes are also widely utilized as molecular catalysts for C-H activation, hydrogen transfer reactions and water oxidation.[69,70] However, the anticancer applications of half-sandwich iridium complexes are still in their infancy in comparison with arene Ru complexes.

Ir^{III} is often considered to be inert with a low spin d^6 configuration, which is a more stable oxidation state than Ir^I. The coordination number of 6 also provides extensive structure diversity. Particularly, unlike the Ru^{II}/Os^{II}, Ir^{III} is relatively unstable with benzene derivatives as π-bound ligands, albeit stabilized by cyclopentadienyl ligands, especially the electron-rich Cp^* ligand.[71] A general structure feature of half-sandwich Ir^{III} complexes is as shown in Figure 1.11. The π-bound negatively changed Cp^X ligand (Cp^*, Cp^{xph}, or Cp^{xbiph}) occupies three coordination sites. The chelating ligand L^L' provides additional stability for the complex, and the monodentate ligand Z provides a labile site for substitution reaction with target sites.

In recent years, the Sadler research group have explored a library of half-sandwich Ir(III) cyclopentadienyl complexes of the type $[(\eta^5\text{-}Cp^X)Ir(L^{\wedge}L')Z]^{0/n+}$ (Cp^X = Cp^*, Cp^{xph} or Cp^{xbiph}, $L^{\wedge}L'$ = bidentate $N^{\wedge}N$-, $N^{\wedge}O$-, $O^{\wedge}O$-, or $C^{\wedge}N$-chelating ligand, Z = Cl, pyridine or SH) as shown in Figure 1.12, which exhibited promising (nanomolar) activity toward a range of cancer cells.[71-73]
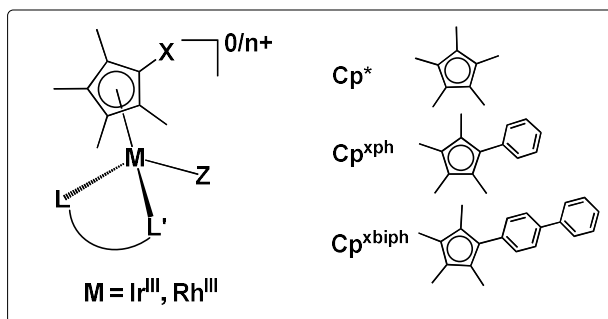
Figure 1.11. The general structure of a half-sandwich cyclopentadienyl Ir(III)/Rh(III) complex with the various Cp^X rings.

The exploration began with N^N and N^O chelating complexes with chloride as the leaving group (Figure 1.12a-d). Surprisingly, such Cp* complexes were too labile toward hydrolysis to be cytotoxic. When the one or two phenyl rings were added to the Cp* ring, the complexes exhibited medium to high potency against cancer cells. The rationale behind this behaviour is that not only the increased hydrophobicity of Cp^{xbiph} and Cp^{xph} ring increases more iridium passage across cell membranes and accumulation in cells, but also phenyl rings intercalate between DNA bases, which is believed to be a major target for these complexes.

Furthermore, the alteration of a N^N to a C^N coordinating mode of the bidentate ligand led to a switch of the antiproliferative activity (Figure 1.12a *versus* 1.12e), suggesting an alternative mechanism of action for the C^N chelated complexes. As expected, apart from DNA damage, half-sandwich iridium complexes were subsequently demonstrated to exert redox modulation mechanism of action involving ROS induction or redox catalytic activity with biomolecules.[74-77]
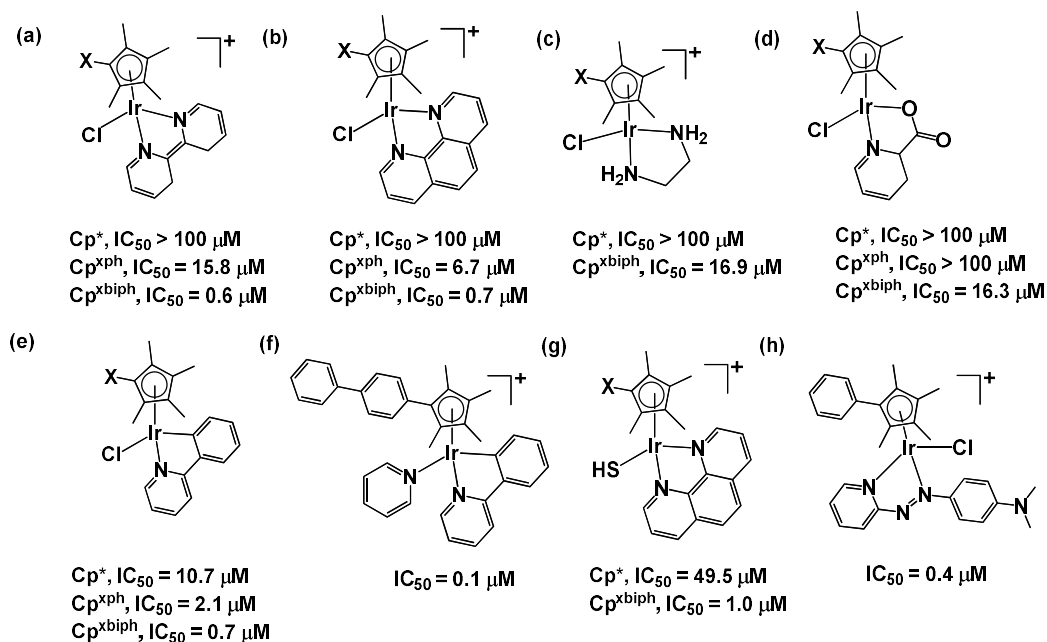
Figure 1.12. Chemical structures of reported half-sandwich iridium complexes in the Sadler research group (2011-2018), varying with Cp^X rings, chelating ligands, or the monodentate leaving groups. IC_{50} values against human A2780 ovarian cancer cells of the complex with different Cp^X rings are listed below the corresponding structure.

The deactivation caused by rapid hydrolysis of chlorido iridium complexes has further inspired the replacement of chloride ligand with pyridine or hydrosulfide ligands.[72,78] Interestingly, the resulting pyridine complexes (Figure 1.12f) have proved to be oxidative catalysts in cancer cells (described in detail in Section **1.6.4.3**), with much higher potency than cisplatin or carboplatin in the NCI-60 cell line screen.[78] In addition, the introduction of azopyridine ligands similar to the arene Os(II) azopyridine complex FY026, has led to the resulting Ir(III) complex shown in Figure 1.12h, being 36x more potent than cisplatin on average towards 916 cancer cell lines and exhibiting a markedly different pattern of antiproliferative activity compared to

the 253 drugs in the Sanger Cancer Genome database.[73]

More recently, studies have been reported on half-sandwich iridium complexes bearing ligands with other chelating modes, such as the P^N,[79] P^P,[80] P^O,[81] C^C,[82] C^O,[83] which exhibit various redox mechanisms of action. Furthermore, certain smaller counteranions, e.g. Cl$^-$, PF$_6^-$, BF$_4^-$, CF$_3$SO$_3^-$, with better coordination ability have been found to contribute to the chemical reactivity and anticancer activity of the complex shown in Figure 1.13a.
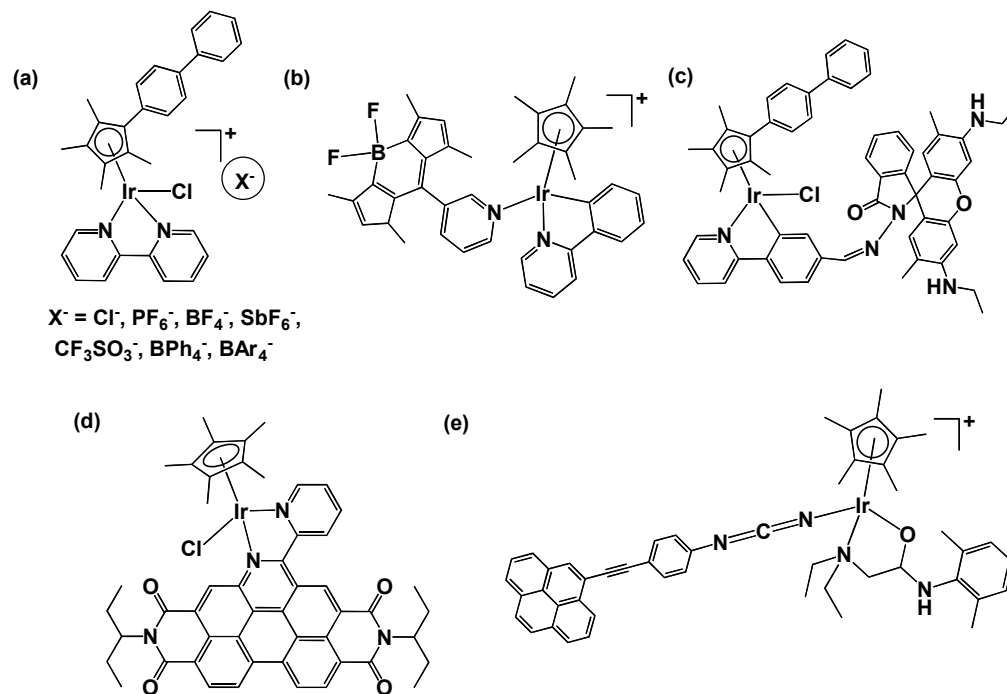
Figure 1.13. Chemical structures of reported iridium complexes studied for (a) the effecting counteranions on the reactivity and anticancer activity; (b) and (c) luminescence with bodipy/rhodamine tags; (d) and (e) photosensitizers for photodynamic therapy.

Half-sandwich iridium complexes have been modified with fluorophores, such as bodipy/rhodamine groups, to make them detectable in cells by fluorescence emission.[84,85] The cell uptake of the bodipy-modified complex shown in Figure 1.13b was allowed to be monitored by living cell fluorescence imaging.[84] The rhodamine-conjugated iridium complex shown in Figure 1.13c entered into the cytoplasm in an energy-dependent manner and specifically targeted lysosomes as studied by confocal microscopy.[85]

In addition, half-sandwich iridium complexes have also been developed as photodynamic therapy agents. For example, Gasser and colleagues have investigated the mitochondria-targeting Cp^* Ir complex in Figure 1.13d, which showed nanomolar IC_{50} values when irradiated with 420 nm blue light (9.27 J cm^{-2}).[86] Tabrizi has explored the Cp^* iridium complex shown in Figure 1.13e as a PDT agent, based on the phenylcyanamide-pyrene ligand. This complex targets the cell-nucleus with low dark toxicity ($IC_{50} > 100$ µM) and higher phototoxicity than the commercial available photosensitizer Photofrin in HeLa cells when irradiated with visible light of 450 nm (10 J cm^{-2}), while with less toxicity toward normal MRC-5 cells.[87]

1.6 Catalytic Metallodrugs

Transition metal complexes are well-known as potent catalysts for selective molecular transformations, such as the Mo/Ru-based catalysts for metathesis reactions (Nobel Prize in 2005) and Pd-based catalysts for C-C bond formation (Nobel Prize in 2010).[88] These great discoveries for chemical transformations stimulated studying the equivalent catalytic transformations in bacterial or

mammalian cells for bio-medicinal purposes.[88] Distinct from the stoichiometric reactions, the catalytic reactions are capable of amplifying the chemical signals thus allowing lower drug dosage, and the intrinsic catalytic selectivity limits off-target effects.[89] Furthermore, catalytic metallodrugs tend to have novel mechanisms of action which might be beneficial to overcoming drug resistance. Since the small molecular catalysts are easily poisoned by nucleophiles, maintaining the catalytic activity in the complex biological media is challenging. Here several classes of catalytic metal complexes which have been developed as anticancer agents, are introduced as follows.

1.6.1. Singlet Oxygen Generation in PDT

Photodynamic therapy (PDT) is a prototypical example of a catalysis-based therapeutic approach, which relies on the photoinduced catalytic production of singlet oxygen and other reactive oxygen species (ROS) mainly hydroxyl radicals and superoxide, by the photosensitizer (Figure 1.14a). These reactive species can cause oxidative damage to cellular components such as unsaturated lipids, amino acid residues, or nucleic acids, thus triggering the targeted-cell death within the light irradiated area. Although organic chromophores, such as Photofrin, have been approved by the FDA as clinical PDT agents, metal coordination complexes have greatly improved the disadvantages of organic PDT agents (poor aqueous solubility, photobleaching, prolonged retention in tissues, low selectivity toward cancer cells).[90] For example, the polypyridyl complexes of Ru^{II}, Os^{II}, Re^{I}, and cyclometalated Ir^{III} complexes have been developed as attractive candidates for PDT.[90] Especially, the

Pd-based WST11[91] (Figure 1.14a) and Ru-based TLD-1433[31] (Figure 1.5) have entered clinical trials for PDT.
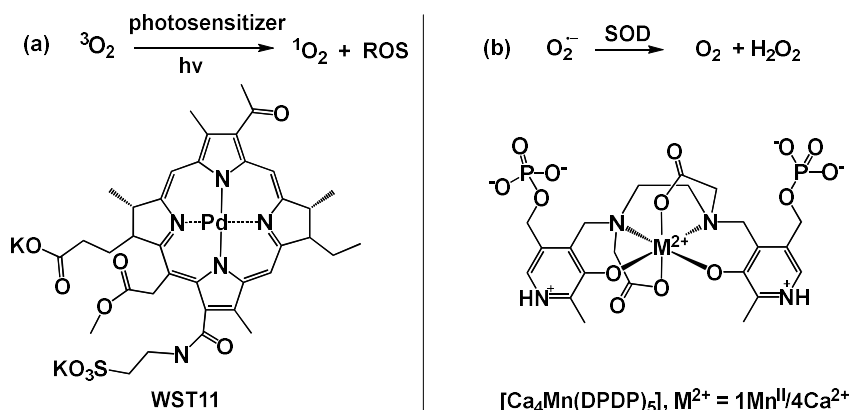
Figure 1.14. Redox reactions catalyzed by (a) the photosensitizers in photodynamic therapy generating singlet oxygen and (b) the superoxide dismutase SOD (mimics) generating hydrogen peroxide, and chemical structures of WST11 and calmangafodipir currently in clinical trials.

1.6.2 Superoxide Dismutase Mimics

Superoxide dismutase (SOD) enzyme is a ubiquitous endogenous metalloprotein that acts as the first line of defense against reactive oxygen species by converting $O_2^{\bullet-}$ to H_2O_2 and molecular oxygen (Figure 1.14b). Metal-based catalysts as SOD mimics have been found to have therapeutic potential in combination with chemotherapy and radiotherapy by enhancing the effectiveness and attenuating the drug side effects and toxicity issues related to radiation.[92] Most common compounds are the Mn-SOD mimics, including Mn salen, Mn porphyrin, Mn cyclic polyamines.[93] The Mn^{II} complex calmangafodipir (Figure 1.14) is in clinical trials for metastatic colorectal

cancer patients in combination with chemotherapy FOLFOX (5-fluorouracil/folinic

acid).[94]

1.6.3 Oxidation of Glutathione

1.6.3.1 GSH

The tripeptide glutathione (GSH) is the most abundant low molecular mass thiol in

animal cells, with concentrations ranging from 0.5-10 mM. As a carrier of an active

thiol group, GSH acts as an antioxidant by reacting with reactive oxygen/nitrogen

species (ROS/RNS) and electrophiles or by operating as a cofactor of various

enzymes.[95] The reduced and oxidized form of glutathione (GSH and GSSG, shown

in Figure 1.15) act in concert with other redox-active compounds e.g. NAD(P)H to

maintain and regulate the cell redox status.
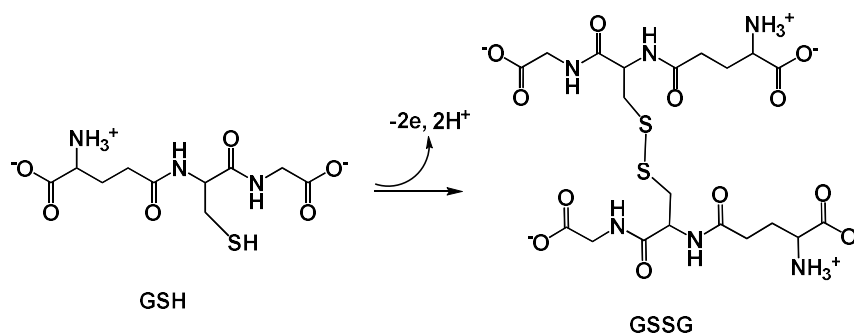
Figure 1.15. Glutathione (GSH) and its oxidized disulfide form.

The most important roles of GSH are to prevent ROS/RNS damage to the cellular

components and detoxify the endogenous and exogenous toxins of an electrophilic

nature, such as metal ions. Taking account of the significance of GSH, depletion of

GSH has been an effective approach for cancer treatment. For example, the specific inhibitor of gamma-glutamylcysteine synthetase in the first step of glutathione synthesis, buthionine sulfoximine (BSO), is an adjunct in cancer chemotherapy.[95]

1.6.3.2. Catalytic GSH Oxidation

Recently, catalytic depletion of GSH by metal complexes has also been studied,[88] although GSH is widely reported as a detoxification agent. The initial report of Ru arene azopyridine complexes shown in Figure 1.16a catalyzing GSH oxidation to GSSG under an inert atmosphere was presented by Sadler and co-workers.[96] The catalytic reaction was proposed as an azo ligand-centered redox reaction. Although the reaction was quite slow with a TOF of 0.37 h^{-1} and cellular GSH was not quantified, the formation of reactive oxygen species in A549 cells suggested the occurrence of catalytic reactions in cells.
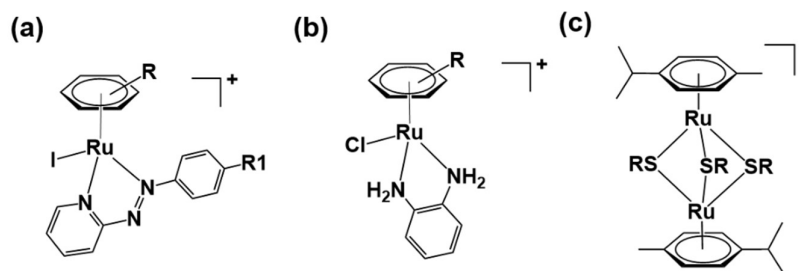
Figure 1.16. Complexes with catalytic activity toward GSH oxidation.

Next, other typical Ru complexes capable of oxidizing GSH were discovered as shown in Figure 1.16. The Ru arene complexes with a diamine ligand (Figure 1.16b) were not claimed as catalysts, but interestingly they were able to oxidize GSH to

GSSG and be regenerated by O_2.[97] Therrien et al. also reported thiolato-bridged Ru arene dimers (Figure 1.16c) with higher antiproliferative activity toward cancer cells as well as cisplatin-resistant cell lines.[98] These complexes catalyze the oxidation of GSH with a TOF of 7.4 h^{-1} even in the presence of 50 mM NaCl.[99] Meanwhile, these Ru dimers showed higher catalytic activity than highly cytotoxic Rh^{III} and Ir^{III} analogues.[100] No direct correlation between GSH oxidation and cytotoxicity could be drawn, but the toxicity might be at least partially due to their catalytic ability toward GSH. Other multinuclear Ru^{II} complexes with "cage" structures were also reported by Therrien *et. al.* which oxidize GSH and cysteine catalytically.[101] More recently, the half-sandwich iridium complex $[(Cp^{xbiph})Ir(1,10\text{- phenanthroline})SH]^+$ shown in Figure 1.12g with higher potency than cisplatin toward A2780 cells could catalyse GSH oxidation in the test tube.[102]

1.6.4 NAD$^+$ Reduction and NADH Oxidation

1.6.4.1 NAD

Nicotinamide adenine dinucleotide (NAD) is a co-enzyme that plays a critical role in cellular redox metabolic reactions. The interconversion of NAD between oxidized (NAD$^+$) and reduced (NADH) forms plays vital roles in cellular metabolic processes such as cytosol energy metabolism, gene expression, immunological functions, and cell death.[103] Recent studies indicate that enhanced NAD metabolism is involved in cancer development and progression, and is considered a promising therapeutic target in cancer treatment.[104] Various metal-based anticancer complexes with catalytic reactivity for interfering with the NAD$^+$/NADH ratio have been reported.[88]

1.6.4.2 NAD⁺ Reduction

Metal-complexes catalyzing regioselective reduction of NAD^+ to NADH via hydride

transfer reactions with sodium formate as a hydride donor (shown in Figure 1.17a)

were pioneered by Steckhan and co-workers using the substituted 2,2'-bipyridine Cp*

Ir/Rh complexes.[105] Furthermore, a detailed mechanism was proposed by Fish *et al.*

as shown in Figure 1.17b.[106,107]
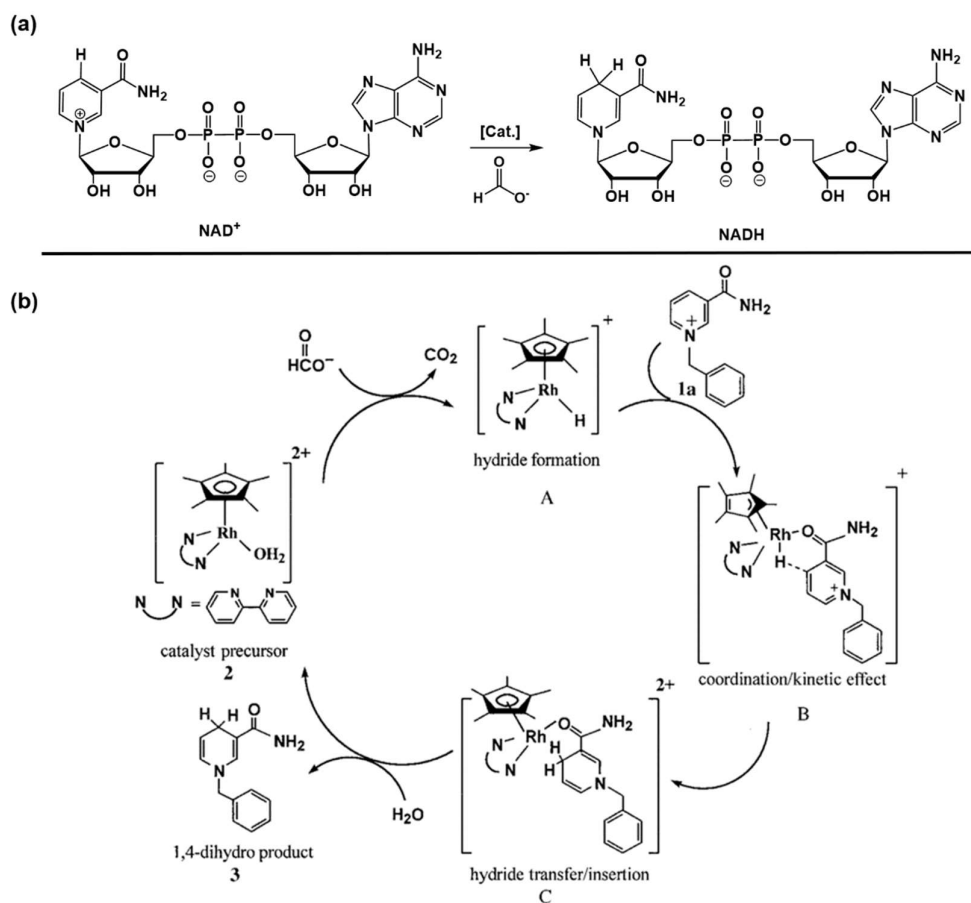
Figure 1.17. (a) The regeneration of NADH by metal-based catalysts with formate

as a hydride donor; (b) the catalyzing mechanism for Cp* rhodium aqua adducts in

reduction of a NAD^+ analogue (1a) with formate as a hydride source. Adapted from

ref. 107.

In the catalytic process, sodium formate reacts with the Cp* Rh(bpy)-aqua precursor (compound 2 in Figure 1.17b) to generate a Rh-H intermediate (A in Figure 1.17b) through a β-hydrogen elimination reaction to produce CO_2. A subsequent regioselective hydride transfer step from the Rh centre to NAD^+ is crucially initiated by the coordination of the amide carbonyl group to the Rh centre with a ring-slipped Cp^* in η^3 coordination mode.[107]
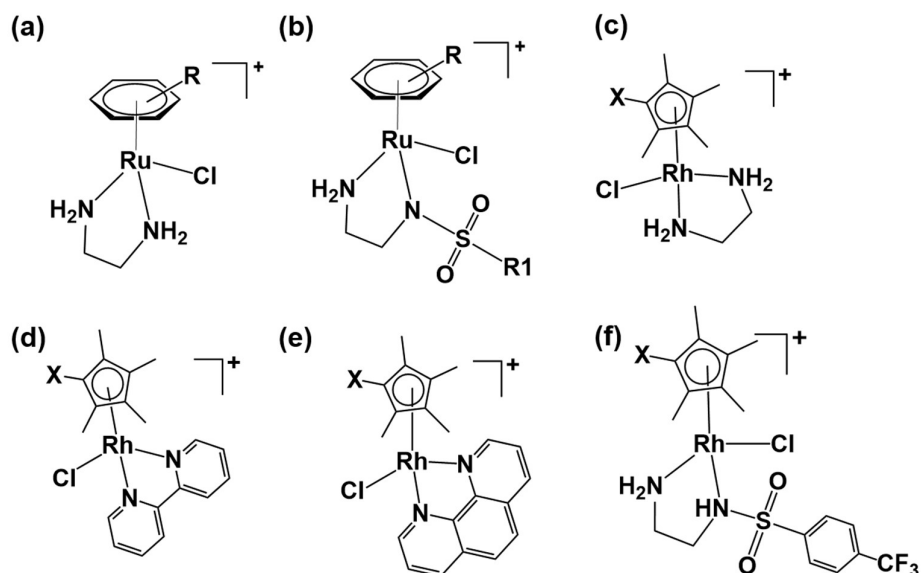
Figure 1.18. Chemical structures of metal complexes studied as hydride transfer catalysts from sodium formate in the reduction of NAD^+ to NADH.

Sadler *et. al* started to exploit the cellular regeneration of coenzyme NADH by metal complexes from 2006.[108] The catalytic activity of a series of Ru(II) en complexes bearing different arenes (Figure 1.18a) toward reduction of NAD^+ using formate as hydride donor was initially studied. Their catalytic activity was found to depend on the arenes, and the tolerated co-adminstrated formate by A549 cells was

up to 2.5 mM.[108] Although the most active complex owned low turnover frequency TOF (0.82 h^{-1}) in the test tube, this work provided a foundation that such catalytic reactions could be performed *in vitro* with more active catalysts.

Subsequently, cellular catalytic ability toward NAD$^+$ reduction by Noyori-type Ru(II) arene complexes (Figure 1.18b) was studied by incubating these complexes with formate in human A2780 ovarian cancer cells.[109] Excitingly, a formate concentration-dependent increase of antiproliferative activity of these Ru complexes was observed and the cellular NAD$^+$/NADH ratio decreased steadily over 24 h, confirming that the catalytic reduction reaction could occur inside cells.[109]

In addition, a series of Rh(III) half-sandwich complexes [(Cp^X)Rh(N^N)Cl]$^+$ (Cp^X = Cp*, Cp^{xph}, Cp^{xbiph}) as shown in Figure 1.18c-f, were synthesised and their catalytic activity for reduction of NAD$^+$ in the test tube was found to be higher than the activity of the Ru^{II} analogues.[110] The extension of Cp^X ring from Cp* to Cp^{xbiph} increased the activity, although decreased the aqueous solubility. Some complexes were not active towards A2780 cells, but their antiproliferative activity increased after co-administration with formate.[110]

1.6.4.3 NADH Oxidation

Apart from formate as hydride donor forming reactive metal-hydride adducts, organometallic catalysts can also accept hydride from NADH to generate NAD$^+$. The Sadler research group have reported a series of Ru(II) arene complexes containing the bipyrimidine bidentate ligands (Figure 1.19a), which were able to oxidize NADH to NAD$^+$ through formation of Ru-H intermediates detected by ^{1}H NMR at δ -7.5

ppm. The Ru-H intermediates subsequently reduced pyruvate to lactate, although formation of lactate-Ru adducts was observed as a side reaction.[111] Similarly, the Cp^* iridium complex with phenanthroline ligand (phen) shown in Figure 1.19b also displayed the ability of oxidizing NADH to generate NAD^+, by forming Ir-hydride species at δ -11.3 ppm.[111] The hydride adducts formed by analogous complex $[Cp^{xph}Ir(phen)Cl]^{2+}$ with NADH can reduce quinones (Q) to semiquinones ($Q^{\bullet-}$).[75] This iridium complex was highly active against ovarian A2780 cancer cells with an IC_{50} value of 6.7 μM, and increased the cellular NAD^+/NADH ratio significantly from 8 to almost 15 in 6 h, suggesting these complexes can behave as catalysts in cancer cells.[75]

Recently, a series of half-sandwich Ir complexes $[(\eta^5\text{-}Cp^X)Ir(ppy)Z]^{0/+}$ (ppy = 2-phenylpyridine or its derivatives, Z = Cl or pyridine, as shown in Figure 1.19c and 1.19d), were also found to be efficient catalysts toward NADH oxidation by generating Ir-hydride species and NAD^+.[78,112] In particular, the Cp^{xbiph} complex $[(\eta^5\text{-}Cp^{xbiph})Ir(ppy)py]^{0/+}$ with a pyridine ligand displayed 10-fold higher potency than cisplatin against A2780 cells, and 13 times lower toxicity towards normal human lung fibroblast cells than A2780 cancer cells.[78] Hydrogen peroxide was detected during reaction of the complex with NADH in the test tube due to the catalytic hydride transfer from NADH to oxygen.[78] Consistently, significant ROS levels in A2780 cancer cells were also generated by the pyridine iridium complex, which was likely to contribute to the cytotoxicity.[78] The proposed cellular reaction pathways for the pyridine complex are shown in Figure 1.19g. With the cellular abundant GSH present, the iridium complex was able to form Ir-SG adducts which inhibiting the catalytic

activity. However, the pyridine complex with a slower hydrolysis rate ($t_{1/2}$ = 78 min) reacted less readily with GSH compared to the chlorido analogue which hydrolyzes within minutes at 310 K, thus leading to less deactivation.[78]
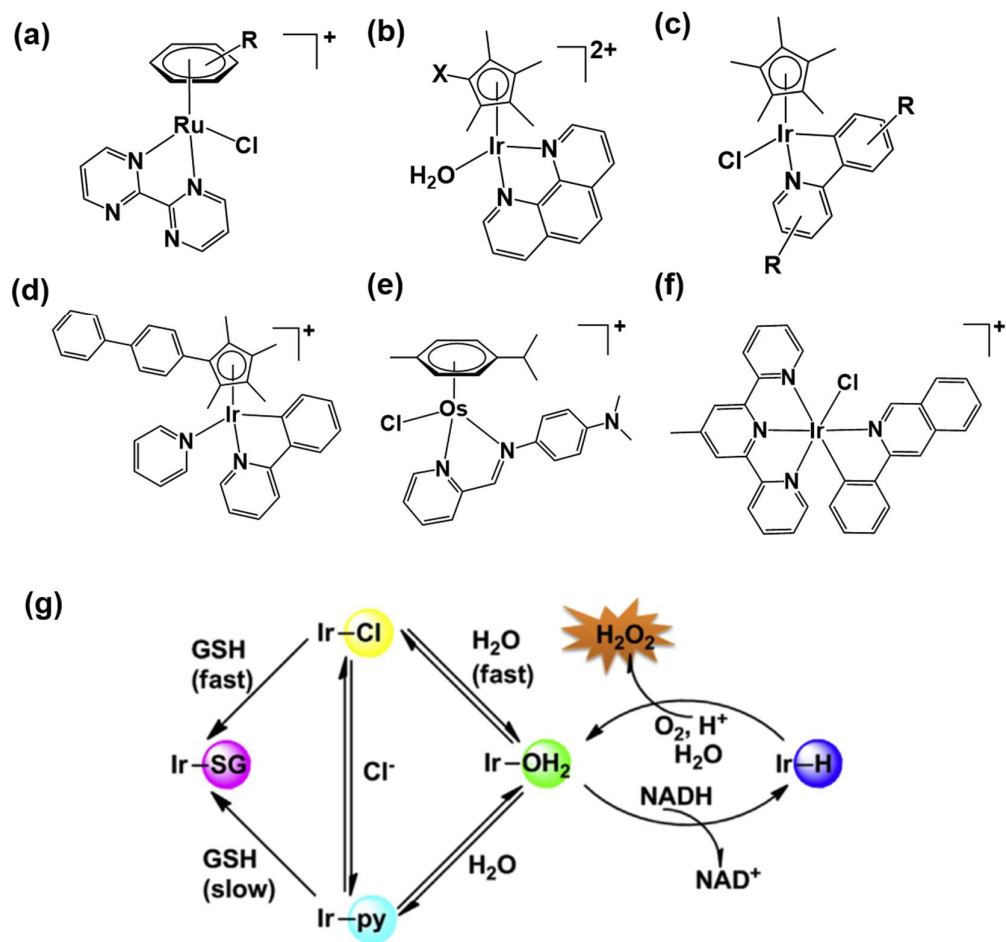
Figure 1.19. (a)-(f) Chemical structures of metal complexes reported as catalysts in the oxidation of NADH to NAD$^+$; (g) the catalytic reactions of Ir^{III} pyridine and its Cl analogue for generation of H$_2$O$_2$ and their deactivation by GSH. Adapted from ref. 78.

A series of Os(II) arene complexes of the type [(arene)Os(iminopyridine)X] (X = I, Cl) were also studied as catalysts toward NADH oxidation under physiological conditions.[113] The Os(II) complex shown in Figure 1.19e was observed to form Os-H species at δ -4.2 ppm.[113] Oxygen was also proved to be the crucial factor in the catalysis process. The complex increased the NAD$^+$/NADH ration from 2.54 to 5.44 after 6 h incubation with A2780 cells.[113]
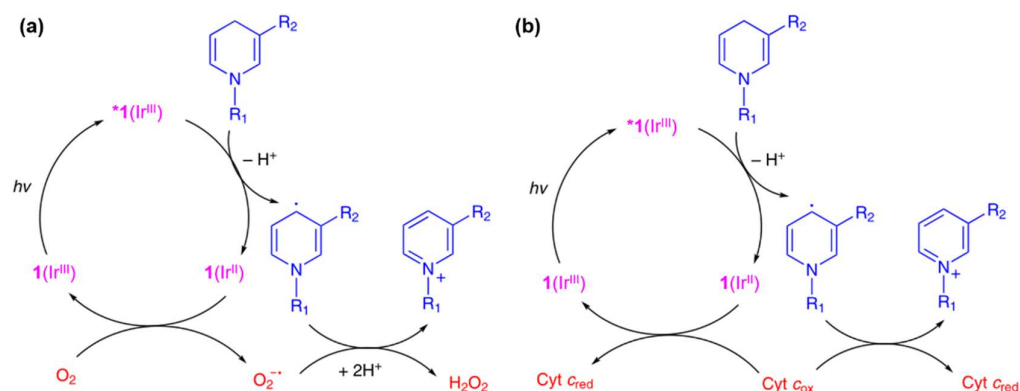
Figure 1.20. The photocatalytic cycles for oxidation of NADH by the iridium complex shown in Figure 1.19f, which produces NAD$^\bullet$ radicals, (a) under normoxia with the involvement of oxygen and hydrogen peroxide production; (b) under hypoxia with the reduction of Fe^{3+}-cyt c. Adapted from ref. 114.

More recently, another organoiridum(III) photocatalyst shown in Figure 1.19f has been reported to induce cellular NADH depletion, intracellular redox imbalance in A549 lung cancer cells and immunogenic apoptotic cell death.[114] Impressively, upon light irradiation in biological media, this complex catalytically oxidizes NADH with two orders of magnitude higher turnover frequency than the half-sandwich

iridium catalyst shown in of Figure 1.19c.[114] The generation of NAD$^\bullet$ radicals intermediates was the significant step in the catalytic cycle, instead of the metal-hydride adducts found in the reaction of the abovementioned half-sandwich Ir or Ru/Os arene complexes with NADH.[114] As shown in Figure 1.20, the NAD$^\bullet$ radicals can facilitate the conversion of the superoxide anion to hydrogen peroxide under normoxia, whereas under hypoxia, they can reduce Fe^{3+}-cytochrome c.[114] Such an oxygen-independent mechanism indicates that this type of iridium complexes is promising candidates for photodynamic therapy in combating the hypoxic tumours.

1.7 Aims

Based on the reported structure-activity relationships for organometallic anticancer complexes, general aim of this thesis is to explore new families of half-sandwich iridium(III)/rhodium(III) complexes as anticancer agents with novel mechanisms of action, and their possible catalytic properties which might contribute to the cytotoxicity. Ligand-controlled chemical (catalytic) reactivity, cytotoxicity, and cellular mechanisms of action (MoAs) are investigated. More specific objectives were as follows.

1. Synthesis, characterisation, evaluation of the chemical reactivity with biomolecules and the antiproliferative activity of half-sandwich iridium(III) iodido complexes of the type $[(\eta^5\text{-Cp}^X)\text{Ir}(R_1\text{-azpy-}R_2)I]^+$ containing different substituted 2-phenylazopyridine (azpy) ligands.

2. Synthesis, characterisation, comparison of the chemical reactivity, cytotoxicity, and MoAs of half-sandwich rhodium(III) complexes with the general formula of $[(\eta^5\text{-Cp}^X)\text{Rh}(C^\wedge N)Z]^+$, where $C^\wedge N$ is benzo[h]quinoline chelating ligand and the leaving group Z is chlorido or pyridine.

3. Synthesis and characterisation of a half-sandwich iridium anticancer complex $[(\eta^5\text{-Cp}^*)\text{Ir}(4\text{-methyl-}4'\text{-carboxy-}2,2'\text{-bipyridine})\text{Cl}]\text{PF}_6$ conjugated to a tumour-targeting peptide via copper free click chemistry.

4. Synthesis, characterisation, and exploration of the chemical reactivity and cytotoxicity of half-sandwich iridium complexes conjugated to ferrocene and luminescent probes.

1.8 References

1   Retrieved March 10, 2020, from https://www.who.int/news-room/fact-sheets/detail/cancer.

2   D. Hanahan and R. A. Weinberg, *Cell*, 2000, **100**, 57-70.

3   D. Hanahan and R. A. Weinberg, *Cell*, 2011, **144**, 646-674.

4   Retrieved March 10, 2020, from https://www.cancerresearchuk.org/about-cancer/cancer-in-general/treatment.

5   S. Norn, H. Permin, E. Kruse and P. Kruse, *Med. Hist.*, 2008, **36**, 21-40.

6   U. Ndagi, N. Mhlongo and M. E. Soliman, *Drug Des. Dev. Ther.*, 2017, **11**, 599-616.

7   R. J. Papac, *Yale J. Biol. Med.*, 2001, **74**, 391.

8   S. Dasari and P. B. Tchounwou, *Eur. J. Pharmacol.*, 2014, **740**, 364-378.

9   P. Köpf-Maier, *Eur. J. Clin. Pharmacol.*, 1994, **47**, 1-16.

10   I. Ott and R. Gust, *Arch. Pharm.*, 2007, **340**, 117-126.

11   M. Galanski, M. A. Jakupec and B. K. Keppler, *Curr. Med. Chem.*, 2005, **12**, 2075-2094.

12   T. C. Johnstone, K. Suntharalingam and S. J. Lippard, *Chem. Rev.*, 2016, **116**, 3436-3486.

13   T. C. Johnstone, J. J. Wilson and S. J. Lippard, *Inorg. Chem.*, 2013, **52**, 12234-12249.

14   R. C. Todd and S. J. Lippard, *Metallomics*, 2009, **1**, 280-291.

15   P. M. Bruno, Y. Liu, G. Y. Park, J. Murai, C. E. Koch, T. J. Eisen, J. R. Pritchard, Y. Pommier, S. J. Lippard and M. T. Hemann, *Nat. Med.*, 2017, **23**,

461-471.

16   J. W. Reishus and D. S. Martin Jr, *J. Am. Chem. Soc.*, 1961, **83**, 2457-2462.

17   P. Abada and S. B. Howell, *Met.-Based Drugs*, 2010, **2010**, 317581.

18   S. Zhang, K. S. Lovejoy, J. E. Shima, L. L. Lagpacan, Y. Shu, A. Lapuk, Y. Chen, T. Komori, J. W. Gray and X. Chen, *Cancer Res.*, 2006, **66**, 8847-8857.

19   A. I. Ivanov, J. Christodoulou, J. A. Parkinson, K. J. Barnham, A. Tucker, J. Woodrow and P. J. Sadler, *J. Biol. Chem.*, 1998, **273**, 14721-14730.

20   D.-W. Shen, L. M. Pouliot, M. D. Hall and M. M. Gottesman, *Pharmacol. Rev.*, 2012, **64**, 706-721.

21   N. P. Farrell, *Chem. Soc. Rev.*, 2015, **44**, 8773-8785.

22   N. Muhammad and Z. Guo, *Curr. Opin. Chem. Biol.*, 2014, **19**, 144-153.

23   S. Leijen, S. A. Burgers, P. Baas, D. Pluim, M. Tibben, E. van Werkhoven, E. Alessio, G. Sava, J. H. Beijnen and J. H. Schellens, *Investig. New Drugs.*, 2015, **33**, 201-214.

24   E. Alessio and L. Messori, *Molecules*, 2019, **24**, 1995.

25   P. V. Simpson, N. M. Desai, I. Casari, M. Massi and M. Falasca, *Future Med. Chem.*, 2019, **11**, 119-135.

26   N. P. Barry and P. J. Sadler, *Chem. Commun.*, 2013, **49**, 5106-5131.

27   L. S. Flocke, R. Trondl, M. A. Jakupec and B. K. Keppler, *Invest. New Drugs*, 2016, **34**, 261-268.

28   M. J. Clarke, *Coord. Chem. Rev.*, 2002, **232**, 69-93.

29   F. Heinemann, J. Karges and G. Gasser, *Acc. Chem. Res.*, 2017, **50**, 2727-2736.

30   N. J. Farrer, L. Salassa and P. J. Sadler, *Dalton Trans.*, 2009, **48**, 10690-10701.

31   S. Monro, K. L. Colón, H. Yin, J. Roque III, P. Konda, S. Gujar, R. P. Thummel, L. Lilge, C. G. Cameron and S. A. McFarland, *Chem. Rev.*, 2018, **119**, 797-828.

32   G. Gasser, I. Ott and N. Metzler-Nolte, *J. Med. Chem.*, 2010, **54**, 3-25.

33   P. M. Abeysinghe and M. M. Harding, *Dalton Trans.*, 2007, 3474-3482.

34   G. Gasser, I. Ott and N. Metzler-Nolte, *J. Med. Chem.*, 2011, **54**, 3-25.

35   P. Köpf-Maier, H. Köpf and E. W. Neuse, *Angew. Chem. Int. Ed. Engl.*, 1984, **23**, 456-457.

36   V. J. Fiorina, R. J. Dubois and S. Brynes, *J. Med. Chem.*, 1978, **21**, 393-395.

37   C. Ornelas, *New J. Chem.*, 2011, **35**, 1973-1985.

38   A. Nguyen, A. Vessières, E. A. Hillard, S. Top, P. Pigeon and G. Jaouen, *Chimia*, 2007, **61**, 716-724.

39   V. C. Jordan, *Nat. Rev. Drug Discov.*, 2003, **2**, 205-213.

40   S. Top, A. Vessières, G. Leclercq, J. Quivy, J. Tang, J. Vaissermann, M. Huché and G. Jaouen, *Chem. Eur. J.*, 2003, **9**, 5223-5236.

41   E. Hillard, A. Vessières, L. Thouin, G. Jaouen and C. Amatore, *Angew. Chem. Int. Ed.*, 2006, **45**, 285-290.

42   O. Novakova, H. Chen, O. Vrana, A. Rodger, P. J. Sadler and V. Brabec, *Biochemistry*, 2003, **42**, 11544-11554.

43   H. K. Liu, F. Wang, J. A. Parkinson, J. Bella and P. J. Sadler, *Chem. Eur. J.*, 2006, **12**, 6151-6165.

44   R. Aird, J. Cummings, A. Ritchie, M. Muir, R. Morris, H. Chen, P. Sadler and

D. Jodrell, *Br. J. Cancer*, 2002, **86**, 1652-1657.

45   F. Wang, J. Xu, A. Habtemariam, J. Bella and P. J. Sadler, *J. Am. Chem. Soc.*, 2005, **127**, 17734-17743.

46   S. Krueger, C. Haeckel, F. Buehling and A. Roessner, *Cancer Res.*, 1999, **59**, 6010-6014.

47   P. L. Fernández, X. Farré, A. Nadal, E. Fernández, N. Peiró, B. F. Sloane, G. P. Shi, H. A. Chapman, E. Campo and A. Cardesa, *Int. J. Cancer*, 2001, **95**, 51-55.

48   S. Mohanam, S. L. Jasti, S. R. Kondraganti, N. Chandrasekar, S. S. Lakka, Y. Kin, G. N. Fuller, A. W. Yung, A. P. Kyritsis and D. H. Dinh, *Oncogene*, 2001, **20**, 3665-3673.

49   A. Casini, C. Gabbiani, F. Sorrentino, M. P. Rigobello, A. Bindoli, T. J. Geldbach, A. Marrone, N. Re, C. G. Hartinger and P. J. Dyson, *J. Med. Chem.*, 2008, **51**, 6773-6781.

50   P. J. Dyson and G. Sava, *Dalton Trans.*, 2006, 1929-1933.

51   S. Betanzos-Lara, L. Salassa, A. Habtemariam and P. J. Sadler, *Chem. Commun.*, 2009, 6622-6624.

52   F. Barragán, P. López-Senín, L. Salassa, S. Betanzos-Lara, A. Habtemariam, V. Moreno, P. J. Sadler and V. Marchán, *J. Am. Chem. Soc.*, 2011, **133**, 14098-14108.

53   R. Carter, A. Westhorpe, M. Romero, A. Habtemariam, C. Gallevo, Y. Bark, N. Menezes, P. Sadler and R. Sharma, *Sci. Rep.*, 2016, **6**, 20596.

54   M. Hanif, M. V. Babak and C. G. Hartinger, *Drug Discovery Today*, 2014, **19**,

1640-1648.

55   A. F. A. Peacock, A. Habtemariam, S. A. Moggach, A. Prescimone, S. Parsons and P. J. Sadler, *Inorg. Chem.*, 2007, **46**, 4049-4059.

56   A. F. Peacock, A. Habtemariam, R. Fernández, V. Walland, F. P. Fabbiani, S. Parsons, R. E. Aird, D. I. Jodrell and P. J. Sadler, *J. Am. Chem. Soc.*, 2006, **128**, 1739-1748.

57   A. F. Peacock, S. Parsons and P. J. Sadler, *J. Am. Chem. Soc.*, 2007, **129**, 3348-3357.

58   S. H. van Rijt, A. F. Peacock, R. D. Johnstone, S. Parsons and P. J. Sadler, *Inorg. Chem.*, 2009, **48**, 1753-1762.

59   S. H. v. Rijt, H. Kostrhunova, V. Brabec and P. J. Sadler, *Bioconjugate Chem.*, 2011, **22**, 218-226.

60   Y. Fu, A. Habtemariam, A. M. B. H. Basri, D. Braddick, G. J. Clarkson and P. J. Sadler, *Dalton Trans.*, 2011, **40**, 10553-10562.

61   S. D. Shnyder, Y. Fu, A. Habtemariam, S. H. van Rijt, P. A. Cooper, P. M. Loadman and P. J. Sadler, *Med. Chem. Comm*, 2011, **2**, 666-668.

62   R. J. Needham, C. Sanchez-Cano, X. Zhang, I. Romero-Canelón, A. Habtemariam, M. S. Cooper, L. Meszaros, G. J. Clarkson, P. J. Blower and P. J. Sadler, *Angew. Chem. Int. Ed.*, 2017, **56**, 1017-1020.

63   X. Zhang, F. Ponte, E. Borfecchia, A. Martini, C. Sanchez-Cano, E. Sicilia and P. J. Sadler, *Chem. Commun.*, 2019, **55**, 14602-14605.

64   C. Sanchez-Cano, I. Romero-Canelón, Y. Yang, I. J. Hands-Portman, S. Bohic, P. Cloetens and P. J. Sadler, *Chem. Eur. J.*, 2017, **23**, 2512-2516.

65   C. Sanchez-Cano, D. Gianolio, I. Romero-Canelon, R. Tucoulou and P. J. Sadler, *Chem. Commun.*, 2019, **55**, 7065-7068.

66   J. Maksimoska, D. S. Williams, G. E. Atilla-Gokcumen, K. S. M. Smalley, P. J. Carroll, R. D. Webster, P. Filippakopoulos, S. Knapp, M. Herlyn and E. Meggers, *Chem. Eur. J.*, 2008, **14**, 4816-4822.

67   Retrieved   March   10,   2020,   from https://www.statista.com/statistics/585840/demand-for-iridium-worldwide/.

68   M. Iglesias and L. A. Oro, *Chem. Soc. Rev.*, 2018, **47**, 2772-2808.

69   J. D. Blakemore, R. H. Crabtree and G. W. Brudvig, *Chem. Rev.*, 2015, **115**, 12974-13005.

70   J. Liu, X. Wu, J. A. Iggo and J. Xiao, *Coord. Chem. Rev.*, 2008, **252**, 782-809.

71   Z. Liu and P. J. Sadler, *Acc. Chem. Res.*, 2014, **47**, 1174-1185.

72   P. Štarha, A. Habtemariam, I. Romero-Canelón, G. J. Clarkson and P. J. Sadler, *Inorg. Chem.*, 2016, **55**, 2324-2331.

73   J. M. Hearn, G. M. Hughes, I. Romero-Canelón, A. F. Munro, B. Rubio-Ruiz, Z. Liu, N. O. Carragher and P. J. Sadler, *Metallomics*, 2018, **10**, 93-107.

74   J. M. Hearn, I. Romero-Canelón, B. Qamar, Z. Liu, I. Hands-Portman and P. J. Sadler, *ACS Chem. Biol.*, 2013, **8**, 1335-1343.

75   Z. Liu, R. J. Deeth, J. S. Butler, A. Habtemariam, M. E. Newton and P. J. Sadler, *Angew. Chem. Int. Ed.*, 2013, **52**, 4194-4197.

76   S. Betanzos-Lara, Z. Liu, A. Habtemariam, A. M. Pizarro, B. Qamar and P. J. Sadler, *Angew. Chem. Int. Ed.*, 2012, **51**, 3897-3900.

77   V. Novohradsky, L. Zerzankova, J. Stepankova, A. Kisova, H. Kostrhunova,

Z. Liu, P. J. Sadler, J. Kasparkova and V. Brabec, *Metallomics*, 2014, **6**, 1491-1501.

78   Z. Liu, I. Romero-Canelón, B. Qamar, J. M. Hearn, A. Habtemariam, N. P. Barry, A. M. Pizarro, G. J. Clarkson and P. J. Sadler, *Angew. Chem. Int. Ed.*, 2014, **53**, 3941-3946.

79   Y. Yang, L. Guo, Z. Tian, X. Ge, Y. Gong, H. Zheng, S. Shi and Z. Liu, *Organometallics*, 2019, **38**, 1761-1769.

80   J. Li, M. Tian, Z. Tian, S. Zhang, C. Yan, C. Shao and Z. Liu, *Inorg. Chem.*, 2018, **57**, 1705-1716.

81   Q. Du, L. Guo, M. Tian, X. Ge, Y. Yang, X. Jian, Z. Xu, Z. Tian and Z. Liu, *Organometallics*, 2018, **37**, 2880-2889.

82   C. Wang, J. Liu, Z. Tian, M. Tian, L. Tian, W. Zhao and Z. Liu, *Dalton Trans.*, 2017, **46**, 6870-6883.

83   Z. Xu, Y. Zhang, S. Zhang, X. Jia, G. Zhong, Y. Yang, Q. Du, J. Li and Z. Liu, *Cancer letters*, 2019, **447**, 75-85.

84   J. M. Zimbron, K. Passador, B. Gatin-Fraudet, C.-M. Bachelet, D. Plażuk, L.-M. Chamoreau, C. Botuha, S. Thorimbert and M. Salmain, *Organometallics*, 2017, **36**, 3435-3442.

85   W. Ma, X. Ge, Z. Xu, S. Zhang, X. He, J. Li, X. Xia, X. Chen and Z. Liu, *ACS Omega*, 2019, **4**, 15240-15248.

86   C. Mari, H. Huang, R. Rubbiani, M. Schulze, F. Würthner, H. Chao and G. Gasser, *Eur. J. Inorg. Chem.*, 2017, **2017**, 1745-1752.

87   L. Tabrizi, *Dalton Trans.*, 2017, **46**, 7242-7252.

88   J. J. Soldevila-Barreda and N. Metzler-Nolte, *Chem. Rev.*, 2019, **119**, 829-869.

89   S. Alonso-de Castro, A. Terenzi, J. Gurruchaga-Pereda and L. Salassa, *Chem. Eur. J.*, 2019, **25**, 6651-6660.

90   L. K. McKenzie, H. E. Bryant and J. A. Weinstein, *Coord. Chem. Rev.*, 2019, **379**, 2-29.

91   C. M. Moore, A.-R. Azzouzi, E. Barret, A. Villers, G. H. Muir, N. J. Barber, S. Bott, J. Trachtenberg, N. Arumainayagam, B. Gaillac, C. Allen, A. Schertz and M. Emberton, *BJU International*, 2015, **116**, 888-896.

92   C. Nicco and F. Batteux, *Molecules*, 2018, **23**, 84.

93   I. Batinic-Haberle and M. E. Tome, *Redox Biology*, 2019, **25**, 101139.

94   P. Pfeiffer, C. Qvortrup, K. Muro, M. B. Lustberg, F. Nagahama, Y. Sonehara, M. H. Bengtson, M. Nittve, C. Sonesson and C. S. Carlsson, *J. Clin. Oncol.*, 2019, **37**, TPS722-TPS722.

95   V. I. Lushchak, *J. Amino Acids*, 2012, **2012**, 26.

96   S. J. Dougan, A. Habtemariam, S. E. McHale, S. Parsons and P. J. Sadler, *Proc. Natl. Acad. Sci. U.S.A.*, 2008, **105**, 11628-11633.

97   T. Bugarcic, A. Habtemariam, R. J. Deeth, F. P. A. Fabbiani, S. Parsons and P. J. Sadler, *Inorg. Chem.*, 2009, **48**, 9444-9453.

98   M. Gras, B. Therrien, G. Süss-Fink, O. Zava and P. J. Dyson, *Dalton Trans.*, 2010, **39**, 10305-10313.

99   F. Giannini, G. Süss-Fink and J. Furrer, *Inorg. Chem.*, 2011, **50**, 10552-10554.

100   G. Gupta, A. Garci, B. S. Murray, P. J. Dyson, G. Fabre, P. Trouillas, F. Giannini, J. Furrer, G. Süss-Fink and B. Therrien, *Dalton Trans.*, 2013, **42**,

15457-15463.

101   F. Giannini, J. Furrer, G. Süss-Fink, C. M. Clavel and P. J. Dyson, *J. Organomet. Chem.*, 2013, **744**, 41-48.

102   P. Starha, A. Habtemariam, I. Romero-Canelón, G. J. Clarkson and P. J. Sadler, *Inorg. Chem.*, 2016, **55**, 2324-2331.

103   W. Ying, *Antioxid. Redox Sign.*, 2008, **10**, 179-206.

104   K. Yaku, K. Okabe, K. Hikosaka and T. Nakagawa, *Front. Oncol.*, 2018, **8**.

105   E. Steckhan, S. Herrmann, R. Ruppert, E. Dietz, M. Frede and E. Spika, *Organometallics*, 1991, **10**, 1568-1577.

106   H. C. Lo, C. Leiva, O. Buriez, J. B. Kerr, M. M. Olmstead and R. H. Fish, *Inorg. Chem.*, 2001, **40**, 6705-6716.

107   H. C. Lo, O. Buriez, J. B. Kerr and R. H. Fish, *Angew. Chem. Int. Ed.*, 1999, **38**, 1429-1432.

108   Y. K. Yan, M. Melchart, A. Habtemariam, A. F. Peacock and P. J. Sadler, *JBIC, J. Biol. Inorg. Chem.*, 2006, **11**, 483-488.

109   J. J. Soldevila-Barreda, I. Romero-Canelón, A. Habtemariam and P. J. Sadler, *Nat.Commun.*, 2015, **6**, 6582.

110   J. J. Soldevila-Barreda, A. Habtemariam, I. Romero-Canelón and P. J. Sadler, *J. Inorg. Biochem.*, 2015, **153**, 322-333.

111   S. Betanzos-Lara, Z. Liu, A. Habtemariam, A. M. Pizarro, B. Qamar and P. J. Sadler, *Angew. Chem. Int. Ed.*, 2012, **51**, 3897-3900.

112   A. J. Millett, A. Habtemariam, I. Romero-Canelón, G. J. Clarkson and P. J. Sadler, *Organometallics*, 2015, **34**, 2683-2694.

113   Y. Fu, M. J. Romero, A. Habtemariam, M. E. Snowden, L. Song, G. J. Clarkson, B. Qamar, A. M. Pizarro, P. R. Unwin and P. J. Sadler, *Chem. Sci.*, 2012, **3**, 2485-2494.

114   H. Huang, S. Banerjee, K. Qiu, P. Zhang, O. Blacque, T. Malcomson, M. J. Paterson, G. J. Clarkson, M. Staniforth and V. G. Stavros, *Nat. Chem.*, 2019, **11**, 1041-1048.

Chapter 2

Materials and Methods

In this Chapter, the materials including the synthesis and characterisation of iridium and rhodium dimmer precursors, instrumental and experimental methods are described. More detailed experimental methods are given in each Chapter.

2.1 Materials

2.1.1 Chemicals

Iridium(III) trichloride hydrate and rhodium(III) trichloride hydrate were purchased from Precious Metals Online. 1,2,3,4,5-pentamethylcyclopentadiene, 2,3,4,5-tetramethyl-2-cyclopenta-2-enone, n-butyllithium solution (1.6 M in hexanes), and phenyl-lithium (1.9 M in dibutyl ether), ammonium hexafluorophosphate, potassium iodide, analytical grade sodium chloride, 9-ethylguanine and guanosine 5'-monophosphate disodium salt hydrate, $[(Cp^*)Rh(\mu\text{-Cl})Cl]_2$, silver nitrate, sodium formate, sodium pyruvate, β-nicotinamide adenine dinucleotide reduced disodium salt (NADH), Quantofix® peroxides test sticks (1-100 mg/L range), anhydrous sodium acetate, triethylamine (TEA), celite, Δ-trisphat tetrabutylammonium salt, cisplatin, dimethyl sulfoxide (DMSO) for cell culture use, and sulforhodamine B sodium salt were purchased from Sigma-Aldrich. Reduced glutathione was obtained from Alfa Aesar. Analytical grade disodium hydrogen phosphate dihydrate, disodium hydrogen phosphate dodecahydrate and nitric acid (68%-70% v/v) were obtained from Fisher Scientific. The iridium/platinum inductively coupled plasma (ICP) standard (1000 ± 10 µg/ml in 10% v/v HCl) and the rhodium standard (1000 ± 10 µg/ml in 15% v/v HCl) were obtained from Inorganic Ventures.

Solvents of laboratory grade used for syntheses, HPLC grade water and acetonitrile, HPLC grade trifluoroacetic acid (Htfa) are obtained from Fisher Scientific or Sigma-Aldrich. NMR solvents ($\geq$ 99.8 atom D %) methanol-d_4, deuterium oxide-d_2 chloroform-d_1, DMSO-d_6, acetone-d_6, acetonitrile-d_3 were purchased from Sigma-Aldrich.

2.1.2 Biological Materials

A2780cisR (cisplatin resistant), A549 human lung and A2780 human ovarian cancer cell lines were purchased from the European Collection of Animal Cell Culture (ECACC, Salisbury, U.K.). Roswell Park Memorial Institute (RPMI-1640) medium and Dulbecco's phosphate-buffered saline (DPBS) containing 2.7 mM KCl,1.5 mM KH_2PO_4, 136.9 mM NaCl, and 8.9 mM Na_2HPO_4 were purchased from Lonza Verviers SPRL, fetal bovine serum (FBS) and solution stabilized penicillin-streptomycin with 10,000 units penicillin and 10 mg streptomycin/mL from Sigma-Aldrich.

2.1.3 Synthesis of Ligands
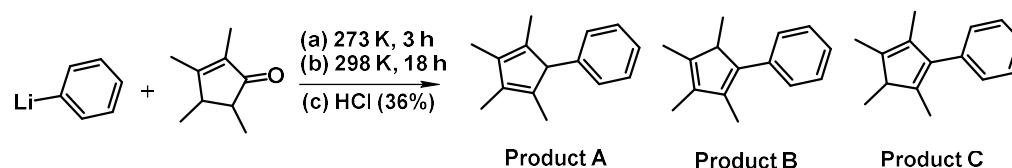
Figure 2.4. Synthetic route for the HCp^{xph} ligand.[1]

A solution of phenyllithium (100 mL, 190 mmol, 1.9 M in dibutyl ether) in a dry three-neck flask was added dropwise 2,3,4,5-tetramethyl-2-cyclopentanone (25 mL, 168 mmol) under nitrogen atmosphere. The solution was kept at 273 K using ice water and NaCl. The reaction was warmed to ambient temperature whist stirring over overnight. The yellow solution was cooled down by addition of ice and then acidified with HCl (36%) to pH 2.0. The resulted yellow solution was extracted with diethyl ether (3 x 50 mL) and washed with brine. The combined organic portions were dried over anhydrous MgSO4, filtered and reduced to dryness under vacuum. This crude product was purified by distillation under vacuum with the fraction obtained at 410 K, 0.4 mbar. Finally, 30.78 g yellow liquid was collected. Yield 85%. ^{1}H-NMR (400 MHz, CDCl3) δ 7.60-7.58 (0.17H, m), 7.45-7.42 (0.19H, m), 7.38-7.32 (4H, m), 7.27-7.23 (4.8H, m), 7.20-7.14 (2.68H, m), 6.93-6.91 (0.87H, m), 3.22-3.17 (1.31 H, m), 2.72-2.66 (0.57H, m), 2.02 (3.78H, s), 1.93 (3.63H, s), 1.89 (1.48H, s), 1.86 (5.36H, s), 1.83 (2.70H, s), 1.72 (1.45H, s), 1.67 (2.69H, s), 1.12 (1.63H, d, J = 7.5 Hz), 0.95 (4.02H, d, J = 7.5 Hz).

2.1.4 Synthesis of Chlorido Iridium Dimer
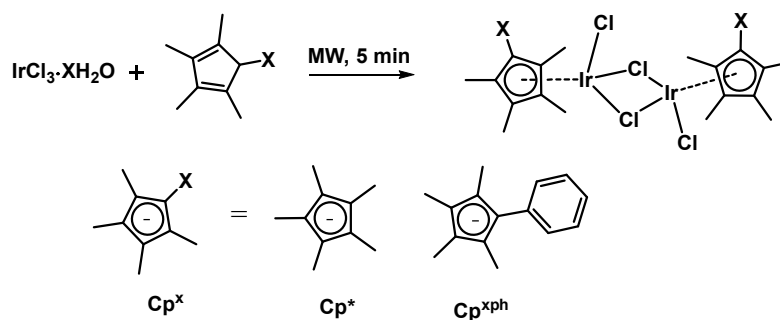
Figure 2.1. Synthetic route for $[(\eta^5\text{-}Cp^X)Ir(\mu\text{-}Cl)Cl]_2$ ($Cp^X = Cp^*$ or Cp^{xph}).[2]

General procedure: $IrCl_3$ was reacted with 2.0 mol equiv. of HCp^* (yellow liquid),

HCp^{xph} (yellow liquid) or HCp^{xbiph} (yellow solid) in 10 mL degassed methanol within

a microwave reactor at 413 K, 5 min, 150 W. The product was washed with *n*-pentane

and recrystallized with DCM/Et$_2$O, then characterised by ^{1}H NMR in CDCl$_3$. [(η^5-

Cp*)Ir(μ-Cl)Cl]$_2$ orange solid, yield 61%. ^{1}H NMR (300 MHz, CDCl$_3$): 1.58 (15H,

s). [(η^5-Cp^{xph})Ir(μ-Cl)Cl]$_2$ orange solid, yield 32%. ^{1}H NMR (400 MHz, CDCl$_3$): δ

7.58-7.55 (dd, 4H), 7.36-7.34 (m, 6H), 1.72 (12H, s), 1.63 (12H, s).

2.1.5 Synthesis of Chlorido Rhodium Dimer
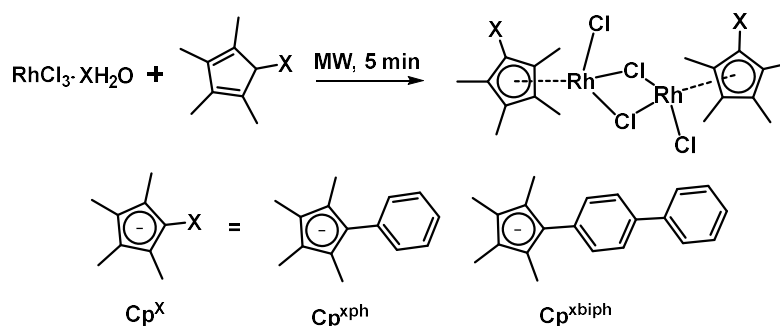
Figure 2.2. Synthetic route for [(η^5-Cp^X)Rh(μ-Cl)Cl]$_2$ (Cp^X = Cp^{xph} or Cp^{xbiph}).[2]

General procedure: RhCl$_3$ was reacted with 2.0 mol equiv. of HCp^{xph} (yellow liquid)

or HCp^{xbiph} (yellow solid) in 10 mL degassed methanol within a microwave reactor

at 413 K, 5 min, 150 W. Product was washed with *n*-pentane and recrystallized with

DCM/Et$_2$O, then characterised by ^{1}H NMR in CDCl$_3$. [(η^5-Cp^{xph})Rh(μ-Cl)Cl]$_2$ red

solid, yield 63%. ^{1}H NMR (300 MHz, CDCl$_3$): δ 7.65 (t, 4H), 7.37-7.38 (m, 6H), 1.71

(12H, s), 1.68 (12H, s). [(η^5-Cp^{xbiph})Rh(μ-Cl)Cl]$_2$, orange solid, yield 50%. ^{1}H NMR

(300 MHz, CDCl$_3$): δ 7.74 (d, 4H), 7.62-7.58 (m, 8H),7.46-7.42 (m, 4H), 7.38-7.33 (t, 2H), 1.74 (s, 24H).

2.1.6 Synthesis of Iodido Iridium Dimer
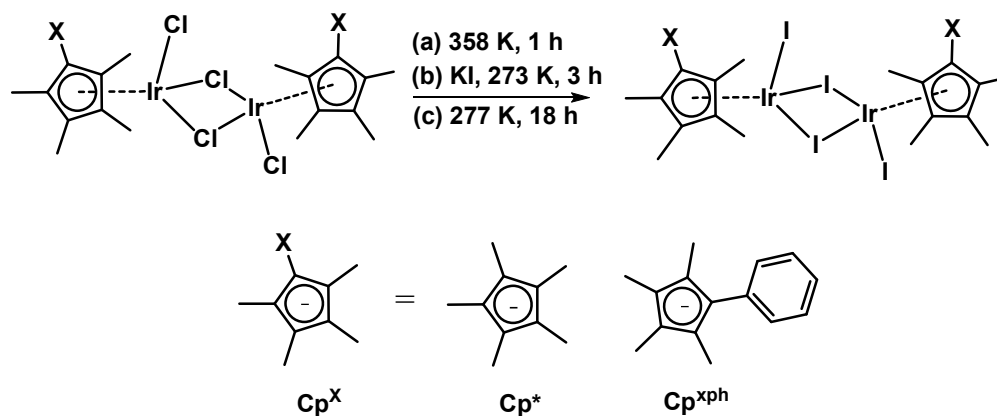
Figure 2.3. Synthetic route for [(η^5-Cp^X)Ir(μ-I)I]$_2$ (Cp^X = Cp* or Cp^{xph}).

Modified procedure from the literature[3]: the [(η^5-Cp^X)Ir(μ-Cl)Cl]$_2$ (Cp^X = Cp* or Cp^{xph}) dimer was dissolved in 20 mL MeOH and 40 mL H$_2$O under reflux at 358 K for 1 h to form clear solution. KI solid (100 mol equiv.) was added to the solution and stirred on an ice bath for 3 h. The reaction mixture was stored at 277 K overnight. The final precipitate was filtered on a Buchner funnel, then dissolved with DCM, and dried with anhydrous MgSO$_4$. Then the DCM solution was filtered and dried under vacuum. A red solid was obtained. [(η^5-Cp*)Ir(μ-I)I]$_2$ red solid, yield 92%, ^{1}H NMR (400 MHz, CDCl$_3$): δ 1.83 (15H, s). [(η^5-Cp^{xph})Ir(μ-I)I]$_2$ red solid, yield 72%, ^{1}H NMR (400 MHz, CDCl$_3$): δ 7.45-7.43 (2H, m), 7.34-7.32 (3H, m), 1.97 (6H, s), 1.94 (6H, s).

51

2.2 Methods

2.2.1 X-ray Crystallography

X-ray diffraction data collection and analyses were conducted by Dr. Guy Clarkson in Department of Chemistry, University of Warwick. Suitable crystals were selected and mounted on a glass fiber with Fomblin oil and placed on a Rigaku Oxford Diffraction SuperNova diffractometer with a dual source (Cu at zero) equipped with an AtlasS2 CCD area detector. The crystals were kept at 150 ± 2 K or 296 ± 2 K, during data collection. Using Olex2,[4] all the structures were solved with the ShelXT[5] structure solution program using direct methods and refined with the ShelXL[6] refinement package using least squares minimization. The structural image reproduction was using Mercury 3.3.

2.2.2 Nuclear Magnetic Resonance (NMR) Spectroscopy[7-9]

Nuclear Magnetic Resonance (NMR) is based on the concept that the nucleus of atoms having an odd number of protons and/or neutrons will behave like a magnet with inherent angular momentum or "spin" and there is an energy associated with each spin state. Most studied nuclei by NMR are ^{1}H, ^{13}C, ^{15}N, ^{31}P, and ^{19}F. NMR spectroscopy operates by applying a magnetic field to nuclei and then measuring the energy necessary to induce resonance. For example, when an external magnetic field (B_0) is applied, nuclei of ^{1}H (spin quantum number $I = \frac{1}{2}$) will distribute with $2I + 1 = 2$ different spin states (α and β) parallel and antiparallel to the magnetic field, which makes it possible for the energy transfer between the lower energy level (α spin state) and the higher energy level (β spin state) if a radio frequency is applied to fit the

energy gap of the two energy levels. However, the precise resonant frequency depends on the applied magnetic field and the electron shielding effects of the chemical environment, thus electronic and structural information can be obtained by the absorption frequencies of NMR spectra. The NMR signals arise as the net magnetization vector precesses around the direction of B_0 (z axis) at a characteristic frequency (called the Larmor frequency), which are detected only when the magnetization has a component in the xy plane. Thus, a pulse of radio frequency power close to Larmor frequency is applied to tip the magnetic moment (M) from z axis, bringing a component vector (Mxy) in xy plane. However, the transverse component M_{xy} dephases with time because of the magnetic field inhomogeneity and intrinsic spin-spin relaxation, thus generating the free induction decay (FID). Fourier transformation of the FID coverts the time domain signals to the frequency domain, leading to the formation of NMR spectrum. The repetition rate for acquiring an NMR signal is governed by the spin-lattice relaxation (T_1, also known as longitudinal relaxation) with a shorter T_1 time meaning less time is needed between pulses and the acquisition of a spectrum. The line width of an NMR signal is determined by the spin-spin (T_2) relaxation with shorter T_2 giving broader lines. Broad peaks in the NMR spectra can represent inhomogeneities in the magnetic field which may be caused by poor shimming, and paramagnetic impurities in the sample. Broaden peaks also may because of the exchange processes in the NMR time scale, which usually exhibit broadening of the product peaks and having no effect on the deuterated solvent.

^{1}H, ^{13}C{^{1}H}, ^{1}H-^{1}H gs (gradient selected) COSY (correlation spectroscopy), ^{1}H-^{13}C HSQC (heteronuclear single quantum coherence), and HMBC (heteronuclear

multiple bond coherence) NMR spectra in this thesis were obtained at 298 K (unless stated otherwise) on Bruker AV300, or DPX 400, or AVIII 500M or AVIII 600 NMR spectrometers. ^{1}H NMR chemical shifts were internally referenced to the residual signals of the solvents. ^{13}C{^{1}H} NMR chemical shifts were internally referenced to CDCl$_3$ (77.16 ppm) for chloroform-d$_1$, (CD$_3$)$_2$SO (39.52 ppm) for DMSO-d$_6$, and CD$_3$CN (1.39 ppm) for acetonitrile-d$_3$ and CD$_3$OD (49.15 ppm) for methanol-d$_4$. The data were processed using Mestronova and Topspin (version 2.1 Bruker UK Ltd.).

2.2.3 Electron Paramagnetic Resonance (EPR) Spectroscopy[10]

EPR is used to probe the interaction of magnetic dipoles with an applied magnetic field and electromagnetic radiation of a certain wavelength, with similar principles as NMR. The magnetic dipoles in EPR arise from one or more unpaired electrons. Due to a larger magnetic moment for an electron than the nucleus studied by NMR, the much higher frequency of electromagnetic radiation with microwaves (9-10 GHz) is needed for EPR to induce an electron-spin resonance. In practice, EPR spectra is usually generated by exposing the unpaired electrons to microwaves at a fixed frequency, then by increasing the external magnetic field to widen the energy gap between the two spin states ($m_s = \pm$ ½) of an unpaired electron until it matches the microwave energy. An EPR spectrum is the first derivative of the absorption spectrum showing the energy absorbed by free electrons in a varying magnetic field. Hyperfine splitting observed in EPR spectrum is due to spin of an electron coupling with nearby nuclear spins. The splitting number of EPR lines of a radical having M equivalent nuclei is predicted to be 2MI +1 (nuclear spin I = ½ for ^{1}H, ^{19}F, ^{31}P; I = 1

for ^{14}N), while of a radical having multiple-M_1 and M_2- equivalent nuclei is $(2M_1I_1$

$+1)(2M_2I_2 +1)$. All EPR experiments were performed with the help of Dr. B. Breeze

(Spectroscopy Research Technology Platform, University of Warwick) on a Bruker

EMX spectrometer operating at X-band with a cylindrical cavity (ER 4122 SHQE).

Unless otherwise stated, experimental parameters were as follows: modulation

amplitude 0.1 mT; conversion time and time constant 40.96 ms; number of scans 20.

In spin-trapping experiments, the microwave power was 20 mW at ca. 9.8 GHz. GSH

(40 mM) solution was prepared in a 0.1 M phosphate buffer at pH 7.8. Adventitious

metals were removed from the phosphate buffer using Chelex 100 sodium form resin

(50-100 mesh).

2.2.4 Mass Spectrometry

Mass spectrometry is an analytical technique which provides both qualitative

(structural) and quantitative (molecular mass or concentration) for the analyte

molecules after being ionized to positively or negatively charged ions by the

inonisation source. These ions reach the detector according to their mass/charge (m/z)

ratio, and the corresponding signals are recorded by the computer graphically with

the abundance of signals correlative with their m/z ratio.[11]

2.2.4.1 Electrospray Ionization Mass Spectrometry (ESI-MS)[12]

Electrospray ionization (ESI) is an ionization process to produce ions by an

electrospray, in which a high voltage is applied to a liquid to create an aerosol.

Electrospray ionization mass spectra (ESI-MS) were obtained on a Bruker Esquire

2000 spectrometer for samples dissolved in methanol. The mass spectra were recorded with a scan range of either *m/z* 50-500 or 400-1000 in positive ion mode.

2.2.4.2 High Resolution Mass Spectrometry (HR-MS)

High resolution mass spectrometry (HR-MS) allows detection of analyte to the nearest 0.001 atomic mass units which measures the exact mass of a compound and can distinguish minor changes in the structure. The Quadrupole-Time of flight (Q-TOF) combines the quadrupole (and collision cell) generating an electric field to hold the ions in a stable orbit with a time-of-flight analyzer, allowing high mass accuracy analysis. High resolution mass spectrometry analysis was carried out by Dr. Lijiang Song (Department of Chemistry, University of Warwick) using a Bruker MaXis plus Q-TOF mass spectrometer equipped with electrospray ionization source. Samples were prepared in methanol/acetonitrile.

2.2.4.3 Liquid Chromatography-Mass Spectrometry (LC-MS)[13]

LC-MS is a tandem analytical technique that combines the separational capability of high-performance liquid chromatography (HPLC) with the mass analysis capability of mass spectrometry (MS). LC-MS is used to analyze biochemical, organic, or inorganic compounds in a liquid mixture. LC-MS was carried out on a Bruker Amazon X with a scan range of m/z 50-2000 in positive mode connected online to an Agilent 1260 HPLC with the same detection wavelength as HPLC analyses. The mobile phases and solvent gradient method were the same as for HPLC described below.

2.2.5 High Performance Liquid Chromatography (HPLC)

Reverse phase HPLC is an advanced technique of column liquid chromatography, which pumps a sample mixture or analyte in the polar mobile phase at high pressure (50-350 bar) through a column packed with solid non polar (hydrophobic) materials (stationary phase) to separate, identify or quantify each constituent of mixture.[14] The common mobile phases are water with acetonitrile/methanol, into which trifluoroacetic acid is added to assist in the separation of sample components by lowering the pH to inhibit the basic analytes interacting with deprotonated silica surfaces leading to peak tailing or by acting an ion pair to aid retention. The columns are made with smaller adsorbent particles with size of 2-50 μm on average as stationary phase. The most popular column is an octadecyl carbon chain (C18)-bonded silica. The HPLC analysis was performed on a HP 1100 Series HPLC System (Agilent) using a ZORBAX Eclipse Plus C-18 column (250 x 4.6 mm, 5 μm). Mobile phases: A-water (0.1% v/v TFA), B-acetonitrile (0.1% v/v TFA). The general solvent gradient method: 0-30 min, 10%-80% B; 30-40 min, 80% B; 40-41min, 80%-10% B; 40-55min, 10% B. A flow rate of 1 mL min^{-1} was used with UV detection wavelength 254 nm except for the cyclic peptide studied in Chapter 5 (230 nm).

2.2.6 Elemental Analysis

Elemental analysis was to determine the ratio of elements in a sample by combustion, which is useful to identify if the sample is a desired compound and confirm the purity of a compound. The percentage of C, H, and N elements in a sample was determined by elemental analysis on a CE-440 elemental analyzer by Warwick Analytical (UK)

Ltd. In this thesis, the deviation of the obtained percentage of the C, H, N elements from the theoretical values is used as a purity evaluation of compounds.

2.2.7 pH Measurements

pH or pH* (pH meter reading without correction for effect of deuterium on the sensor) values for samples in H_2O or D_2O were measured at *ca.* 298 K, using a HATCH minilab pocket pH meter with ISFET silicon chip pH sensor, calibrated with buffer solutions of pH 4, 7, and 10.

2.2.8 Ultraviolet-Visible (UV-Vis) Spectroscopy

Ultraviolet-visible spectrometry is a quantitative technique to measure the amount of ultraviolet (190-380 nm) or visible (380-800 nm) radiation absorbed by a substance in solution.[15] A Cary 300 UV-vis recording spectrophotometer was used with 1 cm path-length quartz cuvettes (3.0 mL) and a PTP1 Peltier temperature controller. The spectral scan was from 800 to 200 nm and the bandwidth was 1.0 nm; the scan rate was set to 600 nm/min. Spectra were recorded using UV Winlab software and plotted using Origin 2018.

2.2.9 Inductively Coupled Plasma (ICP)

Inductively coupled plasmas are types of flame-like discharges that can reach 10,000 K in temperature and form in a stream of argon or other gases flowing through an electromagnetic filed, which is an excellent source for elemental vaporization/atomization/ionization/excitation.[16]

2.2.9.1 Inductively Coupled Plasma-Optical Emission Spectroscopy (ICP-OES)

ICP-OES was used to measure the photon wavelength corresponding to the emission rays released by the excited ground-state atoms returning to low energy states. The elements are distinguished by the wavelengths of the photon rays and the content of each element is determined by the rays' intensity. ICP-OES is used to determine the metal concentration in the stock solutions prepared for the cytotoxicity related tests on a PerkinElmer Optima 5300 DV series Optical Emission Spectrophotometer. The plasma standard solution of the metal ion was diluted with 3.6% HNO_3 in type-1 Milli-Q water to give freshly-prepared calibrants at concentrations of 700, 600, 500, 400, 300, 200, 100, 50, and 0 ppb, which were adjusted to match the sample matrix by standard addition of sodium chloride. Total dissolved solids did not exceed 0.2% w/v. Data were acquired and processed using WinLab32 V3.4.1 for Windows.

2.2.9.2 Inductively Coupled Plasma-Mass Spectrometry (ICP-MS)[17]

In ICP-MS, the plasma torch is positioned horizontally to generate positively charged ions which are extracted through a series of cones into a mass spectrometer, where they are separated by the mass to charge ratio. The detector receives an ion signal proportional to the concentration based on the calibration with certified reference standards. In this thesis, ICP-MS was used to determine the iridium/rhodium concentration in the digested cell pallets. The whole cell pellet was digested in 200 µL 72% nitric acid at 353 K overnight. Digested samples were then diluted in the ratio of 1:20 (v/v) to give a final concentration of 3.6% nitric acid in 4 mL volume and analysed using an Agilent 7500 series or Agilent 7900 series instrument with an

internal standard of ^{166}Er (50 ppb) in both no-gas and He-gas mode. Data were acquired and processed using Agilent ChemStation for Windows (7500 series ICP-MS) or Agilent Mass Hunter 4.3 for Windows (7900 series ICP-MS). Biological triplicates were analysed for each sample and statistical significance was calculated (Welch's unpaired t-test).

2.2.10 Cyclic Voltammetry[18]

Cyclic voltammetry (CV) is a powerful and popular electrochemical technique used to investigate the reduction and oxidation processes of molecular species,[18] which is performed by varying the potential of a working electrode cyclically with time, and measuring the resulting current *vs* potential. The separation of the two peaks of the cyclic wave should be about 57 mV apart to be reversible for one-electron process. If they are further apart, the wave is not reversible. Focusing on the current, if the cathodic current equals the anodic current, the redox couple is reversible, otherwise not. In this thesis, CV scans were carried out using a CH Instrument model 600D Electrochemical Analyzer/Workstation (Austin, TX), which controls the electrode potential. The electrolysis cell consists of a three-electrode configuration and the electrolytic solution. The reference electrode was $Ag/AgNO_3$ (0.1 M in acetonitrile), the working electrode was a polished platinum disc and the counter electrode was a large surface area platinum wire. The potential of the working electrode is measured against reference electrode which maintains a constant potential during the cyclic potential scans. The counter electrode provides a means of applying input potential to the working electrode and allowing the charge to flow in the circuit.

The electrolyte solution was 0.1 M [Bu$_4$N]PF$_6$ in HPLC grade acetonitrile solution. The concentration of the metal samples, including the ferrocene reference, was 1 mM in 5 ml electrolyte which was scanned as background after being degassed under nitrogen for 15 min. Between each sample interval, all the electrodes were washed with acetone three times and dried under an air flow.

2.2.11 Microwave Reactor

Microwave radiation has been demonstrated as an effective tool to heat the chemical reactions effectively, which relies on dipolar polarization and ionic conduction.[19] Synthesis of dinuclear iridium(III) and rhodium(III) staring materials has been reported by microwave heating within a few minutes without compromising the yields.[2] In this thesis, the CEM Discovery-SP microwave reactor was used in the synthesis of chlorido iridium(III)/rhodium(III) dimer precursor under conditions of 140 °C, 5 min, 150 W.

2.2.12 Cell culture

Cancer cells were grown in Roswell Park Memorial Institute medium (RPMI-1640) supplemented with 10% (v/v) of fetal calf serum, 1% (v/v) of 2 mM glutamine, and 1% (v/v) penicillin-streptomycin solubilized solution. Cells were grown as adherent monolayers at 310 K in a 5% CO$_2$ humidified atmosphere and passaged at ca. 80% confluency using trypsin-EDTA. A2780cis cisplatin-resistant cells were exposed to cisplatin for 24 h upon reaching 80-90% confluence. After this time, the cells were washed with PBS and supplied with fresh medium.

2.2.13 *In vitro* Cell Growth Inhibition Assays

Briefly, 5000 cells in 150 μL cell culture medium were seeded per well in 96-well plates and pre-incubated at 310 K for 48 h in a 5% CO_2 humidified atmosphere before adding different concentrations of test compounds. Stock solutions of the tested compounds (ca. 0.1 mM) were prepared in DMSO (0.5%, v/v)/cell culture medium and the concentration of each compound in the stock solution was determined by ICP-OES based on metal. The supernatants were removed by suction and cells were treated with six concentrations of the tested compounds using 200 μL per well for 24 h at 310 K in a 5% CO_2 humidified atmosphere. After this, supernatants were removed by suction and each well was washed with 100 μL PBS. The cells were allowed a further 72 h recovery in compound-free fresh medium at 310 K in a 5% CO_2 humidified atmosphere. The SRB assay[20] was then used to determine cell viability. Absorbance measurements of the solubilized dye (on a BioRad iMark microplate reader using a 470 nm filter) allowed the determination of viable treated cells compared to untreated controls. IC_{50} values were determined as duplicates of triplicates in two independent sets of experiments and their standard deviations were calculated.

2.2.14 Toxicity in Zebrafish

The zebrafish embryo a low-cost, high-throughput animal model in the biomedical research for drug screening and toxicity assessment.[21] Singapore wild-type zebrafish embryos were used as the models for the toxicity assessment of the iodido iridium azopyridine complexes in this thesis. The experiments were carried out by Dr. James

P. C. Coverdale and Hannah Bridgewater in the School of Life Sciences, University of Warwick. Embryos were collected and transferred to petri dishes. Zebrafish embryos were harvested and seeded in 24-well plates at one embryo/well. A serial dilution of six concentrations of the compound to be tested was added to 20 of these wells with the other 4 wells as negative controls. DMSO at an identical percentage to that present in the tested compound solutions was used as the solvent control and 3,4-dichloroaniline used as the positive control. Embryos incubated at 301.5 K for 96 h, after which percentage of zebrafish survival was assessed by embryo coagulation, visible heartbeat, tail detachment and somite formation. Experiments were carried out in duplicate. Complex concentrations were corrected by ICP-OES and percentage of survival was plotted against complex concentration and fitted as Boltzmann sigmoidal curves to determine the LC_{50} values and standard deviations. Maintenance of animals was carried out in accordance with ASPA1986 and approved by the University Ethical Review Committee. Zebrafish were housed in 3.5 L tanks and fed 2–4 times a day. Fish were mated once a week starting at two pairs per 1 L breeding tank.

2.3 References

1   M. Björgvinsson, S. Halldorsson, I. Arnason, J. Magull and D. Fenske, *J. Organomet. Chem.*, 1997, **544**, 207-215.

2   J. Tönnemann, J. Risse, Z. Grote, R. Scopelliti and K. Severin, *Eur. J. Inorg. Chem.*, 2013, **2013**, 4558-4562.

3 A. J. Blacker, M. J. Stirling and M. I. Page, *Org. Process Res. Dev.*, 2007, **11**, 642-648.

4 O. V. Dolomanov, L. J. Bourhis, R. J. Gildea, J. A. Howard and H. Puschmann, *J. Appl. Cryst.*, 2009, **42**, 339-341.

5 G. M. Sheldrick, *Acta Cryst.*, 2015, **A71**, 3-8.

6 G. M. Sheldrick, *Acta Cryst.*, 2015, **C71**, 3-8.

7 S. Bank, *Concepts Magn. Reson.*, 1997, **9**, 83-93.

8 B. Diehl, in *NMR Spectroscopy in Pharmaceutical Analysis*, eds. U. Holzgrabe, I. Wawer and B. Diehl, Elsevier, Amsterdam, 2008, pp. 1-41.

9 N. Bloembergen, E. M. Purcell and R. V. Pound, *Phys. Rev.*, 1948, **73**, 679-712.

10 M. M. Roessler and E. Salvadori, *Chem. Soc. Rev.*, 2018, **47**, 2534-2553.

11 C. S. Ho, C. Lam, M. Chan, R. Cheung, L. Law, L. Lit, K. Ng, M. Suen and H. Tai, *Clin. Biochem. Rev.*, 2003, **24**, 3-12.

12 B. L. Milman, *TrAC, Trends Anal. Chem.*, 2015, **69**, 24-33.

13 W. A. Korfmacher, *Drug Discov.*, 2005, **10**, 1357-1367.

14 M. Thammana, *Res. Rev. J. Pharm. Anal. RRJPA*, 2016, **5**, 22-28.

15 A. Davidson, *Practical pharmaceutical chemistry*, 1988, **4**, 301-302.

16 Soltanpour, P.N., Johnson, G.W., Workman, S.M., Jones, J.B., Jr. and Miller, R.O. (2018). Inductively Coupled Plasma Emission Spectrometry and Inductively Coupled Plasma-Mass Spectrometry. In Methods of Soil Analysis (eds D. Sparks, A. Page, P. Helmke, R. Loeppert, P.N. Soltanpour, M.A. Tabatabai, C.T. Johnston and M.E. Sumner). doi:10.2136/sssabookser5.3.c5.

17   R. Thomas, Practical guide to ICP-MS: a tutorial for beginners, CRC Press, 2013.

18   N. Elgrishi, K. J. Rountree, B. D. McCarthy, E. S. Rountree, T. T. Eisenhart and J. L. Dempsey, *J. Chem. Educ.*, 2018, **95**, 197-206.

19   P. Priecel and J. A. Lopez-Sanchez, *ACS Sustainable Chem. Eng.*, 2019, **7**, 3-21.

20   V. Vichai and K. Kirtikara, *Nat. Protoc.*, 2006, **1**, 1112-1116.

21   G. J. Lieschke and P. D. Currie, *Nat. Rev. Genet.*, 2007, **8**, 353-367.

Chapter 3

Ligand-Centred Redox Activation of Inert Half-Sandwich Iridium Anticancer Catalysts

This Chapter is based on the submitted manuscript "Ligand-centred redox activation of inert organoiridium anticancer catalysts" by Wen-Ying Zhang, Samya Banerjee, George M. Hughes, Hannah E. Bridgewater, Ji-Inn Song, Ben Breeze, Guy J. Clarkson, James P. C. Coverdale, Carlos Sanchez-Cano, Fortuna Ponte, Emilia Sicilia, and Peter J. Sadler.

Preparation, hydrolysis studies by ^{1}H NMR, and the cytotoxicity determination of complexes **9** and **10** were performed by Dr. George Hughes, which were part of his PhD thesis. IC$_{50}$ values of other complexes were determined by Ji-Inn Song; ROS detection and cellular iridium quantification conducted by Hannah Bridgewater; zebrafish toxicity study conducted by Dr. James Coverdale and Hannah Bridgewater; EPR spectroscopy data provided by Dr. Ben Breeze; X-ray crystallographic data analysed by Dr. Guy Clarkson; DFT calculations carried out by Fortuna Ponte and Prof. Emilia Sicilia. All the other experimental data collection and analysis were carried out by the author.

3.1 Introduction

Three key platinum drugs, cisplatin, carboplatin, and oxaliplatin are widely administered in worldwide cancer chemotherapy.[1] However, platinum resistance and undesirable side effects are now limiting their future use.[2] Therefore, it is important to discover other metal-based complexes with different modes of action compared with platinum drugs.[3-9] Third-row $5d^6$ iridium(III) complexes offer potential structural diversity of octahedral coordination geometry and slow ligand exchange kinetics, as well as facile synthesis.[10-12] For example, kinetically-inert octahedral iridium pyridocarbazole scaffolds can act as selective protein kinase inhibitors,[13] and inert iridium polypyridine anticancer complexes can have targets other than DNA.[14] Also, inert bis-cyclometalated iridium complexes are promising photosensitizers for singlet oxygen production,[15,16] and a diselenobenzoquinone-based iridium complex which targets cytochrome P450 reductase exhibits comparable potency to cisplatin.[17] Half-sandwich organometallic iridium cyclopentadienyl complexes $[(\eta^5\text{-}Cp^X)Ir(L^\wedge L')Z]^{n+/0}$, where $Cp^X = Cp^*$ (pentamethyl-cyclopentadienyl), Cp^{xph} (tetramethyl(phenyl)-cyclopentadienyl), or Cp^{xbiph} (tetramethyl(biphenyl)-cyclopentadienyl), not only can bind to DNA, but also can target lysosomes and perturb the redox status of cells.[18-20] The chelated ligand $L^\wedge L'$, the ancillary leaving group Z and the π-bound Cp^X ligand together modulate the overall electronic structure and chemical reactivity of such iridium complexes. Reported half-sandwich iridium anticancer complexes with Z = Cl are labile and most likely activated in cancer cells through fast hydrolysis (minutes) of the chlorido ligand.[11] Extension of the Cp^X ring from Cp* to Cp^{xph} then to Cp^{xbiph} can slow down the hydrolysis rate, and

increase the extent of hydrolysis.[21] Rapid hydrolysis sometimes compromises the anticancer activity due to rapid deactivation by side reactions in advance of reaching targets. For example, compared to the pyridine analogue $[(\eta^5\text{-Cp}^{xbiph})\text{Ir}(ppy)py]^+$ (ppy = 2-phenylpyridine), the chlorido complex $[(\eta^5\text{-Cp}^{xbiph})\text{Ir}(ppy)Cl]$ is more reactive, hydrolyzes rapidly, and reacts readily with the abundant (*ca.* 0.5-10 mM) cellular thiol glutathione (GSH), but has only one third the potency of the pyridine analogue toward cancer cells.[18] Hence, a major aim is to design potent iridium(III) anticancer agents by rational control of their reactivity.

In this Chapter, two complementary approaches are explored to optimize the anticancer activity of Ir(III) half-sandwich complexes. Firstly, iodide is used as the monodentate ancillary leaving group, a 'soft' ligand expected to be strongly bound and a poor leaving group.[22] Only a few biologically active half-sandwich iodido iridium complexes appear to have been reported, namely, $[(\text{Cp}^*)\text{Ir}(dpa)I]^+$ (dpa = 2, 2′-dipyridylamine),[23] $[(\text{Cp}^{xbiph})\text{Ir}(tolbig)I]^+$ (tolbig = 1-(o-Tolyl)biguanide),[24] and $[(\text{Cp}^*)\text{Ir}(pp)I]^+$ (pp = pyridylphosphinate)[25]. Secondly, the presence of a chelated azo-pyridine ligand provides low-lying π^* orbitals of from the azo bond, and a pathway for electron transfer and redox reactions.[26] Previously it has been found that glutathione undergoes interesting reactions with phenyl-azo-pyridine ligands in arene Ru(II) and Os(II) complexes.[27-29] Chlorido complex $[\text{Cp}^{xph}\text{Ir}(azpy\text{-NMe}_2)Cl]PF_6$ containing N,N-dimethylphenylazopyridine (azpyNMe$_2$) ligand exhibits a markedly different pattern of antiproliferative activity in over 800 cancer cell lines compared to the 253 standard drugs, generating cellular redox-modulation and DNA damage, allowing Pt resistance to be overcome.[30]

Herein, eight novel half-sandwich organoiridium(III) iodido complexes bearing variously substituted bidentate phenyl-azo-pyridine ligands (shown in Chart 3.1) and two novel chlorido analogues have been prepared as shown in Chart 3.2. The *in vivo* toxicity of iodido and chlorido complexes in zebrafish embryos as well as their antiproliferative activity against human cancer cell lines are compared. Correlations between the antiproliferative activity of the iodido complexes and their aqueous chemistry, lipophilicity, cellular accumulation of iridium, and generation of reactive oxygen species (ROS) are investigated. Redox reactions with GSH are studied and the mechanism elucidated by DFT calculations. This work reveals the roles of the chelated azopyridine ligands as well as iridium centre in controlling the activation pathways, and nature of the reactive species responsible for activity in cancer cells.
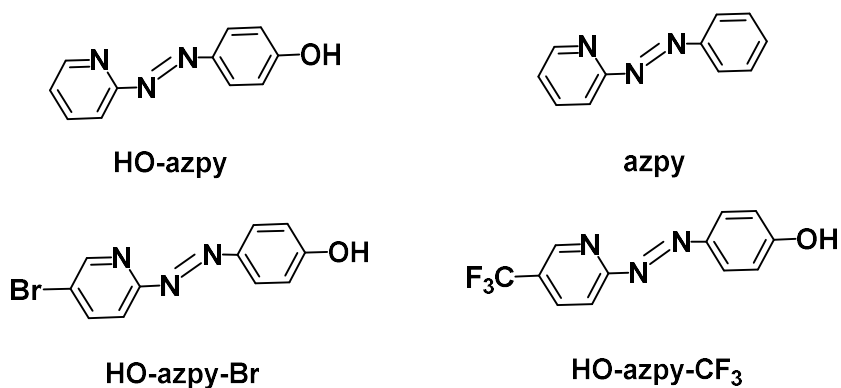
Chart 3.1. The chemical structures of substituted azopyridine ligands.
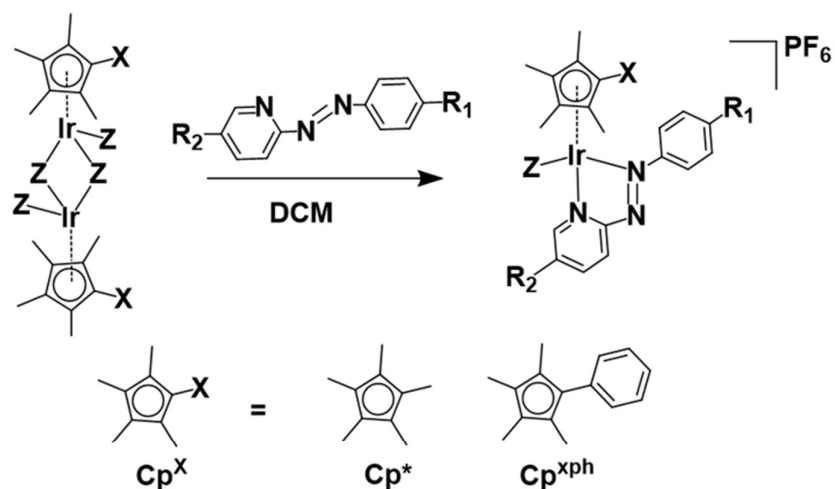
Complex	R_1	R_2	Z	Yield
$[(Cp^*)Ir(HO\text{-}azpy)I]PF_6$ (**1**)	OH	H	I	68%
$[(Cp^{xph})Ir(HO\text{-}azpy)I]PF_6$ (**2**)	OH	H	I	85%
$[(Cp^*)Ir(HO\text{-}azpy\text{-}Br)I]PF_6$ (**3**)	OH	Br	I	85%
$[Cp^{xph})Ir(HO\text{-}azpy\text{-}Br)I]PF_6$ (**4**)	OH	Br	I	60%
$[(Cp^*)Ir(HO\text{-}azpy\text{-}CF_3)I]PF_6$ (**5**)	OH	CF_3	I	58%
$[(Cp^{xph})Ir(HO\text{-}azpy\text{-}CF_3)I]PF_6$ (**6**)	OH	CF_3	I	65%
$[(Cp^*)Ir(azpy)I]PF_6$ (**7**)	H	H	I	95%
$[(Cp^{xph})Ir(azpy)I]PF_6$ (**8**)	H	H	I	83%
$[(Cp^*)Ir(HO\text{-}azpy)Cl]PF_6$ (**9**)	OH	H	Cl	73%
$[(Cp^{xph})Ir(HO\text{-}azpy)Cl]PF_6$ (**10**)	OH	H	Cl	63%

Chart 3.2. Synthesis route for the organoiridium(III) complexes studied in this Chapter, and formulae of the complexes (azpy = 2-phenylazopyridine).

3.2 Experimental Section

3.2.1 Materials

β-Alanine, N-acetyl-L-cysteine, N-acetyl-L-methionine, L-histidine, L-tryptophan, L-arginine, chelex 100 sodium form, DMPO and DEPMPO were obtained from Sigma-Aldrich. The iridium dimer precursor $[(Cp^*)Ir(\mu\text{-Cl})Cl]_2$, $[(Cp^{xph})Ir(\mu\text{-Cl})Cl]_2$, $[(Cp^*)Ir(\mu\text{-I})I]_2$, and $[(Cp^{xph})Ir(\mu\text{-I})I]_2$ were prepared by the procedures described in Chapter 2. The substituted azopyridine ligands HO-azpy-Br, HO-azpy-CF$_3$, and azpy (shown in Chart 3.1) were synthesised and characterised according to a reported procedure.[31]

3.2.2 Synthesis

3.2.2.1 Synthesis of Phenol-azo-pyridine (HO-azpy) Ligand

Benzoquinone (1.479 g, 13.6 mmol) was dissolved in water (100 mL) and 0.1 M perchloric acid (9 mL). 2-Hydrazinopyridine (1.493 g, 13.6 mmol) in water (20 mL) was added dropwise and the solution colour changed from green to red violet. The solution was stirred at ambient temperature for 1 h before filtration, and the precipitate was quickly washed with cold water (1 x 10 mL) to an orange crystalline solid. The solid was dissolved in MeOH (50 mL) with formic acid (5 mL), and the solution was bubbled ammonia gas for 1 h. The final solution was left at 277 K for 72 h and red crystals were obtained after filtration and dried under vacuum. Yield: 0.4 g (15 %). ESI found $[M\text{-H}]^+$ m/z 198.0, calcd 198.1. ^{1}H NMR (400 MHz, DMSO-d$_6$) δ 8.65 (d, J = 8.2 Hz, 1H), 8.00 (m, 1H), 7.85 (d, J = 8.6 Hz, 2H), 7.64 (d, J = 4.4 Hz, 1H), 7.49 (m, 1H), 6.96 (d, J = 8.6 Hz, 2H).

3.2.2.2 Synthesis of Iridium Complexes

All the iridium iodido complexes were synthesised following a general procedure: the ligand (0.10 mmol, 2.0 mol equiv.) was added to a 10.0 mL dichloromethane solution of $[(\eta^5\text{-Cp}^X)\text{Ir}(\mu\text{-I})\text{I}]_2$ ($\text{Cp}^X = \text{Cp}^*$ or Cp^{xph}) (0.05 mmol, 1.0 mol equiv.). The mixture immediately turned to dark red and was stirred at ambient temperature for 24 h. The solvent was reduced to dryness on a rotary evaporator, then the minimum volume of methanol was added to dissolve the crude product, and an excess of NH_4PF_6 (0.50 mmol, 10.0 mol equiv.) was added. A precipitate was obtained after storage for 2-3 days at 253 K. The final solid products were collected by filtration, washed by diethyl ether, and dried under vacuum.

$[(\eta^5\text{-Cp}^*)\text{Ir}(\text{HO-azpy})\text{I}]\text{PF}_6$ (**1**): black solid, yield 68%; ^1H NMR (500 MHz, CD$_3$OD): δ 8.94 (1H, d, $J = 5.6$ Hz, s), 8.81 (1H, d, $J = 8.0$ Hz), 8.31 (1H, t, $J= 7.8$ Hz), 8.03 (2H, d, $J = 8.9$ Hz), 7.82 (1H, t, $J = 6.9$ Hz, 6.4 Hz), 6.90 (2H, d, $J = 8.9$ Hz), 1.74 (15H, s); $^{13}\text{C}\{^1\text{H}\}$ NMR (125 MHz, CD$_3$OD): δ 167.47, 166.65, 152.80, 148.98, 143.40, 130.07, 129.17, 127.94, 117.12, 96.26, 9.56. ESI-MS: m/z calcd for $[(\eta^5\text{-Cp}^*)\text{Ir}(\text{HO-azpy})\text{I}]^+$: 654.0, found: 654.1; elemental analysis calcd for $C_{21}H_{24}F_6IIrN_3OP$: C, 31.59; H, 3.03; N, 5.26; found: C, 30.98; H, 2.86; N, 5.26.

$[(\eta^5\text{-Cp}^{xph})\text{Ir}(\text{HO-azpy})\text{I}]\text{PF}_6$ (**2**): dark blue solid, yield 85%; ^1H NMR (500 MHz, CD$_3$OD): δ 8.83 (1H, d, $J = 8.0$ Hz), 8.72 (1H, d, $J=5.6$ Hz), 8.29 (1H, t, $J = 7.8$ Hz), 8.04 (2H, d, $J = 9.0$ Hz), 7.71 (1H, t, $J = 7.0$ Hz), 7.46 (1H, t, $J = 7.4$ Hz), 7.40 (2H, t, $J = 7.7$ Hz, 7.2 Hz), 7.20 (2H, d, $J = 7.2$ Hz), 6.86 (2H, d, $J = 9.0$ Hz), 2.04 (3H, s), 1.96 (3H, s), 1.89 (3H, s), 1.46 (3H, s); $^{13}\text{C}\{^1\text{H}\}$ NMR (125 MHz, CD$_3$OD): δ 167.65, 167.61, 152.32, 148.81, 143.63, 130.96, 130.64, 130.43, 130.43, 129.34, 128.97,

128.07, 117.37, 103.65, 102.53, 94.34, 93.26, 92.64, 10.80, 10.70, 10.09, 9.78. ESI-MS: *m/z* calcd for $[(\eta^5\text{-Cp}^{xph})\text{Ir(HO-azpy)I}]^+$: 716.0, found 716.0; elemental analysis calcd for $C_{26}H_{26}F_6IIrN_3OP\cdot H_2O$: C, 35.54; H, 3.21; N, 4.78; found: C, 35.70; H, 3.17; N, 4.63.

$[(\eta^5\text{-Cp}^*)\text{Ir(HO-azpy-Br)I}]\text{PF}_6$ (3): dark blue solid, yield 85%; ^{1}H NMR (500 MHz, CD3OD): δ 8.90 (1H, d, *J* = 1.8 Hz), 8.59 (1H, d, *J* = 8.6 Hz), 8.45 (1H, d, *J* = 2.0 Hz, *J* = 8.6 Hz), 8.06 (1H, d, *J* = 9.0 Hz), 6.90 (1H, d, *J* = 9.0 Hz), 1.76 (15H, s). ^{13}C{^{1}H} NMR (125 MHz, CD3OD): δ 166.48, 152.53, 148.63, 146.03, 130.78, 127.07, 123.36, 121.41, 118.14, 96.23, 9.54. ESI-MS: *m/z* calcd for $[(\eta^5\text{-Cp}^*)\text{Ir(HO-azpy-Br)I}]^+$: 731.9, found 732.0; elemental calcd for $C_{21}H_{23}BrF_6IIrN_3OP\cdot 2H_2O$: C, 27.61; H, 2.98; N, 4.60; found: C, 27.48; H, 2.79; N, 4.67.

$[(\eta^5\text{-Cp}^{xph})\text{Ir(HO-azpy-Br)I}]\text{PF}_6$ (4): dark blue solid, yield 60%; ^{1}H NMR (500 MHz, CD3OD): δ 8.72 (1H, d, *J* = 8.6 Hz), 8.61 (1H, d, *J* = 1.8 Hz), 8.48 (1H, dd, *J* = 1.9 Hz, 8.6 Hz), 8.05 (1H, d, *J* = 9.1 Hz), 7.53 (1H, t, *J* = 7.3 Hz), 7.48 (2H, t, J_1 = 7.6 Hz, 7.0 Hz) 7.33 (2H, d, *J* = 7.1 Hz), 6.89 (2H, d, *J* = 9.0 Hz), 2.03 (6H, s), 1.83 (3H, s), 1.49 (3H, s). ^{13}C{^{1}H} NMR (125 MHz, CD3OD): δ 166.47, 151.92, 148.93, 146.38, 131.10, 130.91, 130.64, 130.59, 128.88, 128.21, 124.24, 121.91, 117.51, 105.27, 101.53, 96.46, 92.35, 92.15, 11.35, 10.56, 10.06, 9.42. ESI-MS: *m/z* calcd for $[(\eta^5\text{-Cp}^{xph})\text{Ir(HO-azpy-Br)I}]^+$: 793.9, found 794.0; elemental analysis calcd for $C_{26}H_{25}BrF_6IIrN_3OP\cdot H_2O$: C, 32.61; H, 2.84; N, 4.39; found: C, 32.26; H, 2.80; N, 4.40.

$[(\eta^5\text{-Cp}^*)\text{Ir(HO-azpy-CF}_3\text{)I}]\text{PF}_6$ (5): black solid, yield 58%. ^{1}H NMR (500 MHz, CD3OD): δ 9.03 (1H, s), 8.90 (1H, d, *J*= 8.5 Hz), 8.58 (1H, dd, *J* = 8.5 Hz), 8.11 (2H,

d, $J = 9.0$ Hz), 6.97 (2H, d, $J = 9.0$ Hz), 1.77 (15H, s); ^{19}F NMR (376 MHz, CD$_3$OD): δ -63.53 (s, CF$_3$), -74.89 (d, $J_{P-F} = 707.5$ Hz, PF$_6$); ^{13}C{^{1}H} NMR (125 MHz, CD$_3$OD): δ 169.37, 149.45, 149.30, 140.65, 131.14, 129.35, 129.50, 129.23, 128.95, 126.86, 124.70, 122.55, 117.96, 96.96, 9.58. ESI-MS: m/z calcd for [(η^5-Cp*)Ir(HO-azpy-CF$_3$)I]$^+$: 722.1, found 722.0; elemental analysis calcd for C$_{22}$H$_{23}$F$_9$IIrN$_3$OP·H$_2$O: C, 29.87; H, 2.85; N, 4.75; found: C, 30.00; H, 2.80; N, 4.69.

[(η^5-Cp^{xph})Ir(HO-azpy-CF$_3$)I]PF$_6$ (6): dark green solid, yield 65%; ^{1}H NMR (500 MHz, CD$_3$OD): δ 8.48 (1H, s), 8.40 (1H, d, $J = 8.9$ Hz), 8.26 (1H, d, $J = 8.5$ Hz), 8.16 (1H, d, $J = 9.3$ Hz), 7.52 (1H, t, $J = 7.2$ Hz), 7.47 (2H, t, $J = 7.6$ Hz, 7.1 Hz), 7.41 (2H, d, $J = 7.2$ Hz), 6.55 (1H, d, $J = 9.1$ Hz), 2.01 (3H, s), 1.99 (3H, s), 1.81 (3H, s), 1.55 (3H, s). ^{13}C{^{1}H} NMR (125 MHz, CD$_3$OD): δ 170.09, 149.19, 147.95, 139.19, 133.19, 131.18, 130.69, 130.56, 129.99, 129.58, 129.27, 128.85, 129.30, 124.92, 122.71, 121.99, 121.41, 104.13, 100.14, 95.33, 91.18, 90.36, 11.44, 10.59, 10.22, 9.29. ESI-MS: m/z calcd for [(η^5-Cp^{xph})Ir(HO-azpy-CF$_3$)I]$^+$: 784.0, found 784.0; elemental analysis calcd for C$_{27}$H$_{25}$F$_9$IIrN$_3$OP·0.1H$_2$O: C, 34.86; H, 2.73; N, 4.52; found: C, 35.19; H, 2.78; N, 4.57.

[(η^5-Cp*)Ir(azpy)I]PF$_6$ (7): black solid, yield 95%; ^{1}H NMR (500 MHz, CD$_3$OD): δ 9.02 (1H, d, $J = 6.6$ Hz), 9.00 (1H, d, $J = 7.8$ Hz), 8.39 (1H, t, $J = 7.7$ Hz), 8.04 (2H, d, $J = 7.6$ Hz), 7.91 (1H, t, $J = 7.7$ Hz), 7.77 (1H, t, $J = 7.3$ Hz), 7.70 (2H, t, $J = 7.7$ Hz), 1.74 (15H, s). ^{13}C{^{1}H} NMR (125 MHz, CD$_3$OD): δ 166.30, 155.32, 153.04, 143.60, 135.30, 130.64, 130.64, 129.69, 126.68, 97.07, 9.61. ESI-MS: m/z calcd for [(η^5-Cp*)Ir(azpy)I]$^+$ 638.0, found 638.1; elemental analysis calcd for C$_{21}$H$_{24}$F$_6$IIrN$_3$P·H$_2$O: C, 31.51; H, 3.27; N, 5.25; found: C, 31.36; H, 3.01; N, 5.41.

Diastereomer_I(SR)　　　　　Diastereomer_II(RR)
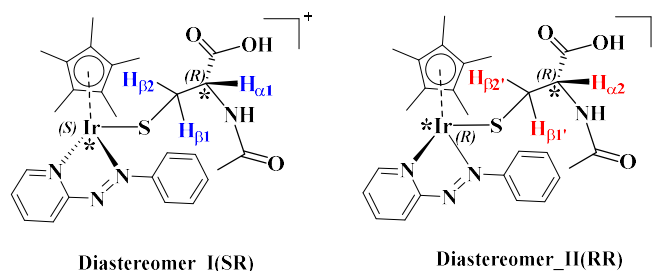
*denotes the chiral centre

[(η^5-Cp*)Ir(azpy)(NAC)]PF$_6$ (7-NAC): dark brown solid, yield: 97%; ^{1}H NMR (500 MHz, 70% D$_2$O-30% CD$_3$OD set δ (CD$_3$OD) 3.26 ppm): δ 8.89 (1H, d, J = 8.2 Hz), 8.78 (1H, d, J = 5.7 Hz), 8.31 (1H, tt), 7.97 (1H, m), 7.73 (2H, t, J = 7.7 Hz), 7.67-7.69 (3H, t, J = 7.3 Hz), 3.86-3.84 (0.5H, q, J (**H$_{α1}$-H$_{β1}$**) = 7.3 Hz, J (**H$_{α1}$-H$_{β2}$**) = 4.3 Hz, **H$_{α1}$**), 3.77-3.75 (0.5H, q, J (**H$_{α2}$-H$_{β1'}$**) = 6.5 Hz, J (**H$_{α2}$-H$_{β2'}$**) = 4.3 Hz, **H$_{α2}$**), 2.08-2.04 (0.5H, q, J (**H$_{β1'}$-H$_{α2}$**) = 6.5 Hz, J (**H$_{β1'}$-H$_{β2'}$**) = 12.0 Hz, **H$_{β1'}$**), 1.80-1.84 (0.5 H, q, J (**H$_{β1}$-H$_{α1}$**) = 7.3 Hz, J (**H$_{β1}$-H$_{β2}$**) = 12.0 Hz, **H$_{β1}$**), 1.77-1.75 (0.5H, q, J (**H$_{β2}$-H$_{α1}$**) = 4.3, J (**H$_{β2}$-H$_{β1}$**) = 12.0 Hz, **H$_{β2}$**), 1.74-1.72 (0.5H, q, J (**H$_{β2'}$-H$_{α2'}$**) = 4.3 Hz, J (**H$_{β2'}$-H$_{β1'}$**) = 12.0 Hz, **H$_{β2'}$**), 1.86 (1.5H, s), 1.73(1.5H, s), 1.54 (15H, s); ^{13}C{^{1}H} NMR (125 MHz, 70% D$_2$O-30% CD$_3$OD set δ (CD$_3$OD) = 49.00 ppm): δ 176.93, 176.81, 173.55, 173.27, 165.4, 166.96, 155.42,150.75, 150.70, 142.98, 142.88, 134.65, 134.72, 130.61,130.55, 129.51, 129.47, 128.90, 128.85, 125.32,125.28, 98.07, 97.95, 56.83, 57.26, 29.23, 29.15, 22.93, 22.83, 8.37, 8.33. ESI-MS: m/z calcd for [(η^5-Cp*)Ir(azpy)NAC]$^+$: 673.2, found 673.3; m/z calcd for [(η^5-Cp*)Ir(azpy)(NAC-H+Na)]$^+$: 695.2, found 695.3; elemental analysis calcd for C$_{26}$H$_{32}$F$_6$IrN$_4$O$_3$PS: C, 38.19; H, 3.94; N, 6.85; found: C, 38.25; H, 3.98; N, 6.54.

[(η^5-Cp^{xph})Ir(azpy)I]PF$_6$ (8): black solid, yield 83%; ^{1}H NMR (500 MHz, CD$_3$OD): δ 9.07 (1H, d, J = 7.9 Hz), 8.80 (1H, d, J = 5.5 Hz), 8.39 (1H, t, J = 7.7 Hz), 8.03 (2H,

d, J = 7.7 Hz), 7.84 (1H, t, J = 6.1 Hz), 7.72 (1H, t, J = 7.5 Hz), 7.61 (2H, t, J = 8.0 Hz), 7.47 (1H, t, J = 7.4 Hz), 7.42 (2H, t, J = 7.5 Hz), 7.20 (2H, d, J = 7.2 Hz), 2.01 (3H, s), 1.96 (3H, s), 1.91 (3H, s), 1.38 (3H, s); $^{13}C\{^1H\}$ NMR (125 MHz, CD$_3$OD): δ 167.37, 156.15, 152.58, 143.93, 135.47, 131.04, 130.81, 130.60, 130.56, 130.49, 130.22, 128.93, 126.75, 104.65, 102.47, 96.26, 94.12, 93.38, 10.96, 10.57, 9.84, 9.75. ESI-MS: m/z calcd for $[(\eta^5\text{-Cp}^{xph})\text{Ir(azpy)I}]^+$:700.0, found 700.1; elemental analysis calcd for C$_{26}$H$_{25}$F$_6$IIrN$_3$P·H$_2$O: C, 36.24; H, 3.16; N, 4.88; found: C, 37.02; H, 2.99; N, 4.90.

$[(\eta^5\text{-Cp}^*)\text{Ir(HO-azpy)Cl}]\text{PF}_6$ (9): black solid, yield 73%; ^1H NMR (400 MHz, CD$_3$CN): δ 8.77 (1H, d, J = 5.5 Hz), 8.66 (1H, d, J = 7.7 Hz), 8.31 (1H, t, J= 7.8 Hz), 7.95 (2H, d, J = 8.8 Hz), 7.87 (1H, t, J = 6.7 Hz), 7.28 (2H, d, J = 8.9 Hz), 1.57 (15H, s). $^{13}C\{^1H\}$ NMR (125 MHz, CD$_3$CN): δ 166.27, 164.25, 150.67, 147.63, 143.35, 129.98, 128.17, 127.68, 116.80, 94.63, 8.54. ESI-MS: m/z calcd for $[(\eta^5\text{-Cp}^*)\text{Ir(HO-azpy)Cl}]^+$:562.1, found 562.1; elemental analysis calcd for C$_{21}$H$_{24}$F$_6$ClIrN$_3$OP: C, 35.67; H, 3.42; N, 5.94; found: C, 35.67; H, 3.34; N, 5.90.

$[(\eta^5\text{-Cp}^{xph})\text{Ir(HO-azpy)Cl}]\text{PF}_6$ (10): black solid, yield 63%; ^1H NMR (400 MHz, CD$_3$CN): δ 8.50 (1H, d, J = 7.9 Hz), 8.26 (1H, d, J = 5.5 Hz), 8.15 (1H, t, J = 7.8 Hz), 7.92 (2H, d, J = 8.6 Hz), 7.56-7.46 (4H, m), 7.32 (2H, d, J = 7.3 Hz), 7.22 (2H, d, J = 8.4 Hz), 1.79 (3H, s), 1.67 (3H, s), 1.61 (3H, s), 1.43 (3H, s). $^{13}C\{^1H\}$ NMR (125 MHz, CD$_3$CN): δ 166.36, 164.60, 150.47, 147.43, 143.50, 130.45, 130.08, 129.88, 128.83, 128.35, 127.99, 116.86, 104.79, 100.74, 94.24, 91.46, 87.35, 9.74, 9.43, 9.00, 8.57. ESI-MS: m/z calcd for $[(\eta^5\text{-Cp}^{xph})\text{Ir(HO-azpy)Cl}]^+$: 624.1, found 624.0;

elemental analysis calcd for $C_{26}H_{26}F_6ClIrN_3OP$: C, 40.60; H, 3.41; N, 5.46; found: C, 40.89; H, 3.31; N, 5.50.

3.2.3 Methods

The X-ray Crystallography, NMR spectroscopy, EPR spectroscopy, ESI-MS analysis, elemental analysis, UV-vis spectroscopy, pH measurements, HPLC, LC-MS, cyclic voltammetry, ICP-OES, ICP-MS, cell culture, and cell viability assay were carried out as described in Chapter 2.

3.2.3.1 X-ray Crystallography

The X-ray crystal structures were solved by Dr. Guy Clarkson (Department of Chemistry, University of Warwick). The crystals were kept at 150 ± 2 K during data collection, except the crystal of complex **5** kept at 296 ± 2 K. X-ray crystallographic data for complexes **1-I**·MeOH, **2**, **3**·MeOH, **5**·MeOH, **7-I**, and **8-I** have been deposited in the Cambridge Crystallographic Data Centre under the accession numbers CCDC 1860992, 1860993, 1860994, 1860995, 1860996, 1860997, respectively. X-ray crystallographic data in CIF format are available from the Cambridge Crystallographic Data Centre (http://www.ccdc.cam.ac.uk/).

3.2.3.2 Determination of pK_a

The UV-vis absorption changes from pH 2-12 were monitored by UV-Vis spectroscopy, firstly after the addition of µL amounts of either dilute perchloric acid in acetic acid, then of a dilute solution of KOH, to 20-30 µM solutions of complexes

1-6 and **9-10** in 10% methanol/90% Milli-Q water with 1 cm path-length quartz cuvettes (3.0 mL). Changes in absorbance maxima at different pH values were plotted and the sigmoidal curve fitted using Maxwell-Boltzmann curve-fitting to determine the pK_a.

3.2.3.3 Determination of Molar Extinction Coefficients

The UV-vis spectra of the iridium complexes **1-6** were recorded at 3 different concentrations from 800 nm to 200 nm, and the concentrations were subsequently determined by ICP-OES protocol. Linear plots of absorbance versus concentrations for each complex gave the molar extinction coefficient as the gradient, according to the Beer-Lambert law.

3.2.3.4 Hydrolysis Kinetics

HPLC analysis with the detected UV absorption at 254 nm relative to 610 nm was conducted for complex **9** (50 μM) dissolved in MeOH/H$_2$O (5/95, v/v) and incubated at 310 K, at different time interval over 24 h. The normalized peak integral of complex **9** was calculated based on the aqua complexes. The graph of the integral versus time (min) was were plotted and fitted to the pseudo first-order kinetics to determine the hydrolysis rate and half-life time.

3.2.3.5 Electron Paramagnetic Resonance (EPR)

The basic concepts are described in Chapter 2. Complex **7** was mixed with GSH stock solution to give 1 mM **7** and 20 mM GSH. Samples (*ca.* 100 μL) were transferred

using a plastic syringe with metal needle to a standard quality quartz tube with an inner diameter of 1.0 mm and an outer diameter of 2.0 mm (Wilmad LabGlass). Data were processed by Matlab R2016b with Easyspin 5.1.12.

3.2.3.6 Catalysis of GSH Oxidation

The catalysis of GSH oxidation to GSSG by iodido iridium complexes **1**, **3**, **7** and **8**, free ligand phenol-azopyridine (HO-azpy), and the Ir-SG complexes **7-SG** and **3-SG** was studied by ^{1}H NMR spectroscopy. The tested compound and GSH were in 5% d_6-acetone and 95% phosphate buffer D$_2$O (v/v, 30 mM, pH* 7.4) in a sealed vial with a final concentration ratio of [Ir]/[GSH] = [100 µM]/[10 mM]. The dissolved oxygen concentration in the starting mixture was determined to be 4.33 ± 0.05 mg/L using a FiveGo^{TM} F4 DO meter which was calibrated in the air and oxygen-zero solution. Oxygen is involved in the catalytic cycle (Figure 3.36 in the main text). After 24 h at 310 K, the reaction solution was placed in a 5 mm NMR tube for recording the ^{1}H NMR spectrum (128 scans, 7 min).

The turnover number (TON) for the reactions was calculated as follows:

$$\text{TON} = \frac{I_{GSSG}}{I_{GSH} + I_{GSSG}} \frac{[GSH]_0}{[Ir]}$$

where I_{GSSG}/I_{GSH} are the peak integrals for oxidized/reduced glutathione at δ 3.30-3.36/2.90-3.03 ppm, respectively, and [GSH]$_0$ is the initial concentration of GSH. The TON is the average of three independent experiments with similar results.

3.2.3.7 Determination Partition of Coefficients

1-Octanol saturated 2 mM phosphate buffer and 2 mM phosphate buffer-saturated 1-octanol were prepared by stirring the mixtures of 100 mL octanol and 100 ml 2 mM phosphate buffer (pH 7.4, made with Milli-Q water) for 24 h and separated in a separating funnel after 3-4 h equilibration. 3.0-4.0 mg of iridium complexes were dissolved in 10 mL octanol-saturated 2 mM phosphate buffer by shaking the suspension solution on an IKA Vibrax VXC basic shaker for 5 h at the speed of 1000 r/min to give saturated solutions. Then the mixture was filtered using a hydrophobic filter. A 2 mL aliquot of the final filtrate was added into 2 mM phosphate buffer-saturated octanol (2 mL) in triplicate, and the two-layer solution was shaken on an IKA Vibrax VXC basic shaker for 15 h at a speed of 1000 r/min and subsequently, equilibrated for 4.5 h. Aqueous samples before and after partitioning in octanol were diluted in the ratio of 1: 100 and 1:10 v/v, respectively, with ca. 3.6 % HNO_3 to the appropriate range for ICP-MS analysis. The iridium concentration was calibrated using aqueous standards in ca. 3.6 % HNO_3 (0-1000 ppb). These procedures were carried out at ambient temperature (ca. 298 K). Log P values for iridium complexes were calculated from log $P_{o/w}$ = log($[Ir]_{oct}/[Ir]_{aq}$).[32]

3.2.3.8 Ir Accumulation in Cancer Cells

The accumulation of iridium in human carcinoma cells was determined by ICP-MS. 1×10^6 cells were seeded onto a 100 mm Petri dish and incubated in compound-free media for 24 h at 310 K in a 5% CO_2 humidified atmosphere. For a further 24 h the cells were incubated in medium containing complex **3** or **7** with certain concentration

determined by ICP-OES in advance. Following this, cells were counted and cell pellets were collected and digested as the ICP-MS protocol described in Chapter 2.

3.2.3.9 ROS Determination

ROS determination was conducted by Hannah E. Bridgewater (School of Life Science, University of Warwick). Flow cytometry analysis of ROS/superoxide generation in A549 cells caused by exposure to complexes **3** and **7** was carried out using the Total ROS/Superoxide detection kit (Enzo-Life Sciences) according to the instructions. A total of 5×10^5 A549 cells per well were seeded in a six-well plate. Cells were preincubated in compound-free medium at 310 K for 24 h in a 5% CO_2 humidified atmosphere, and then compound at 2x IC_{50} concentration was added by triplicates. After 24 h of compound exposure, supernatants were removed by aspiration. Cells were washed with PBS and harvested. Staining was achieved by resuspending the cell pellets in buffer containing the orange/green fluorescent reagents. Cells were analysed in a Becton Dickinson FACScan flow cytometer using FL1 channel Ex/Em 490/525 nm for the oxidative stress and FL2 channel Ex/Em 550/620 nm for superoxide detection. Positive controls were obtained by exposure of cells to pyocyanin for 30 min. Data were processed using Flowjo software. At all times, samples were kept under dark conditions to avoid light-induced ROS production. Welch's t-tests were carried out to establish statistical significance of the variations.

3.2.3.10 Computational Details

All calculations were performed by Fortuna Ponte and Prof. Emilia Sicilia (Department of Chemistry and Chemical Technologies, University of Calabria) in the framework of Density Functional Theory employing the hybrid Becke three-parameter exchange functional[33] and the Lee–Yang–Parr correlation functional, B3LYP.[34] To carry out such calculations the Gaussian 09 suite of program[35] was used. Grimme approach was adopted to include dispersion corrections for nonbonding interaction using atom pair-wise additive schemes,[36] denoted as DFT-D3 method.

The LANL2DZ effective core potential was used for the Ir atom,[37] along with the split valence basis set. The standard triple-ζ quality 6-311+G** basis sets of Pople and coworkers were used for the atoms directly participating in the process, whereas in order to reduce the computational effort, the 6-31G* basis sets were employed for peripheral atoms.

In order to establish both the nature of intercepted stationary points as minima and transition states and calculate zero-point energy (ZPE) and Gibbs free energy corrections, vibrational frequencies at the same level of theory were calculated. The intercepted transition states are first order saddle points on a potential energy surface (PES) and their vibrational spectrum is characterised by one imaginary frequency, corresponding to a negative force constant, which means that in one direction, in the nuclear configuration space, the energy has a maximum, while in all the other directions the energy has a minimum. Furthermore, IRC (intrinsic reaction coordinate) analysis was employed to carefully check transition state structures to be properly connected to the correct minima.[38,39]

The effects due to the presence of the solvent were included using the Tomasi's implicit Polarizable Continuum Model (PCM)[40-42] as implemented in Gaussian09 and the UFF set of radii was adopted to build-up the cavity in which the solute molecules are accommodated. Solvation Gibbs free energies were calculated performing single-point calculations for all *in vacuum* stationary points structures in implicit water (ε = 78.4) at the same level of theory. Enthalpies and Gibbs free energies were obtained using standard statistical procedures[43] at 298 K and 1 atm from total energies, including zero-point, thermal and solvent corrections. As the free energy corrections in the Gaussian's default standard state corresponds to an ideal gas at a standard pressure of 1 atm, the computed free energies were converted to yield Gibbs energies with a solution phase standard state of 1 mol L^{-1} for all the species except water solvent.[44] For water molecules a standard state of 55.5 M has been used. That is, to the free energy of each species, as computed in Gaussian, a free energy correction term equal to RT $\ln(V_{molar\ gas}/V_{molar\ solution})$, (R = gas constant, T = absolute temperature) was added, where $V_{molar\ gas}$ is the volume occupied by one mole of ideal gas at the considered temperature, and $V_{molar\ solution}$ is the volume occupied by one mole of species in a standard solution of concentration 1 mol L^{-1} .

3.3 Results

3.3.1 Synthesis and Characterisation

Ten novel iridium(III) phenyl-azo-pyridine complexes were synthesised in good yields by stirring a mixture of the iridium chlorido/iodido dimer precursor with 2 mol equiv. of the appropriate chelating azo-pyridine ligand in dichloromethane (Chart 3.2). All the complexes were characterised by NMR spectroscopy (^{1}H, ^{1}H-^{1}H COSY, ^{13}C, HSQC, HMBC), elemental analysis and ESI-MS (details in the Section **3.2.2.2**).

3.3.1.1 Enantiomers in Solution

The complexes are chiral at the Ir(III) centre. ^{1}H NMR spectra of complexes **1** and **2** in d_4-MeOD after addition of the anionic chiral shift regent Δ-trisphat at 298 K (Figures 3.1 and 3.2) show splitting of the aromatic proton signals in a *ca.* 1:1 ratio, indicating the presence of two enantiomers in equal abundance, similar to previously reported chiral osmium/ruthenium arene picolinamide and iminopyridine anticancer complexes.[45,46]
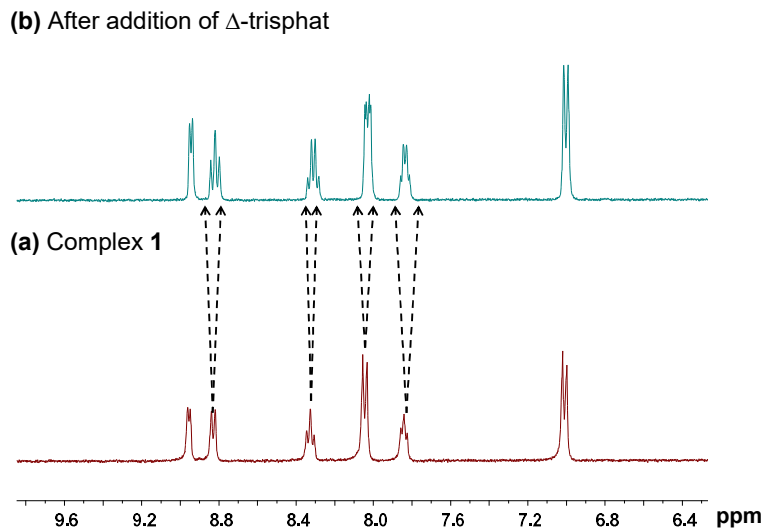
Figure 3.1. ^{1}H NMR (400 MHz, d_4-MeOD) of (a) complex **1** (ca. 1 mM); (b) complex **1** with 3 mol equiv. of Δ-trisphat tetrabutylammonium salt at 298 K, showing the splitting of peaks due to the presence of the two enantiomers of **1**.
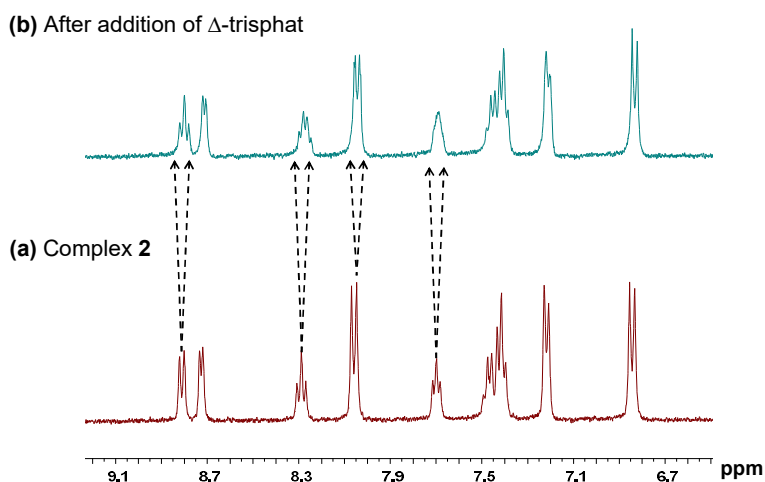
Figure 3.2. ^{1}H NMR (400 MHz, d_4-MeOD) of (a) complex **2** (ca. 1 mM); (b) complex **2** with 5 mol equiv. of Δ-trisphat tetrabutylammonium salt at 298 K, showing the splitting of peaks due to the presence of the two enantiomers of **2**.

3.3.1.2 X-ray Crystal Structures

Single crystals suitable for X-ray diffraction of **1-I·**MeOH, **2**, **3·**MeOH, **5·**MeOH, **7-I**, **8-I** as PF$_6$ salts (**1-I**, **7-I**, **8-I** as iodide salts) were obtained at ambient temperature by slow diffusion of Et$_2$O into saturated methanol or dichloromethane (**8-I**) solutions.

X-ray crystal structures are shown in Figure 3.3. X-ray crystallographic data are listed in Tables A3.1 and A3.2 in the **Appendix**, and selected bond lengths and bond angles in Table 3.1. All the complexes adopt a typical pseudo-octahedral geometry with a "piano-stool" shape. The Ir-I bond lengths in the structures range from 2.6799(5)-2.6943(3) Å. Except for complex **5** (1.870 Å), the distances from the Cp^X ring centroid to iridium are within 1.820 ± 0.009 Å, which are similar to the C^N chelated complex [(Cp*)Ir(ppy)Cl] (1.82 Å) (ppy = 2-phenylpyridine), but slightly longer than the N^N chelated complex [(Cp*)Ir(bpy)Cl]Cl (1.78 Å) (bpy = 2,2'-bipyridine).[21,47,48] The N=N azo bond lengths are correspondingly lengthened to 1.27-1.29 Å from the uncoordinated mean length of N=N bond (1.25 Å)[49]. In addition, the length of Ir-N1(pyridine nitrogen) bond is longer than that of Ir-N8 (azo nitrogen) in the iodido Cp* complexes. However, in the iodido Cp^{xph} complexes, Ir-N1 is of similar length to Ir-N8. The crystal structures of complexes **1**, **3**, and **5** contain protonated phenolic groups, while complexes **2** has a bridging proton shared between the two phenol oxygens.
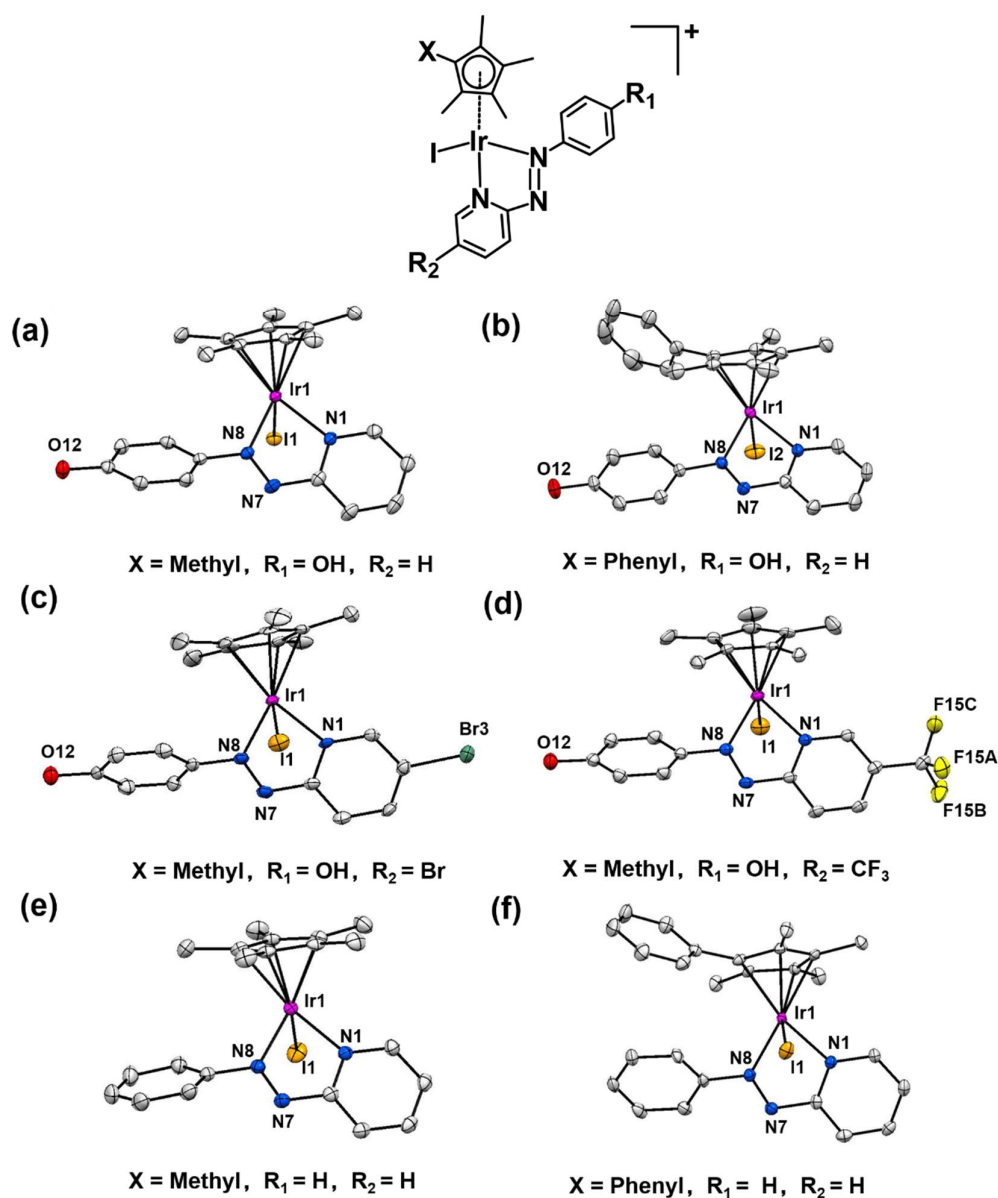
Figure 3.3. ORTEP views of the X-ray crystal structures with thermal ellipsoids drawn at 50% probability for complexes (a) $[(\eta^5\text{-Cp}^*)\text{Ir(azpy-OH)I}]\text{I·MeOH}$ (**1-I·MeOH**), (b) $[(\eta^5\text{-Cp}^{\text{xph}})\text{Ir(HO-azpy)I}]\text{PF}_6$ (**2**), (c) $[(\eta^5\text{-Cp}^*)\text{Ir(HO-azpy-Br)I}]\text{PF}_6\text{·MeOH}$ (**3·MeOH**), (d) $[(\eta^5\text{-Cp}^*)\text{Ir(HO-azpy-CF}_3\text{)I}]\text{PF}_6\text{·MeOH}$ (**5·MeOH**), (e) $[(\eta^5\text{-Cp}^*)\text{Ir(azpy)I}]\text{I}$ (**7-I**), (f) $[(\eta^5\text{-Cp}^{\text{xph}})\text{Ir(azpy)I}]\text{I}$ (**8-I**). The hydrogen atoms, counter anion and solvent molecules have been omitted for clarity.

Table 3.1. Selected bond lengths [Å] and angles [°] for iodido complexes **1-I**·MeOH, **2**, **3**·MeOH, **5**·MeOH, **7-I**, and **8-I**.

	1-I·MeOH	**2**	**3**·MeOH	**5**·MeOH	**7-I**	**8-I**
Ir-C(centroid)	1.823	1.819	1.828	1.870	1.817	1.829
Ir-I	2.68371(16)	2.69042(16)	2.6817(3)	2.6799(5)	2.6851(2)	2.6943(3)
Ir-N1	2.0799(19)	2.0624(17)	2.082(3)	2.082(4)	2.065(2)	2.068(3)
Ir-N8	2.0479(18)	2.0664(17)	2.042(3)	2.032(4)	2.049(2)	2.065(3)
N7-N8	1.281(3)	1.297(2)	1.277(5)	1.282(6)	1.270(3)	1.278(5)
N1-Ir-N8	74.72(7)	75.11(7)	74.77(12)	74.68(18)	74.66(9)	74.69(13)
N1-Ir-I	85.23(5)	85.80(5)	86.35(8)	86.84(11)	85.16(6)	86.81(9)
N8-Ir-I	89.01(5)	90.32(5)	88.07(8)	89.26(12)	90.65(6)	88.28(9)

3.3.2 UV-vis Spectra

Complexes $[(Cp^*)Ir(azpy-OH)I]PF_6$ (**1**), $[(Cp^*)Ir(Br-azpy-OH)I]PF_6$ (**3**) and $[(Cp^*)Ir(CF_3-azpy-OH)I]PF_6$ (**5**) containing a phenolic group on the ligand showed pH-dependent UV-vis spectra in water/acetone (95/5 v/v), illustrated in Figure 3.4a. At pH = 3.0, the spectra of **1**, **3**, and **5**, display a MLCT (metal-to-ligand charge-transfer) absorption band at 439-464 nm (ε= 8000-23000 $M^{-1} \cdot cm^{-1}$). Raising the pH to 11.0 led to a dramatic red-shift of this MLCT band to 558-586 nm with a much higher extinction coefficient (26900-57200 $M^{-1} \cdot cm^{-1}$). The maximum absorption wavelengths and the corresponding molar extinction coefficients of phenolic complexes **1-6** at pH = 3.0 ± 0.1 and pH = 11.0 ± 0.3 are listed in Table 3.2.
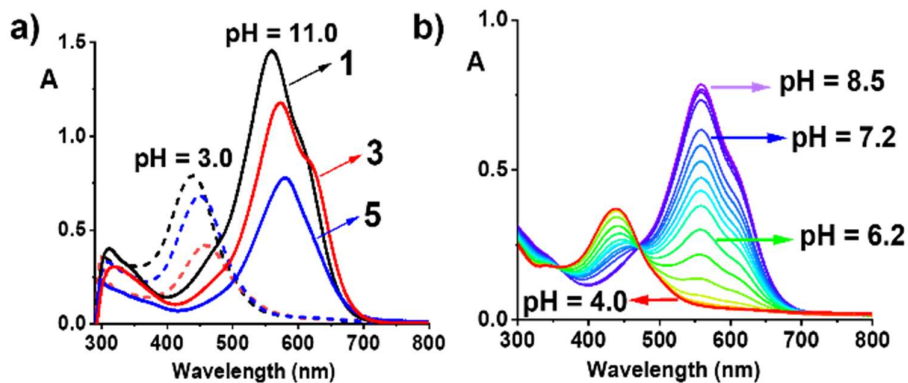
Figure. 3.4. (a) UV-vis spectra of complexes **1** (41 µM, black), **3** (33 µM, red) and **5** (29 µM, blue) at pH = 3.0 ± 0.3 (dash lines) and pH = 11.0 ± 0.3 (solid lines) in water/acetone (95/5 v/v); (b) UV-vis changes for complex **1** from pH 4 to 8.5.

Table 3.2. Absorption wavelengths and molar extinction coefficients for complexes **1-6** containing HO-azpy-R_2 (pH = 3.0 ± 0.1) and O⁻-azpy-R_2 (pH = 11.0 ± 0.3) in water/acetone (5/95, v/v). [sh]: shoulder.

Complex at pH 3.0	λ_{max} /nm	ε/ M⁻¹·cm⁻¹	Complex at pH 11.0	λ_{max} /nm	ε/ M⁻¹·cm⁻¹
1(OH)	307	8500	**1**(O⁻)	310	9700
	439	19300		558(sh)	35500
2(OH)	308	14900	**2**(O⁻)	310	13200
	443	25800		563(sh)	43900
3(OH)	310	10000	**3**(O⁻)	319	9200
	450	20700		573(sh)	35800
4(OH)	307	23600	**4**(O⁻)	309	28600
	455	40500		586(sh)	56300
5(OH)	298	12600	**5**(O⁻)	299	8100
	459	14400		579	26900
6(OH)	306	23600	**6**(O⁻)	307	36000
	464	40000		571	57200

89

3.3.3 pK_a Values of the Phenolic Group

The changes of UV-vis absorbance with pH (e.g. absorbance of complex **1** in Figure 3.4b and of other complexes in Figure 3.5) allowed determination of the pK_a values of the phenolic groups in complexes **1-6** and **9-10** as 5.90-6.50, with the exception of the more acidic [(Cp^{xph})Ir(CF$_3$-azpy-OH)I]PF$_6$ (**6**), with a pK_a 3.90 (all shown in Chart 3.3). Compared to the pK_a values of iodido Cp* analogues, all the iodido Cp^{xph} complexes have lower pK_a values. For example, ΔpK_a = -0.22 from **1** to **2** (R$_1$ = H), -0.35 from **3** to **4** (R$_1$ = Br), and -2.55 from **5** to **6** (R$_1$ = CF$_3$). The chlorido Cp* complex **9** and its Cp^{xph} analogue complex **10** have the same pK_a value of 5.88, which is much lower than their respective iodido analogues **1** and **2**.
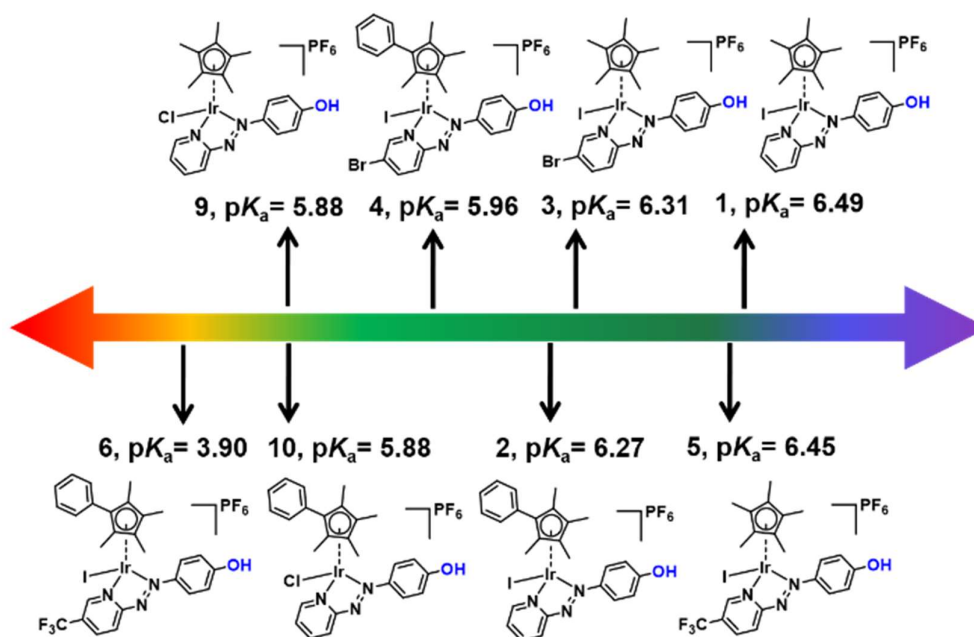
Chart 3.3. The pK_a values of phenolic groups of iodido complexes **1-6** and chlorido complexes **9-10**.
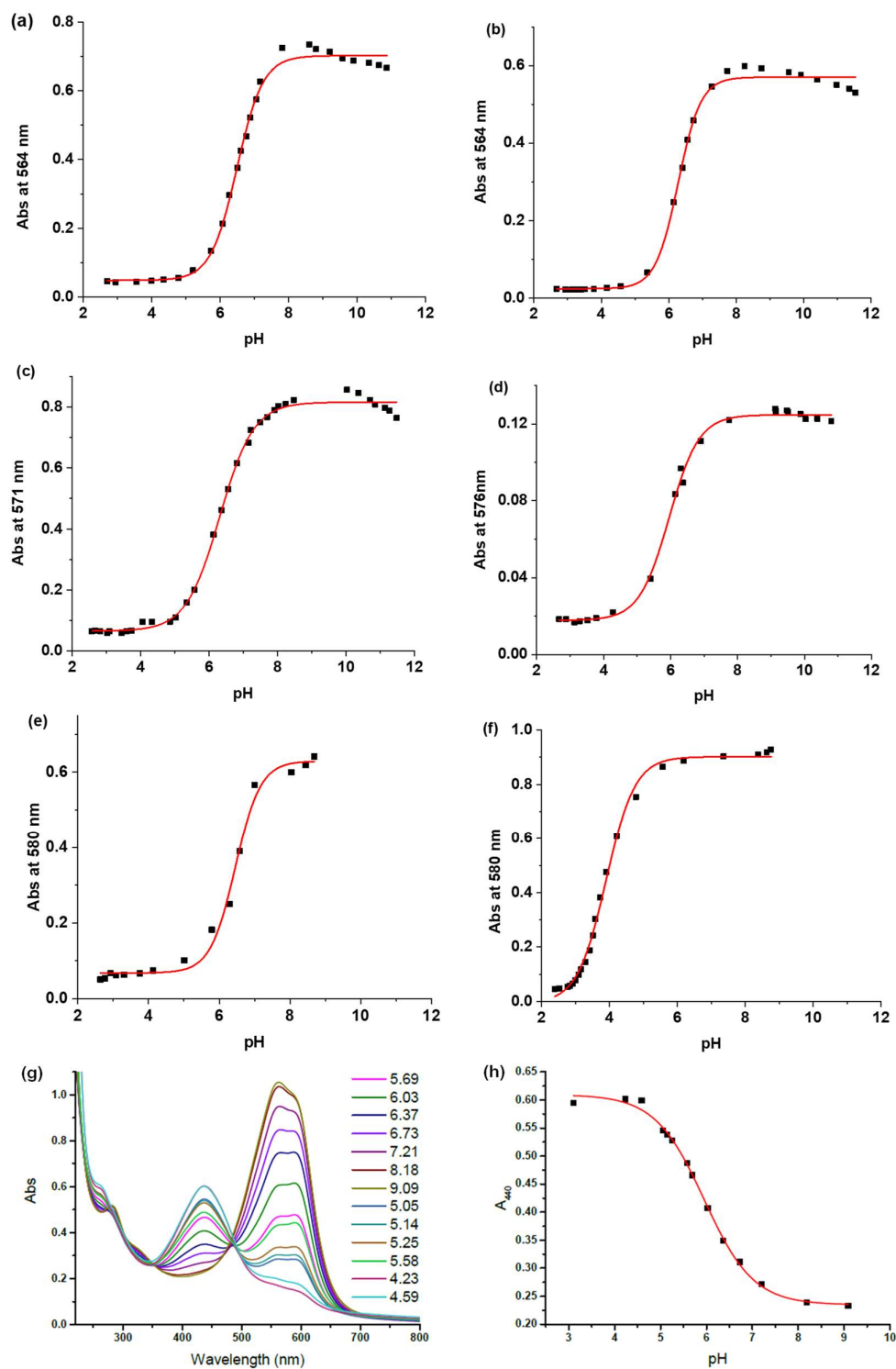
Figure 3.5. Dependence on pH of the UV-vis absorbance of complexes in MeOH/H$_2$O (1/99, v/v) at selected wavelengths. (a) [(η^5-Cp*)Ir(HO-azpy)I]PF$_6$ (**1**); (b) [(η^5-Cp^{xph})Ir(HO-azpy)I]PF$_6$ (**2**); (c) [(η^5-Cp*)Ir(HO-azpy-Br)I]PF$_6$ (**3**); (d) [(η^5-

Cp^{xph})Ir(HO-azpy-Br)I]PF$_6$ (**4**); (e) [(η^5-Cp*)Ir(HO-azpy-CF$_3$)I]PF$_6$ (**5**); (f) [(η^5-Cp^{xph})Ir(HO-azpy-CF$_3$)I]PF$_6$ (**6**); (g) dependence of the UV-vis spectrum on pH for complex [(η^5-Cp*)Ir(azpy-OH)Cl]PF$_6$ (**9**); (h) curve fit for change in absorbance at 440 nm with pH for **9**, corresponding to a pK_a of 5.88 ± 0.02.

3.3.4 Electrochemistry of Iodido Iridium Complexes

Electrochemical reduction of complexes **1**, **3** and **7** in comparison with unbound azpy (phenyl-azo-pyridine), HO-azpy (phenol-azo-pyridine) ligands and iridium dimeric precursor [(Cp*)Ir(μ-I)I]$_2$, was studied by cyclic voltammetry (CV) under N$_2$ versus a Ag$^+$/Ag reference electrode. Complexes **1**, **3**, and **7** exhibited more facile sequential reduction than the corresponding free ligands as well as the iridium precursor [(Cp*)Ir(μ-I)I]$_2$. The first reduction step is quasi-reversible, ranging from -0.07 to -0.28 V. The second is irreversible, ranging from -0.58 to -0.79 V (Table 3.3, cyclic voltammograms shown in Figure 3.6).

Table 3.3. Electrochemical reduction potentials of selected ligands and complexes.

Ligand/Complex[a]	E$_{red}$ (V)	Complex[a]	E$_{red}$ (V)
Azpy	-1.07, -1.93	1	-0.28, -0.79
Azpy-OH	-0.94, -1.76	3	-0.13, -0.58
[Cp*Ir(μ-I)I]$_2$	-1.21, -1.69	7	-0.07, -0.63
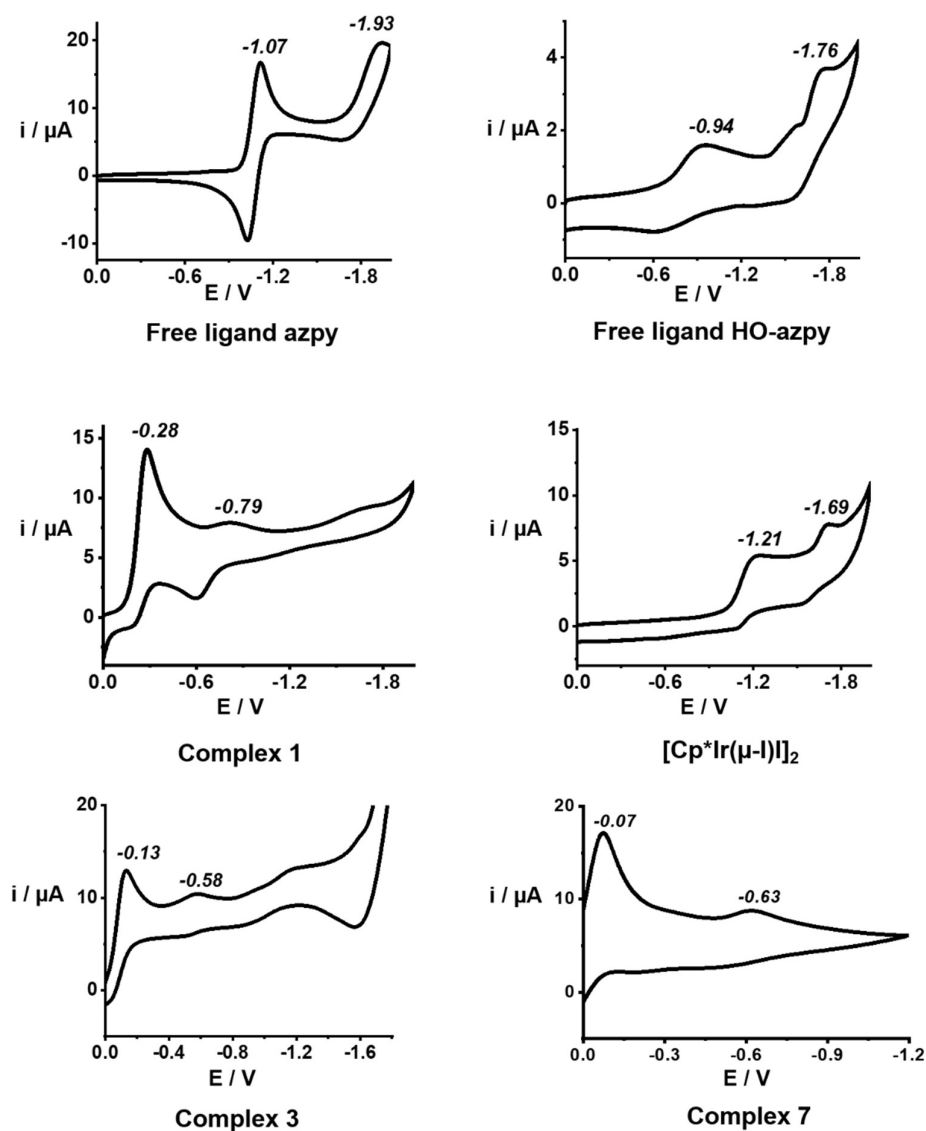
Figure 3.6. Electrochemical cyclic voltammograms for selected ligands and complexes, showing complexes **1**, **3**, and **7** undergo more facile sequential reduction than the free azpy ligand as well as the iridium precursor [Cp*Ir(μ-I)I]$_2$. The second

step of reduction for complex **7** is irreversible due to dissociation of the two-electron

reduction product phenyl-hydrazo-pyridine from the metal.

3.3.5 Hydrolysis

^{1}H NMR spectra of iodido complexes **1-8** were recorded in d_4-MeOD/D$_2$O (1/5 v/v)

at 310 K at various time intervals up to 24 h. No changes in the spectra were observed

after 24 h. Over this time the ESI-MS analysis of the NMR solutions showed only

peaks assignable to cation [M-PF$_6$]$^+$ of the intact iodido complexes. To verify that the

^{1}H NMR spectrum contained only peaks for the intact complexes, and that therefore

no hydrolysis had occurred, complex [(Cp*)Ir(Br-azpy-OH)I]PF$_6$ (**3**) was reacted

with 1.2 mol equiv. AgNO$_3$ at 310 K to remove the coordinated iodide in MeOD/D$_2$O

(1/1, v/v). The resulting NMR peaks for the aqua adduct **3-H$_2$O** were assigned (Figure

3.7a) and contrasted with the hydrolysis-inert complex **3** (Figure 3.7b).

The hydrolysis of the chlorido analogues was also investigated at 310 K for

comparison. ^{1}H NMR spectra of 100 μM solutions of [(Cp*)Ir(HO-azpy)Cl]PF$_6$ (**9**)

and [(Cp^{xph})Ir(HO-azpy)Cl]PF$_6$ (**10**) in d$_6$-DMSO/D$_2$O (1/9, v/v) showed that these

complexes hydrolyzed to the extent of 53% and 66%, respectively, at equilibrium

over 24 h. The aqua adduct of complex **9** was also detected by ESI-MS, giving a

positive ion peak m/z at 543.99 corresponding to of the formula [(Cp*)(Ir-H$_2$O)(O$^-$-

azpy)]$^+$ (**9-H$_2$O**) (calcd 544.15). The hydrolysis complex **9** followed pseudo first-

order kinetics with a hydrolysis rate constant of 0.00698 ± 0.00096 min^{-1} at 310 K

and the half-life of 99.3 min determined by HPLC analysis (Figure 3.8b).
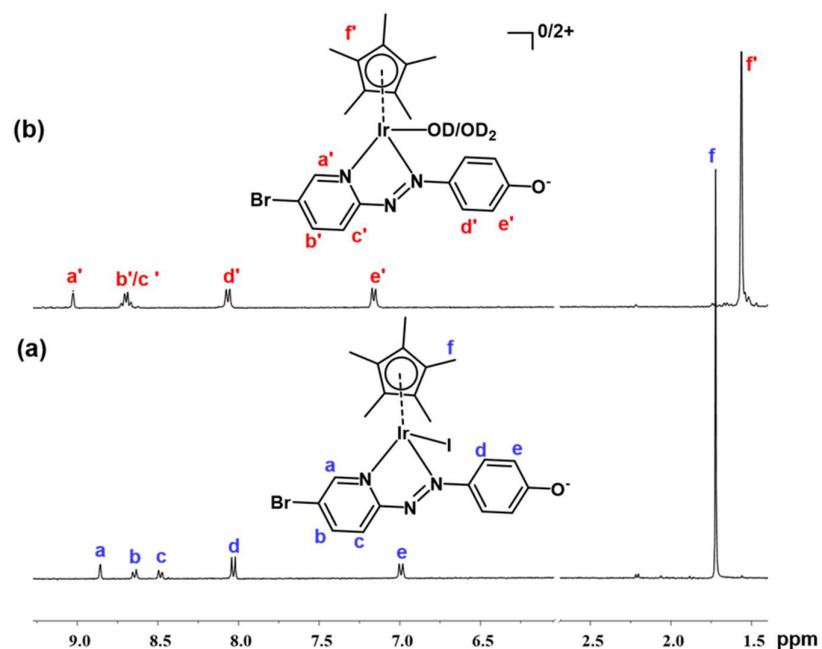
Figure 3.7. ^{1}H NMR (400 MHz, 298 K) of (a) **3** alone at 310 K after 24 h; (b) **3** with

1.2 mol equiv. AgNO$_3$ in d$_4$-MeOD/D$_2$O (1/1, v/v) at 310 K after 24 h, showing

complex **3** is inert towards hydrolysis.
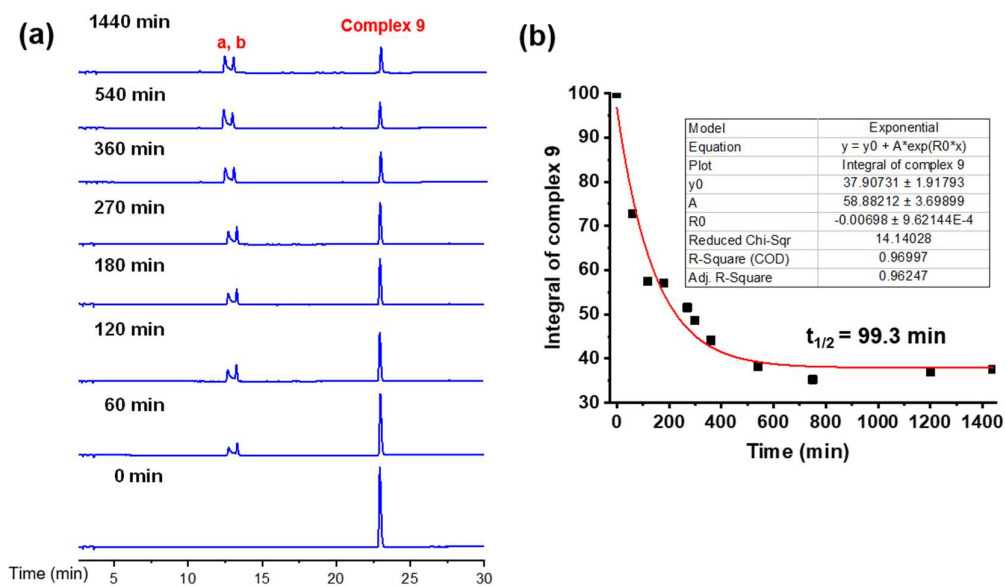
Figure 3.8. (a) Time-dependent HPLC chromatograms (detection wavelength 254

nm) of complex **9** (50 µM) in MeOH/H$_2$O (5/95, v/v) at 310 K. (b) First-order kinetic

fitting of the time versus the corresponding HPLC peak integral for complex **9** confirmed by ESI-MS. Peak a and b are assigned respectively as the aqua adduct and the acetonitrile adduct, corresponding to the same ion peak assigned as [**9**-Cl]$^+$.

3.3.6 Stability in Aqueous NaCl and DMSO

Next, the stability of iodido complex [(Cp*)Ir(HO-azpy-Br)I]PF$_6$ (**3**) (1.0 mM) in MeOD/D$_2$O (1/1, v/v, pH* 7.0) was studied in the presence of 4.0 mM, 23.0 mM, or 103.0 mM NaCl, physiologically relevant extracellular and intracellular concentrations, over 24 h at 310 K. Integration of the methyl ^{1}H NMR peaks for Cp* at δ 1.73 ppm (**3**) and δ 1.59 ppm (**3-Cl**, the chlorido analogue of **3**), showed that the amount of **3-Cl** formed by iodide/chloride ligand exchange at these three NaCl concentrations was 2.7%, 7.8%, and 16.5%, respectively (Figure 3.9). LC-MS spectra for complex **3** at micromolar concentrations with the three different NaCl concentrations showed a positive-ion peak for the chlorido analogue **3-Cl** with a shorter retention time of *ca.* 17.6 min (c.f. *ca.* 21.0 min for **3**, Figure 3.10). In addition, ^{1}H NMR spectra of the iodido and chlorido complexes in d$_6$-DMSO were monitored over a time course of 19 d to investigate their stability at 298 K, since DMSO was used as a solvent in cell growth inhibition assays. However, no changes to any ^{1}H NMR peaks were observed (Figures A3.1 and A3.2 in the **Appendix**). ESI-MS data showed peaks only for the original complexes, providing evidence for the inertness of these iridium complexes toward solvolysis in DMSO.
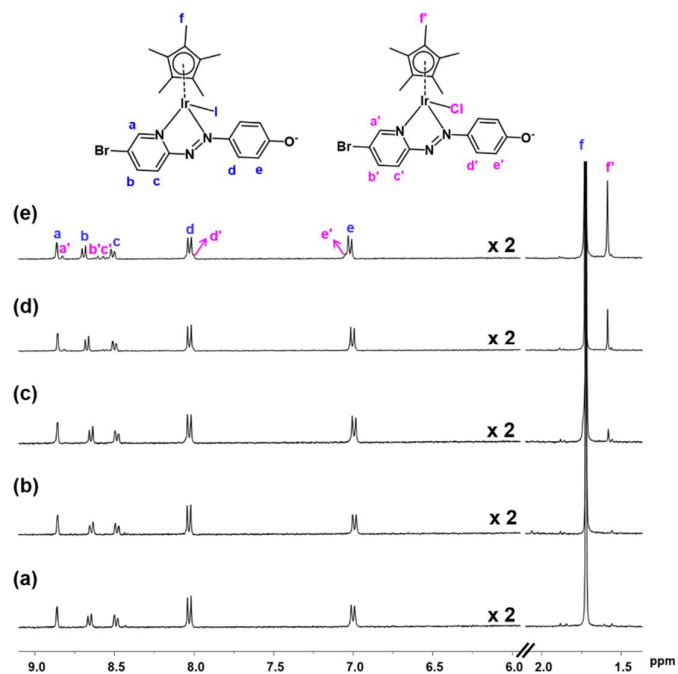
Figure 3.9. ^{1}H NMR (400 MHz, 50% d$_4$-CD$_3$OD/D$_2$O, pH* 7.0) of complex **3** (a) alone after 5 min; (b) alone after 24 h; (c) with 4.0 mM NaCl; (d) with 23.0 mM NaCl; (e) with 103.0 mM NaCl at 310 K after 24 h, showing that complex **3** resists hydrolysis and undergoes only < 16.5 % ligand exchange under physiologically relevant concentrations of chloride by ^{1}H NMR peak integrals.
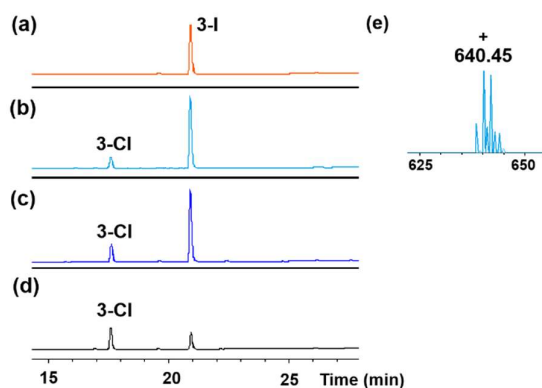
Figure 3.10. HPLC chromatograms (detection wavelength 254 nm) of iodido complex complex **3** (a) before, and (b) after incubation with 4.0 mM NaCl, (c) 23

mM NaCl, and (d) 103 mM NaCl, at 310 K for 24 h. (e) The detected MS peak for the chlorido analogue of complex **3** in 103 mM NaCl solution at 310 K after 24 h by LC-MS.

3.3.7 Interaction with Nucleobase Models and Amino Acids

Reactions of complex $[(Cp^*)Ir(HO\text{-}azpy\text{-}Br)I]PF_6$ (**3**) with 3.0 mol equiv. nucleotide guanosine 5'-monophosphate (5'-GMP), nucleobase 9-ethylguanine (9-EtG), and amino acids L-histidine, N-acetyl-L-methionine, L-tryptophan, and L-arginine were also studied over 24 h at 310 K in 0.1 M phosphate buffer $D_2O/d_4\text{-MeOD}$ (1/1, v/v, pH^* 7.8) by ^1H NMR and ESI-MS. No adducts were observed between complex **3** and 5'-GMP or 9-EtG (Figure A3.3 in the **Appendix**), nor with L-Trp or L-Arg by NMR or by ESI-MS. Only small amounts of adducts with N-acetyl-L-methionine (29%) or L-histidine (7%) were observed (Figure 3.11) based on ^1H NMR peak integrals, evidenced by ESI-MS with assignable peaks for adducts (Table 3.4).

The chlorido complex **9** not only reacted with 9-EtG to the extent of 15% (Figure 3.12), but also almost completely formed adducts with N-acetyl-L-methionine and L-histidine (Figure 3.13) based on ^1H NMR peak integrals. These adducts were also characterised by ESI-MS, shown in Table 3.4.
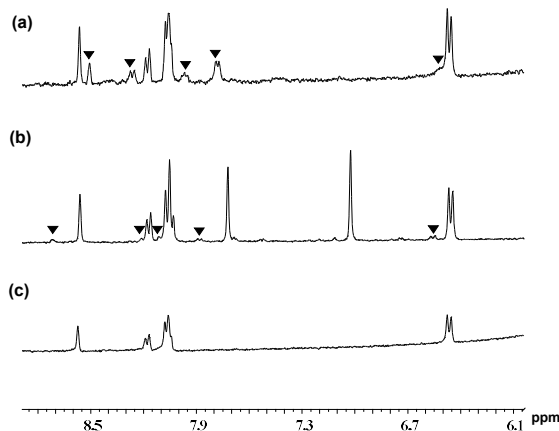
Figure 3.11. ^{1}H NMR spectra (400 MHz, d$_4$-MeOD/D$_2$O, 1/1, v/v, pH* 7.8) showing the aromatic region of (a) complex **3** with 3.0 mol equiv. N-acetyl L-methionine at 310 K after 24 h; (b) **3** with 3.0 mol equiv. L-histidine at 310 K after 24 h; (c) **3** at 310 K after 24 h. Arrows indicate new peaks for minor adducts of **3** with the amino acid confirmed by ESI-MS (Table 3.4).
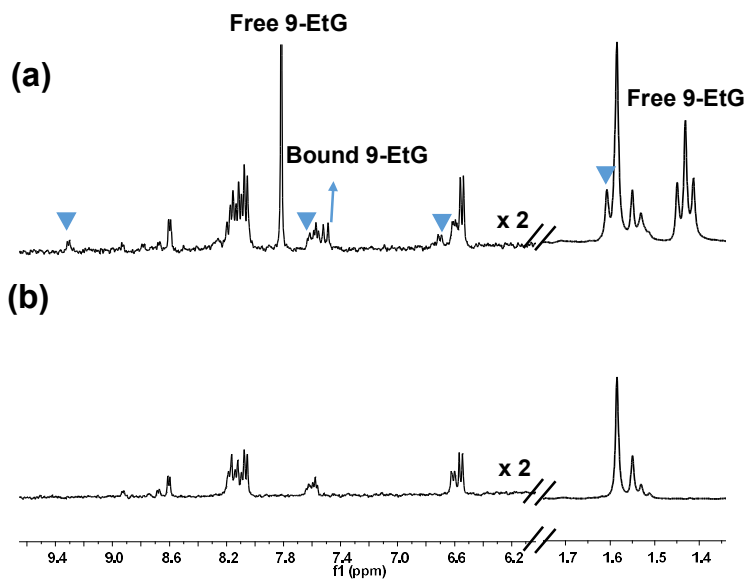
Figure 3.12. ^{1}H NMR (400 MHz, d$_4$-MeOD/D$_2$O, 1/1, v/v, pH* 7.8) of (a) complex **9** with 3.0 mol equiv. 9-EtG at 310 K after 24 h; (b) complex **9** at 310 K after 24 h. The blue triangles indicate the adduct **9**_9-EtG.

Table 3.4. The extent of adduct formation and the detected ESI-MS peaks for iodido complex **3** and chlorido complex **9** with 9-EtG, N-acetyl-L-methionine (Ac-Met) and L-histidine (His).

Adducts	Extent[a] (%)	Detected[b] m/z	Calcd m/z
[Cp*(Ir-His)(O⁻-azpy-Br)]⁺(**3**_His)	7	758.92⁺	759.12⁺
[Cp*(Ir-Ac_Met)(O⁻-azpy-Br)]⁺(**3**_Ac-Met)	29	795.11⁺	795.11⁺
[Cp*(Ir-9-EtG)(O⁻-azpy)]⁺ (**9**_9-EtG)	15	705.10	705.22⁺
[Cp*(Ir-His)(O⁻-azpy)]⁺ (**9**_His)	100	681.11⁺	681.21⁺
[Cp*(Ir-Ac_Met)(O⁻-azpy)]⁺ (**9**_Ac-Met)	100	717.06⁺	717.20⁺

[a] The extent was determined by the ^{1}H NMR integral of the adduct.

[b] The MS peak of the adduct was detected by LC-MS.
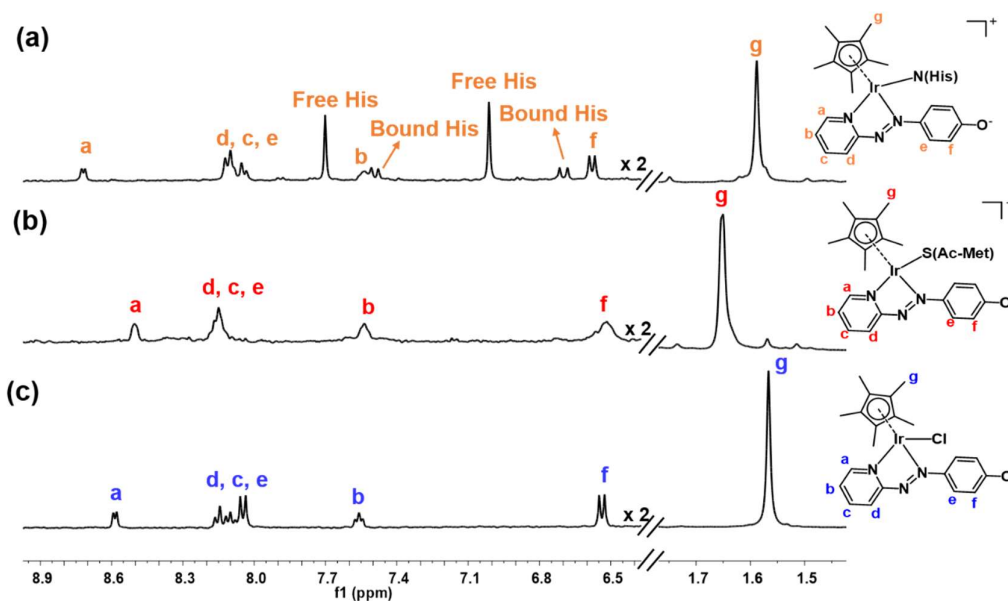
Figure 3.13. ^{1}H NMR spectra (400 MHz, d₄-MeOD/D₂O, 1/1, v/v, pH* 7.8) showing the adduct formation of (a) complex **9** with 3.0 mol equiv. L-histidine at 310 K after

24 h; (b) complex **9** with 3.0 mol equiv. N-acetyl-L-methionine at 310 K after 24 h;

(c) **9** at 310 K.

3.3.8 Reactions with N-Acetyl-L-Cysteine

Initially reactions of complexes **1**, **3** and **7** with N-acetyl-L-cysteine (NAC), as an

example of a biologically important thiol, were studied by ^{1}H NMR spectroscopy.

Time-dependent ^{1}H NMR spectra of [(Cp*)Ir(HO-azpy)I]PF$_6$ (**1**) (1 mM) with 3 mol

equiv. NAC in d$_4$-MeOD/0.1 M phosphate buffer D$_2$O (3/7 v/v, pH* 7.4) were

recorded up to 24 h at 310 K (Figure 3.14). In the aromatic region, a new set of ligand-

based peaks appeared while the set of ligand peaks of iodido complex **1** decayed

during the first hour (Figure 3.14). While in the aliphatic area, the peak for Cp*

protons of complex **1** shifted completely from δ 1.71 to 1.59 ppm within the first hour,

and two new sets of peaks in a 1:1 ratio for acetyl methyl protons of NAC appeared

at δ 1.88 and 1.77 ppm (Figure 3.14).
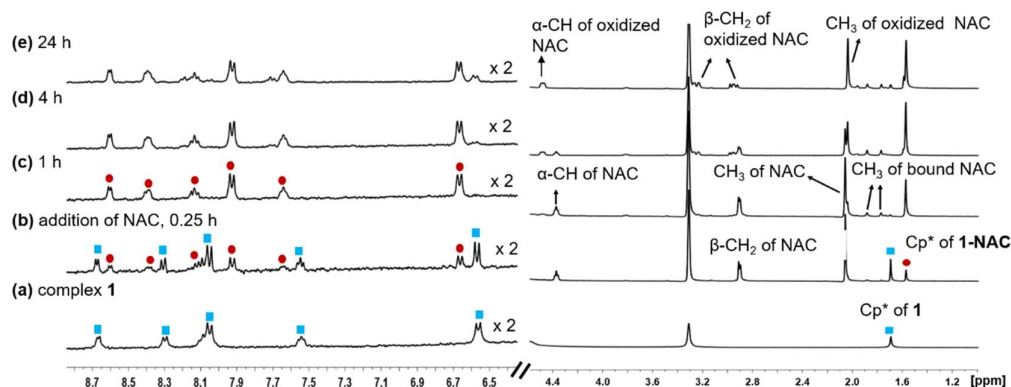
Figure 3.14. Time-dependent ^{1}H NMR spectra (400 MHz) of (a) complex **1** alone;

and complex **1** with 3 mol equiv. NAC at (b) 0.25 h, (c) 1.0 h, (d) 4 h, (e) 24 h in 0.1

M phosphate buffer D_2O/d_4-MeOD (7/3, v/v, pH* 7.4). Blue squares indicate **1**, and red circles indicate **1-NAC**. The presence of diastereomers of **1-NAC** is indicated by the two sets of peaks in a 1:1 ratio for the acetyl methyl protons of bound NAC.
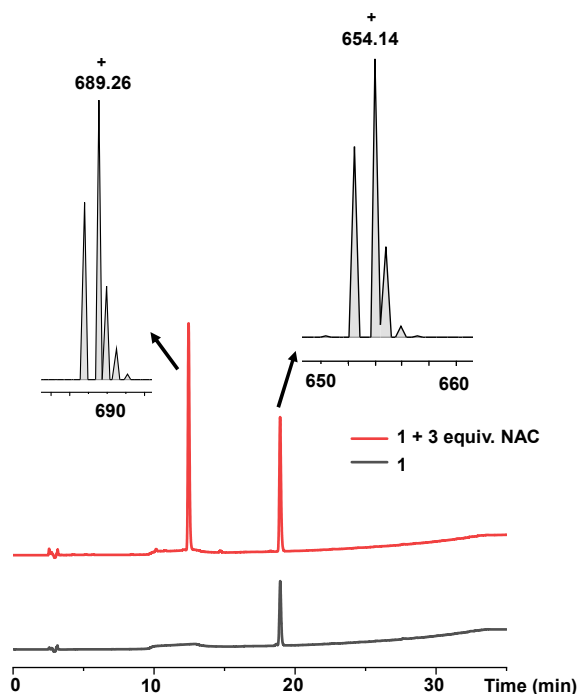
Figure 3.15. HPLC chromatograms (detection wavelength 254 nm) for complex **1** (black), and complex **1** with 3 mol equiv. NAC (red) after 1 h incubation in CH_3CN/H_2O (1/9, v/v) at 310 K. MS peaks with *m/z* $[654.14]^+$ assignable as $[\mathbf{1}]^+$ and *m/z* $[689.26]^+$ assignable as $[(\mathbf{1}\text{-NAC})\text{-I}]^+$ which indicates the formation of **1-NAC** adducts.

After reaction of **1** (100 μM) with 3 mol equiv. NAC for 1 h, LC-MS analysis showed a new ESI-MS peak with a shorter retention time of *ca.* 12.5 min with *m/z* 689.26, assignable as $[(\mathbf{1}\text{-NAC})\text{-I}]^+$ with a bound deprotonated NAC thiolate (calcd

689.18, NAC is [CH$_3$CONHCH(COOH)(CH$_2$S)]$^-$ in Figure 3.15). This confirmed that the new sets of NMR peaks for ligand, Cp* and NAC were from **1-NAC** adducts. The two sets of acetyl methyl peaks for bound NAC can be assigned to the diastereomers of **1-NAC** (Figure 3.14) due to the chirality of the iridium centre and NAC. Diastereomers were also evident in the ^{1}H NMR spectra of isolated adducts of complex **7** (Figure 3.16) and **3** (Figure 3.17) with NAC, as two sets of peaks. Similarly, all the ^{13}C NMR signals showed equally intense pairs of peaks for **7-NAC** (details of ^{13}C NMR assignments for **7-NAC** in Section **3.2.2.2**). This appears to be the first characterisation of half-sandwich iridium NAC adducts.

In contrast, no adduct was observed by LC-MS upon incubation of complex **7** with 10 mol equiv. of the amino acid β-alanine under the same reaction conditions. Hence, the thiol group of NAC appears to be a crucial site for reaction with these iodido iridium complexes.
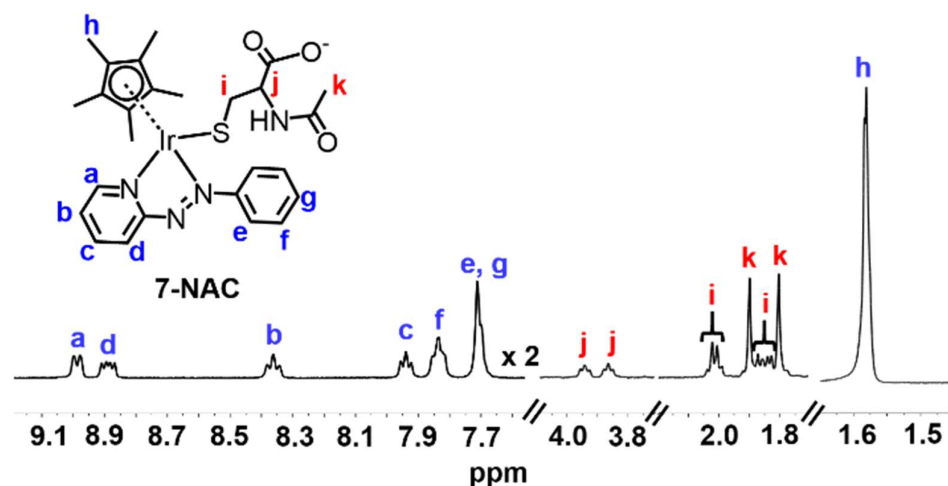
Figure 3.16. ^{1}H NMR spectrum (400 MHz, d$_4$-MeOD/0.1 M phosphate buffer D$_2$O, 3/7, v/v, pH* 7.4, 298 K) of isolated **7-NAC** adducts. The bound NAC (assigned as

103

red i, j, and k), the Cp* ring methyl (assigned as blue h) and the protons assigned as

a and d on the azo ligand show two sets of peaks due to the presence of diastereomers.
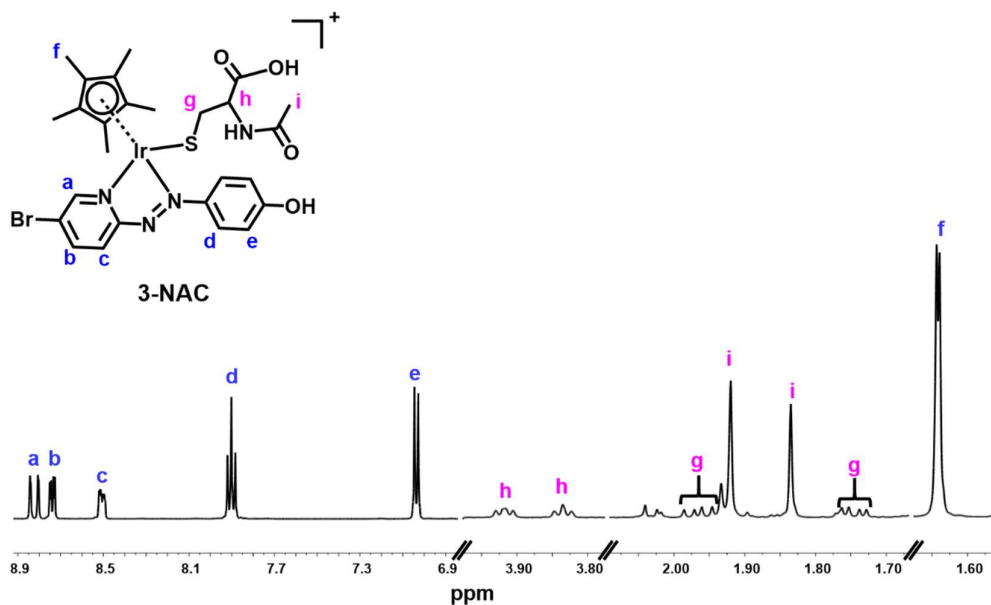
Figure 3.17. ^{1}H NMR (400 MHz, d$_4$-MeOD) spectrum of **3-NAC**. The presence of diastereomers is evident from the double sets of peaks for all protons.

3.3.9 Reactions with Glutathione

Next the reactivity of complex **7** with glutathione (GSH) was investigated. In the ^{1}H

NMR spectrum of [(Cp*)Ir(azpy)I]PF$_6$ (**7**) (1 mM) within 15 min after the addition of

GSH (2 mM) in d$_4$-MeOD/ phosphate buffer D$_2$O (0.1 M, 3/7 v/v, pH* 7.4) at 310 K,

a new set of aromatic ligand peaks as well as a new set of GSH protons appeared

(Figure 3.18), and the Cp* methyl peak shifted from 1.70 to 1.53 ppm and split into

two peaks indicative of diastereomers of [(Cp*)(Ir-SG)(azpy)]$^+$ (**7-SG**).
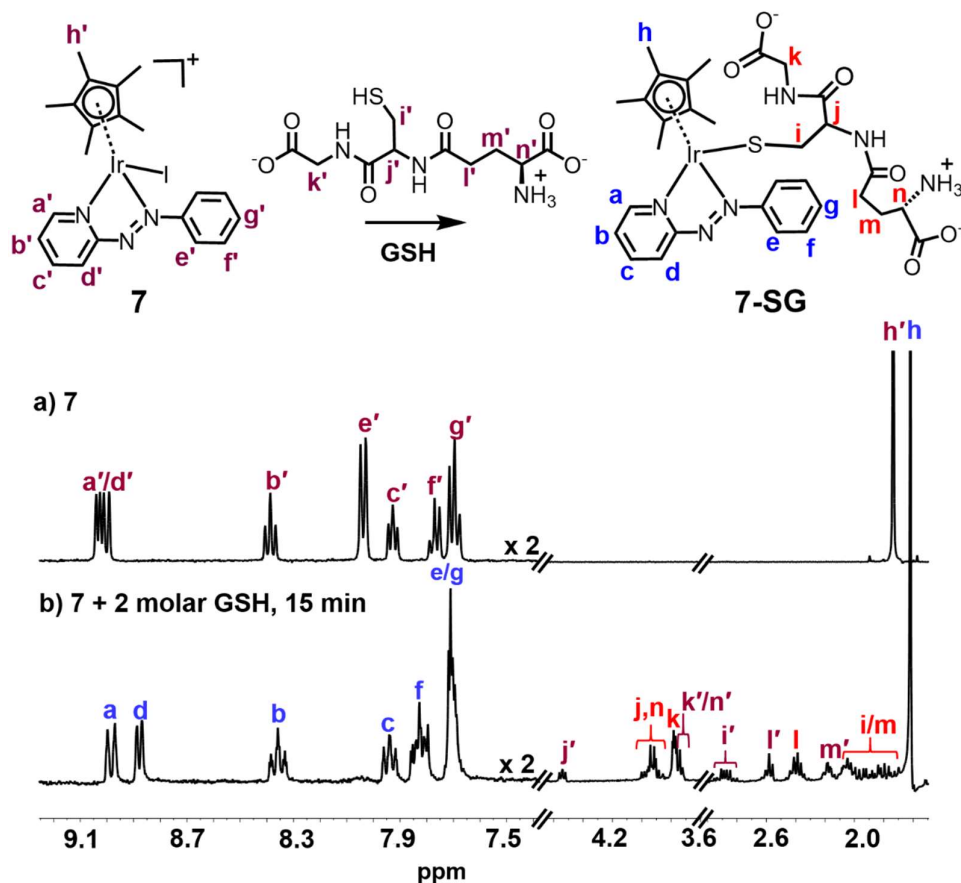
Figure 3.18. ^{1}H NMR spectra (400 MHz, d$_4$-MeOD/0.1 M phosphate buffer D$_2$O, 3/7 v/v, pH* 7.4) of (a) complex **7** (1 mM), and (b) 15 min after addition of 2 mol equiv. GSH (2 mM) at 310 K, showing complete formation of **7-SG**.The peak assigned to protons h' is a double peak.

Meanwhile, HPLC separation of the NMR solution revealed a new peak with shorter retention time of *ca.* 12.0 min compared to the parent complex **7** (*ca.* 21.5 min, Figure 3.19). This new ESI-MS peak with detected *m/z* 817.4 indicated the new emerging product in the NMR solution was the glutathione thiolate adduct [(**7-SG**)+H]$^+$ (calcd *m/z* 817.2).
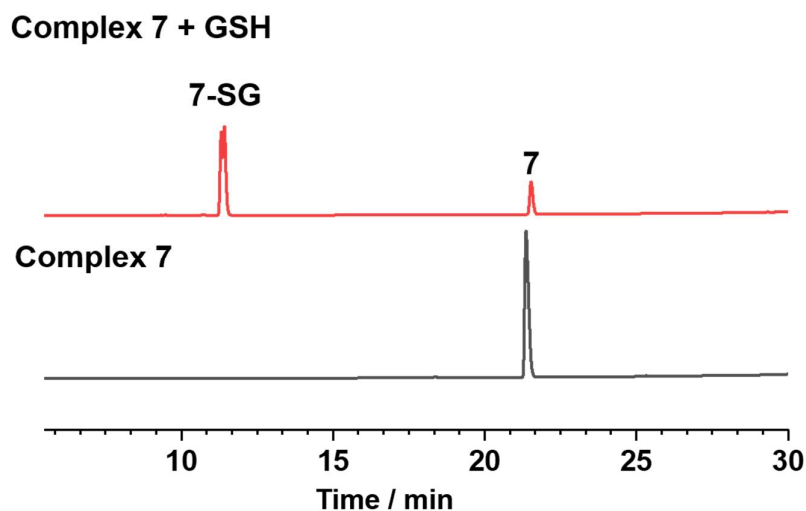
Figure 3.19. HPLC chromatograms (detection wavelength 254 nm) for complex **7** alone (100 μM) and 15 min after reaction of **7** (1 mM) with 2 mol equiv. GSH in 0.1 M phosphate buffer D_2O/d_4-MeOD (7/3, v/v, pH* 7.4) at 310 K. HPLC sample was prepared by 1:10 v/v dilution with MeOH/H_2O (1/9, v/v).

When **7** was reacted with 10 mol equiv. GSH under similar conditions, there was a dramatic loss in intensity of peaks in the aromatic region of the ^{1}H NMR spectrum after 15 min, together with broadening of several peaks in the aliphatic region, as shown in Figure 3.20b, perhaps due to the presence of paramagnetic species. After 3 h, a new set of peaks appeared in the aromatic region combined with a 1:1 doublet at δ 1.79/1.82 ppm as well as new peaks at δ 3.30 ppm assignable to the β-CH_2 of GSSG, Figure 3.20c.

The main species in the NMR reaction mixture after 3 h were subsequently separated by HPLC and analysed by positive-ion mass spectra. The MS peak at *m/z* 183.65 was assigned as unbound azpy ligand [(azpy)+H]$^+$ (calcd 184.08), and the

peak with *m/z* 185.64 as the two-electron-reduced product phenyl-hydrazo-pyridine

$[(H_2azpy)+H]^+$ (calcd 186.10), Figure 3.21. In addition, a MS peak with *m/z* 786.96

was assigned as binuclear $[(Cp^*Ir)_2(\mu\text{-}SG)_3+3H]^{2+}$ (calcd 787.19; Figure 3.21). These

species indicated that after 3 h, the new set of ^{1}H NMR aromatic peaks (Figure 3.20c)

arose from phenyl-hydrazo-pyridine ligand due to the reduction of azpy ligand, with

the peaks at 1.79/1.82 ppm from the Cp* methyls of $[(Cp^*Ir)_2(\mu\text{-}SG)_3]^+$.
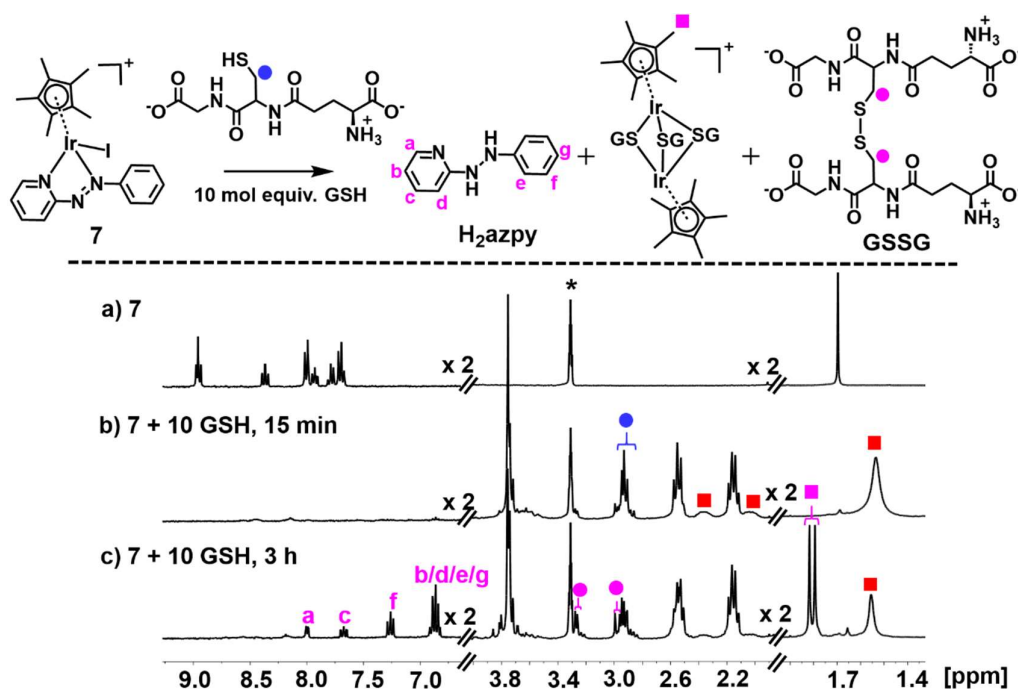
Figure 3.20. ^{1}H NMR spectra (400 MHz, d$_4$-MeOD/0.1 M phosphate buffer D$_2$O, 3/7

v/v, pH* 7.4, 298 K) of (a) complex **7** (1 mM), (b) 15 min, and (c) 3 h after reaction

with 10 mol equiv. GSH at 310 K. The broadening of peaks in (b) can be ascribed to

paramagnetic effects, and the new set of peaks in (c) assigned to the released phenyl-

hydrazo-pyridine (H$_2$azpy) and tri-SG bridged iridium dimer $[(Cp^*Ir)_2(\mu\text{-}SG)_3]^+$. Red

squares denote the **7-SG** adduct and * denotes residual CHD$_2$OD.
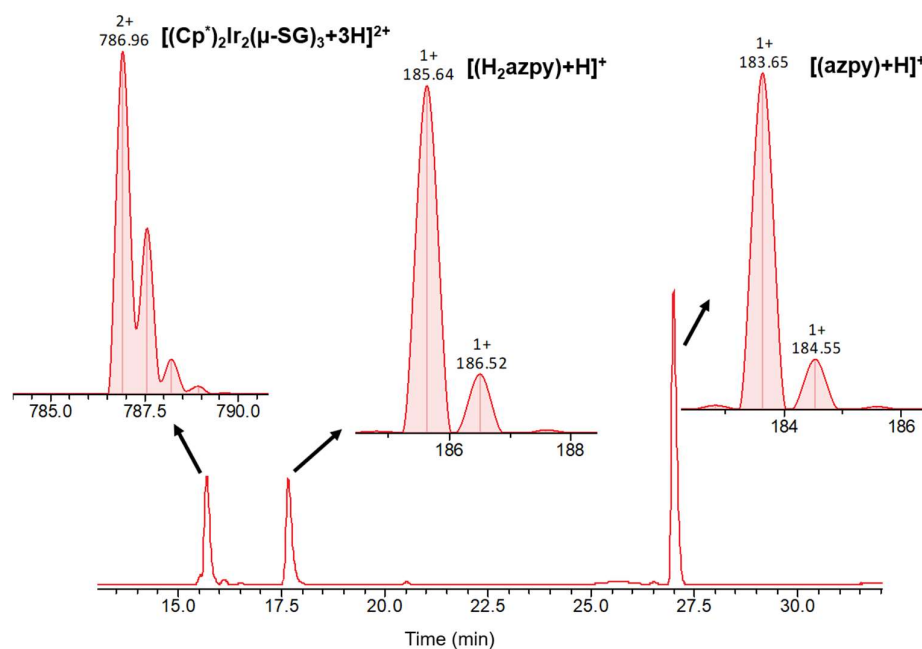
Figure 3.21. LC-MS study of a ^{1}H NMR sample 3 h after reaction of complex **7** (1 mM) with GSH (10 mM) as described in Figure 3.20c, indicating the formation of phenyl-hydrazo-pyridine (H$_2$azpy) and SG-bridged iridium adduct $[(Cp^*)_2Ir_2(\mu\text{-}SG)_3]^+$. Eluents: A-water (0.1% v/v TFA), B-acetonitrile (0.1% TFA). 0-10 min, 2%-15% B; 10-40 min, 15%-80% B; 40-45 min, 80%-2% B; 40-55 min, 2% B.

3.3.10 Radical Trapping by EPR

Whether the NMR peak broadening (Figure 3.20b) due to presence of radicals was investigated by attempting to detect them by electron paramagnetic resonance (EPR) using a spin trap. EPR spectra of a solution containing **7** (1 mM) with GSH (20 mol equiv.) in phosphate buffer (0.1 M, pH 7.4) and the spin trap DMPO (Figure 3.22a) or DEPMPO (Figure 3.23b). DMPO/$^\bullet$OH adduct showed a 4-line spectrum in ratio of 1:2:2:1 due to the equivalent hyperfine splitting constants. DEPMPO/$^\bullet$OH showed a strong doublet quartet signals in ratio of 1:2:2:1 within the first 87 min, which

decreased in intensity thereafter. These EPR signals are assignable by simulation to trapped hydroxyl radicals (Figures 3.22b and 3.23c). GSH alone in the phosphate buffer (0.1 M, pH 7.4) (Figure 3.23a) or complex **7** (1 mM) with GSH (20 mol equiv.) in pre-deaerated phosphate buffer (0.1 M, pH 7.4) with argon, were EPR-silent. In addition, when superoxide dismutase was added to the starting reaction mixture of complex **7** with GSH in aerated phosphate buffer, the formation of hydroxyl radicals was also not observed.
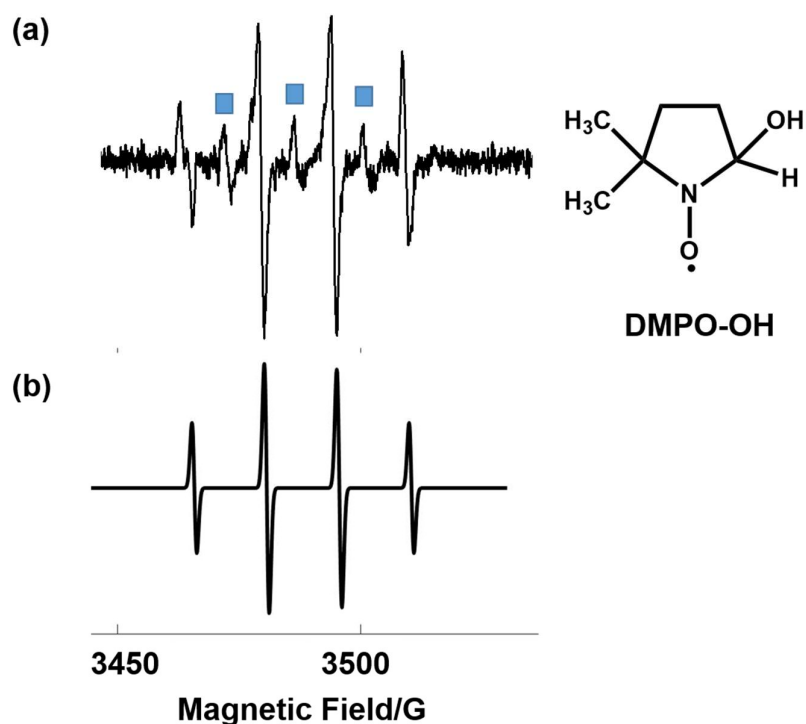
Figure 3.22. (a) EPR spectrum of hydroxyl radicals trapped as DMPO-OH over the first 87 min from reaction of complex **7** (1 mM) with GSH (20 mM) in 0.1 M phosphate buffer (pH 7.4) at ambient temperature in the presence of DMPO (100 mM). (b) Simulated spectrum of DMPO-OH using Easyspin ($a^N = a^{\beta H} = 15$ G). The blue squares indicate oxidized intermediates[50] arising from DMPO-OH ($a^N = 15.1$ G).
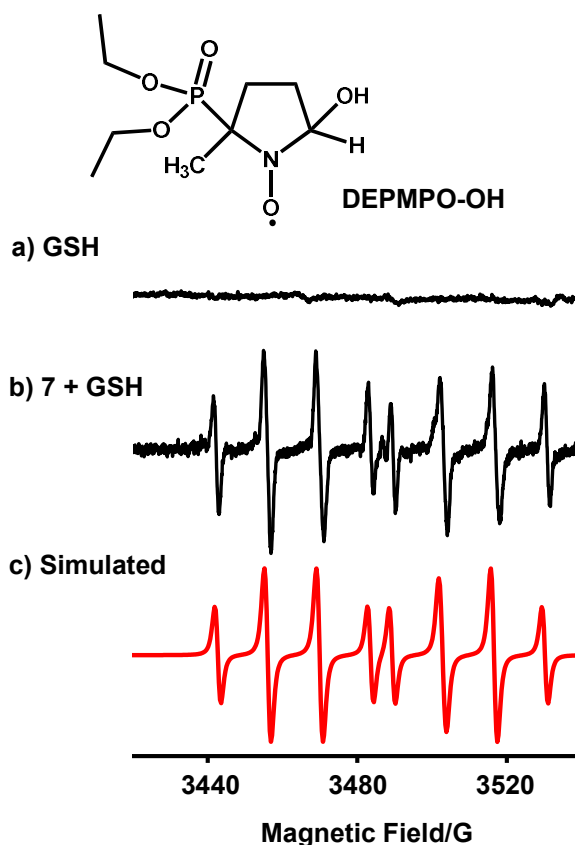
Figure 3.23. EPR spectra of (a) GSH alone; (b) radicals trapped by DEPMPO (100 mM) in the reaction mixture of complex **7** (1 mM) with GSH (20 mol equiv.) in 0.1 M phosphate buffer, pH 7.4, in the initial 87 min at 298 K; (c) simulated spectrum for trapped hydroxyl radicals DEPMPO-OH ($a^N = 14.0$ G, $a^H = 13.2$ G, and $a^P = 47.3$ G)[51] using the EasySpin program.[52]

3.3.11 Catalysis of GSH Oxidation

Whether these $[(Cp^X)Ir(R_1\text{-azpy-}R_2)I]^+$ complexes are catalysts in the oxidation of GSH to GSSG is investigated. Reactions of complexes **1** (Cp*, $R_1 = OH$, $R_2 = H$), **3** (Cp*, $R_1 = OH$, $R_2 = Br$), **7** (Cp*, $R_1 = R_2 = H$), and **8** (Cp^{xph}, $R_1 = R_2 = H$), (Chart 3.2, 100 µM) with GSH (10 mM) in phosphate buffer (30 mM, pH* 7.4) at 310 K for

110

24 h was monitored by ^{1}H NMR (Figure 3.24). The formation of GSSG was evident from the appearance of new peaks at e.g. δ 3.30 ppm corresponding to the β-CH$_2$ of GSSG (Figure 3.24),[53] and was further confirmed by the HPLC/LC-MS peak with *m*/*z* at 612.62 (calcd 613.15 for [GSSG+3H]$^+$), Figure 3.25.
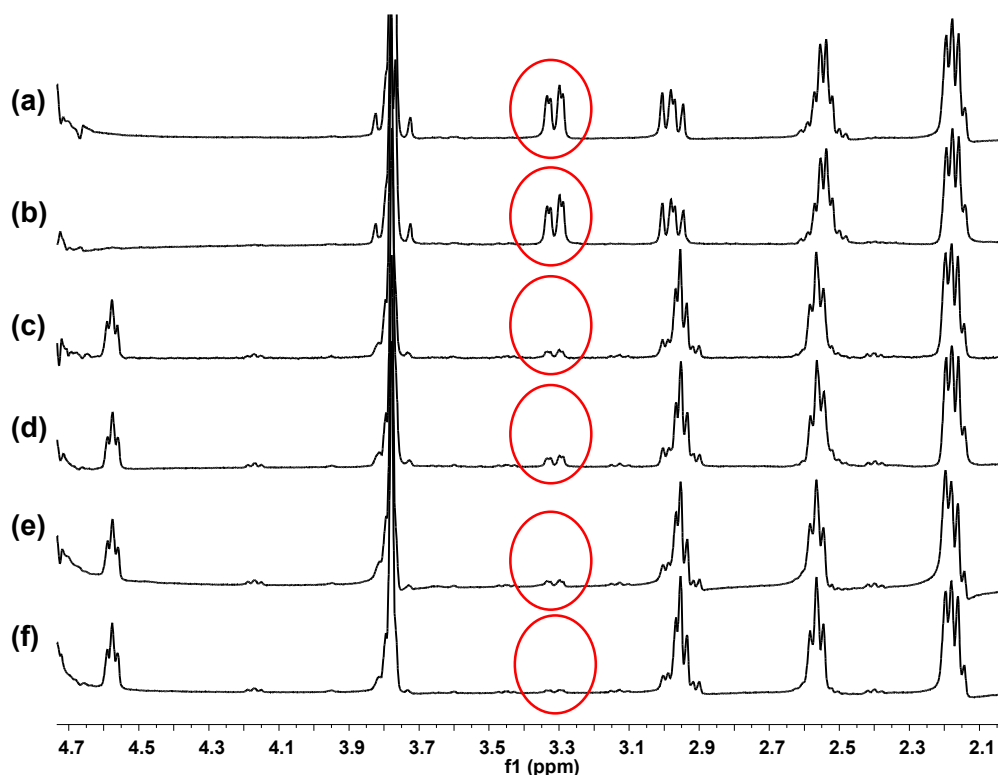
Figure 3.24. ^{1}H NMR spectra (400 MHz, 5% d$_6$-acetone/95% phosphate buffer D$_2$O, 30 mM, v/v, pH* 7.4) for catalysis of GSH oxidation by (a) 100 μM complex **8**; (b) 100 μM complex **7**; (c) 100 μM complex **3**; (d) 100 μM complex **1**; (e) 100 μM phenol-azo-pyridine (HO-azpy) ligand, for 10 mM GSH at 310 K for 24 h; (f) 10 mM GSH control without addition of the catalyst at 310 K for 24 h. Peaks at δ 3.30 ppm in the red circles are assigned to a β-CH$_2$ proton of GSSG.
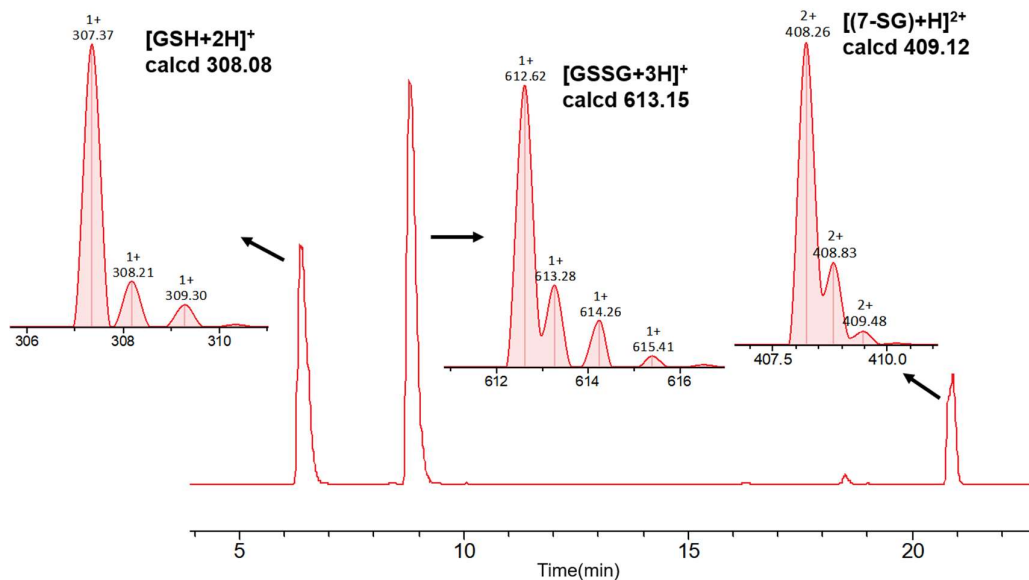
Figure 3.25. HPLC-ESI-MS analysis of reactions of **7** (100 µM) with GSH (10 mM) in the aerated water (pH = 7.0) after 24 h at 310 K. Eluents: A-water (without TFA), B-acetonitrile (without TFA). 0-10 min, 2%-15% B; 10-40 min, 15%-80% B; 40-45 min, 80%-2% B; 40-55 min, 2% B.

The turnover numbers (TONs) for complexes **7** and **8**, with unsubstituted azpy phenyl substituents, of 100 ± 4 and 100 ± 2, respectively, are much higher than those of the phenolate azpy complexes **1** and **3** (29 ± 2 and 18 ± 1, respectively, Figure 3.26). By contrast, the free ligand phenol-azopyridine (HO-azpy) showed negligible catalytic activity (low TON of 9 ± 1, Figure 3.26), and the GSH alone underwent negligible oxidation (Figure 3.24f). No gas bubbles or pH changes were observed over 24 h incubation for the complexes, nor was H_2O_2 detected by peroxide test sticks (even with 1 mM catalyst).
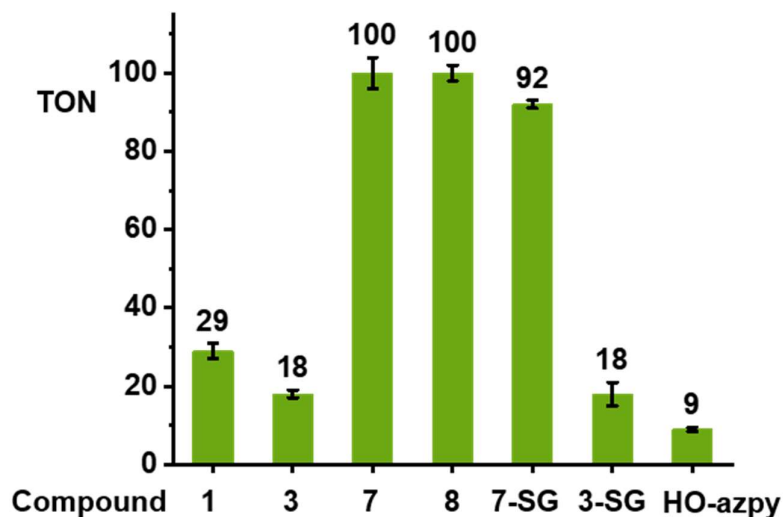
Figure 3.26. Turnover numbers for the catalytic oxidation of GSH by complexes **1**, **3**, **7**, **8**, **7-SG**, **3-SG** and free HO-azpy ligand. Reactions were carried out in d_6-acetone/phosphate buffered D_2O (5/95, v/v, 30 mM, pH* 7.4) at 310 K for 24 h and monitored by ^{1}H NMR spectroscopy.

To identify the active iridium catalyst, the reaction of complex **7** (100 μM) with GSH (10 mM) in phosphate buffer (30 mM, pH 7.4) was monitored over 24 h by HPLC/LC-MS. From the ESI-MS of the HPLC peaks, *ca.* 100% of **7** was converted to the glutathione adduct $[(Cp^*)(Ir\text{-}SG)(azpy)(SG)]^+$ (**7-SG**) within the first 3 min after mixing, and this was the major species in the solution over 24 h (Figure 3.27). Hence the Ir-SG adduct appears to be the active catalyst in GSH oxidation. This was further confirmed by studying reactions of isolated complexes **7-SG** or **3-SG** (100 μM) with GSH (10 mM) under similar conditions (Figure 3.28). These reactions gave TONs of 92 ± 1 and 18 ± 3, respectively, exhibiting similar catalytic activity as the iodido complexes **7** and **3**.
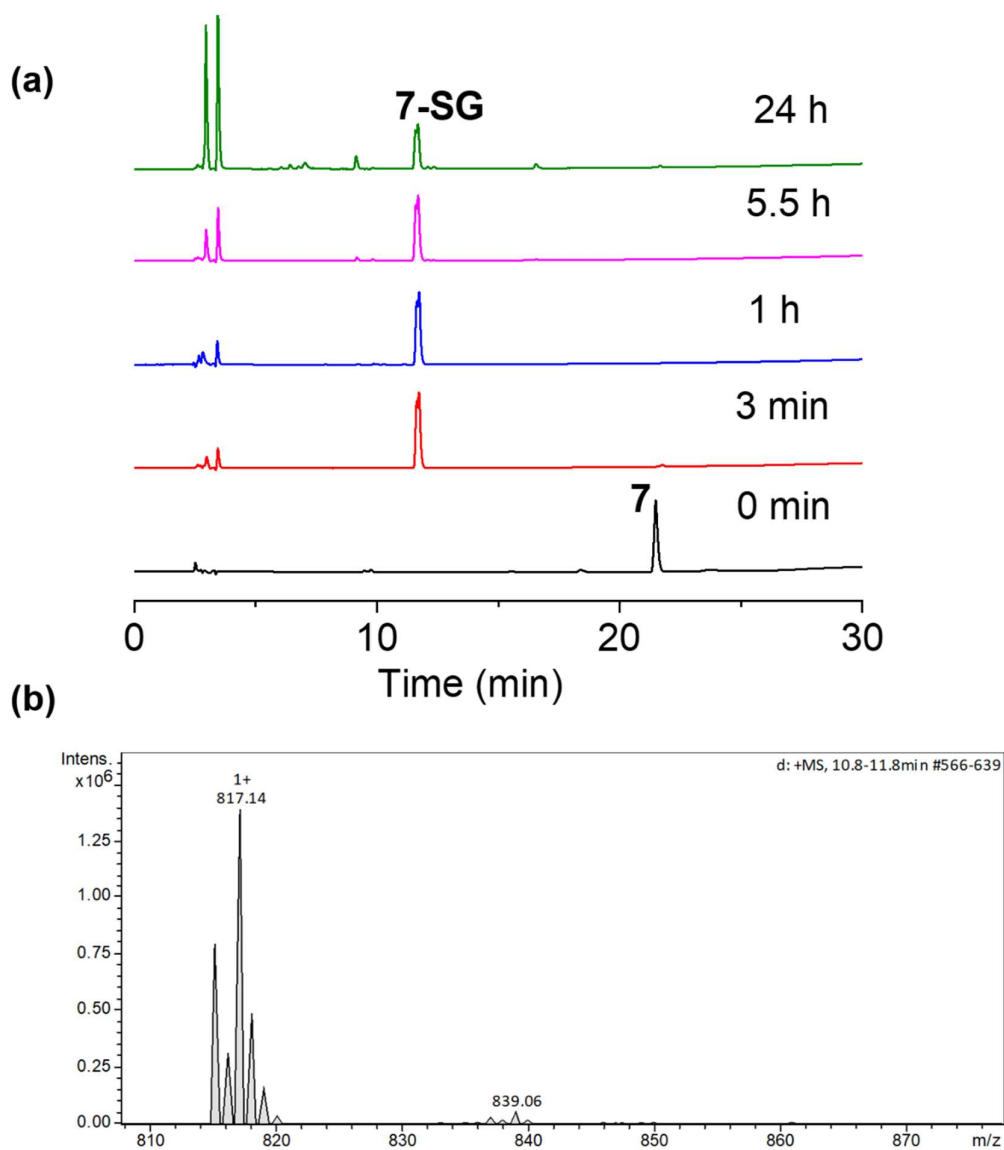
Figure 3.27. (a) Time-dependent HPLC chromatograms for reaction of complex **7** (100 µM) with GSH (10 mM) in 5% methanol-95% H_2O (30 mM phosphate buffer, v/v, pH 7.4) at 310 K. (b) The ESI-MS of the HPLC peak with *m/z* at 817.14 (calcd 817.23 for [(**7-SG**)+H]$^+$ with a retention time of *ca.*12 min is assignable to **7-SG**.
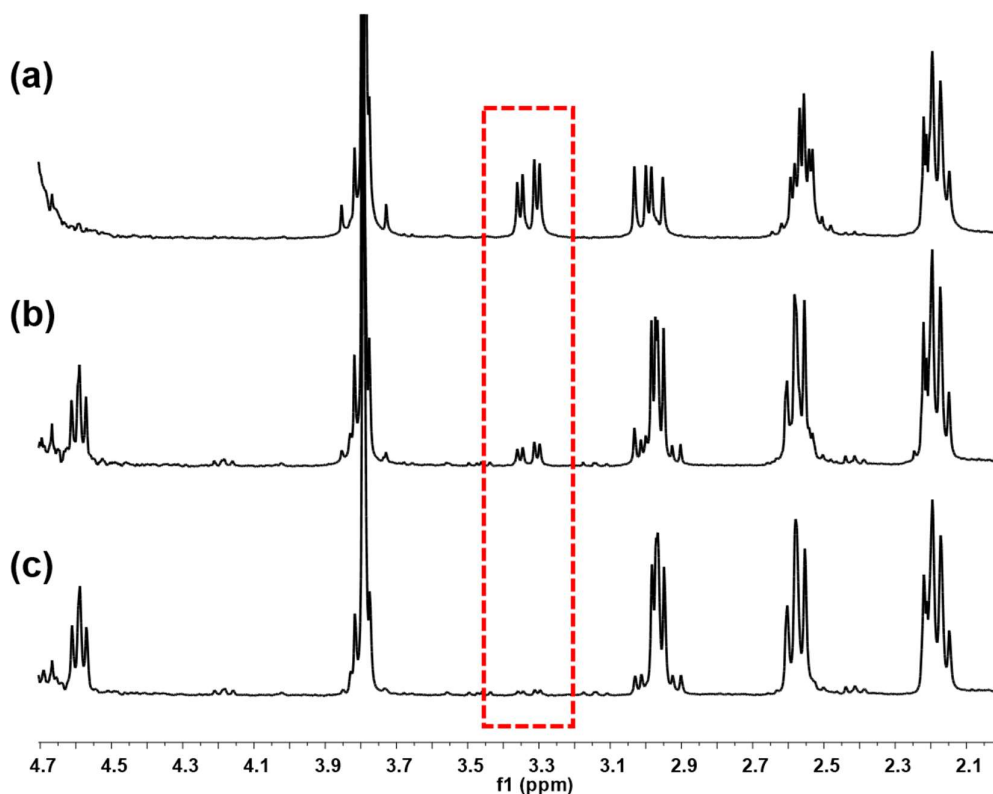
Figure 3.28. ^{1}H NMR spectra (400 MHz, 5% d_6-acetone/95% phosphate buffer D_2O, 30 mM, v/v, pH* 7.4) for catalysis of GSH oxidation by (a) 100 μM complex **7-SG**; (b) 100 μM complex **3-SG**, for 10 mM GSH at 310 K for 24 h; (c) 10 mM GSH alone at 310 K for 24 h. Peaks at δ 3.30 ppm in the red rectangle are assigned to a β-CH$_2$ proton of GSSG. **7-SG** and **3-SG** gave TONs of 92 ± 1 and 18 ± 3, respectively, similar with the TONs of their corresponding parent iodido complexes **7** and **3** (Figure 3.26).

Since the EPR studies indicated that oxygen is involved in the generation of hydroxyl radicals during these reactions, the reaction of complex **7** with GSH was carried out under a N$_2$ atmosphere, which decreased the TON to 17 ± 2 after 24 h at

310 K. Furthermore, the final reaction mixture analysed by LC-MS, gave peaks assignable to the free azpy ligand, the free (reduced) H$_2$azpy ligand, and the dinuclear adduct $[(Cp^*Ir)_2(\mu\text{-SG})_3]^+$ (Figure 3.29). These are different from the major peaks which were **7-SG** (Figure 3.27) captured under aerated conditions.

(a)

(b)

Peak assignment	Detected m/z	Calcd m/z
$[(Cp^*Ir)_2(\mu\text{-SG})_3+3H]^{2+}$ (peak 1)	787.02	786.69
$[(H_2azpy)+H]^{2+}$ (peak 2)	185.72	186.10
$[(azpy)+H]^{2+}$ (peak 3)	183.65	184.08
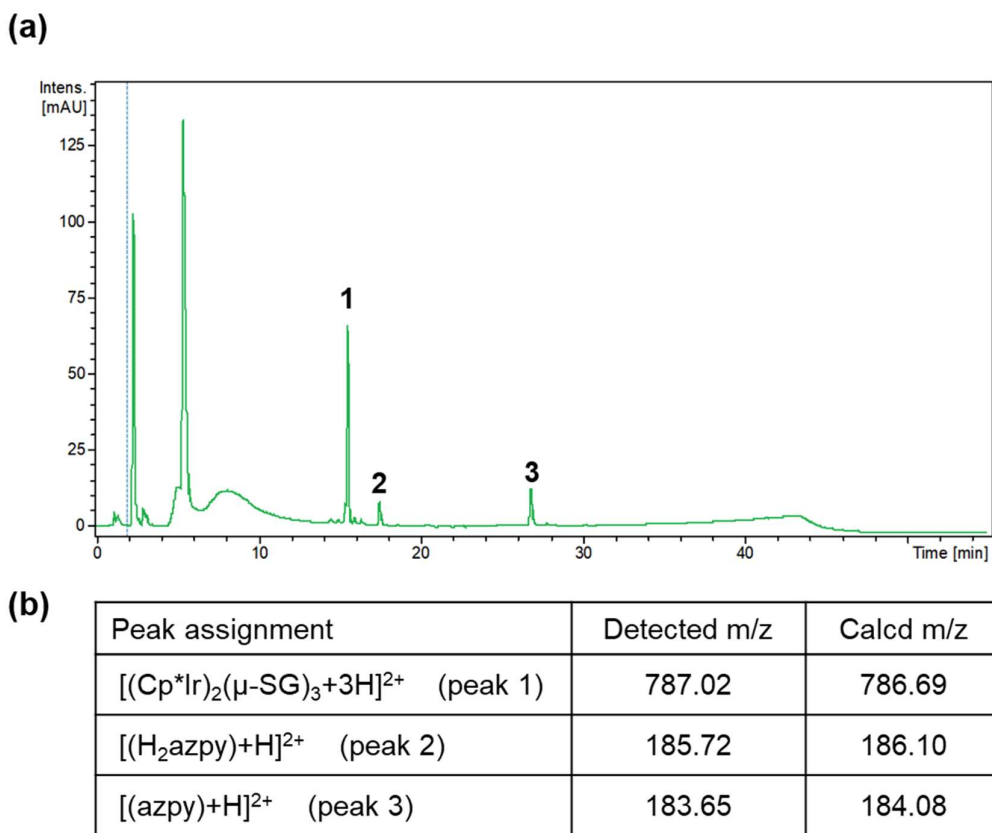
Figure 3.29. (a) HPLC chromatogram (254 nm detection) for a solution of **7** (100 μM) with GSH (10 mM) in water (pH = 7.0) under a N$_2$ atmosphere after 24 h at 310 K. Eluents: A-water (without TFA), B-acetonitrile (without TFA). 0-10 min, 2%-15% B; 10-40 min, 15%-80% B; 40-45 min, 80%-2% B; 40-55 min, 2% B. (b) Peak assignments based on observed and calculated ESI-MS values.

3.3.12 DFT Simulations of Aquation and GSH Reactions

The X-ray crystal structure of the $[(Cp^{xph})Ir(HO\text{-azpy})I]PF_6$ complex (**2**) was used as a starting point for DFT calculations (details ESI). DFT calculations suggested that all the investigated lowest energy pathways involve deprotonated GSH (GS$^-$). Although the pK_a of the Cys thiol in GSH is high (*ca.* 9.4),[54] there will be a small but significant amount (*ca.* 0.3%) of deprotonated GSH present at pH 7.[55]

DFT calculations were conducted first on the direct attack of H_2O or GS$^-$ on the Ir centre to displace the iodide ligand. That is, after initial formation of slightly less stable adducts between **2** and H_2O or GS$^-$, the reactions proceed by second-order nucleophilic substitution (S$_N$2). The activation barriers for formation of the transition states for these associative attacks are similar (19.9 vs. 20.2 kcal·mol^{-1}, Figure 3.30). In contrast, the thermodynamics for displacement of the iodide by H_2O or GS$^-$ are different, being endergonic by 10.7 kcal·mol^{-1} for H_2O, and exergonic by 30.3 kcal·mol^{-1} to form Ir-SG.

3.3.13 DFT Simulations of Attack of GSH on the Azo Bond

DFT exploration of possible, less energy-demanding, alternative pathways for the substitution of iodide by GS$^-$ or H_2O showed that the reversible attack of GS$^-$ on the N=N bond of the azopyridine ligand can assist in the process (Scheme 3.1).
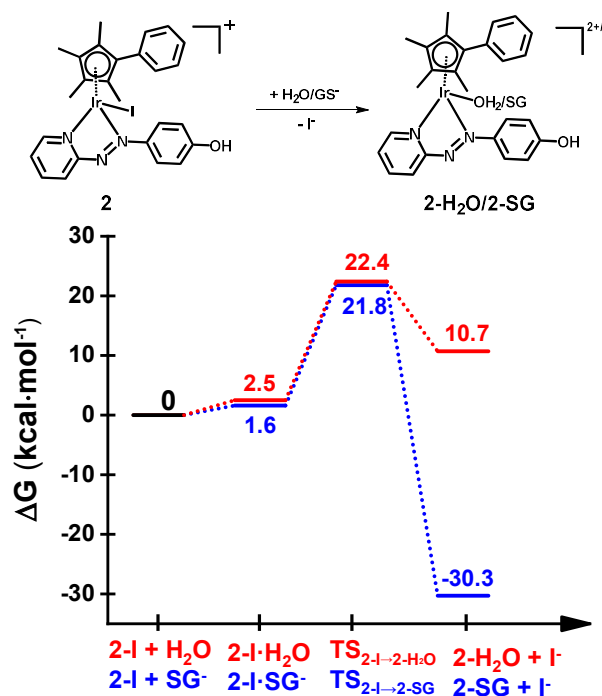
Figure 3.30. DFT calculated free energy profiles for direct substitution of iodide in complex **2** by water (aquation) or GS$^-$. Relative energies are in kcal·mol^{-1} and calculated with respect to separated reactants.
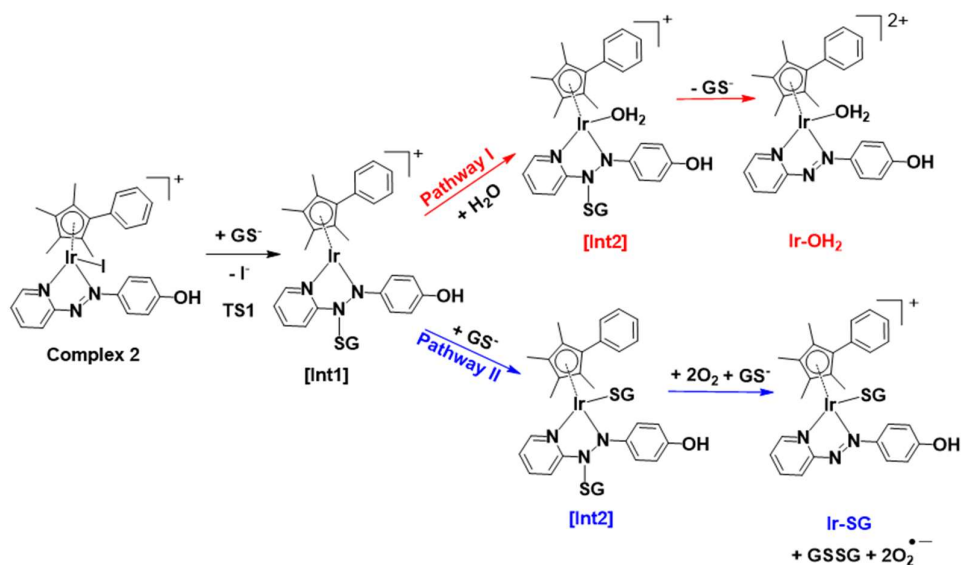
Scheme 3.1. Pathways **I** and **II** for the formation of Ir-OH$_2$ and Ir-SG, as investigated

by DFT calculations. Intermediates (abbreviated as [Int]) and products are assisted by the reversible attack of GS⁻ on the azo bond.

Along pathway **I** for the substitution of iodide by H_2O in Figure 3.31a, the attack of GS⁻ on the non-coordinated N atom of the azo double bond, involves a barrier of only 9.2 kcal·mol^{-1} to reach the transitional state TS1. Then water coordination to the vacant site on Ir (TS2 in Figure 3.31a) occurs by surmounting an energy barrier of 8.7 kcal·mol^{-1}. To complete the substitution of I⁻ by water, detachment of GS⁻ from the N atom (the TS3 in Figure 3.31a) corresponds to a very low energy barrier of only 0.2 kcal·mol^{-1}. The whole reaction is almost thermoneutral.

Along pathway **II** for the substitution of iodide by GS⁻ in Figure 3.31b, the first step involving attack by GS⁻ on the N atom of the azo bond and the simultaneous release of the iodide ligand occur by surmounting a much low energy barrier of 5.6 kcal·mol^{-1}. The free energy profile for the next step (coordination of the second GS⁻ to iridium) is very flat with a barrier of only 1.3 kcal·mol^{-1} to the transitional state TS2 in Figure 3.31b. With respect to pathway **I**, attack of water on the iridium centre (Figure 3.31a), the GS⁻ bound to the N atom of the azo group in pathway **II** is not spontaneously released. Instead, in the presence of a third GS⁻, the detachment of GS⁻ from the N atom occurs to form oxidized glutathione-GSSG, which involves the transfer of two electrons to other molecules. Computations suggest that the ground state O_2 ($^3\Sigma$) molecule can act as an electron acceptor for this step.
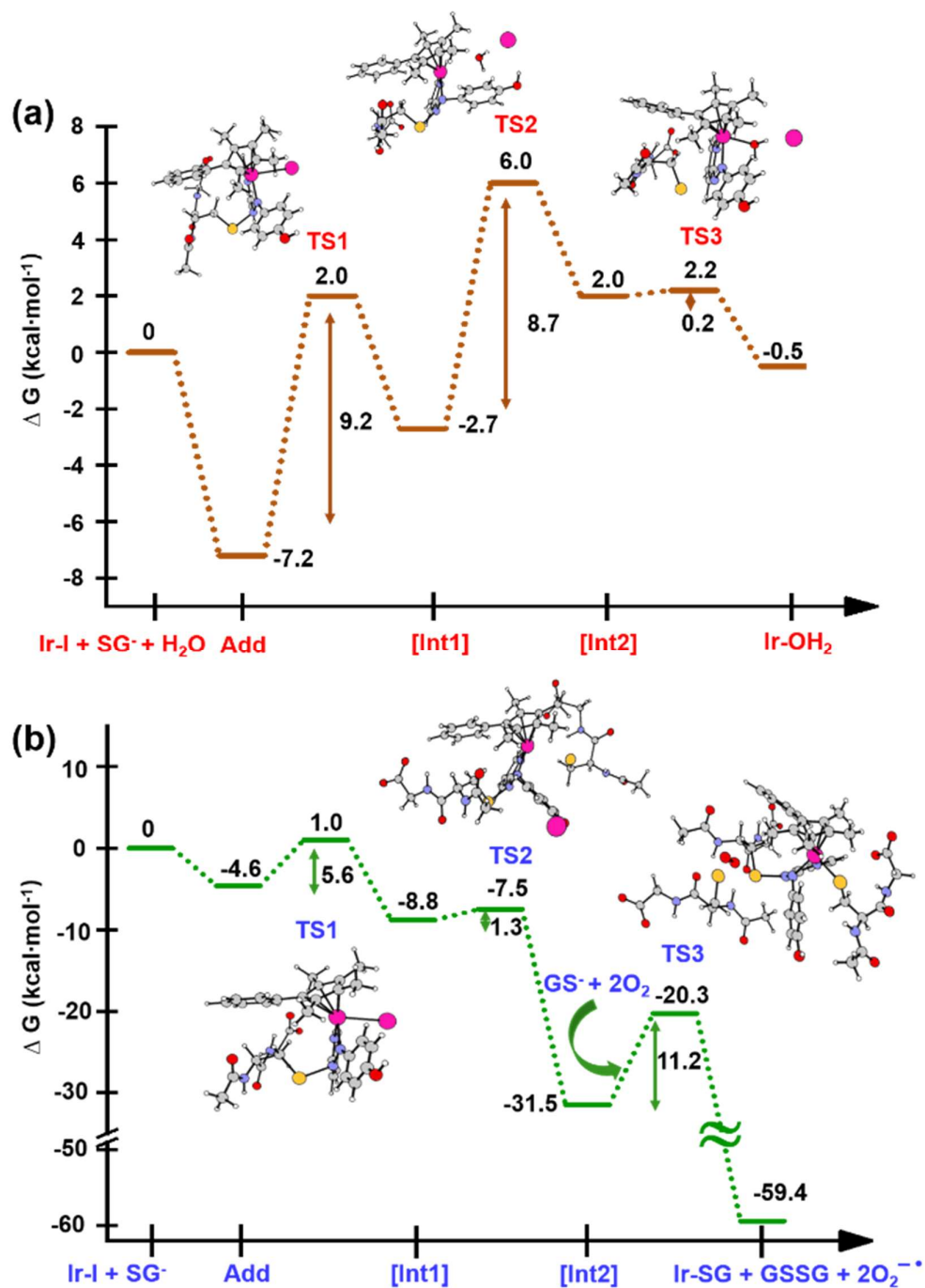
Figure 3.31. Calculated free energy profiles describing iodide substitution by (a) water in pathway **I**, and (b) GS⁻ in pathway **II**. Calculated energies are in kcal·mol⁻¹ with respect to reference energy of separated reactants.

Indeed, the O-O bond elongates, consistent with formation of superoxide $O_2^{-\bullet}$, whereas the second electron is localized on the N atom of N-N single bond which was previously bound to GS$^-$. The whole system is in a triplet state again, and the spin is conserved. The singlet multiplicity of the complex can be recovered due to the presence of a second O_2 molecule to form a second superoxide. In pathway **II** of Scheme 3.1, the final products are the singlet state **Ir-SG** complex, GSSG, and two $O_2^{-\bullet}$ radicals, to conserve the triplet multiplicity. Overall, this reaction is largely exergonic.

3.3.14 Antiproliferative Activity

The antiproliferative activity of the complexes toward human lung A549 cancer cells was determined using the SRB assay[56] and compared with cisplatin (CDDP), Figure 3.32. Iodido complexes **1-6** and chlorido complexes **9** and **10**, which share the common feature of a phenolic substituent on the azopyridine ligand. The complexes are highly potent with IC_{50} values (the concentration that inhibits cell growth by 50%) in the range of 0.3-1.6 µM. Particularly potent is the complex [(Cp*)Ir(HO-azpy-Br)I]PF$_6$ (**3**) with an IC_{50} value of 0.33 µM, 10x more active than cisplatin. By contrast, complexes **7** and **8** bearing an unsubstituted azpy ligand are less active than other iodido complexes **1-6**. The substitution of one methyl group on Cp* by a phenyl substituent to give Cp^{xph} does not enhance the anticancer activity for iodido complexes, while the Cp^{xph} chlorido complex **10** is slightly more active than its Cp* analogue **9**.
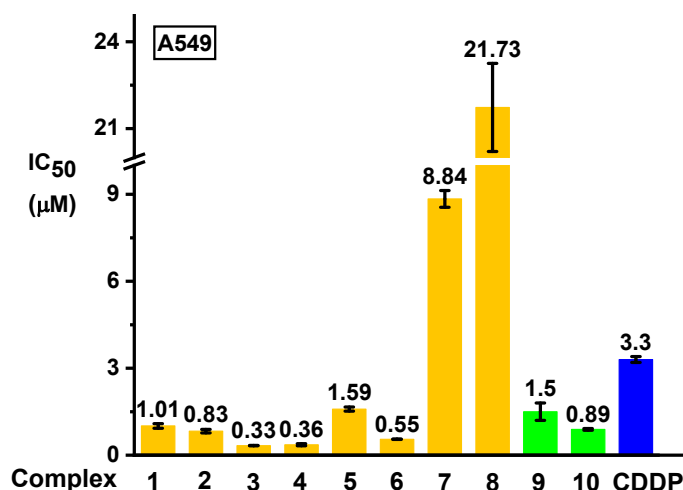
Figure 3.32. Inhibition of growth of A549 human lung cancer cells *in vitro* by complexes **1-10** in comparison with cisplatin (CDDP). The values of half maximal growth inhibitory concentration (IC_{50}) are given as the mean ± standard deviations for three independent experiments with cancer cells exposed to the tested complex for 24 h followed by recovery for 72 h in fresh medium. See Table 3.5 for full numerical data.

Table 3.5. Values of IC_{50} ± mean SD for ten iridium complexes against human A549 lung cancer cells in comparison with cisplatin (CDDP).

Complex	IC_{50} (µM)	Complex	IC_{50} (µM)
1	1.01 ± 0.08	6	0.55 ± 0.01
2	0.83 ± 0.06	7	8.84 ± 0.29
3	0.33 ± 0.01	8	21.73 ± 1.52
4	0.36 ± 0.04	9	1.5 ± 0.3
5	1.59 ± 0.07	10	0.89 ± 0.03
CDDP	3.30 ± 0.10		

Based on their promising *in vitro* activity, the potent iodido complex **1** and its chlorido analogue **9** were selected for further screening against human CNE2 (nasopharyngeal), A2780 (ovarian), and A2780cisR (ovarian) cancer cell lines to study the influence of the halido ligand on the anticancer activity (Table 3.6). A2780cisR is cisplatin-resistant through reduced drug transport, enhanced DNA repair/tolerance and elevated GSH levels.[57]

Iodido complex **1** exhibits similar potency to chlorido analogue **9** against A549, CNE2, and A2780 cell lines, both more potent than cisplatin (see IC_{50} values in Table 3.6). Surprisingly, iodido complex **1** is *ca.* 2x more potent than the chlorido analogue **9** toward the A2780cisR cisplatin-resistant cell line. Both complexes are not cross-resistant with cisplatin, with resistance factors (IC_{50}(A2780cisR)/IC_{50}(A2780)) for **1** and **9** of 0.2 and 0.95, respectively. This suggests that these iodido complexes have a different mechanism of action compared to cisplatin.

Table 3.6. Antiproliferative activity of iodido complex **1** and chlorido analogue **9** against human A549 lung, CNE2 nasopharyngeal, A2780 ovarian, and A2780cisR cisplatin-resistant ovarian cancer cells.

IC_{50} (µM)	**1** [(Cp*)Ir(HO-azpy)I]PF$_6$	**9** [(Cp*)Ir(HO-azpy)Cl]PF$_6$	**Cisplatin**
A549	1.01 ± 0.08	1.5 ± 0.3	3.3 ± 0.1
CNE2	1.26 ± 0.04	2.3 ± 0.3	7.7 ± 0.3
A2780	0.25 ± 0.02	0.12 ± 0.04	1.2 ± 0.2
A2780cisR (RF)[a]	0.049 ± 0.001(0.20)	0.114 ± 0.003 (0.95)	11.5 ± 0.3 (6.41)

[a] resistance factor RF = IC_{50}(A2780cisR)/IC_{50}(A2780).

3.3.15 Partition Coefficients and Cellular Iridium Accumulation

Anticancer activity of metal complexes often correlates with cellular uptake and lipophilicity.[58] Partition coefficients (log P values) provide measurements of the lipophilicity of compounds. The lipophilicity of complexes **3** and **7** was compared by determining their octanol-phosphate buffer (2 mM, pH 7.4) partition coefficients using the "shake-tube" method.[59] On account of the deprotonation of the phenolic group at physiological pH, which would affect the partition of the complex, phosphate buffer (pH 7.4) was used to mimic the physiological environment. As listed in Table 3.7, phenolic complex **3**, which would mainly exist as a neutral zwitterion [(Cp*)Ir(Br-azpy-O$^-$)I] at pH 7.4, has a higher partition coefficient and is much more lipophilic than positively-charged complex **7** [(Cp*)Ir(azpy)I]PF$_6$.

Table 3.7. The partition coefficients (log P$_{7.4}$) between octanol and phosphate buffer water (2 mM, pH 7.4) at 298 K for complexes **3** and **7**, and the cellular iridium accumulation in A549 lung cancer cells treated with complex **3** or **7** at equipotent IC$_{50}$ concentrations for 24 h.

Complex	log P$_{7.4}$	IC$_{50}$ (µM)	Ir Accumulation (ng/10^6 cells)
[(Cp*)Ir(O$^-$-azpy-Br)I]PF$_6$ (**3**)	-0.08	0.33 ± 0.01	101 ± 1.3
[(Cp*)Ir(azpy)I]PF$_6$ (**7**)	-0.59	8.84 ± 0.29	51.3 ± 10.1

Accumulation of iridium in A549 lung cancer cells after 24 h treatment with complex **3** or **7** at equipotent concentrations of 0.5x, 1.0x, and 2.0x IC$_{50}$ was

quantified by inductively coupled-plasma mass spectrometry (ICP-MS). The cellular Ir accumulation of **3** is *ca.* 2-fold higher than that of **7** at equipotent IC_{50} concentrations (Table 3.7).

3.3.16 *In vivo* Toxicity

The toxicity *in vivo* of the antiproliferative potent iodido complex **1** and its chlorido analogue **9** was determined in zebrafish (*Danio rerio*) embryos by Dr. James P. C. Coverdale and Hannah E. Bridgewater. Zebrafish embryos as a high-throughput vertebrate model are often used as a predictor for drug toxicity in humans.[60-63] Strikingly, iodido complex **1** ($LC_{50} = 0.26 \pm 0.08$ µM) was *ca.* 25x less toxic than its chlorido analogue **9** ($LC_{50} = 0.010 \pm 0.003$ µM), although both are more toxic than cisplatin ($LC_{50} = 0.6 \pm 0.2$ µM).[64]

3.3.17 ROS Detection

The levels of reactive oxygen species (ROS) in A549 human lung cancer cells treated with complex **3** or **7** were determined at equipotent 2x IC_{50} concentrations (Figure 3.33) by Hannah E. Bridgewater. Superoxide production was monitored by following the orange channel FL1, and total ROS species, including H_2O_2, peroxy and hydroxyl radicals, peroxynitrite and NO, were monitored by the green channel FL2. After exposure to the complex for 24 h, an increase in ROS/SO levels in cells treated with **3** or **7** was observed, when compared to untreated cells. Furthermore, a burst of superoxide production was also observed in cells treated with complex **7**.
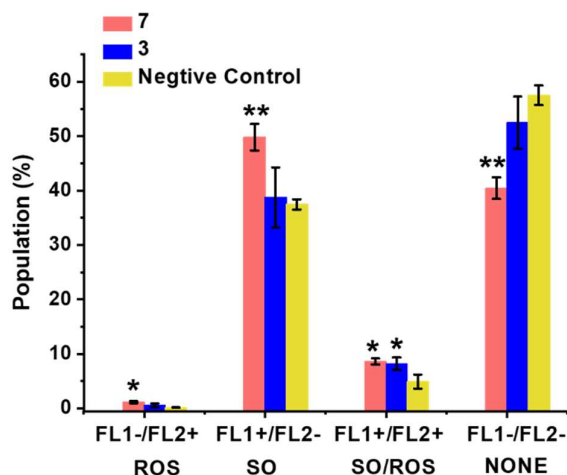
Figure 3.33. ROS induction in A549 cancer cells exposed to complex **3** or **7** at 2x IC_{50} concentrations for 24 h with untreated cells as the negative control. FL1 channel detects superoxide production, and FL2 channel detects total oxidative stress. Normalized population data are presented as the mean ± SD of triplicate samples for one experiment. *p*-Values were calculated after a t-test against the negative control data, *$p < 0.05$, **$p < 0.01$. See Table 3.8 for full numerical data.

Table 3.8. ROS induction in A549 cancer cells treated with complexes **3** and **7** at 2x IC_{50} concentrations. FL1 channel detects superoxide production and FL2 channel detects total oxidative stress.

Cell Population	Cell treatment (dose)		
(%)	Untreated	3 (2x IC_{50})	7 (2x IC_{50})
FL1-/FL2+	0.17 ± 0.027	0.58 ± 0.34	1.14 ± 0.19
FL1+/FL2+	4.91 ± 1.29	8.21 ± 1.14	8.61 ± 0.55
FL1+/FL2-	37.48 ± 0.95	38.74 ± 5.50	49.81 ± 2.44
FL1-/FL2-	57.51 ± 1.80	52.48 ± 4.80	40.44 ± 1.99

3.4 Discussion

Iridium(III) is a classically-inert low-spin $5d^6$ metal ion, exemplified by the half-life for coordinated aqua ligands exchange on $[Ir(H_2O)_6]^{3+}$ of > 300 years.[65] However, it was apparent during our study of $[Ir(Cp^*)(N,N)Cl]^+$ anticancer complexes (N,N = e.g. phenanthroline),[21] and a previous report[66] that the introduction of a Cp^* ligand into the coordination sphere can increase ligand exchange rates by many orders of magnitude. Here the inertness of Ir(III) can be restored even in Cp* complexes when the N,N-chelated ligand is a strong π-acceptor, and the monodentate ligand is a 'soft' iodido ligand.

The aim was to explore pathways by which such inert Cp* complexes might become activated in cancer cells, to shed light on possible mechanisms of action. In so doing this Chapter has discovered some unusual reaction pathways for half-sandwich organoiridium complexes, involving not only attack on the azo bond of coordinated azopyridine by glutathione, but also catalysis of GSH oxidation and generation of reactive oxygen species, and reductive release of the azopyridine ligand, suggesting that these iodido iridium complexes are likely to have a unique mechanism of action.

3.4.1 Inertness of Iodido Complexes

Transition metal anticancer complexes containing chlorido ligands, including cisplatin and Ru(II) arene complexes, often undergo activation by hydrolysis, giving more reactive aqua adducts.[67] For the iodido complexes studied here, due to the softer character of iodide, the Ir-I bonds have stronger covalency, strengthened by π-

acceptor chelated azopyridine ligands, and become inert towards hydrolysis. This is paralleled by the more stable iodido Ru(II)/Os(II) azopyridine complexes compared to their chlorido counterparts.[68] Thus chlorido complex **9** hydrolyses much more slowly than diamine and diimine N^N chelated chlorido half-sandwich Cp* Ir(III) anticancer complexes.[69]

The inertness of iodido iridium complexes toward hydrolysis also leads to their much lower chemical reactivity toward the nucleobase 9-EtG and various amino acids compared to the chlorido analogue (Table 3.4). Also, the iodido complexes are not readily converted into their chlorido analogues even at high (extracellular) NaCl concentration (103 mM), Figure 3.9e, suggesting that intact iodido complexes will persist for transport into cells. Thus activation of the iodido iridium complexes is likely to involve novel pathways, distinct from chlorido complexes, and have targets other than coenzyme NADH[11] or DNA[70].

3.4.2 Enhanced Antiproliferative Activity of Zwitterionic Complexes

On account of their low pK_a values (Chart 3.3), complexes **1**-**6** exist mainly in neutral zwitterionic forms (Figure 3.34) at physiological pH (7.4) in cell culture media under cell-screening conditions.

These complexes all show higher anticancer potency against human A549 lung cancer cells than non-phenolic complexes **7** or **8** (Figure 3.32). The anticancer activity of metal complexes often correlates with cellular uptake and lipophilicity.[58] The accumulation of iridium in the lung cancer cells treated with the most potent complex $[(Cp^*)Ir(HO\text{-}azpy\text{-}Br)I]PF_6$ (**3**) was 2-fold higher than that in the cells treated with

$[(Cp^*)Ir(azpy)I]PF_6$ (**7**) at equipotent IC_{50} concentrations (Table 3.7). The *n*-octanol/water (pH 7.4) partition coefficients (log $P_{7.4}$) for complexes **3** (-0.08) and **7** (-0.59) (Table 3.7), reveal that complex **3**, with a pK_a of 6.31 (Chart 3.3) and being predominantly in its zwitterionic form, is more lipophilic relative to the +1-charged complex **7**. The higher lipophilicity contributes to the higher cellular iridium accumulation and anticancer activity of complex **3**.
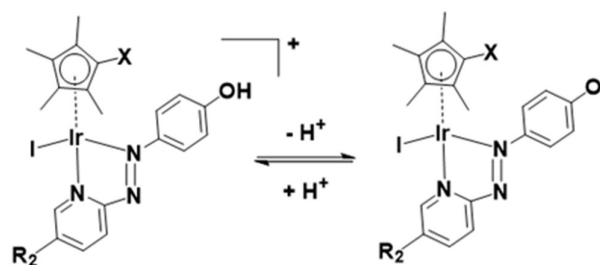
Figure 3.34. Acidity of complexes **1-6**.

3.4.3 Antiproliferative Activity and *In vivo* Toxicity

The Ir(III) analogue of the Ru(III) clinical trial drug NAMI-A, *trans*-$[IrCl_4(DMSO)(Im)][ImH]$, (DMSO = dimethyl sulfoxide, ImH = imidazole), exhibits low cytotoxic activity, attributable partly to its inertness towards hydrolysis.[71] The cytotoxicity of Ru^{II} arene complexes is generally greater for complexes which hydrolyse relatively rapidly, and low for complexes which do not hydrolyse.[72] However, for half-sandwich iridium complexes bearing C^N chelating ligands, replacement of Cl by pyridine decreases the rate of hydrolysis, but enhances the anticancer activity.[73] In this work, replacement of Cl by I in the iridium azopyridine complexes does not result in loss of anticancer activity towards A549 lung cancer

cells (complexes **1** and **9**, Chart 3.2, Figure 3.32, Table 3.5). Remarkably, iodido complex **1** has 2-fold higher activity toward A2780cisR cisplatin-resistant human ovarian cancer cells with a much lower resistance factor (0.2 *versus* 0.95) than the chlorido analogue **9** (Table 3.6). This suggests that the potent iodido complexes have a potential to overcome the cisplatin resistance.

The toxicity of iodido complex **1** towards zebrafish embryos is 25x lower than that of chlorido complex **9** which opens up a wider therapeutic window. However, this selectivity is lower than for scaffold-inert iridium pyridocarbazole complexes[74] and Os(II) azopyridine complexes,[64] but there is scope in further work for improving this by changes in ligand substituents.

3.4.4 GSH-mediated Ligand-Centred Activation

These iodido iridium complexes are resistant towards hydrolysis and nucleobase binding, but exhibit more potent antiproliferative activity compared to the clinical anticancer drug cisplatin against A549 lung, CNE2 nasopharyngeal, and A2780 ovarian cancer cell lines (Figure 3.32 and Table 3.6). Moreover, iodido complex **1** is more active than the chlorido analogue toward A2780cisR cisplatin-resistant ovarian cancer cells. The high potency of these inert iodido complexes raises intriguing questions about their activation mechanism.

GSH is an important cellular antioxidant which detoxifies various xenobiotics as well as protecting cells from toxic reactive oxygen species.[75] Thus, reactions of metal complexes with GSH can perturb the redox state of cells. Unlike the detoxification of platinum drugs by conjugation with GSH, some chlorido Ru^{II} arene ethylenediamine

anticancer complexes form Ru thiolate adducts which are not the dead-end products, but further oxidized to sulfenato and sulfinato adducts, facilitating the interaction of Ru complexes with DNA.[76] Other Ru(II)[77,78], Os(II)[28,29], and Pt (IV)[79] complexes have been reported to be activated by GSH. The high affinity of these iodido Ir(III) azopyridine complexes for NAC or GSH to form Ir-thiolate adducts under physiologically relevant conditions is evident (Figures 3.16 - 3.18).

DFT calculations show that displacement of iodide by GS$^-$ to yield Ir-SG is thermodynamically favorable, being exergonic overall (Figure 3.30). Regardless of the ratio between the iodido complex **7** and GSH, only the Ir-SG adduct is observed in the reaction (Figures 3.27 and A3.4 in the **Appendix**). This is quite different from the iodido Os^{II} azopyridine complexes, which undergo hydrolysis to Os-OH species in the presence of equimolar GSH.[28] In this study, neither Ir-OH nor Ir-sulfenato species were observed.

The first-step in the electrochemical reduction of azo ligands can be assigned to the one-electron addition into the π^* orbital centred on the azo group to give the azo anion radical.[80-82] The second one-electron reduction gives rise to the dianionic species ($[-N-N-]^{2-}$). In aqueous media, two-electron reduction is also accompanied by proton transfer to give hydrazo groups [-NH-NH-].[27] The azo bond undergoes more facile reduction after metalation with Cp*-Ir (Table 3.3). The redox potential of GSH/GSSG (-240 mV at pH 7) in cells and tissues,[83,84] is more negative than that of the azo bonds in the active iridium anticancer complexes (-130 mV and -70 mV for **3** and **7**, respectively, Table 3.3), suggesting that azo bonds in the ligands are likely to be reduced by GSH.

Furthermore, in the NMR study of reactions of complex **7** with 10 mol equiv. GSH under physiologically relevant conditions (Figure 3.20b), there was a rapid disappearance (severe broadening) of the aromatic signals and the broadening of Cp* methyl peaks of the **7-SG** adducts after 15 min, which persisted for a few hours. This broadening may be due to ligand exchange reactions occurring at an intermediate rate on the NMR timescale, or to the formation of large, slow-tumbling polymeric species, or to paramagnetic species arising from redox reactions, such as azo ligand-centred radicals. The latter case seemed the most likely since the azo bond can take part in one- and two-electron reduction processes (Table 3.3).

EPR studies using spin traps for reactions carried out under similar conditions to the NMR study, confirmed the formation of hydroxyl radicals (Figures 3.22 and 3.23). Since no radicals were detected in the presence of superoxide dismutase, or in the absence of O_2, it is reasonable to assume that the hydroxyl radicals arise from superoxide, $O_2^{\bullet-}$, formed by the initial attack of glutathione on the N=N azo bond generating GS-N-N- species. It is known that trapped superoxide readily decomposes to hydroxyl radicals.[85] After 3 h, the presence of 1.0 mol equiv. free phenyl-hydrazo-pyridine ligand and 0.5 mol equiv. tri-SG bridged di-iridium $[(Cp^*)_2Ir_2(\mu\text{-}SG)_3]^+$ adduct in the solution, suggests that the azo group is the redox-active centre during the reactions of the complexes with GSH (Figure 3.20c).

3.4.5 Activation Mechanisms by DFT Calculations

DFT calculations revealed that the subsequent step after release of the iodido ligand, involves attack by a second GS⁻ on the Ir centre to form an Ir-SG complex requiring

only 1.3 kcal·mol^{-1} along pathway **II** (Scheme 3.1, Figure 3.31b), in contrast to the higher energy requirement of 8.7 kcal·mol^{-1} for water binding to the Ir centre to give Ir-OH$_2$ along pathway **I** (Scheme 3.1, Figure 3.31a). Thus, after the attack of the first GS$^-$ on the N atom of the azo bond, the energy-preferred sequence of steps is pathway **II** (Scheme 3.1), that is attack by a second GS$^-$ on the Ir centre to form [(Cp*)(Ir-SG)(N-N-SG)] (the [Int2] of pathway **II**, Scheme 3.1), instead of [(Cp*)(Ir-OH$_2$)(N-N-SG)]$^+$ ([Int2] in pathway **I**, Scheme 3.1). Next, along pathway **II** the intermediate [(Cp*)(Ir-SG)(N-N-SG)] reacts with a third GS$^-$ by the detachment of the GS$^-$ from the nitrogen atom to form oxidized glutathione GSSG. One electron can be transferred to O$_2$ as evidenced by the O-O bond elongation, and a superoxide anion is formed. Whereas, another electron is localized on the N atom previously attacked by GS$^-$, which can be accepted by another oxygen molecule to form a second superoxide anion with the simultaneous regeneration of N=N bond in the Ir-SG adduct. The overall reaction is largely exergonic by 59.4 kcal·mol^{-1}. This thermodynamically favorable pathway **II** and involvement of oxygen in the activation pathway correlates well with the trapping of hydroxyl radicals by EPR as decay products of superoxide. Such a favorable attack of GSH on the azo bond is also consistent with the observation of iodide release in alkaline solution, where Ir-SG adducts are completely formed within minutes (Figure 3.35).
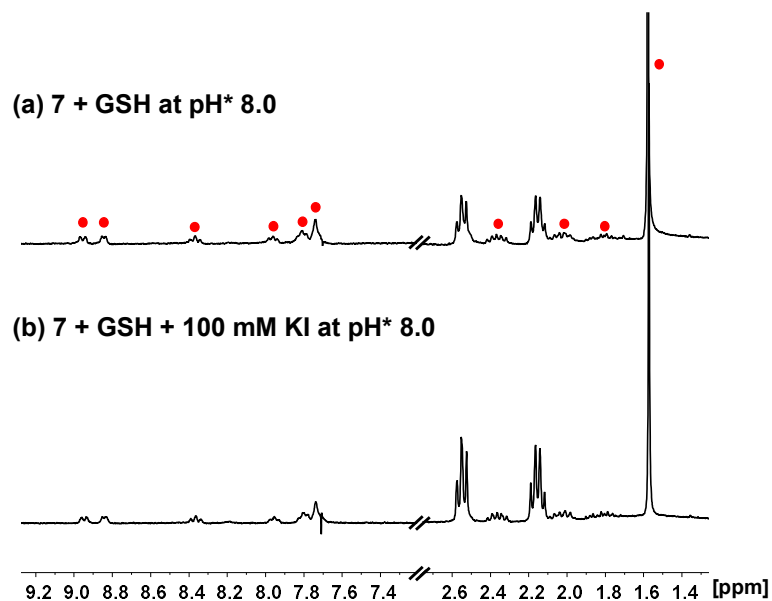
Figure 3.35. ^{1}H NMR (400 MHz, 298 K) spectra for reactions of complex [(Cp*)Ir(azpy)I]PF$_6$ (**7**) (1 mM) with 5 mol equiv. GSH in d$_4$-MeOD/D$_2$O (3/7, v/v, pH* 8.0), (a) without KI, (b) with 100 mM KI at 310 K over 10 min. Red circles: **7-SG**. The reaction of complex **7** with GSH to form **7-SG** was complete within 10 min, even in the presence of 100 mM KI, suggesting that the deprotonated Cys thiol under basic conditions can attack the azo bond and promote the release of iodide to form **7-SG**. In this case, addition of KI (100 mM) does not inhibit the formation of **7-SG**. See Figure 3.18 for the structure and proton assignment for **7-SG**.

Figure 3.36. Proposed activation and catalysis pathways for the reaction of complex **7** with GSH following the DFT-calculated pathway **II** (Scheme 3.1). The paramagnetic species detected by NMR may be a ligand-centred radical species as indicated by [Int3].

Thus, the reaction pathways depicted in Figure 3.36 account for the main features observed in the reaction of complex **7** with GSH. These include the presence of paramagnetic species (Figure 3.20b) during the early stages (as a ligand-based radical [Int3]), the involvement of O_2 as an electron acceptor in formation of Ir-SG adducts, the catalysis of GSH oxidation, and in the later stages, formation of reduced free hydrazopyridine together with thiolate-bridged dinuclear complexes (Figure 3.20c). The formation of hydrazo products by consecutive reductions of azo bonds by thiols has been reported in the case of azo-bipyridine-bridged dinuclear

ruthenium/iridium complexes,[86,87] although it is notable that this appears not to be observed in the activation of iodido arene Ru(II)[27] and Os(II)[28,29] azopyridine complexes by GSH. Furthermore, the released phenyl-hydrazo-pyridine ligands and the dinuclear complex $[(Cp^*Ir)_2(\mu\text{-}SG)_3]^+$ might not be dead-end products as they themselves may play a role in the biological activity. For example, the organic hydrazo compound procarbazine was approved as an anticancer drug in the late 1960s.[88,89] Also Therrien *et al.* have reported that thiolate-bridged dinuclear Ir(III) complexes exhibit high anticancer activity toward A2780 and A2780cisR ovarian cell lines.[90]

3.4.6 Catalysis of GSH Oxidation

Cp* iridium complexes are widely exploited as transfer hydrogenation catalysis with hydride donors such as formate or reduced nicotinamide adenine dinucleotide.[91] Such reactions can lead to imbalance in redox homeostasis in cancer cells. However, the formation of catalytic Ir-hydride intermediates is likely to be inhibited in the presence of GSH, which is present in millimolar concentrations in cells. Catalysis of the oxidation of GSH to GSSG is another potential strategy for modulating cellular redox metabolism, although it has not been well studied. Iridium complexes of the type $[(Cp^X)Ir(N^\wedge N')SH]^+$ are capable of oxidizing the GSH to GSSG, however, the mechanism has yet to be investigated.[92] Thiolato-bridged iridium dimers are highly cytotoxic, but are poor catalyts.[90] Here we have discovered that Cp* Ir(III) azopyridine iodido complexes can catalyse oxidation of GSH to GSSG under physiologically relevant conditions (Figure 3.26).

Based on the experimental data and DFT calculations, the mechanism for activation and catalysis shown in Figure 3.36 for complex **7**, can be proposed. DFT calculated pathway **II** (Scheme 3.1) is largely exergonic, indicating that the activation of iodido complexes leads mainly to Ir-SG adducts. The azo bond of these Ir-SG complexes is attacked by excess GSH giving rise to GSSG and superoxide with oxygen as the one-electron acceptor. Molecular oxygen was shown to play a crucial role in the catalytic cycle since the TON number was lower under a nitrogen atmosphere and the generation of hydroxyl radicals detected by EPR required the presence of oxygen. Under N_2, the Ir-SG adducts readily decompose to give the free H_2azpy ligand and dinuclear thiolato-bridged $[(Cp^*Ir)_2(\mu\text{-SG})_3]^+$ (Figure 3.36, Figure 3.29). In the presence of O_2 as the one-electron acceptor from the paramagnetic species [Int3], the Ir-SG adducts readily form, and participate in the catalytic cycle, thus leading to a higher catalytic efficiency (Figure 3.36, Figure 3.27). ROS accumulation in A549 lung cancer cells treated with complex **7** (Figure 3.33), suggests that such reactions can occur inside cells inducing the oxidative stress. Although the high catalytic activity of complexes **7** and **8** probably contributes to their high cytotoxicity, these complexes are not the most cytotoxic, suggesting that other pathways resulting in the release of reduced azopyridine ligand and dinuclear thiolato-bridged complexes may play important roles in the mechanism of anticancer activity.

3.5 Conclusions

Iodido Ir(III) Cp* azopyridine complexes exhibit potent cytotoxic activity towards cancer cells despite being relatively inert towards aquation and nucleobase binding. Some exhibit a 10-fold higher activity than the anticancer drug cisplatin against human lung cancer cells and are not cross-resistant. Also, complex [(Cp*)Ir(HO-azpy)I]PF$_6$ (**1**) is 25-fold less toxic *in vivo* towards zebrafish embryos than its chlorido analogue.

Experiments and DFT calculations suggest that reactions with the abundant intracellular tripeptide glutathione play a major role in activation of these iodido complexes in cells and in generation of cytotoxic radicals (including superoxide), reduced azopyridine ligand and thiolato-bridged dinuclear complexes. A key feature in the activation is the attack of glutathione on the azo bond of the coordinated azopyridine. Reactions with GSH also give S-bound thiolato adducts which are catalysts for the oxidation of GSH to GSSG in oxygen-dependent mechanisms. It will be interesting in future work to investigate the dependence of cancer cell cytotoxicity on cellular oxygen concentrations because many tumours are hypoxic.

This work suggests that iodido Ir(III) Cp* azopyridine complexes have a unique multi-targeting anticancer mechanism of action, which is potentially important for combatting cisplatin resistance. The existence of both metal- and ligand-centred reactions provides wide scope for the design of novel organoiridium chemotherapeutic compounds.

3.6 References

1   D. Wang and S. J. Lippard, *Nat. Rev. Drug Discov.*, 2005, **4**, 307-320.

2   L. Kelland, *Nat. Rev. Cancer*, 2007, **7**, 573-584.

3   N. P. Barry and P. J. Sadler, *Chem. Commun.*, 2013, **49**, 5106-5131.

4   S. M. Meier-Menches, C. Gerner, W. Berger, C. G. Hartinger and B. K. Keppler, *Chem. Soc. Rev.*, 2018, **47**, 909-928.

5   T. Zou, C. T. Lum, C.-N. Lok, J.-J. Zhang and C.-M. Che, *Chem. Soc. Rev.*, 2015, **44**, 8786-8801.

6   E. Boros, P. J. Dyson and G. Gasser, *Chem*, 2020, **6**, 41-60.

7   M. P. Sullivan, H. U. Holtkamp and C. G. Hartinger, *Met. Ions Life Sci*, 2018, **18**, 351-386.

8   A. Erxleben, *Curr. Med. Chem.*, 2019, **26**, 694-728.

9   Y. Wang, H. Li and H. Sun, *Inorg. Chem.*, 2019, **58**, 13673-13685.

10   A. Cusanelli, U. Frey, D. T. Richens and A. E. Merbach, *J. Am. Chem. Soc.*, 1996, **118**, 5265-5271.

11   Z. Liu and P. J. Sadler, *Acc. Chem. Res.*, 2014, **47**, 1174-1185.

12   Y. Geldmacher, M. Oleszak and W. S. Sheldrick, *Inorg. Chim. Acta*, 2012, **393**, 84-102.

13   E. Meggers, *Angew. Chem. Int. Ed.*, 2017, **56**, 5668-5675.

14   M. A. Scharwitz, I. Ott, R. Gust, A. Kromm and W. S. Sheldrick, *J. Inorg. Biochem.*, 2008, **102**, 1623-1630.

15   R. Gao, D. G. Ho, B. Hernandez, M. Selke, D. Murphy, P. I. Djurovich and M. E. Thompson, *J. Am. Chem. Soc.*, 2002, **124**, 14828-14829.

16   L. He, Y. Li, C.-P. Tan, R.-R. Ye, M.-H. Chen, J.-J. Cao, L.-N. Ji and Z.-W. Mao, *Chem. Sci.*, 2015, **6**, 5409-5418.

17   H. Amouri, J. Moussa, A. K. Renfrew, P. J. Dyson, M. N. Rager and L. M. Chamoreau, *Angew. Chem. Int. Ed.*, 2010, **49**, 7530-7533.

18   Z. Liu, I. Romero-Canelón, B. Qamar, J. M. Hearn, A. Habtemariam, N. P. Barry, A. M. Pizarro, G. J. Clarkson and P. J. Sadler, *Angew. Chem. Int. Ed.*, 2014, **53**, 3941-3946.

19   A. J. Millett, A. Habtemariam, I. Romero-Canelón, G. J. Clarkson and P. J. Sadler, *Organometallics*, 2015, **34**, 2683-2694.

20   Y. Yang, L. Guo, Z. Tian, Y. Gong, H. Zheng, S. Zhang, Z. Xu, X. Ge and Z. Liu, *Inorg. Chem.*, 2018, **57**, 11087-11098.

21   Z. Liu, A. Habtemariam, A. M. Pizarro, S. A. Fletcher, A. Kisova, O. Vrana, L. Salassa, P. C. Bruijnincx, G. J. Clarkson and V. Brabec, *J. Med. Chem.*, 2011, **54**, 3011-3026.

22   K. Fagnou and M. Lautens, *Angew. Chem. Int. Ed.*, 2002, **41**, 26-47.

23   P. Štarha, Z. Dvořák and Z. Trávníček, *J. Organomet. Chem.*, 2018, **872**, 114-122.

24   F. Chen, J. Moat, D. McFeely, G. Clarkson, I. J. Hands-Portman, J. P. Furner-Pardoe, F. Harrison, C. G. Dowson and P. J. Sadler, *J. Med. Chem.*, 2018, **61**, 7330-7344.

25   J. M. Cross, N. Gallagher, J. H. Gill, M. Jain, A. W. McNeillis, K. L. Rockley, F. H. Tscherny, N. J. Wirszycz, D. S. Yufit and J. W. Walton, *Dalton Trans.*, 2016, **45**, 12807-12813.

26   S. Sinha, S. Das, R. Sikari, S. Parua, P. Brandaõ, S. Demeshko, F. Meyer and N. D. Paul, *Inorg. Chem.*, 2017, **56**, 14084-14100.

27   S. J. Dougan, A. Habtemariam, S. E. McHale, S. Parsons and P. J. Sadler, *Proc. Natl. Acad. Sci. U.S.A.*, 2008, **105**, 11628-11633.

28   R. J. Needham, C. Sanchez-Cano, X. Zhang, I. Romero-Canelón, A. Habtemariam, M. S. Cooper, L. Meszaros, G. J. Clarkson, P. J. Blower and P. J. Sadler, *Angew. Chem. Int. Ed.*, 2017, **56**, 1017-1020.

29   X. Zhang, F. Ponte, E. Borfecchia, A. Martini, C. Sanchez-Cano, E. Sicilia and P. J. Sadler, *Chem. Commun.*, 2019, **55**, 14602-14605.

30   J. M. Hearn, G. M. Hughes, I. Romero-Canelón, A. F. Munro, B. Rubio-Ruiz, Z. Liu, N. O. Carragher and P. J. Sadler, *Metallomics*, 2018, **10**, 93-107.

31   S. J. Dougan, M. Melchart, A. Habtemariam, S. Parsons and P. J. Sadler, *Inorg. Chem.*, 2006, **45**, 10882-10894.

32   A. Leo, C. Hansch and D. Elkins, *Chem. Rev.*, 1971, **71**, 525-616.

33   A. D. Becke, *J. Chem. Phys.*, 1993, **98**, 5648-5652.

34   C. Lee, W. Yang and R. Parr, *Phys. Rev, vol. B*, 1988, **37**, 785-789.

35   Gaussian 09, Revision D.01, G. W. T. M. J. Frisch, H. B. Schlegel, G. E. Scuseria, M. A. Robb, J. R. Cheeseman, G. Scalmani, V. Barone, B. Mennucci, G. A. Petersson, H. Nakatsuji, M. Caricato, X. Li, H. P. Hratchian, A. F. Izmaylov, J. Bloino, G. Zheng, J. L. Sonnenberg, M. Hada, M. Ehara, K. Toyota, R. Fukuda, J. Hasegawa, M. Ishida, T. Nakajima, Y. Honda, O. Kitao, H. Nakai, T. Vreven, J. A. Montgomery, Jr. , J. E. Peralta, F. Ogliaro, M. Bearpark, J. J. Heyd, E. Brothers, K. N. Kudin, V. N. Staroverov, T. Keith, R.

Kobayashi, J. Normand, K. Raghavachari, A. Rendell, J. C. Burant, S. S. Iyengar, J. Tomasi, M. Cossi, N. Rega, J. M. Millam, M. Klene, J. E. Knox, J. B. Cross, V. Bakken, C. Adamo, J. Jaramillo, R. Gomperts, R. E. Stratmann, O. Yazyev, A. J. Austin, R. Cammi, C. Pomelli, J. W. Ochterski, R. L. Martin, K. Morokuma, V. G. Zakrzewski, G. A. Voth, P. Salvador, J. J. Dannenberg, S. Dapprich, A. D. Daniels, O. Farkas, J. B. Foresman, J. V. Ortiz, J. Cioslowski, and D. J. Fox, Gaussian, Inc., Wallingford CT, 2010.

36   S. Grimme, J. Antony, S. Ehrlich and H. Krieg, *J. Chem. Phys.*, 2010, **132**, 154104-154122.

37   P. J. Hay and W. R. Wadt, *J. Chem. Phys.*, 1985, **82**, 299-310.

38   K. Fukui, *J. Phys. Chem*, 1970, **74**, 4161-4163.

39   C. Gonzalez and H. B. Schlegel, *J. Chem. Phys.*, 1989, **90**, 2154-2161.

40   S. Miertuš, E. Scrocco and J. Tomasi, *Chem. Phys.*, 1981, **55**, 117-129.

41   S. Miertus and J. Tomasi, *Chem. Phys.*, 1982, **65**, 239-245.

42   J.-L. Pascual-ahuir, E. Silla and I. Tunon, *J. Comput. Chem.*, 1994, **15**, 1127-1138.

43   J. D. S. D. A. McQuarrie, *Molecular Thermodynamics, University Science Books*, Sausalito, 1999.

44   R. W. Ashcraft, S. Raman and W. H. Green, *J. Phys. Chem. B*, 2007, **111**, 11968-11983.

45   Y. Fu, M. J. Romero, A. Habtemariam, M. E. Snowden, L. Song, G. J. Clarkson, B. Qamar, A. M. Pizarro, P. R. Unwin and P. J. Sadler, *Chem. Sci.*, 2012, **3**, 2485-2494.

46   S. H. van Rijt, A. J. Hebden, T. Amaresekera, R. J. Deeth, G. J. Clarkson, S. Parsons, P. C. McGowan and P. J. Sadler, *J. Med. Chem.*, 2009, **52**, 7753-7764.

47   L. Li, W. W. Brennessel and W. D. Jones, *J. Am. Chem. Soc.*, 2008, **130**, 12414-12419.

48   Z. Liu, L. Salassa, A. Habtemariam, A. M. Pizarro, G. J. Clarkson and P. J. Sadler, *Inorg. Chem.*, 2011, **50**, 5777-5783.

49   M. Shivakumar, J. Gangopadhyay and A. Chakravorty, *Polyhedron*, 2001, **20**, 2089-2093.

50   J. M. Fontmorin, R. C. Burgos Castillo, W. Z. Tang and M. Sillanpää, *Water Res.*, 2016, **99**, 24-32.

51   H. Karoui, N. Hogg, C. Fréjaville, P. Tordo and B. Kalyanaraman, *J. Biol. Chem.*, 1996, **271**, 6000-6009.

52   S. Stoll and A. Schweiger, *J. Magn. Reson.*, 2006, **178**, 42-55.

53   T. Nakayama, T. Isobe, K. Nakamiya, J. S. Edmonds, Y. Shibata and M. Morita, *Magn. Reson. Chem.*, 2005, **43**, 543-550.

54   N. W. Pirie and K. G. Pinhey, *J. Biol. Chem.*, 1929, **84**, 321-333.

55   S. G. Tajc, B. S. Tolbert, R. Basavappa and B. L. Miller, *J. Am. Chem. Soc.*, 2004, **126**, 10508-10509.

56   P. Skehan, R. Storeng, D. Scudiero, A. Monks, J. McMahon, D. Vistica, J. T. Warren, H. Bokesch, S. Kenney and M. R. Boyd, *JNCI: Journal of the National Cancer Institute*, 1990, **82**, 1107-1112.

57   J. Ruiz, C. Vicente, C. n. de Haro and D. Bautista, *Inorg. Chem.*, 2013, **52**, 974-982.

58   M. J. McKeage, S. J. Berners-Price, P. Galettis, R. J. Bowen, W. Brouwer, L. Ding, L. Zhuang and B. C. Baguley, *Cancer Chemother. Pharmacol.*, 2000, **46**, 343-350.

59   Y. Fu, A. Habtemariam, A. M. B. H. Basri, D. Braddick, G. J. Clarkson and P. J. Sadler, *Dalton Trans.*, 2011, **40**, 10553-10562.

60   T. V. Bowman and L. I. Zon, *ACS Chem. Biol.*, 2010, **5**, 159-161.

61   P. M. Eimon and A. L. Rubinstein, *Expert Opin. Drug Metab. Toxicol.*, 2009, **5**, 393-401.

62   A. J. Rennekamp and R. T. Peterson, *Curr. Opin. Chem. Biol.*, 2015, **24**, 58-70.

63   W. B. Barbazuk, I. Korf, C. Kadavi, J. Heyen, S. Tate, E. Wun, J. A. Bedell, J. D. McPherson and S. L. Johnson, *Genome Res.*, 2000, **10**, 1351-1358.

64   J. P. C. Coverdale, H. E. Bridgewater, J.-I. Song, N. A. Smith, N. P. E. Barry, I. Bagley, P. J. Sadler and I. Romero-Canelón, *J. Med. Chem.*, 2018, **61**, 9246-9255.

65   L. Helm and A. E. Merbach, *Coord. Chem. Rev.*, 1999, **187**, 151-181.

66   T. Poth, H. Paulus, H. Elias, C. Dücker-Benfer and R. van Eldik, *Eur. J. Inorg. Chem.*, 2001, **2001**, 1361-1369.

67   C. X. Zhang and S. J. Lippard, *Curr. Opin. Chem. Biol.*, 2003, **7**, 481-489.

68   I. Romero-Canelón, L. Salassa and P. J. Sadler, *J. Med. Chem.*, 2013, **56**, 1291-1300.

69   Z. Liu, A. Habtemariam, A. M. Pizarro, S. A. Fletcher, A. Kisova, O. Vrana, L. Salassa, P. C. A. Bruijnincx, G. J. Clarkson, V. Brabec and P. J. Sadler, *J.*

Med. Chem., 2011, **54**, 3011-3026.

70   S. Parveen, M. Hanif, E. Leung, K. K. H. Tong, A. Yang, J. Astin, G. H. De
        Zoysa, T. R. Steel, D. Goodman, S. Movassaghi, T. Söhnel, V. Sarojini, S. M.
        F. Jamieson and C. G. Hartinger, *Chem. Commun.*, 2019, **55**, 12016-12019.

71   L. Messori, G. Marcon, P. Orioli, M. Fontani, P. Zanello, A. Bergamo, G. Sava
        and P. Mura, *J. Inorg. Biochem.*, 2003, **95**, 37-46.

72   F. Wang, A. Habtemariam, E. P. van der Geer, R. Fernández, M. Melchart, R.
        J. Deeth, R. Aird, S. Guichard, F. P. Fabbiani and P. Lozano-Casal, *Proc. Natl.*
        Acad. Sci. U.S.A., 2005, **102**, 18269-18274.

73   Z. Liu, I. Romero-Canelón, A. Habtemariam, G. J. Clarkson and P. J. Sadler,
        Organometallics, 2014, **33**, 5324-5333.

74   A. Wilbuer, D. H. Vlecken, D. J. Schmitz, K. Kräling, K. Harms, C. P.
        Bagowski and E. Meggers, *Angew. Chem. Int. Ed.*, 2010, **49**, 3839-3842.

75   A. Meister, *Trends Biochem. Sci*, 1981, **6**, 231-234.

76   F. Wang, J. Xu, A. Habtemariam, J. Bella and P. J. Sadler, *J. Am. Chem. Soc.*,
        2005, **127**, 17734-17743.

77   L. Zeng, S. Kuang, G. Li, C. Jin, L. Ji and H. Chao, *Chem. Commun.*, 2017,
        53, 1977-1980.

78   Q.-X. Zhou, Y. Zheng, T.-J. Wang, Y.-J. Chen, K. Li, Y.-Y. Zhang, C. Li, Y.-J.
        Hou and X.-S. Wang, *Chem. Commun.*, 2015, **51**, 10684-10686.

79   Y. Shi, S.-A. Liu, D. J. Kerwood, J. Goodisman and J. C. Dabrowiak, *J. Inorg.*
        Biochem., 2012, **107**, 6-14.

80   J. L. Sadler and A. J. Bard, *J. Am. Chem. Soc.*, 1968, **90**, 1979-1989.

81   W. Kaim, R. Reinhardt, S. Greulich and J. Fiedler, *Organometallics*, 2003, **22**, 2240-2244.

82   L. Sun, G. Li, X. Chen, Y. Chen, C. Jin, L. Ji and H. Chao, *Sci. Rep.*, 2015, **5**, 14837.

83   W. G. Kirlin, J. Cai, S. A. Thompson, D. Diaz, T. J. Kavanagh and D. P. Jones, *Free Radical Biol. Med.*, 1999, **27**, 1208-1218.

84   F. Q. Schafer and G. R. Buettner, *Free Radical Biol. Med.*, 2001, **30**, 1191-1212.

85   V. Khramtsov, L. J. Berliner and T. L. Clanton, *Magn. Reson. Med.*, 1999, **42**, 228-234.

86   G.-Y. Li, J.-P. Liu, H.-Y. Huang, Y. Wen, H. Chao and L.-N. Ji, *J. Inorg. Biochem.*, 2013, **121**, 108-113.

87   G. Li, Y. Chen, J. Wu, L. Ji and H. Chao, *Chem. Commun.*, 2013, **49**, 2040-2042.

88   Y. Kenis, J. De Smedt and H. J. Tagnon, *Eur. J. Cancer*, 1966, **2**, 51-57.

89   S. H. Kuttab, S. Tanglertpaibul and P. Vouros, *Biomed. Mass Spectrom.*, 1982, **9**, 78-84.

90   G. Gupta, A. Garci, B. S. Murray, P. J. Dyson, G. Fabre, P. Trouillas, F. Giannini, J. Furrer, G. Süss-Fink and B. Therrien, *Dalton Trans.*, 2013, **42**, 15457-15463.

91   A. H. Ngo and L. H. Do, *Inorg. Chem. Front.*, 2020, **7**, 583-591.

92   P. Štarha, A. Habtemariam, I. Romero-Canelón, G. J. Clarkson and P. J. Sadler, *Inorg. Chem.*, 2016, **55**, 2324-2331.

Chapter 4

Ligand-Controlled Reactivity and Cytotoxicity of Cyclometalated Rhodium(III) Complexes

4.1 Introduction

The approval of cisplatin as an anticancer drug in the late 1970s has not only led to new generations of platinum drugs in clinical use (carboplatin and oxaliplatin) or trials, but also to the search for a new era of transition metal-based anticancer agents.[1-4] Group 9 metals iridium and rhodium have attracted much attention although are less widely studied than platinum.[5-8] Ir^{III} and Rh^{III} complexes with low spin d^6 configurations are usually considered to be kinetically inert, however, recent studies have revealed that their reactivity toward biological targets can be adjusted by the rational selection of the surrounding ligands directly coordinated to the metal.[6] Kinetically stable iridium/rhodium pyridocarbazole complexes have been synthesised by Meggers and co-workers as potent enzyme inhibitors,[9,10] and Sheldrick and co-workers have reported various pentamethyl-cyclopentadienyl (Cp^*) iridium/rhodium complexes with chelating polypyridine ligands as potent anticancer agents.[11] More recently, attention has turned to cyclometalated iridium and rhodium complexes in which five-membered chelate rings contain a strong M-C σ bond.[12,13] Nevertheless, research on cyclometalated rhodium complexes has largely focused on non-cyclopentadienyl cyclometalated rhodium complexes that target DNA, enzyme or protein-protein interfaces.[5,14,15] Reported cyclopentadienyl rhodium anticancer complexes to date, have mainly contained N^N,[16,17] N^S,[18] N^O,[19-21] or O^O[17,22,23] chelating ligands.

Recent work has demonstrated that replacing the N^N coordinating ligand 2,2'-bipyridine or 1,10-phenanthroline with C^N chelating 2-phenylpyridne or benzo[h]quinoline in pentamethyl-cyclopentadienyl (Cp^*) iridium complexes, not

only enhances nucleobase binding and lipophilicity, but also switches on anticancer activity towards human A2780 ovarian cancer cells.[24,25] Moreover, the chelated iridium(III) 1-biphenyl-2,3,4,5-tetramethylcyclopentadienyl complex [(Cp^{xbiph})Ir(phenylpyridine)(pyridine)]$^+$ can utilize NADH as a hydride source to transfer hydride electrons to oxygen, generating hydrogen peroxide and reactive oxygen species in cancer cells to trigger cell death.[26] Recently, it has been reported that rhodium anticancer complexes [(Cp^X)Rh(N^N)Cl]$^+$ (Cp^X = Cp*, Cp^{xph}, or Cp^{xbiph} and N^N is ethylenediamine, 2,2'-bipyridine, 2,2'-dimethylbipyridine, or 1,10-phenanthroline) which can be effective transfer hydrogenation catalysts inducing reductive stress when co-administrated with a non-toxic dose of formate as the hydride donor in cancer cells.[27] Intriguingly, the Cp^X ring in these catalytic [(Cp^X)Rh(N^N)Cl]$^+$ complexes can be readily activated by deprotonation and undergo rapid deuteration in aqueous media, so providing a novel activation pathway for half-sandwich Rh(III) complexes.[28] Based on these interesting discoveries, in this Chapter, studies are extended to cyclometalated cyclopentadienyl rhodium anticancer complexes with potential catalytic properties.

Six cyclometalated rhodium complexes (Scheme 4.1) bearing different cyclopentadienyl Cp^X rings with C^N chelating ligand benzo[h]quinoline have been synthesised and fully characterised by ^{1}H NMR, ^{13}C NMR, high resolution ESI-MS and elemental analysis. Five novel complexes **2a**, **3a**, **1b-3b** are reported, and the X-ray crystal structures of complexes **2a**, **3a** and **1b·PF$_6$** have been determined. Complexes **1a-3a** contain chloride, while complexes **1b-3b** feature pyridine as the monodentate ligand. Their aqueous chemistry including hydrolysis, binding to

nucleobase 9-ethylguanine (9-EtG) or abundant cellular thiol glutathione (GSH, γ-L-Glu-L-Cys-Gly), as well as catalytic activity in the oxidation of coenzyme NADH are evaluated and compared. Cytotoxicity has been screened against the human A549 lung and A2780 ovarian cancer cell lines. Cellular Rh accumulation, ROS induction and apoptosis in A549 cancer cells induced by complexes **3a** and **3b** at equipotent concentrations have been investigated to elucidate their possible mechanism of action.
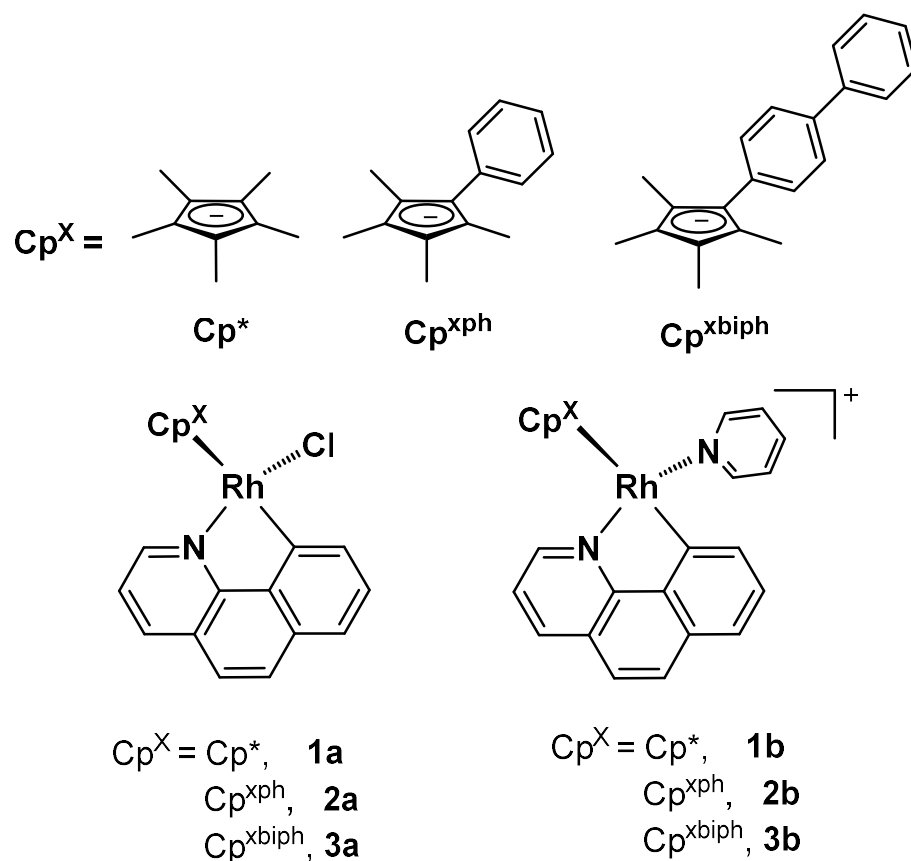
Scheme 4.1. Structures of the six cyclometalated rhodium(III) benzo[h]quinoline complexes studied in this Chapter. (**a** denotes chloride, **b** denotes pyridine, the counterions for **1b-3b** are NO_3^- unless specified.)

4.2 Experimental section

4.2.1 Materials

Benzo[h]quinoline was purchased from Sigma-Aldrich, the total ROS/superoxide detection kit from Enzo Life Sciences, the apoptosis detection regents from Abcam. The rhodium dimer precursors [(Cp*)Rh(μ-Cl)Cl]₂, [(Cp^xph)Rh(μ-Cl)Cl]₂ and [(Cp^xbiph)Rh(μ-Cl)Cl]₂ were synthesised as the described in Chapter 2.

4.2.2 Synthesis

4.2.2.1 Synthesis of Chlorido Rhodium Complexes

The complex [(Cp*)Rh(benzo[h]quinoline)Cl] (**1a**) was synthesised according to the literature.[29] Complexes **2a** and **3a** were synthesised using the general procedure: [(Cp^X)Rh(μ-Cl)Cl]₂ (0.12 mmol) with benzo[h]quinoline (0.36 mmol) and anhydrous sodium acetate (0.98 mmol) in 20 mL anhydrous DCM was stirred under nitrogen for 48 h. Then the solution was filtered through celite and purified on a 10 g silica cartridge on a Biotage Isolera instrument (methanol/dichloromethane, 5/95, v/v). Then the column-purified powder was recrystallized from dichloromethane/diethyl ether at 277 K to give a red crystalline solid.

[(Cp^xph)Rh(benzo[h]quinoline)Cl] (2a): 43 mg, yield 70%; ^{1}H NMR (500 MHz, CDCl₃, 298 K): δ 8.69 (d, J = 5.1 Hz, 1H,), 8.14 (d, J = 8.0 Hz, 1H), 7.97 (d, J = 6.7 Hz, 1H), 7.79 (d, J = 8.7 Hz, 1H), 7.62-7.53 (m, 5H), 7.43-7.3 (m, 4H), 1.85 (s, 3H), 1.78 (s, 3H), 1.75 (s, 3H), 1.45 (s, 3H); ^{13}C{^{1}H} NMR (125 MHz, CDCl₃, 298 K): δ 175.18 (d, $J_{\text{C-Rh}}$ = 33.8 Hz), 155.32, 149.49, 140.54, 135.64, 133.83, 133.54, 131.99, 130.89, 129.71, 128.79, 127.77, 127.21, 123.13, 121.53, 121.32, 107.6, 100.31, 95.87,

94.64, 88.79, 10.84, 10.48, 9.54, 9.22. HR-MS (ESI): *m/z* calcd for [(Cp^{xph})Rh(benzo[h]quinoline)]$^+$: 478.1037; found: 478.1032; elemental analysis calcd (%) for C$_{28}$H$_{25}$ClRhN: C, 65.45; H, 4.90; N, 2.73; found: C, 64.55; H, 4.86; N, 2.69.

[(Cp^{xbiph})Rh(benzo[h]quinoline)Cl] (3a): 41 mg, yield 58%; ^{1}H NMR (500 MHz, CDCl$_3$, 298 K): δ 8.73 (d, *J* = 5.1 Hz, 1H,), 8.14 (d, *J* = 7.9 Hz, 1H), 8.00 (d, *J* = 6.9 Hz, 1H), 7.80 (d, *J* = 8.7 Hz, 1H), 7.68-7.55 (m, 9H), 7.48 (t, *J* = 7.6 Hz, 2H), 7.40-7.34 (m, 2H), 1.89 (s, 3H),1.80 (s, 3H), 1.77 (s, 3H), 1.50 (s, 3H); ^{13}C{^{1}H} NMR (125 MHz, CDCl$_3$, 298 K): δ 175.14 (d, *J*$_{C-Rh}$ = 33.8 Hz), 155.30, 149.51, 140.59, 140.54, 140.31, 135.66, 133.83, 133.53, 131.26, 131.02, 130.20, 129.71, 129.04, 127.65, 127.36, 127.21, 127.11, 123.14, 121.59, 121.34, 107.56, 100.39, 95.44, 94.73, 88.91, 10.91, 10.53, 9.54, 9.23. HR-MS (ESI): *m/z* calcd for [(Cp^{xbiph})Rh(benzo[h]quinoline)]$^+$ 554.1350; found 554.1353; elemental analysis calcd (%) for C$_{34}$H$_{29}$ClRhN: C, 69.22; H, 4.95; N, 2.37; found: C, 69.31; H, 4.96; N, 2.17.

4.2.2.2 Synthesis of Pyridine Rhodium Complexes

Complexes **1b-3b** were synthesised using the general procedure: [(Cp^X)Rh(benzo[h]quinoline)Cl] (0.05 mmol) was stirred with silver nitrate (0.05 mmol) in 10 mL methanol for 1.5 h. Then the solution was centrifuged and pyridine (0.5 mmol) was added to the upper clear layer. The colour changed from orange to bright yellow, and the solution was stirred 24 h. Then the solution was concentrated,

with the yellow solid product recrystallized from diethyl ether and dried under vacuum.

[(Cp*)Rh(benzo[h]quinoline)py]NO₃ (1b): 18 mg, yield 65%; ^{1}H NMR (500 MHz, d$_4$-MeOD, 298 K): δ 9.44 (d, J = 5.0 Hz, 1H), 8.54 (d, J = 7.4 Hz, 1H), 8.50 (d, J = 5.6 Hz, 2H), 8.35 (d, J = 7.2 Hz, 1H), 7.91-7.81 (m, 3H), 7.75-7.71 (m, 3H), 7.26 (t, J_1 = 6.8 Hz, J_2 = 7.3 Hz, 2H), 1.65 (s, 15H); ^{13}C{^{1}H} NMR (125 MHz, d$_4$-MeOD, 298 K): δ 175.14 (d, J_{C-Rh} = 35.0 Hz), 155.99, 154.20, 151.45, 141.71, 140.14, 138.82, 135.17, 134.29, 131.98, 130.77, 128.77, 127.51, 124.94, 124.35, 123.77, 98.62, 9.04. HR-MS (ESI): m/z calcd for [(Cp*)Rh(benzo[h]quinoline)pyridine]$^+$ 495.1302, found 495.1297; elemental analysis calcd (%) for C$_{28}$H$_{28}$RhN$_3$O$_3$: C, 60.33; H, 5.06; N, 7.54; found: C, 59.65; H, 4.98; N, 7.50.

[(Cp^{xph})Rh(benzo[h]quinoline)py]NO₃ (2b): 23 mg, yield 74%; ^{1}H NMR (500 MHz, d$_4$-MeOD, 298 K): δ 9.22 (d, J = 5.0 Hz, 1H,), 8.53-8.50 (m, 3H), 8.27 (d, J = 6.8 Hz, 1H), 7.91 (d, J = 8.7 Hz, 1H), 7.82-7.74 (m, 5H), 7.30 (t, J_1 = 6.7 Hz, J_2 = 7.4 Hz , 2H), 7.26 (d, J = 7.5 Hz, 1H), 7.16 (t, J_1 = 7.8 Hz, J_2 = 7.6 Hz, 2H), 6.90 (d, J =7.3 Hz, 2H), 1.90 (s, 3H), 1.76 (s, 3H), 1.71 (s, 3H), 1.68 (s, 3H); ^{13}C{^{1}H} NMR (125 MHz, d$_4$-MeOD, 298 K): δ 175.69 (d, J_{C-Rh} = 33.8 Hz), 155.82, 154.29, 151.54, 141.54, 140.40, 138.98, 135.38, 134.38, 132.14, 131.63, 131.02, 130.85, 129.63, 129.43, 129.02, 127.72, 125.10, 124.27, 124.06, 105.56, 102.90, 102.08, 98.47, 93.07, 10.52, 10.35, 9.00. HR-MS (ESI): m/z calcd for [(Cp^{xph})Rh(benzo[h]quinoline)pyridine]$^+$ 557.1459, found 557.1458; elemental analysis calcd (%) for C$_{33}$H$_{30}$RhN$_3$O$_3$: C, 63.98; H, 4.88; N, 6.78; found: C, 63.91; H, 4.84; N, 6.76.

153

[(Cp^{xbiph})Rh(benzo[h]quinoline)py]NO$_3$ (3b): 22 mg, yield 63%; ^{1}H NMR (500 MHz, d$_4$-MeOD, 298 K): δ 9.24 (d, J = 5.1 Hz, 1H,), 8.54 (d, J = 5.6 Hz, 2H), 8.51 (d, J = 8.0 Hz, 1H), 8.30 (d, J = 7.0 Hz, 1H), 7.91 (d, J = 6.7 Hz, 1H), 7.83-7.74 (m, 5H), 7.53 (d, J = 7.4 Hz, 2H), 7.43 (d, J = 8.2 Hz, 2H), 7.39 (t, J_1 = 7.4 Hz, J_2 = 7.7 Hz, 2H), 7.33-7.28 (m, 3H), 6.99 (d, J = 8.2 Hz, 2H),1.93 (s, 3H), 1.77 (s, 3H), 1.73 (s, 3H), 1.71 (s, 3H); ^{13}C{^{1}H} NMR (125 MHz, d$_4$-MeOD, 298 K): δ 175.67 (d, J_{C-Rh} = 33.8 Hz), 155.81,154.29, 151.59, 142.40, 141,54, 141.21,140.40, 139.00, 135.38, 134.40, 132.16, 131.55, 130.84, 130.57, 129.97, 129.02, 128.79, 149.49, 140.54, 135.64, 133.83, 133.54, 131.99, 130.89, 129.71, 128.79, 128.05, 127.82, 127.73, 126.12, 125.13, 124.35, 124.07, 105.50, 102.72, 101.93, 98.28, 93.41, 10.57, 10.43, 9.02, 9.01. HR-MS (ESI): m/z calcd for [(Cp^{xbiph})Rh(benzo[h]quinoline)pyridine]$^+$ 633.1772; found 633.1768; elemental analysis calcd (%) for C$_{39}$H$_{34}$RhN$_3$O$_3$: C, 67.34; H, 4.93; N, 6.04; found: C, 67.25; H, 4.86; N, 5.95.

4.2.3 Methods

NMR spectroscopy, ESI-MS analysis, elemental analysis, UV-vis spectroscopy, pH measurements, HPLC, LC-MS, X-ray crystallography, ICP-OES, ICP-MS, cell culture, cell viability assay were carried out as described in Chapter 2.

4.2.3.1 X-ray Crystallography

The crystals were kept at 150(2) K except crystals of complex **3a** at 100(2) K during data collection by Dr. Guy Clarkson (Department of Chemistry, University of Warwick). X-ray crystallographic data for complexes **2a**, **3a**, and **1b·PF₆** have been

deposited in the Cambridge Crystallographic Data Centre under the accession numbers CCDC 1952984, 1952985, 1952986, respectively. X-ray crystallographic data in CIF format are available from the Cambridge Crystallographic Data Centre (http://www.ccdc.cam.ac.uk/).

4.2.3.2 Reactions with NADH

The time dependence of reactions of rhodium complexes **1a-3a**, **1b-3b** (0.8 μM) with NADH (75-144 μM) were studied over 24 h in 1.6% MeOH-98.4% phosphate buffer (5 mM, pH 7.4) by UV-vis spectroscopy at 310 K. The concentration of NADH was obtained using the extinction coefficient $\varepsilon(339 \text{ nm}) = 6,220 \text{ M}^{-1}\text{cm}^{-1}$.[26] TON was calculated from the difference in NADH concentration divided by the concentration of metal complex catalyst over 24 h. TOF was calculated from the linear fitting of TON versus time (h) by Origin 2018.

4.2.3.3 Cellular Rh Accumulation

The accumulation of Rh in A549 human lung carcinoma cells was determined by ICP-MS. 1×10^6 cells were seeded into a 100 mm Petri dish and incubated in drug-free media for 24 h at 310 K with a 5% CO_2 humid atmosphere. For a further 24 h, the cells were incubated in RPMI-1640 medium containing 0.5x or 1x IC_{50} concentrated complex **3a** or **3b**. Following this, cells were washed, detached using trypsin-EDTA, resuspended in fresh medium, counted and centrifuged. The cell pellets were digested as ICP-MS protocol for Rh analysis.

4.2.3.4 ROS Determination

ROS detection was conducted by Hannah Bridgewater. 5×10^4 A549 human lung carcinoma cells were seeded per well in a 6-well plate and incubated for 24 h at 310 K. $1 \times$ or $2 \times$ IC$_{50}$ concentrated complex **3a** or **3b** was added to the well and incubated with cells for a further 24 h. Subsequently, total ROS and SO concentrations were analysed by flow cytometry using the total ROS/superoxide detection kit by Enzo Life Sciences. Briefly, the cells were enzymatically detached using trypsin-EDTA, washed in PBS, resuspended in staining solution, prepared according to manufacturer's instructions (25 nM concentration of both dyes, total ROS and SO) and incubated at room temperature for 30 min. Samples were then analysed on the Beckton Dickinson LSRII using Beckton Dickinson FACSDIVA software. Data were processed using FlowJo V10 for Windows. At all times, samples were kept under dark conditions to avoid light-induced ROS production. Welch's t-tests were carried out to establish statistical significance of the variations.

4.2.3.5 Apoptosis Assay

Apoptosis assay was conducted by Hannah Bridgewater. 5×10^4 A549 human lung carcinoma cells were seeded per well in a 6-well plate and incubated for 24 h at 310 K. $1 \times$ or $2 \times$ IC$_{50}$ concentrated complex **3a** or **3b** was added to the cells and incubated for a further 24 h. After which, the cells were enzymatically detached using trypsin-EDTA, washed in PBS, resuspended in staining solution (FITC Annexin V diluted 1 in 100 and 1 μg/mL PI) and incubated at room temperature for 30 min. Samples were then analysed on the Beckton Dickinson LSRII using Beckton Dickinson

FACSDIVA software. Data were processed using FlowJo V10 for Windows. Welch's

t-tests were carried out to establish statistical significance of the variations.

4.3 Results and Discussion

4.3.1 Synthesis and Characterisation

The rhodium chloride complexes **1a-3a** were synthesised via C-H activation of

benzo[h]quinoline by the rhodium dimer aided by sodium acetate in dichloromethane

at ambient temperature as reported previously (Scheme 4.2).[29] In contrast, pyridine

complexes **1b-3b** were obtained in good yields through the reaction of the

corresponding chloride complexes with silver nitrate and then with excess pyridine

(Scheme 4.2). All complexes were characterised by ^{1}H and ^{13}C NMR, elemental

analysis and high resolution ESI-MS.
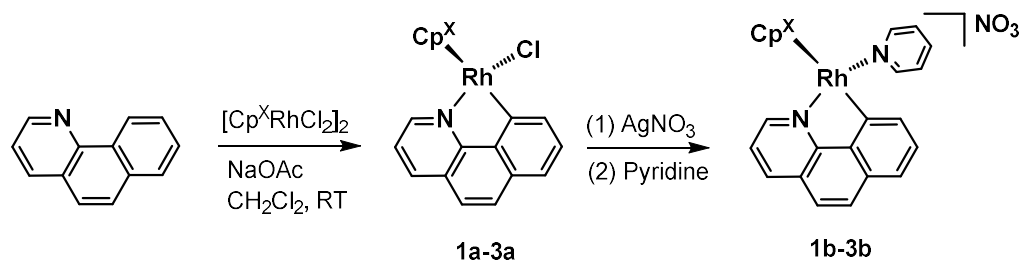
Scheme 4.2. Synthesis route for rhodium complexes containing chloride (**1a-3a**) and

pyridine (**1b-3b**) ligands.

4.3.2 X-ray Crystal Structures

X-ray crystal structures of **2a**, **3a** and **1b·PF₆** with PF₆ as the counterion were determined and are shown in Figure 4.1 with the atom numbering scheme. Crystallographic data are listed in Table A4.1, and selected bond lengths and angles in Table A4.2 in the **Appendix**. All structures adopt the familiar "piano-stool" geometry. The distances between Rh and the centroid of the η^5-cyclopentadienyl ring are within 1.827-1.832 Å. The length of the Rh-C (quinoline) bond in **2a**, **3a**, **1b·PF₆** (2.050(3), 2.0458(15), 2.058(2), respectively) is significantly shorter than the Rh-N (quinoline) bond length (2.082(3), 2.1030(14), 2.1068(18), respectively).
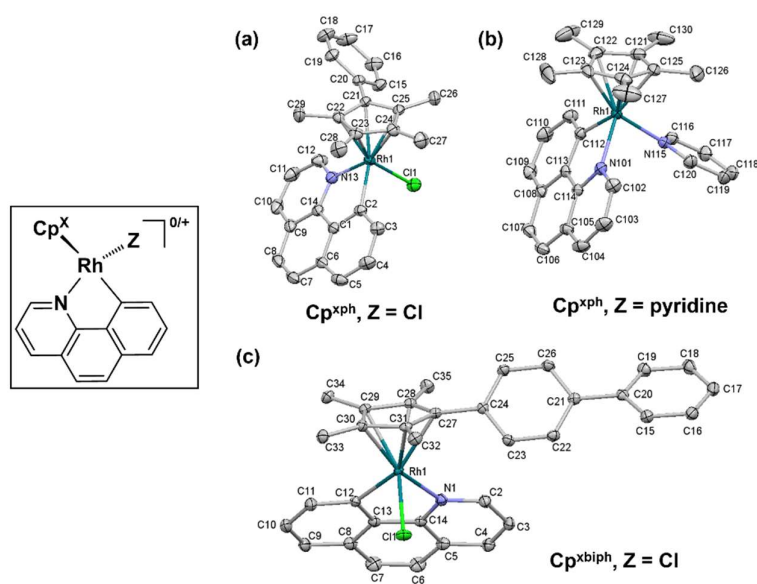
Figure 4.1. X-ray structures with atom numbering of (a) [(Cp^xph)Rh(benzo[h]quinoline)Cl] **(2a);** (b) [(Cp*)Rh(benzo[h]quinoline)pyridine]PF₆ **(1b·PF₆);** (c) [(Cp^xbiph)Rh(benzo[h]quinoline)Cl] **(3a)**, drawn with thermal ellipsoids at 50% probability. Hydrogen atoms and counterions have been omitted for clarity.

4.3.3 Aqueous Solution Chemistry

The hydrolysis of these complexes was monitored through the changes of UV-vis spectra as well as ^{1}H NMR spectra in methanol/water at 310 K and confirmed by the further addition of sodium chloride. Methanol was used to ensure sufficient solubility of the complexes in water. For example, the hydrolysis rates and half-lives for complex **1a** or **1b** were determined by fitting their UV-vis absorption changes *versus* time to pseudo-first-order kinetics, as shown in Figure 4.2.
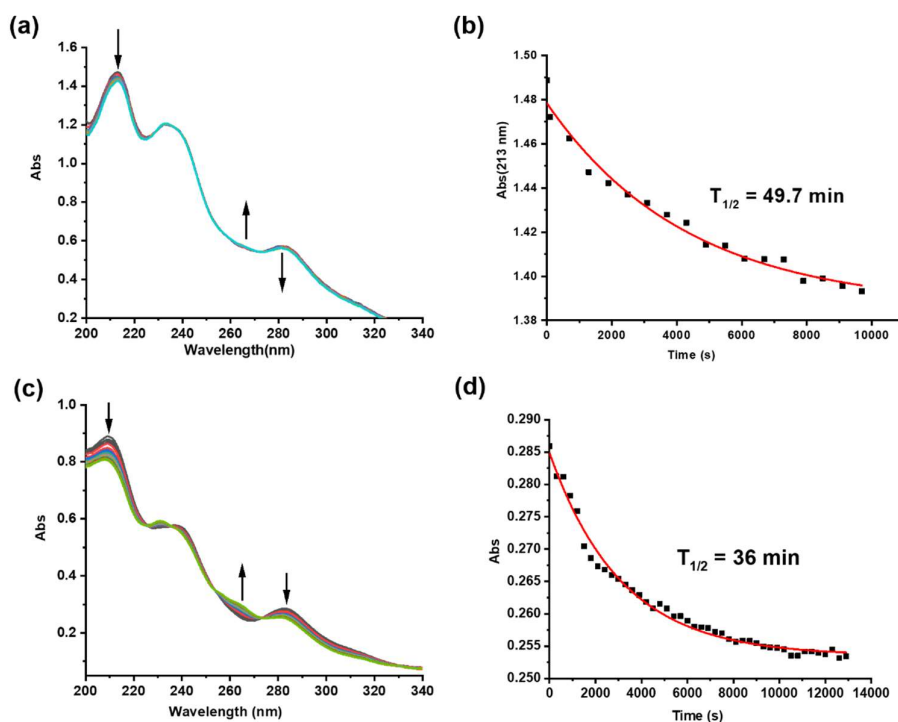
Figure 4.2. Time-dependent UV-vis study of hydrolysis and the pseudo-first-order kinetic fitting between the absorption and time for *ca.* 20 μM complex (a/b) [(Cp*)Rh(benzo[h]quinoline)Cl] (**1a**); and (**c/d**) [(Cp*)Rh(benzo[h]quinoline)pyridine]NO$_3$ (**1b**) in 10%-30% MeOH/H$_2$O in the first three hours at 310 K.

For the ^{1}H NMR studies, peaks corresponding to the aqua species are assigned for complex **1a** in Figure 4.3b. The aqua adduct can be confirmed by addition of 104 mM NaCl (to mimic the chloride concentration in blood plasma) into the hydrolysis equilibrium solution. In Figure 4.3c, when NaCl was added to the 24 h equilibrium hydrolysis solution of complex **1a** (Figure 4.3c), peaks for the aqua adducts all disappeared and those for the parent chloride complexes increased in intensity, confirming that hydrolysis of the chloride complexes is reversible.
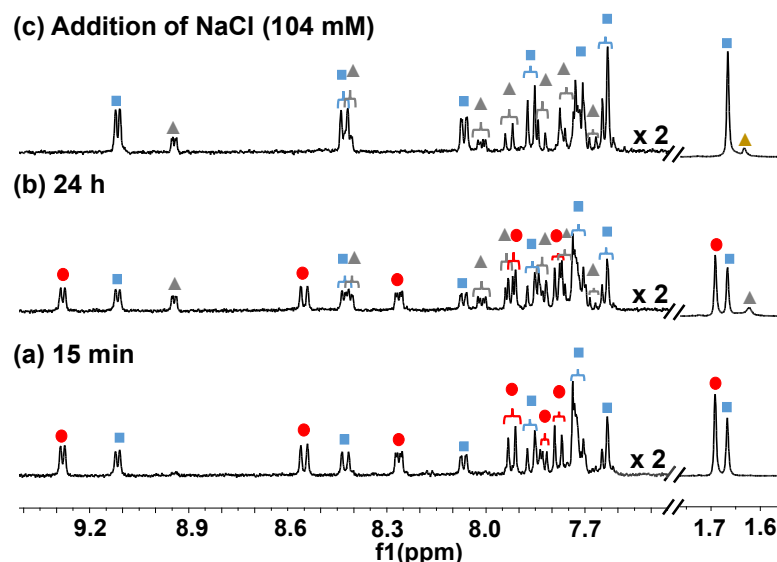
Figure 4.3. 400 MHz ^{1}H NMR spectra of $[(Cp^*)Rh(benzo[h]quinoline)Cl]$ (**1a**) (*ca.* 0.5 mM) in d_4-MeOH/D_2O (v/v 4/1) after (a) 15 min; (b) 24 h; and (c) 10 min after addition of NaCl (104 mM). After 15 min, 60% of the parent complex **1a** (■) hydrolysed to its aqua adduct $[(Cp^*)Rh(benzo[h]quinoline)D_2O]^+$ (●). After 24 h, one third of the aqua adduct $[(Cp^*)Rh(benzo[h]quinoline)D_2O]^+$ had decomposed into the free chelated ligand (▲) and $[(Cp^*)Rh(D_2O)_3]^{2+}$ (▲). After additon of NaCl, all the

aqua adducts were coverted into **1a**, with the released ligand remaining unbound and the $[(Cp^*)Rh(D_2O)_3]^{2+}$ reacting with Cl^- to form $[(Cp^*)RhCl_2]_2$ (▲).

In contrast, after 24 h at 310 K, no apparent change was observed for millimolar solutions of the pyridine complexes **1b-3b** in d_4-MeOD/D_2O (1/9-1/2 v/v) by ^{1}H NMR (Figures A4.1-A4.3 in the **Appendix**). However, hydrolysis of micromolar concentrated complex **1b** could be observed by UV-vis spectroscopy at 310 K (Figure 4.2c).

Table 4.1. Hydrolysis data for complexes **1a-3a** and **1b-3b** at 310 K.

| Complex	Cp^X	Extent[a]	k[b] (min^{-1})	$t_{1/2}$[b] (min)
1a	Cp*	43%	0.014 ± 0.002	49.7
2a	Cp^{ph}	50%	0.026 ± 0.002	26.8
3a	Cp^{biph}	60%	0.138 ± 0.016	5.0
1b	Cp*	0%	0.019 ± 0.001	36.0
2b	Cp^{ph}	0%	0.010 ± 0.001	70.0
3b	Cp^{biph}	0%	0.007 ± 0.001	95.9

[a]: Determined by ^{1}H NMR integral of the aqua adduct at equilibrium of the corresponding complex in millimolar concentration in d_4-MeOH/D_2O. [b]: Determined by fitting the UV-vis absorption changes *versus* time to pseudo-first-order kinetics for the corresponding complex in micromolar concentration in MeOH/H_2O.

As shown in Table 4.1, the hydrolysis extent over 24 h for chloride complexes **1a-3a** was 43%-60% at equilibrium based on integration of ^{1}H NMR peaks. All the chloride complexes showed faster hydrolysis than their pyridine counterparts by UV-vis in micromolar concentrations. With the extension of Cp^* to Cp^{xph}, to Cp^{xbiph}, the hydrolysis half-lives of the chloride complexes become shorter, while the hydrolysis half-lives of the pyridine complexes become longer.

In addition, after 24 h, an additional set of peaks in *ca.* 25% by ^{1}H NMR integral was visible for complexes **1a-3a** which can be attributed to release of the benzo[h]quinoline ligand, as characterised by ^{1}H NMR (Figure 4.4), ^{1}H-^{1}H COSY (Figure 4.5) and confirmed by ESI-MS with *m/z* 180.13 (calculated *m/z* 180.08).
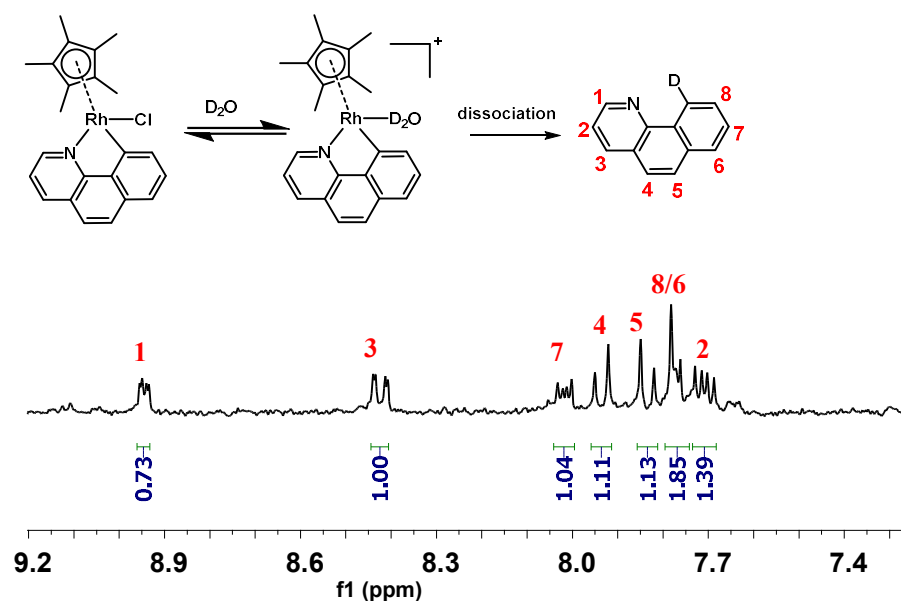
Figure 4.4. 300 MHz ^{1}H NMR spectrum of complex **1a** in d$_4$-MeOD/D$_2$O (4/1 v/v) after 72 h at 310 K showing assignments for peaks of the dissociated ligand (protons numbered as in structure).
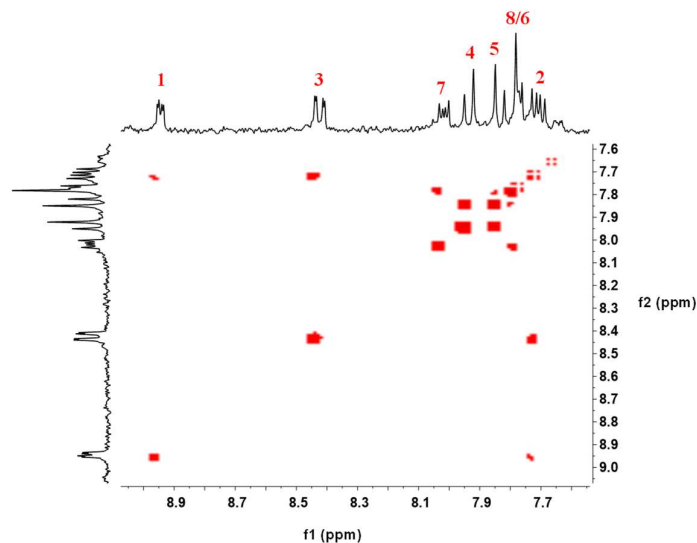
**Figure 4.5.** 500 MHz ^{1}H-^{1}H 2D COSY NMR spectrum of the aromatic region of complex **1a** in d_4-MeOD/D$_2$O (4/1 v/v) after 72 h at 310 K showing assignments of peaks for the dissociated ligand.

4.3.4 Interaction with 9-EtG

Reactions between chloride/pyridine complexes and nucleobase 9-ethylguanine (9-EtG) were studied by ^{1}H NMR spectroscopy. Equimolar 9-EtG was added to an equilibrium solution of [(Cp*)Rh(benzo[h]quinoline)Cl] (**1a**) in d_4-MeOD/D$_2$O (4/1, v/v, pH* 7.4) and the ^{1}H NMR spectra showed that *ca.* 90 % of **1a** had rapidly formed adducts with 9-EtG (within 20 min) based on the integral of the Cp* protons of **1a** (δ 1.71 ppm), aqua adducts of **1a** (δ 1.68 ppm) and 9-EtG adducts (δ 1.66 ppm) (Figure 4.6). The new singlet peak for H8 of the bound 9-EtG appeared at 7.39 ppm, shifted by 0.37 ppm to high field relative to that of free 9-EtG. The ESI-MS of the final NMR solution showed a major peak at m/z 595.3, assignable as the adduct of **1a** with 9-EtG [(Cp*)(Rh-9-EtG)(benzo[h]quinoline)]$^+$ (calcd m/z 595.1). Meanwhile, in the

163

presence of 4 mM NaCl, **1a** still showed a high affinity for 9-EtG with *ca.* 90% **1a**

binding to 9-EtG (Figure 4.7) at 310 K. Adducts of **2a** and **3a** with 9-EtG were also

characterised by ^{1}H NMR and ESI-MS (Table 4.2).

By contrast, a ^{1}H NMR study of the pyridine complex

[(Cp*)Rh(benzo[h]quinoline)py]NO$_3$ (**1b**) with equimolar 9-EtG in d_4-MeOD/D$_2$O

(1/4, v/v, pH* 7.4) showed that only 30% of complex **1b** formed an adduct with 9-

EtG after 24 h at 310 K (Figure 4.8) based on the integral of the Cp* methyl protons

at 1.57 ppm (**1b**) and 1.56 ppm (9-EtG adduct with **1b**). This new adduct of complex

1b with 9-EtG was also confirmed by ESI-MS peak at m/z 595.3 (calcd m/z 595.1).
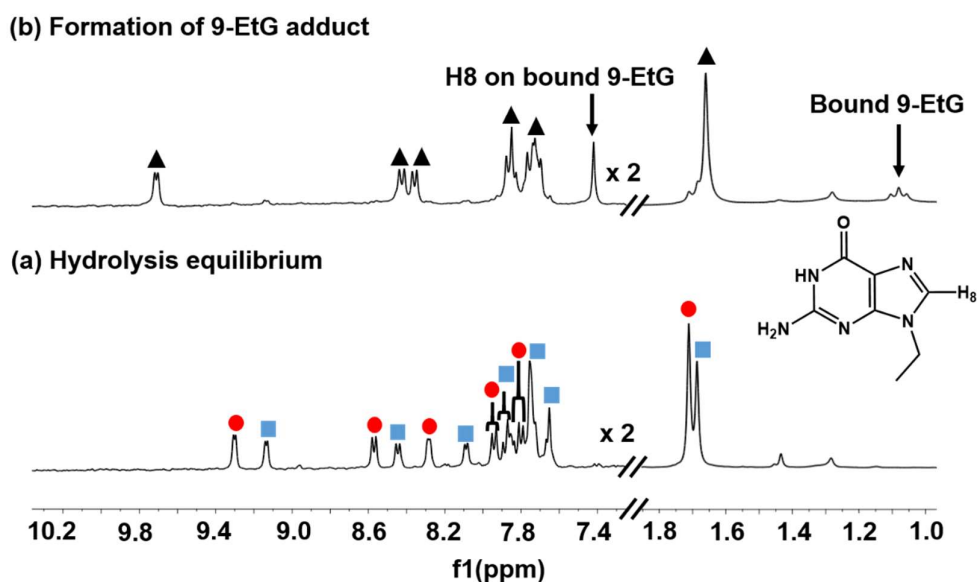
Figure 4.6. 300 MHz ^{1}H NMR spectra of (a) equilibrium solution of *ca.* 1.0 mM

complex [(Cp*)Rh(benzo[h]quinoline)Cl] (**1a**) in d$_4$-MeOD/D$_2$O (4/1 v/v, pH* 7.4),

containing both the chloride complex **1a** (■) and its aqua adduct (●). (b) 20 min after

addition of equimolar 9-EtG, *ca.* 90% of **1a** had formed an adduct (▲) with 9-EtG.
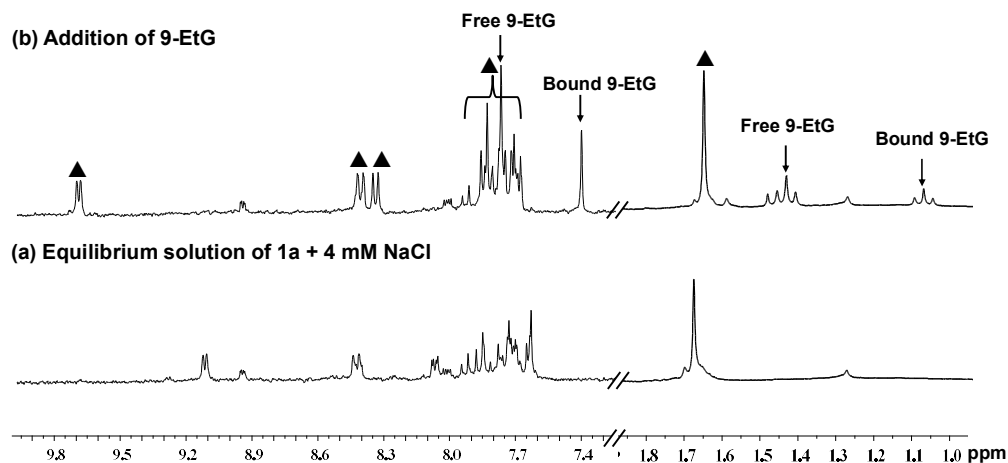
Figure 4.7. 300 MHz ^{1}H NMR spectra of (**a**) Equilibrium solution of [(Cp*)Rh(benzo[h]quinoline)Cl] (**1a**) with 4 mM NaCl in d$_4$-MeOD/D$_2$O (4/1 v/v, pH* 7.4), containing mainly the chloride complex **1a** after 24 h; (**b**) 20 min after addition of 2 mol equiv. 9-EtG, with 90% of **1a** forming the 9-EtG adduct [(Cp*)Rh(9-EtG)(benzo[h]quinoline)]$^+$ (▲).

Table 4.2. ESI-MS peaks for adducts of [(Cp^{xph})Rh(benzo[h]quinoline)Cl] (**2a**) and [(Cp^{xbiph})Rh(benzo[h]quinoline)Cl] (**3a**) with 9-EtG.

Adducts	Found *m/z*	Calculated *m/z*
[(Cp^{xph})Rh(9-EtG)(benzo[h]quinoline)]$^+$	657.3	657.1
[(Cp^{xbiph})Rh(9-EtG)(benzo[h]quinoline)]$^+$	733.3	733.2

165
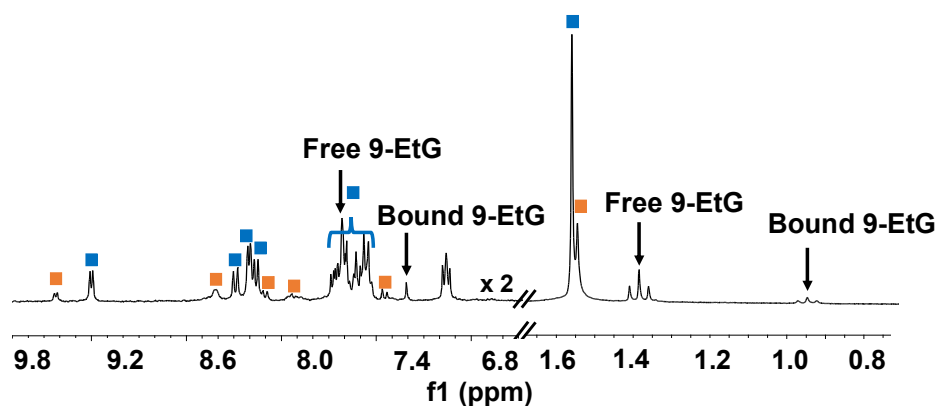
Figure 4.8. 300 MHz ^{1}H NMR spectrum of *ca.* 2.6 mM complex [(Cp*)Rh(benzo[h]quinoline)py]$^+$ (**1b**) (■) in d$_4$-MeOD/D$_2$O (v/v 1/4, pH* 7.4) with equimolar 9-EtG after 24 h at 310 K. 30% of complex **1b** formed an adduct (■) with 9-EtG.

4.3.5 Catalytic NADH Oxidation

NADH is a crucial coenzyme in numerous biological catalytic processes. Previously, it has been found that cyclopentadienyl iridium complexes bearing N^N coordinating ligands can accept hydride from NADH and induce the reduction of protons to H$_2$,[30] and quinones to semiquinones.[31] The Cp^{xbiph} iridium complex with the C^N chelating 2-phenylpyridine can also transfer hydride from NADH to oxygen to produce the reactive oxygen species (ROS) hydrogen peroxide.[26] Therefore, the time dependence of reactions between rhodium complexes (0.8 μM) and NADH (75-144 μM) was studied over 24 h in 1.6%(v/v) MeOH/98.4% phosphate buffer (5 mM, pH 7.4) by UV-vis spectroscopy at 310 K (Figures 4.9 and 4.10). The reactions proceeded via first-order kinetics (Figure 4.11).
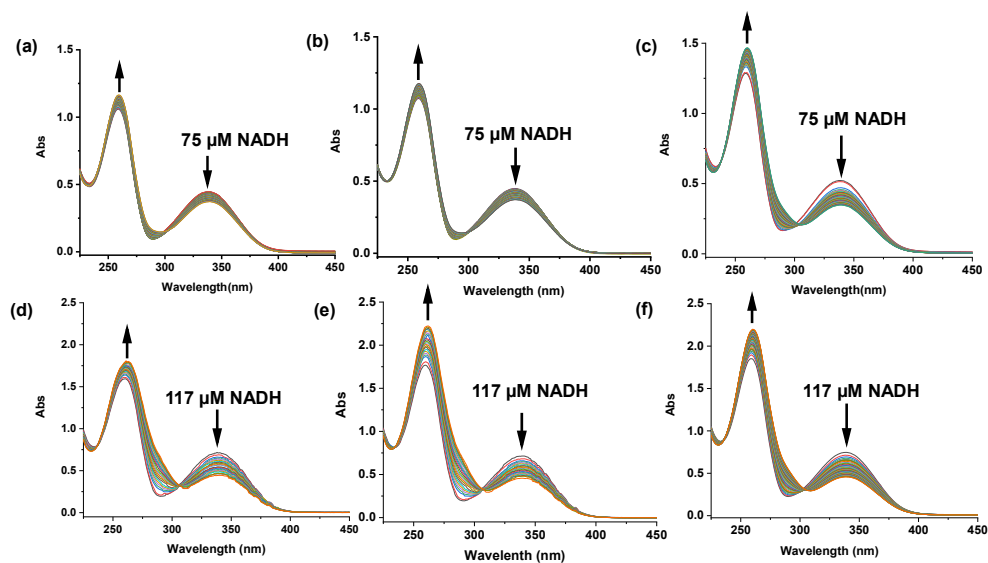
Figure 4.9. UV-vis absorption spectra recorded every hour for 75 or 117 μM NADH in the presence of 0.8 μM complex (a/d) **1a**, (b/e) **2a** and (c/f) **3a** over 24 h in 1.6 % MeOH/98.4 % 5 mM Na_2HPO_4-NaH_2PO_4 buffer (pH 7.2) at 310 K.
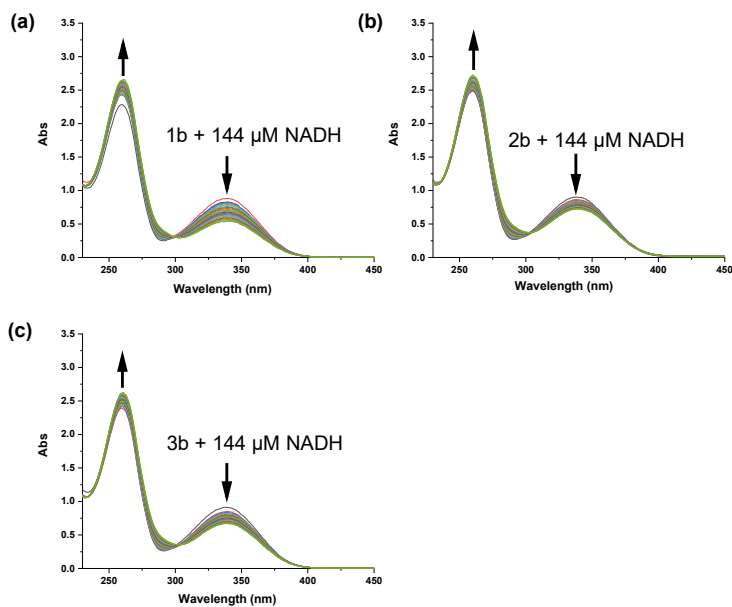
Figure 4.10. UV-vis absorption spectra recorded every hour of 144 μM NADH in the presence of 0.8 μM complex (a) **1b**, (b) **2b** and (c) **3b** over 24 h in 1.6 % MeOH/98.4 % 5 mM Na_2HPO_4-NaH_2PO_4 buffer (pH 7.2) at 310 K.
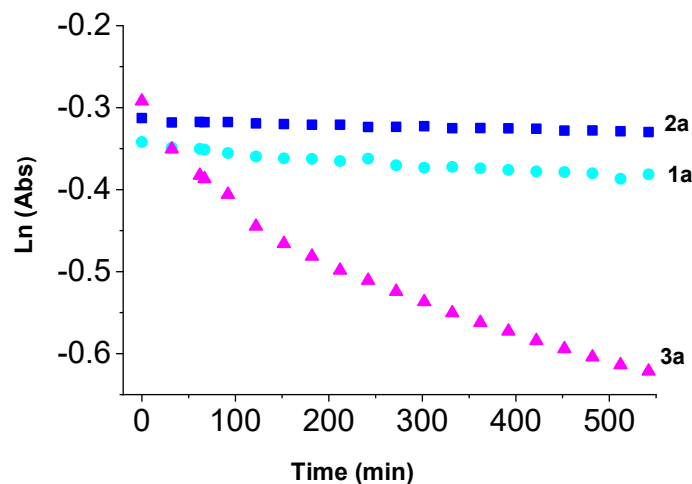
Figure 4.11. Plot of natural log absorbance (339 nm) versus time for the catalytic reaction of NADH (114 µM) by complexes **1a, 2a** and **3a** (0.8 µM) in 1.6 % MeOH/98.4 % 5 mM Na_2HPO_4-NaH_2PO_4 buffer (pH 7.4).

Table 4.3. TONs and TOFs for rhodium complexes (0.8 µM) in the catalytic oxidation of NADH to NAD^+ in 1.6% MeOH/98.4% phosphate buffer (5 mM, pH 7.4) over 24 h at 310 K.

Complex	NADH (µM)	TON	TOF (h^{-1})
1a	75	13	1.16 ± 0.06
	117	49	3.35 ± 0.11
2a	75	14	1.10 ± 0.08
	117	51	3.38 ± 0.15
3a	75	32	2.85 ± 0.12
	117	58	7.58 ± 0.20
1b	144	72	2.85 ± 0.06
2b	144	35	1.63 ± 0.02
3b	144	49	1.73 ± 0.04

The turnover number (TON) and turnover frequency (TOF) were determined based on the decrease in absorption of NADH at 339 nm due to conversion of NADH to NAD^+. In reactions with NADH at a higher concentration (144 µM), pyridine complexes **1b-3b** showed a much lower TOF than their respective chloride analogues **1a-3a** (Table 4.3). This might due to the decrease in hydrolysis of pyridine complexes compared to chloride analogues, as hydrolysis is likely to be the first step in interaction with NADH.[26] In the presence of 75 µM or 117 µM NADH, respectively, complex **3a** bearing a Cp^{biph} ring showed a *ca.* 2.6 x or *ca.* 2.3 x higher TOF than the other chloride complexes **1a** and **2a**. In contrast, in the presence of 144 µM NADH, pyridine complex **1b**, which has the fastest hydrolysis rate among all these pyridine complexes, exhibited the highest TON (72) and TOF (2.85 h^{-1}). Furthermore, hydrogen peroxide was detected (appearance of blue colour on Quantofix test sticks) in the reaction mixture of complex **3a** (*ca.* 1 mM) with 3.5 mol equiv. NADH in MeOH/H_2O (1/1 v/v) after 24 h at 310 K (Figure 4.12).
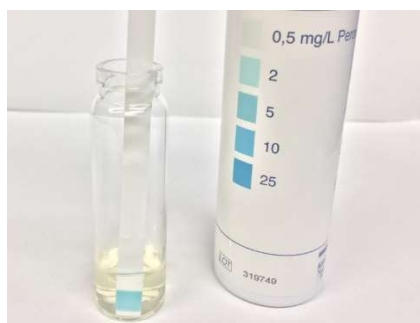
Figure 4.12. Detection of H_2O_2 by Quantofix sticks (blue colour) for reaction of complex **3a** (*ca.* 1 mM) with 3.5 mol equiv. NADH in MeOH/H_2O (1/1 v/v) after 24 h at 310 K.

4.3.6 Sodium Formate as Hydride Donor

Half-sandwich rhodium(III) complexes with N^N chelating ligands can act as transfer hydrogenation catalysts using sodium formate as a hydride source and convert pyruvate to lactate.[27] The ability of complex $[(Cp^*)Rh(benzo[h]quinoline)Cl]$ (**1a**) to reduce pyruvate to lactate was investigated. Upon addition of 10 mol equiv. sodium formate to a solution of **1a** in d_4-MeOD/H_2O (99/1 v/v), the colour turned from orange to red. In the hydride region, a doublet appeared at -12.25 ppm ($J(^1H\text{-}^{103}Rh) = 32$ Hz, Figure 4.13) which can be assigned to the hydride complex $[(Cp^*)Rh(benzo[h]quinoline)H]$ in accord with the reported J value[32] for the same Rh-H species. Meanwhile, a triplet at -19.33 ppm ($J = 24$ Hz) was also observed in Figure 4.13. The J value of this triplet is characteristic of hydride bridging two Rh(III) centres,[33] suggesting a possible nucleophilic attack of the Rh-H bond on the labile coordination site occupied by MeOD or H_2O on another Rh molecule.
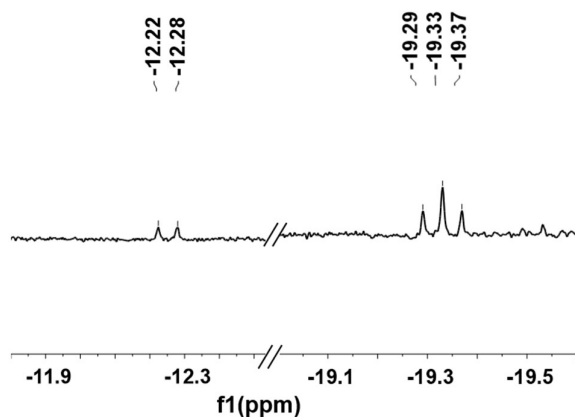
Figure 4.13. 600 MHz ^1H NMR spectrum of a solution containing 10 mol equiv. sodium formate and **1a** in d_4-MeOD/H_2O (v/v 99/1) showing the formation of Rh-

hydride species in the enlarged box with a doublet at δ = -12.25 ppm and a triplet at

δ = -19.33 ppm.

Subsequently, when 5 mol equiv. pyruvate was added to this Rh-hydride solution, *ca.* 17% pyruvate (δ 2.36 ppm, singlet) was reduced to lactate (δ 1.32 ppm, doublet) based on ^{1}H NMR peak integrals over 24 h at 310 K (Figure 4.14).
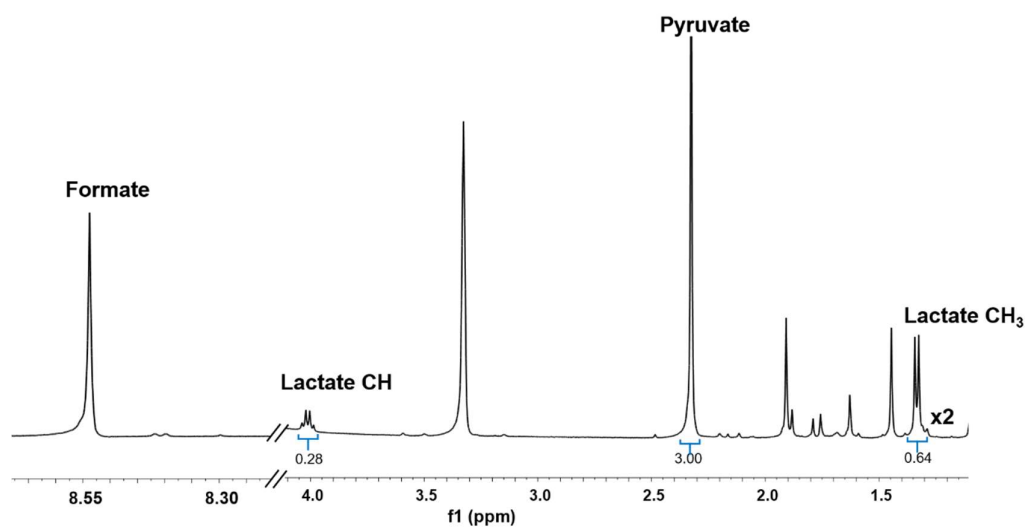
Figure 4.14. 400 MHz ^{1}H NMR spectrum after addition of 5 mol equiv. pyruvate to the rhodium hydride [(Cp*)Rh(benzo[h]quinoline)H] solution in d$_4$-MeOD/H$_2$O (v/v 99/1) at 310 K showing *ca.* 17% pyruvate (δ 2.36 ppm, singlet) was reduced to lactate (δ 1.32 ppm, doublet) over 24 h.

4.3.7 Reactivity with GSH

The abundant cellular tripeptide glutathione (GSH) is a detoxification agent and ROS scavenger. Reactions of [(Cp^{xbiph})Rh(benzo[h]quinoline)Cl] (**3a**) or the pyridine

analogue [(Cp^{xbiph})Rh(benzo[h]quinoline)py]$^+$ (**3b**) with GSH was investigated. LC-MS analysis of **3b** with 2 mol equiv. GSH in MeOH/H$_2$O (1/9 v/v) revealed that most of the parent complex **3b** remained intact within the first 30 min, but after 18 h, **3b** was converted into dinuclear [(Cp^{xbiph}Rh)$_2$(μ-SG)$_3$]$^+$ adducts (Figure 4.15). However, under the same conditions, the chloride complex **3a** formed [(Cp^{xbiph})Rh(SG)+H]$^+$ as detected by ESI-MS with m/z 683.6 (calcd 683.6) as soon as it was mixed with GSH. These differences in reactions with GSH may have a significant effect on the anticancer activity of these two complexes.

Peaks assigned	Found *m/z*	Calculated *m/z*
[1]: [GSH+H]$^+$	307.79	308.09
[2]: {(free benzo[h]quinoline)+H}$^+$	179.71	180.08
[3]: {[(Cp^{xbiph})$_2$Rh$_2$(μ-SG)$_3$]+H}$^{2+}$	835.58	835.18
[4]: {(Cp^{xbiph})(Rh-SG)(benzo[h]quinoline)]+H}$^{2+}$	429.86	430.60
[5]: [Cp^{xbiph}Rh(benzo[h]quinoline)]$^+$	553.97	554.13
[6]: [Cp^{xbiph}Rh(benzo[h]quinoline)py]$^+$	633.05	633.17
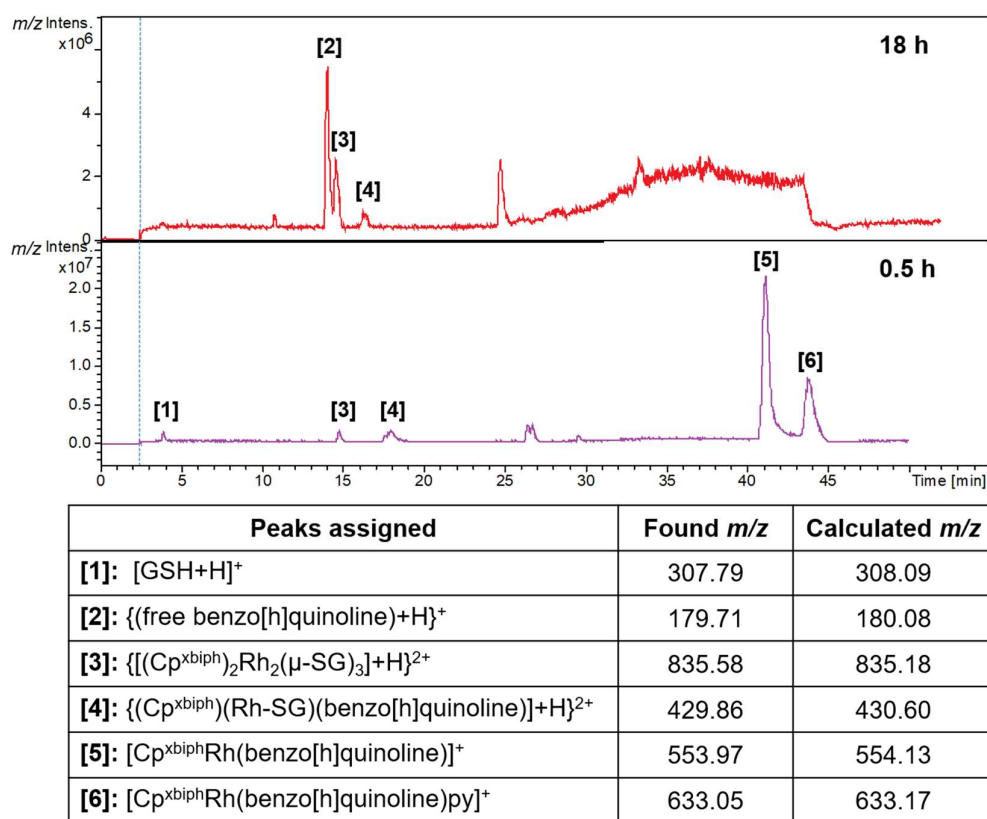
Figure 4.15. ESI-MS traces in LC-MS analyses for the reaction mixture of **3b** (*ca.* 100 μM) with 2 mol equiv. GSH in MeOH/H$_2$O (1/9) at 298 K after 30 min and 18 h

with the detected ESI-MS peaks assigned in the table. Mobile phases: A-water (0.1% v/v TFA) and B-acetonitrile (0.1% v/v TFA) with detection wavelength at 254 nm

4.3.8 Cytotoxicity

The anticancer activity of rhodium complexes against human A549 lung and A2870 ovarian cancer cell lines was evaluated *in vitro* using SRB assay after 24 h treatment and subsequent 72 h of cell recovery. The detailed half maximal inhibitory concentration (IC_{50}) values are listed in Table 4.4 and are shown in Figure 4.16.
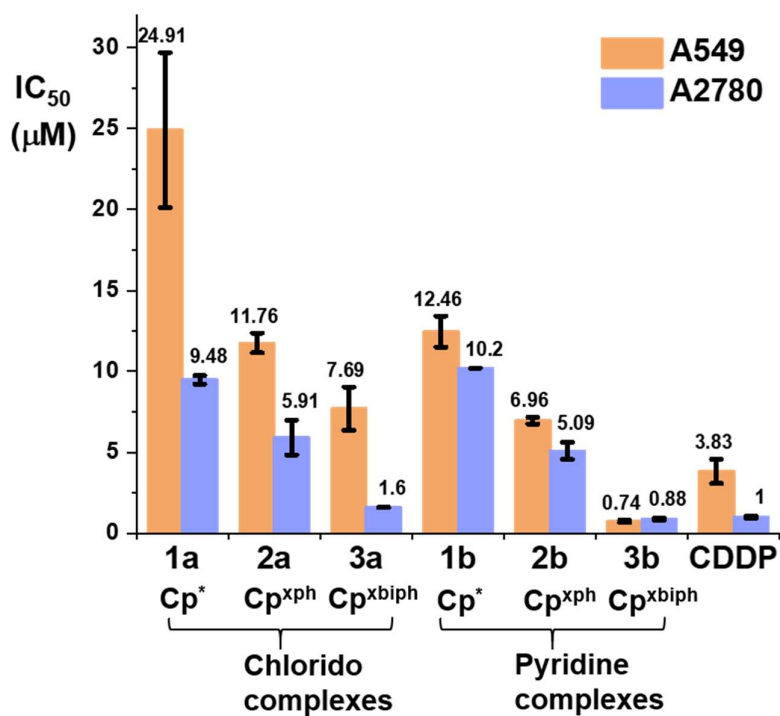
Figure 4.16. Anticancer activity of rhodium complexes towards human A549 lung and A2780 ovarian cancer cells in comparison with cisplatin (CDDP). The values of half maximal growth inhibitory concentration (IC_{50}) are given as the mean ± standard deviations for three independent experiments.

Table 4.4. Values of $IC_{50} \pm$ mean SD for six rhodium complexes toward human A549 lung and A2780 ovarian cancer cells in comparison with cisplatin (CDDP). IC_{50}: Half maximal inhibitory concentrations determined from three independent experiments.

Complex	IC_{50} (μM)	
	A549	A2780
1a	24.91 ± 4.80	9.48 ± 0.26
2a	11.76 ± 0.61	5.91 ± 1.08
3a	7.69 ± 1.34	1.60 ± 0.01
1b	12.46 ± 0.96	10.20 ± 0.001
2b	6.96 ± 0.21	5.09 ± 0.53
3b	0.74 ± 0.07	0.88 ± 0.07
Cisplatin	3.83 ± 0.74	1.00 ± 0.06

Compared to cisplatin (CDDP) as the positive control, chloride complexes **1a-3a** and pyridine complexes **1b-2b** all showed antiproliferative activity towards these two cell lines. In particular, the pyridine complex [(Cp^{xbiph})Rh(benzo[h]quinoline)py]NO$_3$ (**3b**) exhibited the highest activity among all screened rhodium complexes, with *ca.* 5x greater potency ($IC_{50} = 0.74$ μM) than cisplatin ($IC_{50} = 3.83$ μM) against A549 lung cancer cells.

From the study of cyclopentadienyl iridium complexes with the C^N chelating ligand 2-phenylpyridine, the extension of Cp^X ring (from Cp* to Cp^{xph} to Cp^{xbiph}) significantly enhanced the anticancer activity perhaps due to the increased hydrophobicity facilitating passage through the cell membrane or to the extended phenyl or biphenyl ring which can intercalate between DNA bases.[34] Among the Cp^X analogues, Cp^{xbiph} capped complexes **3a** and **3b** were

the most hydrophobic and exhibited the highest potency as expected. Moreover, pyridine complex **3b** was *ca.* 2x and ca. 10x more potent than its chloride analogue **3a** towards A2780 and A549 cancer cells, respectively (A2780: IC$_{50}$ 0.88 µM for **3b** and 1.60 µM for **3a**; A549: IC$_{50}$ 0.74 µM for **3b** and 7.69 µM for **3a**). Therefore, despite the replacement of the chloride with pyridine decreasing hydrolysis, inhibiting adduct formation with 9-EtG/GSH and lowering the catalytic TOF, the *in vitro* anticancer activity of pyridine complexes was higher than that of chloride analogues, in line with the behaviour of cyclometalated iridium pyridine complexes which showed slower hydrolysis/less interaction with biomolecules, but higher potency than their chloride analogues.[26]

4.3.9 Cellular Rh Accumulation

Complexes [(Cp^{xbiph})Rh(benzo[h]quinoline)Cl] (**3a**) and [(Cp^{xbiph})Rh(benzo[h]quinoline)py]NO$_3$ (**3b**) bearing the Cp^{xbiph} ring, were the most potent candidates among the chloride family (**1a-3a**) and pyridine family (**1b-3b**). However, positively charged complex **3b** is 10 x more potent than neutral complex **3a** towards A549 cancer cells (Figure 4.16). Thus, to elucidate their different anticancer activities, the cellular accumulation of rhodium in A549 human lung cancer cells after 24 h treatment with complexes **3a** and **3b** at equipotent concentrations of 0.5 x and 1 x IC$_{50}$ at 310 K was quantified by ICP-MS as shown in Figure 4.17 (values in Table 4.5). From Figure 4.17, the accumulation of Rh in the cells treated with complex **3a** or **3b** increased in a concentration-dependent manner. After 24 h the cellular Rh accumulation of chloride complex **3a** was *ca.* 49-fold (at

0.5x IC_{50}) and *ca.* 59-fold (at 1x IC_{50}) higher than that of complex **3b**. This significant difference correlates with the higher hydrophobicity of neutral complex **3a** compared to the positively charged complex **3b**, in contrast to the reported cyclometalated iridium complex $[(Cp^{xbiph})Ir(2\text{-phenylpyridine})py]^+$ which was found to have 20-fold higher Ir accumulation than the neutral complex $[(Cp^{xbiph})Ir(2\text{-phenylpyridine})Cl]$ in A2780 cancer cells.[26]
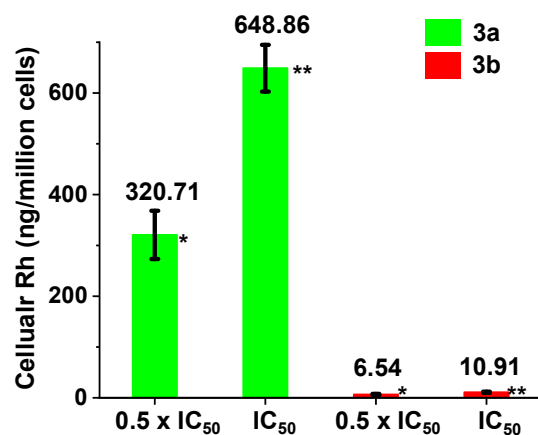
Figure 4.17. Accumulation of Rh (ng/million cells) in A549 human lung cancer cells after 24 h treatment with chloride complex **3a** or pyridine complex **3b** at concentrations of 0.5x IC_{50} and 1x IC_{50}. The values represent mean ± standard deviations for three independent samples. The asterisk denotes the *p*-values obtained by comparing each dataset with the negative control (untreated cells) using a t-test, *p < 0.05, **p < 0.01.

Table 4.5. Accumulation of Rh (ng/million cells) in human A549 lung cancer cells after 24 h treatment without recovery for complexes **3a** and **3b** at concentrations of 0.5x and 1x IC_{50}.

Treatment (dose)	3a		3b		Untreated
	0.5x IC_{50}	IC_{50}	0.5x IC_{50}	IC_{50}	
Rh (ng/10^6 cells)	320.7 ± 47.5	648.9 ± 46.1	6.54 ± 1.20	10.91 ± 1.12	0.006 ± 0.002

4.3.10 ROS Induction

Whether a high level of reactive oxygen species (ROS) in A549 human lung cancer cells is induced after 24 h treatment by complexes $[(Cp^{xbiph})Rh(benzo[h]quinoline)Cl]$ (**3a**) and $[(Cp^{xbiph})Rh(benzo[h]quinoline)py]NO_3$ (**3b**) at concentrations of IC_{50} or 2x IC_{50} was investigated by flow cytometry (Figure 4.18, details in Table 4.6). The experiments were conducted by Hannah E. Bridgewater

Table 4.6. ROS induction in A549 cancer cells treated with complexes **3a** and **3b**. FL1 channel detects total oxidative stress and FL2 channel detects superoxide production.

Cell populations (%)	Treatment (dose)				
	Untreated	3a		3b	
		1x IC_{50}	2 x IC_{50}	1x IC_{50}	2 x IC_{50}
FL1-/FL2+	0.317 ± 0.175	0.005 ± 0.008	0.022 ± 0.027	0.038 ± 0.036	0.240 ± 0.036
FL1+/FL2+	19.11 ± 0.46	18.87 ± 2.52	47.39 ± 2.05	22.33 ± 1.82	10.30 ± 0.30
FL1+/FL2-	74.95 ± 0.31	70.09 ± 2.16	46.10 ± 2.17	59.96 ± 1.95	38.01 ± 0.17
FL1-/FL2-	5.67 ± 0.35	11.04 ± 0.37	6.49 ± 0.11	17.67 ± 0.20	51.45 ± 0.16
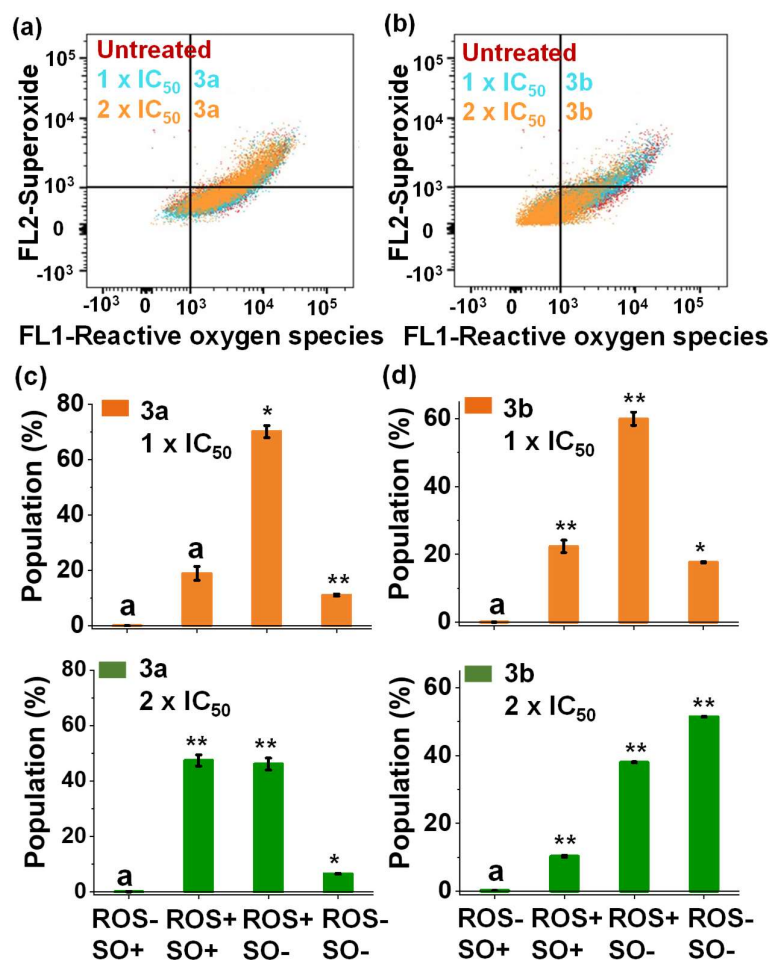
Figure 4.18. Flow cytometry plots of total ROS and superoxide production after 24 h treatment with 1× and 2× IC_{50} concentrations of complexes (a) **3a** and (b) **3b**. Cell population of total ROS and superoxide production after 24 h treatment with 1× and 2× IC_{50} concentrations of complexes (c) **3a** and (d) **3b**. The values represent mean ± standard deviations for three independent samples. The asterisk denotes the *p*-values obtained by comparing each dataset with the negative control (untreated cells) using a t-test, *$p < 0.05$, **$p < 0.01$, ᵃ$p > 0.05$.

This assay not only allowed determination of the level of total ROS consisting of H_2O_2, peroxy and hydroxyl radicals, peroxynitrite, and NO species,

but also the level of superoxide (SO). After 24 h drug treatment, a concentration-dependent ROS level modulation indicated by the fluorescence signals of FL1 (indicating the total ROS level) and FL2 (indicating the SO level) channels was observed: in cells treated with complex **3a**, the ROS+/SO+ cell population increased significantly from 18 ± 2 % at IC_{50} concentration to 47 ± 2 % at 2 x IC_{50} concentration of complex. In contrast, for cells treated with complex **3b**, the cell population producing ROS decreased significantly from 60 ± 2 % (ROS+/SO-)/22 ± 2 % (ROS+/SO+) by IC_{50} concentration treatment to 38 ± 0.1 (ROS+/SO-)/10 ± 0.3 (ROS+/SO+) by 2 x IC_{50} concentration treatment, combined with an increase in the quadrant of ROS-/SO- from 17 ± 0.2 % to 51 ± 0.2 (Figure 4.18, Table 4.6). This observation suggested opposing mechanisms of action for the two complexes: complex **3a** inducing ROS formation, complex **3b** acting as a ROS scavenger.

4.3.11 Apoptosis Assay

Apoptosis is well recognized as a distinct cell death mechanism in tumours responding to anticancer therapies.[35] To investigate whether apoptosis is involved in the anticancer mechanism of action, A549 cells were treated with $[(Cp^{xbiph})Rh(benzo[h]quinoline)Cl]$ (**3a**) and $[(Cp^{xbiph})Rh(benzo[h]quinoline)py]NO_3$ (**3b**) at their equipotent concentrations of IC_{50} and 2x IC_{50} for 24 h, then stained with FITC labelled-annexin V/propidium iodide (PI) and analysed by flow cytometry. The experiments were conducted by Hannah E. Bridgewater. This assay determined cell populations as early apoptosis (annexin V+/PI-, stained by annexin V only), late apoptosis (annexin V+/PI+, stained by annexin V and PI), necrosis (annexin V-/PI+,

stained by PI only), and viable (annexin V-/PI-, unstained by annexin V and PI). No obvious induction of apoptosis by complex **3a** or **3b** was observed at their equipotent concentrations (Figure A4.4 in the **Appendix**). However, there was a significant increase in necrotic cell population induced by the treatment with complex **3b** at 2 x IC$_{50}$ concentration (Table A4.3 in the **Appendix**).

4.4 Conclusions

In summary, the synthesis and characterisation of novel cyclopentadienyl C^N chelated Rh^{III} anticancer complexes [(Cp^X)Rh(C^N)Z]$^{0/+}$ have been achieved, in which Cp^X = Cp*, Cp^{xph}, or Cp^{xbiph}, C^N = benzo[h]quinoline, and Z = chloride or pyridine. Three X-ray crystal structures have been determined showing the expected "piano-stool" configurations.

The reactivity and cytotoxicity of these complexes can be rationally modulated by selection of the monodentate ligand as chloride or pyridine. The chlorido complexes are more labile toward hydrolysis (43%-60% *versus* 0% by ^{1}H NMR integral) in millimolar concentrations, react with 9-ethylguanine to a large extent (90% *versus* 30%), and react faster with glutathione (within mins) compared to their pyridine analogues. The hydrolysis rate determined by UV-vis spectroscopy for chloride complexes increases in the order Cp* < Cp^{xph} < Cp^{xbiph}, showing that incorporation of the extended Cp^X ring confers more labile kinetics on the monodentate chloride ligand. On the contrary, when the chloride is replaced with pyridine, the rate of hydrolysis determined by UV-vis spectroscopy is decreased by

orders of magnitude in the order $Cp^{xbiph} > Cp^{xph} > Cp^*$. This difference in hydrolysis kinetics for the chloride and pyridine complexes leads to the differences in their reactivity, and subsequent differences in cytotoxicity. For example, chlorido complex $[(Cp^{xbiph})Rh(benzo[h]quinoline)Cl]$ (**3a**) shows the greatest catalytic efficiency in NADH oxidation and induces a remarkable increase in the level of ROS in lung cancer cells which might contribute to the cytotoxicity. The pyridine analogue $[(Cp^{xbiph})Rh(benzo[h]quinoline)py]^+$ (**3b**) is 10-fold more active than **3a** and 5-fold more active than cisplatin towards A549 cells, although its catalytic turnover frequency is a 4.5-fold lower than TOF of **3a** and acts as a ROS scavenger.

The pyridine complex **3b** reacts more slowly with glutathione (after half hour) than the chloride analogue **3a** (within minutes), which would result in less cellular deactivation, thus making **3b** 10x more potent than **3a** towards lung cancer cells. Meanwhile, the Rh accumulation in lung cancer cells treated with complex **3b** is 59-fold less than that with **3a** at equipotent IC_{50} concentrations, suggesting that **3b** requires a lower dose than **3a** to achieve the same therapeutic potency. Furthermore, **3b** acts as a ROS scavenger, which is distinct from the similar pyridine iridium complex $[(Cp^{xbiph})Ir(2-phenylpyridine)py]^+$ inducing a higher level of ROS in ovarian cancer cells.[26] Although the reason of its ROS scavenging activity is not clear, pyridine complex **3b** is the first example of an organometallic rhodium complex with such a behaviour. The cyclometalated rhodium complexes such as these may provide a new generation of transition metal-based chemotherapeutic agents and are worthy of further investigation.

4.5 References

1   P. Zhang and P. J. Sadler, *J. Organomet. Chem.*, 2017, **839**, 5-14.

2   N. Shah and D. S. Dizon, *Future Oncol.*, 2009, **5**, 33-42.

3   S. Dasari and P. B. Tchounwou, *Eur. J. Pharmacol.*, 2014, **740**, 364-378.

4   M. Hanif and C. G. Hartinger, *Future Med. Chem.*, 2018, **10**, 615-617.

5   C.-H. Leung, H.-J. Zhong, D. S.-H. Chan and D.-L. Ma, *Coord. Chem. Rev.*, 2013, **257**, 1764-1776.

6   Y. Geldmacher, M. Oleszak and W. S. Sheldrick, *Inorg. Chim. Acta*, 2012, **393**, 84-102.

7   G. Gasser, I. Ott and N. Metzler-Nolte, *J. Med. Chem.*, 2010, **54**, 3-25.

8   Z. Liu and P. J. Sadler, *Acc. Chem. Res.*, 2014, **47**, 1174-1185.

9   M. Doerr and E. Meggers, *Curr. Opin. Chem. Biol.*, 2014, **19**, 76-81.

10   S. Mollin, R. Riedel, K. Harms and E. Meggers, *J. Inorg. Biochem.*, 2015, **148**, 11-21.

11   M. A. Scharwitz, I. Ott, Y. Geldmacher, R. Gust and W. S. Sheldrick, *J. Organomet. Chem.*, 2008, **693**, 2299-2309.

12   N. Cutillas, G. S. Yellol, C. de Haro, C. Vicente, V. Rodríguez and J. Ruiz, *Coord. Chem. Rev.*, 2013, **257**, 2784-2797.

13   I. Omae, *Coord. Chem. Rev.*, 2014, **280**, 84-95.

14   D.-L. Ma, M. Wang, Z. Mao, C. Yang, C.-T. Ng and C.-H. Leung, *Dalton Trans.*, 2016, **45**, 2762-2771.

15   H. Liang, T. Hao, C. Yin, X. Yang, H. Fu, X. Zheng, R. Li, D. Xiao and H. Chen, *Eur. J. Inorg. Chem.*, 2017, **2017**, 4149-4157.

16   A. Gilewska, B. Barszcz, J. Masternak, K. Kazimierczuk, J. Sitkowski, J. Wietrzyk and E. Turlej, *JBIC, J. Biol. Inorg. Chem.*, 2019, **24**, 591-606.

17   J. Markham, J. Liang, A. Levina, R. Mak, B. Johannessen, P. Kappen, C. J. Glover, B. Lai, S. Vogt and P. A. Lay, *Eur. J. Inorg. Chem.*, 2017, **2017**, 1812-1823.

18   W. Su, Z. Luo, S. Dong, X. Chen, J.-a. Xiao, B. Peng and P. Li, *Photodiagn. Photodyn. Ther.*, 2019, **26**, 448-454.

19   T. Stringer, D. R. Melis and G. S. Smith, *Dalton Trans.*, 2019, **48**, 13143-13148.

20   G. Gupta, P. Kumari, J. Y. Ryu, J. Lee, S. M. Mobin and C. Y. Lee, *Inorg. Chem.*, 2019, **58**, 8587-8595.

21   W. D. J. Tremlett, K. K. H. Tong, T. R. Steel, S. Movassaghi, M. Hanif, S. M. F. Jamieson, T. Söhnel and C. G. Hartinger, *J. Inorg. Biochem.*, 2019, **199**, 110768.

22   J. P. Mészáros, J. M. Poljarevic, G. T. Gál, N. V. May, G. Spengler and É. A. Enyedy, *J. Inorg. Biochem.*, 2019, **195**, 91-100.

23   R. Pettinari, F. Marchetti, C. Di Nicola and C. Pettinari, *Eur. J. Inorg. Chem.*, 2018, **2018**, 3521-3536.

24   Z. Liu, L. Salassa, A. Habtemariam, A. M. Pizarro, G. J. Clarkson and P. J. Sadler, *Inorg. Chem.*, 2011, **50**, 5777-5783.

25   V. Novohradsky, Z. Liu, M. Vojtiskova, P. J. Sadler, V. Brabec and J. Kasparkova, *Metallomics*, 2014, **6**, 682-690.

26   Z. Liu, I. Romero-Canelón, B. Qamar, J. M. Hearn, A. Habtemariam, N. P.

Barry, A. M. Pizarro, G. J. Clarkson and P. J. Sadler, *Angew. Chem. Int. Ed.*, 2014, **53**, 3941-3946.

27   J. J. Soldevila-Barreda, A. Habtemariam, I. Romero-Canelón and P. J. Sadler, *J. Inorg. Biochem.*, 2015, **153**, 322-333.

28   S. Banerjee, J. J. Soldevila-Barreda, J. A. Wolny, C. A. Wootton, A. Habtemariam, I. Romero-Canelón, F. Chen, G. J. Clarkson, I. Prokes, L. Song, P. B. O'Connor, V. Schünemann and P. J. Sadler, *Chem. Sci.*, 2018, **9**, 3177-3185.

29   L. Li, W. W. Brennessel and W. D. Jones, *J. Am. Chem. Soc.*, 2008, **130**, 12414-12419.

30   S. Betanzos-Lara, Z. Liu, A. Habtemariam, A. M. Pizarro, B. Qamar and P. J. Sadler, *Angew. Chem. Int. Ed.*, 2012, **51**, 3897-3900.

31   Z. Liu, R. J. Deeth, J. S. Butler, A. Habtemariam, M. E. Newton and P. J. Sadler, *Angew. Chem. Int. Ed.*, 2013, **52**, 4194-4197.

32   Y. Hu, L. Li, A. P. Shaw, J. R. Norton, W. Sattler and Y. Rong, *Organometallics*, 2012, **31**, 5058-5064.

33   Y. Hu and J. R. Norton, *J. Am. Chem. Soc.*, 2014, **136**, 5938-5948.

34   Z. Liu, A. Habtemariam, A. M. Pizarro, G. J. Clarkson and P. J. Sadler, *Organometallics*, 2011, **30**, 4702-4710.

35   D. E. Fisher, *Cell*, 1994, **78**, 539-542.

Chapter 5

Conjugation of Half-sandwich Iridium(III) Anticancer Complexes to Targeting Peptides via Copper-Free Click Chemistry

This Chapter is based on the published paper "Strategies for conjugating iridium(III) anticancer complexes to targeting peptides via copper-free click chemistry" by Wen-Ying Zhang, Samya Banerjee, Cinzia Imberti, Guy J. Clarkson, Qian Wang, Qian Zhong, Lawrence S. Young, Isolda Romero-Canelón, Musheng Zeng, Abraha Habtemariam, and Peter J. Sadler. *Inorg. Chim. Acta*, 2020, **503**, 119396. X-ray crystallographic data were analysed by Dr. Guy Clarkson. All the other experimental data collection and analysis were carried out by the author.

5.1 Introduction

To reduce the toxic side effects and circumvent intrinsic or acquired resistance of the widely used clinical anticancer drug cisplatin,[1-4] new transition metal-based anticancer agents are urgently needed.[5-8] Low-spin $5d^6$ organoiridium(III) complexes have attracted wide attention.[9,10] Especially promising are half-sandwich iridium complexes $[(\eta^5\text{-Cp}^*)\text{Ir(XY)Cl}]^+$ (where Cp^* is pentamethylcyclopentadienyl and XY is a chelating ligand) which have emerged as potential next-generation anticancer agents with novel redox-mediated mechanisms of action to overcome platinum resistance.[11,12] The carbon-bound Cp^* ligand forms highly stable iridium(III) complexes.[13-15] It has been reported that phenyl or biphenyl substituents on the Cp^* ring, or a switch of the chelating ligand from N^N to C^N mode can have pronounced effects on the anticancer activity. Meanwhile, the iridium centre can catalyse hydride transfer from NADH to molecular oxygen, generating hydrogen peroxide in cancer cells to trigger cell death.[11,16] However, achieving selectivity toward tumour cells over normal cells for half-sandwich iridium complexes is still challenging and worthy of further investigation.[17-20]

Ruiz *et al.* have designed a half-sandwich Cp^* iridium steroid hormone conjugate targeted to steroidal receptors, which displayed 6-fold and 2-fold greater potency than cisplatin and a non-steroidal analogue, respectively.[21] Recently, Liu *et al.* have further developed a series of half-sandwich iridium anticancer complexes with lysosome-targeting properties.[22] In addition, Perrier *et al.* have used a cyclic peptide-polymer nanotube to deliver a Cp^* iridium anticancer complex, with

remarkable selectivity toward cancer cells as well as higher activity toward human ovarian cancer cells compared to the free iridium complex.[23]

Tumour-targeting peptides can also be used as vectors[24] and have the potential to provide alternative efficient therapeutic benefit over the drug on its own.[25] The sequence RWY (Arg–Trp–Tyr) within the cyclic peptide of sequence c(CRWYDENAC) has a high affinity and specificity for the integrin α6 receptor on the surface of nasopharyngeal carcinoma.[26] Conjugation of this peptide to the periphery of a Pt[IV] prodrug encapsulated in nanoparticles has resulted in a 100-fold increase of cytotoxicity over free cisplatin *in vitro*.[26] Furthermore, photoactive Pt[IV] prodrugs conjugated to this cyclic peptide exhibit higher photocytotoxicity and cellular Pt accumulation than the parent complex upon light irradiation.[27]

However, it is well known that peptides with specific amino acid residues such as histidine, cysteine, tryptophan, and glutamic acid are natural chelating ligands for metal ions.[28,29] Conventional peptide conjugation methods suffer from poor site-specificity and heterogeneous products related to the ratios of conjugation sites. To improve the site-specific conjugation as well as batch-to-batch reproducibility, ''click'' chemistry has proved to be a highly successful tool.[30-32] While the classic click Cu(I)-catalysed azide-alkyne cycloadditions have been a benchmark in many areas of recent synthetic chemistry, side reactions and toxicity of the copper catalyst often limit its utilization in biological applications.[33,34] By replacing terminal alkynes with strain-promoted cycloalkynes, copper-free azide-alkyne cycloadditions can be achieved under mild conditions without disrupting the function of the biomolecules, including selective derivatization of proteins, sugars, lipids, DNA and RNA.[35] The

simplicity and orthogonality of strain-promoted azide-alkyne cycloadditions, have been widely used in a bioorthogonal fashion at the level of living cells as well as multicellular organisms.[36-38]
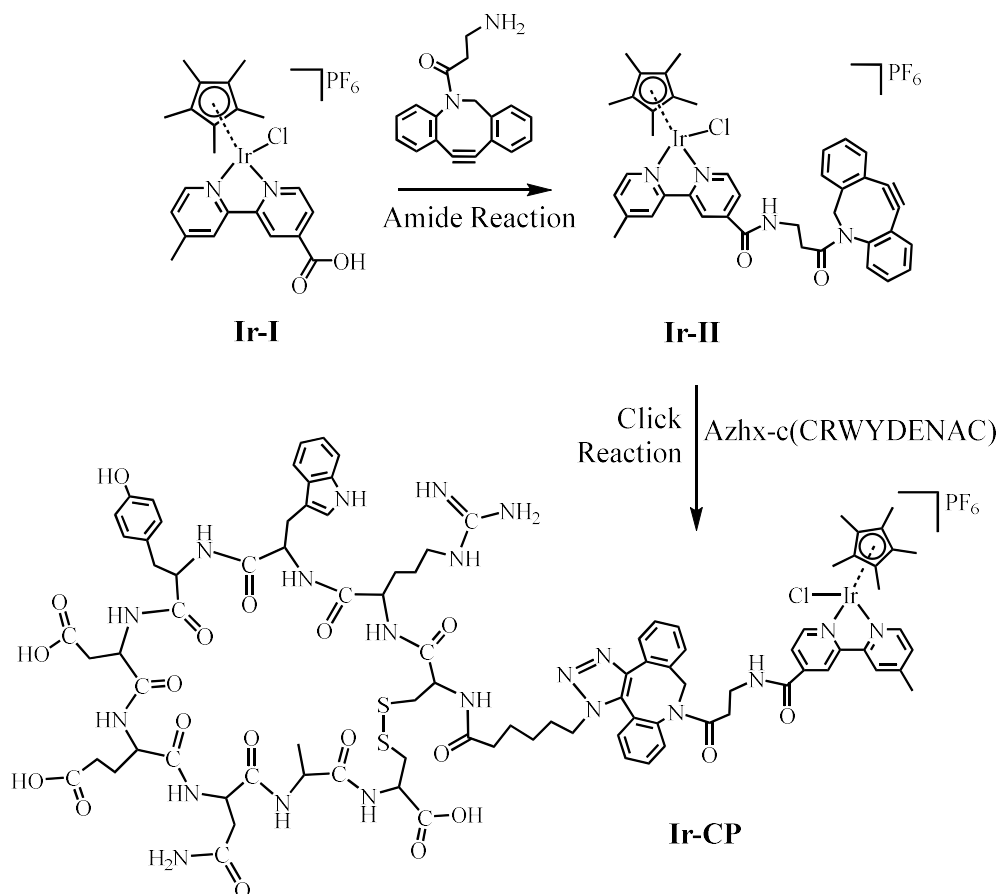
Scheme 5.1. Reaction schemes for the preparation of the clickable iridium complex (**Ir-II**) and its peptide conjugate (**Ir-CP**) in this chapter.

In this Chapter, half-sandwich iridium complex [(Cp*)Ir(4-methyl-4'-carboxy-2,2'-bipyridine)Cl]PF$_6$ (**Ir-I**) and its conjugate (**Ir-CP**) with a tumour-targeting cyclic peptide of sequence c(CRWYDENAC) are synthesised as shown in Scheme 5.1. The conjugation is achieved by an amide formation

reaction first affording the precursor complex **Ir-II** for the subsequent strain-promoted copper-free azide-alkyne cycloaddition reaction between **Ir-II** and azide functionalised-cyclic peptide to generate the final **Ir-CP** (Scheme 5.1). **Ir-I** and **Ir-II** are novel and have been characterised by ^{1}H and ^{13}C NMR, high resolution ESI-MS, HPLC and X-ray crystallography. The cytotoxicity of **Ir-I** and **Ir-II** has been screened against the human ovarian A2780 cancer cell line. The successful synthesis of the peptide conjugate **Ir-CP** has been verified by high resolution ESI-MS, HPLC, and UV-vis spectroscopy.

5.2 Experimental section

5.2.1 Materials

Dibenzocyclooctyne-amine (DBCO-NH$_2$) and 2.0 M oxalyl chloride were purchased from Sigma-Aldrich, 4,4'-Dimethyl-2,2'-bipyridine from Carbosynth, and NH$_4$PF$_6$ from Alfa Aesar. Solvents of laboratory grade were used for synthesis without any further purification. The cyclic azide-functionalized peptide Azhx-c(CRWYDENAC) was purchased from Cambridge Research Biochemicals (Billingham, UK) with a purity of >95% (HPLC/MS) with all L-configured amino acids in the sequence. The iridium dimer precursor [(Cp*)Ir(μ-Cl)Cl]$_2$ was synthesised by the described procedure in Chapter 2.

5.2.2 Synthesis

4-Methyl-4'-carboxy-2,2'-bipyridine was synthesised and characterised as the literature.[39,40]

Ir-I: [(Cp*)Ir(μ-Cl)Cl]$_2$ (39.8 mg, 0.05 mmol) was dissolved in methanol (20 mL) followed by addition of the 4-methyl-4'-carboxy-2,2'-bipyridine ligand (21.4 mg, 0.10 mmol). The mixture was stirred at 313 K overnight. The final yellow solution was filtered, concentrated and NH$_4$PF$_6$ (163 mg, 1.0 mmol) was added to the solution. This solution was kept at 277 K overnight. The yellow precipitate was collected by filtration and dried under vacuum. Yield 66 mg, 91%; ^{1}H NMR (400 MHz, d$_4$-MeOD, 298 K): δ 9.11 (d, 1H, J = 5.8 Hz), 9.00 (s, 1H), 8.81 (d, 1H, J = 5.8 Hz), 8.61 (s, 1H), 8.26 (d, 1H, J = 5.8 Hz), 7.71 (d, 1H, J = 6.1 Hz), 2.70 (s, 3H), 1.72 (s, 15H); ^{13}C{^{1}H} NMR (125 MHz, d$_4$-MeOD, 298 K): 165.79, 158.15, 155.99, 155.08, 154.10, 152.47, 143.72, 131.21, 129.19, 126.65, 124.58, 91.28, 21.39, 8.67; high resolution ESI-MS *m/z* calcd for [(M-PF$_6$-H)+Na]$^+$ 599.1040, found 599.1038. HPLC retention time 13.9 min.

Ir-II: Complex **Ir-I** (26 mg, 0.036 mmol) was dissolved in anhydrous DCM (10 mL) in a two-neck round-bottomed flask to give a clear yellow solution. Oxalyl chloride (0.5 mL 2.0 M) was injected slowly under nitrogen into the solution which was cooled over an ice bath. A catalytic amount of anhydrous DMF was then added and the solution colour changed from yellow to red due to the carboxylic acid group of complex **Ir-I** being converted to the acyl chloride. The reaction mixture was further stirred for 2 h at 298 K and the solvent was taken off under vacuum to obtain a yellow residue. In a new two-neck flask, anhydrous DCM (10 mL), TEA (0.2 mL)

and dibenzocyclooctyne-amine (DBCO-NH$_2$) (10 mg, 0.036 mmol) were added. The acid chloride was resuspended in anhydrous DCM (8 mL) and added dropwise to the ice cooled mixture in the new flask within 0.5 h. The final mixture was stirred at 298 K for 4 h under nitrogen and dark conditions. The solvent was evaporated under vacuum and the crude solid obtained was purified on an Al$_2$O$_3$ column with MeOH/DCM (1/4 v/v). Yield 23 mg, yellow solid, 65%; ^{1}H NMR (400 MHz, d$_4$-MeOD, 298 K): δ 9.09 (d, 0.5 H, J = 5.8 Hz), 9.00 (d, 0.5H, J = 5.9 Hz), 8.86 (d, 0.5H, J = 4.3 Hz), 8.83 (d, 0.5H, J = 4.2 Hz), 8.72 (s, 0.5H), 8.57 (s, 0.5H), 8.47 (s, 0.5H), 8.33 (s, 0.5H), 8.05 (d, 0.5H, J = 5.9 Hz), 7.86 (d, 0.5H, J = 5.8 Hz), 7.75-7.73 (m, 1H), 7.65 (d, 0.5H, J = 7.5 Hz), 7.62 (d, 0.5H, J = 7.6 Hz), 7.51-7.41 (m, 4H), 7.32 (t, 0.5 H, J = 7.6 Hz); 7.20 (t, 0.5 H, J = 7.4 Hz), 7.14 (t, 0.5 H, J = 7.4 Hz), 6.72-6.86 (m, 1H), 6.75 (d, 0.5H, J = 7.5 Hz), 5.13 (d, 1H, J = 14.0 Hz), 3.66 (d, 1H, J = 13.7 Hz), 3.48 (m, 2H), 2.61-2.54 (m, 1H), 2.73 (s, 1.5H), 2.72 (s, 1.5H), 2.47-2.39 (m, 1H), 1.73 (s, 15 H); ^{13}C{^{1}H} NMR (125 MHz, d$_4$-MeOD, 298 K): 173.35, 164.65, 156.07, 154.87, 153.72, 152.75, 152.58, 149.52, 145.82, 133.59, 131.27, 130.56, 130.22, 129.91, 129.07, 128.37, 127.97, 127.46, 126.47, 126.58, 126.53, 126.28, 124.19, 123.64, 122.76, 122.26, 115.62, 91.17, 38.22, 34.96, 21.55, 8.73; high resolution ESI-MS m/z calcd for [M-PF$_6$]$^+$ 835.2379, found 835.2383. HPLC retention time 21.8 min.

Ir-CP: Complex **Ir-II** (14.5 mg, 0.015 mmol) and azide-peptide Azhx-c(CRWYDENAC) (7.0 mg, 0.006 mmol) were dissolved in DMF (2 mL) to make a clear solution. The mixture was stirred under nitrogen and dark conditions at 298 K overnight. The solvent was then removed under vacuum and acetonitrile (2 mL) was

added to wash the residue three times to obtain the final product. Yield 4 mg, light yellow solid, 30%; high resolution ESI-MS, *m/z* calcd for $C_{94}H_{112}IrN_{21}O_{19}S_2$ [(**Ir-CP**)-Cl]$^{2+}$ 1047.8755, found 1047.8739; calcd for $C_{94}H_{113}IrN_{21}O_{19}S_2$ [(**Ir-CP**)-Cl+H]$^{3+}$ 699.9194, found 698.9178.

5.2.3 Methods

The instrumental methods for NMR, high resolution ESI-MS, UV-vis spectroscopy, HPLC analyses, X-ray crystallography, cell culture and *in vitro* cell growth inhibition were carried out as described in Chapter 2.

5.2.3.1 X-ray Crystallography

The X-ray crystal data were analysed by Dr. Guy Clarkson (Department of Chemistry, University of Warwick). Single crystals of **Ir-I·MeOH** were grown from methanol/diethyl ether at room temperature. The crystal was kept at 150(2) K during data collection. X-ray crystallographic data for complex **Ir-I·MeOH** have been deposited in the Cambridge Crystallographic Data Centre under the accession number CCDC 1959197. X-ray crystallographic data in CIF format are available from the Cambridge Crystallographic Data Centre (http://www.ccdc.cam.ac.uk/).

5.3 Results and Discussion

5.3.1 Synthesis and Characterisation of Iridium Complex Ir-I and Ir-II

The half-sandwich iridium complex (**Ir-I**) was obtained by reacting the dimeric

$[(Cp^*)Ir(\mu\text{-}Cl)Cl]_2$ with 4-methyl-4'-carboxy-2,2'-bipyridine, and subsequent anion

exchange to a PF_6^- salt by addition of 10 mol equiv. of NH_4PF_6, shown as step a in

Scheme 5.2. To synthesize complex **Ir-II**, the carboxylic acid group in **Ir-I** was then

reacted with the amine group of DBCO-NH$_2$ to afford **Ir-II**, a process facilitated by

oxalyl chloride and the formation of a reactive acid chloride intermediate (step b in

Scheme 5.2). Interestingly, the chloride ligand bound to the iridium survived under

the amide reaction conditions.
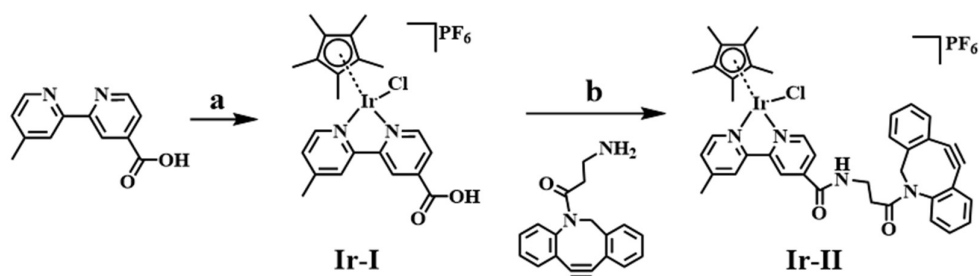
Scheme 5.2. The synthetic route for iridium complex (**Ir-II**). Iridium complex **Ir-I**

was prepared in step a and then subjected to amide coupling in step b to synthesise

complex **Ir-II**. Reaction conditions (a)**:** $[(Cp^*)Ir(\mu\text{-}Cl)Cl]_2$, MeOH, 298 K, 18 h, then

NH_4PF_6, 277 K, 18 h; (b)**:** DBCO-NH$_2$, oxalyl chloride, DCM, catalytic DMF, N$_2$,

298 K, 2 h, then TEA, DCM, N$_2$, 298 K, 4 h.

Both **Ir-I** and **Ir-II** were fully characterised by ^{1}H NMR (Figures 5.1 and 5.3)

and ^{13}C NMR (Figures 5.2 and 5.4) with peaks assigned, as well as high resolution

ESI-MS (Figures 5.5 and 5.6). Half-sandwich iridium complex **Ir-I** containing a monodentate chloride ligand and an unsymmetrical N^N chelating ligand is chiral. Meanwhile, the eight-membered ring of the dibenzocyclooctyne moiety contains both enantiomers with R and S configuration of the amide nitrogen.[41,42] Thus, as a combination of above-mentioned two chiral components, complex **Ir-II** consists of two diastereomers with RS/SR and RR/SS configurations. The presence of two diastereomers was reflected by twin peaks with equal intensity in the UV-vis trace of HPLC corresponding to the same MS peak of *m/z* 835.2 (calcd *m/z* 835.2) assignable as [**Ir-II**]$^+$ (Figure 5.8), and also manifested by double sets of peaks with *ca.* 1:1 ratio in the ^{1}H NMR and ^{13}C NMR spectra of **Ir-II** (Figures 5.3 and 5.4).
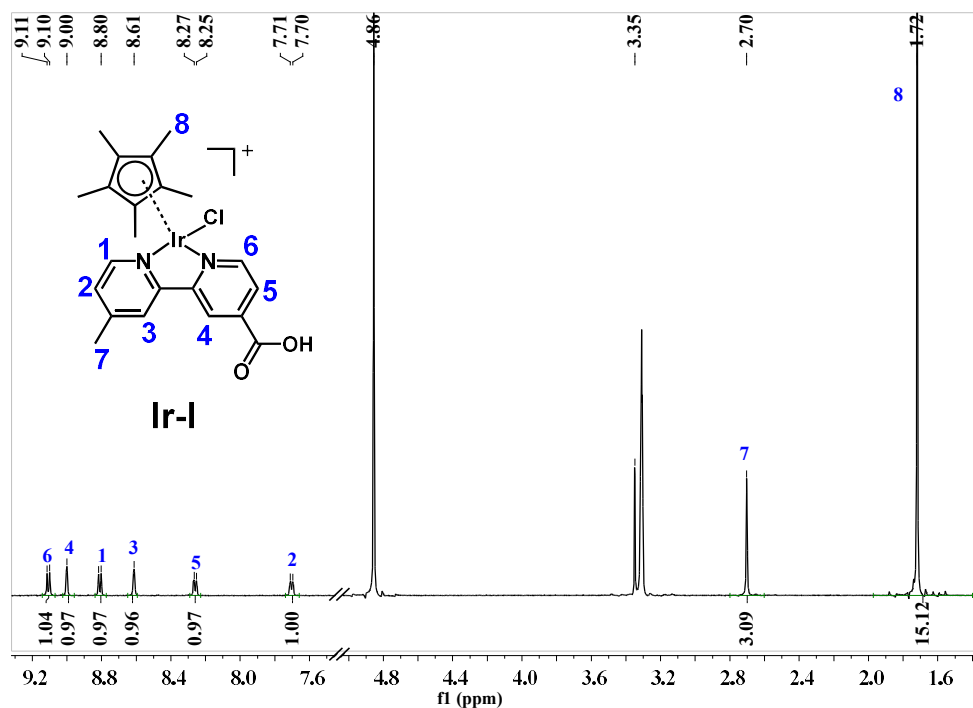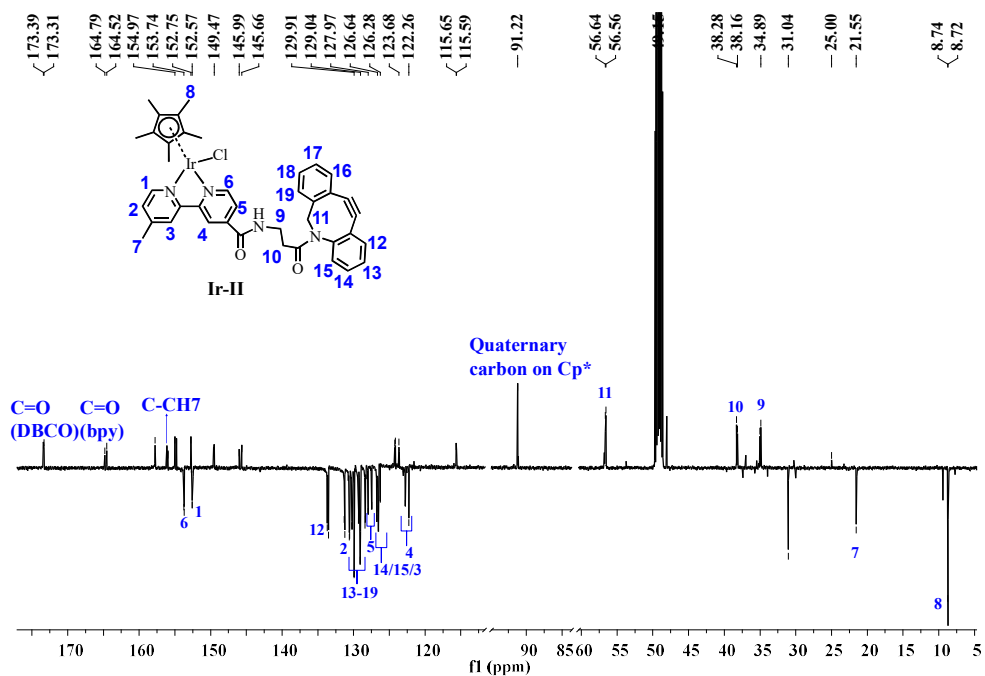

Figure 5.1. ^{1}H NMR (400 MHz, 298 K) spectrum of **Ir-I** in d4-MeOD with peaks assigned.
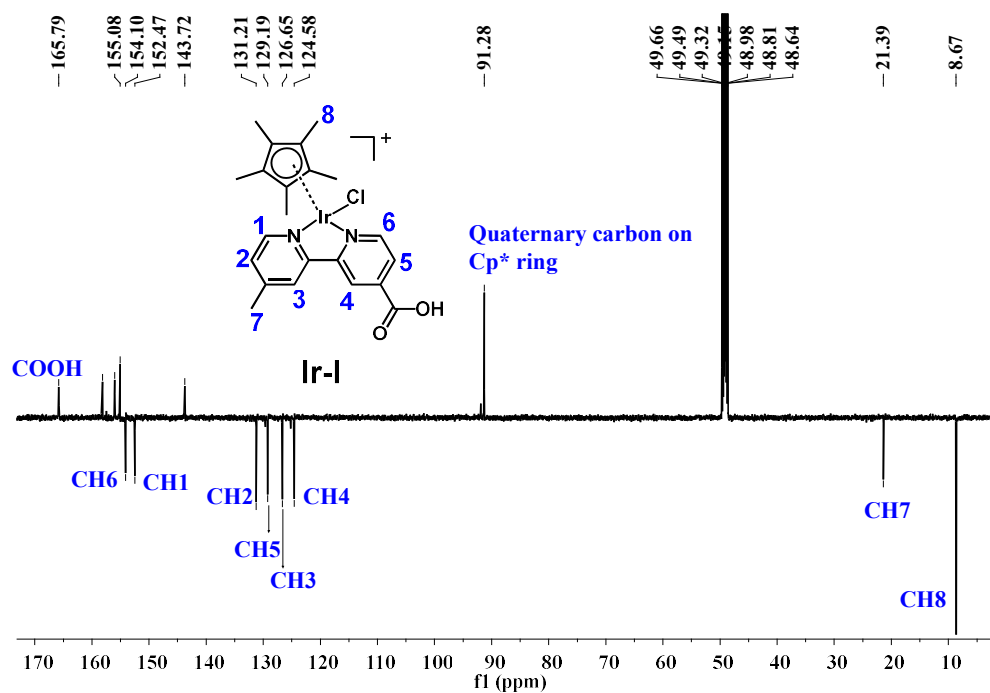
Figure 5.2. $^{13}\text{C}\{^1\text{H}\}$ APT NMR (125 MHz, 298 K) spectrum of **Ir-I** in d_4-MeOD with peaks assigned.
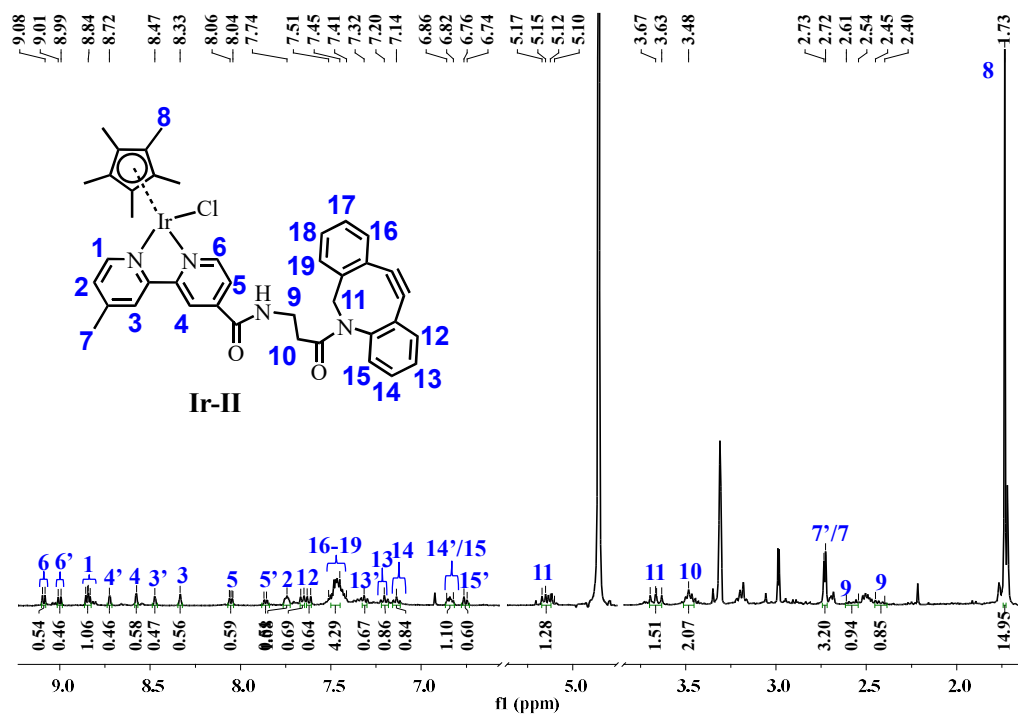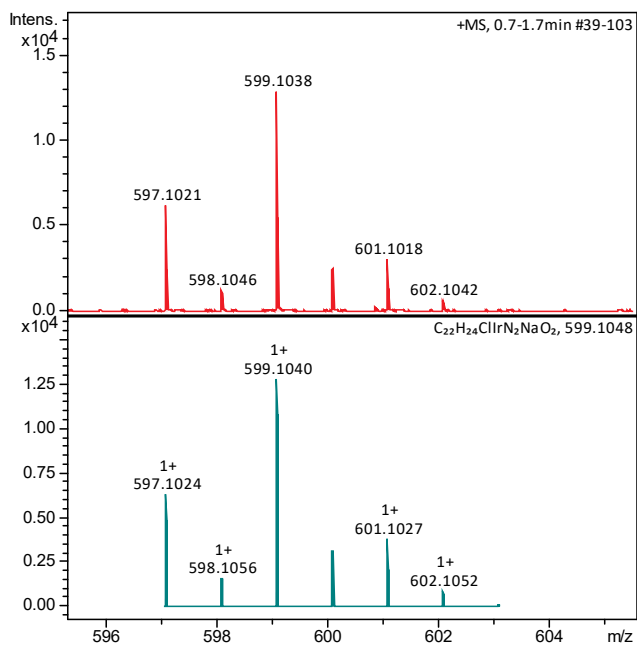
Figure 5.3. ^{1}H NMR (400 MHz, 298 K) spectrum of **Ir-II** in d$_4$-MeOD with peaks assigned to the two diastereomers numbered without and with superscript'.
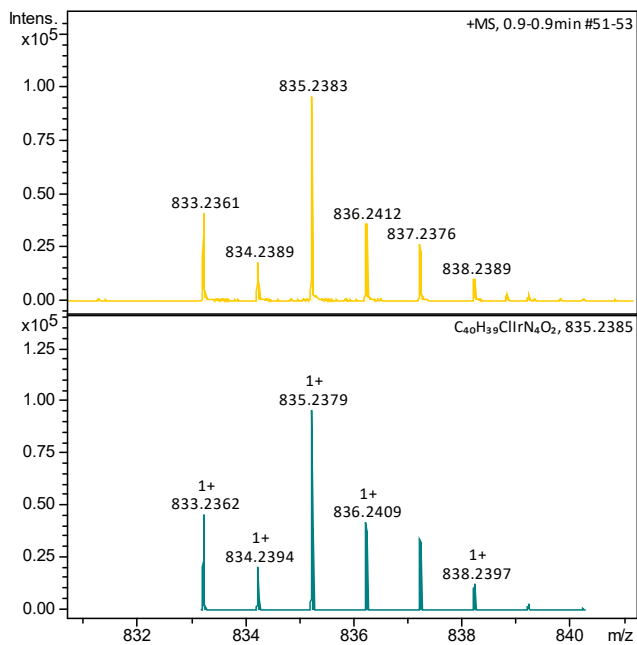
Figure 5.4. $^{13}C\{^1H\}$ APT NMR (125 MHz, 298 K) spectrum of **Ir-II** in d$_4$-MeOD with peaks assigned.

Figure 5.5. Experimental (upper) and calculated (lower) high resolution ESI mass spectra of **Ir-I** for the molecular ion [(**Ir-I**-H)+Na]$^+$.

Figure 5.6. Experimental (upper) and calculated (lower) high resolution ESI mass spectra of **Ir-II** for the molecular ion [(**Ir-II**)-PF$_6$]$^+$.

5.3.2 X-ray Crystal Structure

Yellow block shaped crystals of **Ir-I** were obtained via the diffusion of diethyl ether into a saturated methanol solution at ambient temperature. Crystallographic data are shown in Table 5.1, and selected bond lengths and angles in Table 5.2. The structure with the key atoms numbered is shown in Figure 5.7. The complex adopts the familiar three-legged "piano-stool" geometry. The Ir-N6 bond length of 2.088(4) Å is significantly shorter than the Ir-N10 bond length (2.096(4) Å). The distance between Ir and the centroid of the η^5-pentamethylcyclopentadienyl ring is 1.792 Å, and the Ir-Cl bond length 2.3952(14) Å. The distance between Ir and the centroid of the cyclopentadienyl ring is longer while the Ir-Cl bond is shorter than the corresponding lengths (1.786 and 2.404(2) Å, respectively) in complex [(Cp*)Ir(2,2'-bipyridine)Cl]Cl[43] suggesting that the deviations are due to the electronic effects from the methyl and carboxyl substituents.
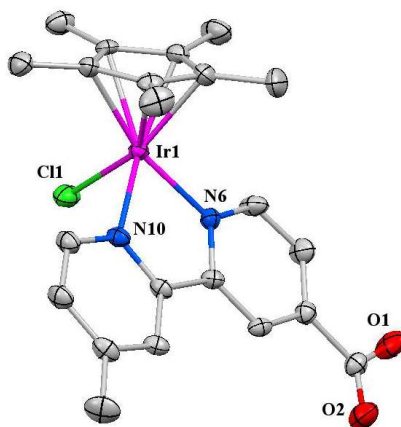
Figure 5.7. X-ray structure with key atom labels of [(Cp*)Ir(4-methyl-4'-carboxy-2,2'-bipyridine)Cl]PF₆·MeOH (**Ir-I·MeOH**), drawn with thermal ellipsoids at 50%

probability level. Hydrogen atoms and one methanol molecule and the PF_6^- counterion have been omitted for clarity.

Table 5.1. Crystal data and refinement for complex **Ir-I·MeOH**.

Parameters	Ir-I·MeOH
Empirical formula	$C_{23}H_{29}ClF_6IrN_2O_3P$
Formula weight	754.10
Temperature/K	150(2)
Crystal system	monoclinic
Space group	$P2_1/n$
a/Å	8.0171(2)
b/Å	15.9750(4)
c/Å	21.1432(5)
α/°	90
β/°	91.390(2)
γ/°	90
Volume/Å^3	2707.09(12)
Z	4
ρ_{calc}g/cm^3	1.850
μ/mm^{-1}	5.159
F(000)	1472.0
Crystal size/mm^3	0.16 × 0.04 × 0.04
Radiation	MoKα (λ = 0.71073)
2Θ range for data collection/°	5.392 to 62.114
Index ranges	-11 ≤ h ≤ 10,
Reflections collected	35859
Independent reflections	7851 [R_{int} = 0.0464]
Data/restraints/parameters	7851/0/343
Goodness-of-fit on F^2	1.116
Final R indexes [I>=2σ (I)]	R_1 = 0.0452, wR_2 = 0.0853
Final R indexes [all data]	R_1 = 0.0582, wR_2 = 0.0898
Largest diff. peak/hole/e Å^{-3}	2.31/-1.54

Table 5.2. Selected bond length (Å) and angles (deg) for complex **Ir-I·MeOH**.

Bond(s)	Ir-I·MeOH
	2.201(5)
	2.160(5)
Ir-C (Cp*)	2.151(5)
	2.158(5)
	2.173(5)
Ir-C (Centroid)	1.792
Ir-N6 (opposite to -COOH)	2.088(4)
Ir-N10 (opposite to -CH$_3$)	2.096(4)
Ir-Cl	2.3952(14)
N6-Ir-N10	76.18(16)
N6-Ir-Cl	86.99(12)
N10-Ir-Cl	86.88(12)

### 5.3.3 Anticancer Activity of Ir-I and Ir-II

The anticancer activity of iridium complexes **Ir-I** and **Ir-II** against A2780 human ovarian cancer cells was determined *in vitro* using the SRB assay after 24 h treatment and subsequent 72 h cell recovery. The IC$_{50}$ value (half maximal inhibitory concentration) of complex **Ir-I** was > 100 μM, showing that it is relatively non-toxic and inactive. But complex **Ir-II** exhibited moderate anticancer activity against human ovarian cancer cells with an IC$_{50}$ value of 33.7 ± 0.3 μM compared to cisplatin of an IC$_{50}$ value of 1.2 ± 0.1 μM.

In contrast, the ligand precursor DBCO-amine was relatively non-toxic (IC$_{50}$ = 80 μM) at the IC$_{50}$ concentration of complex **Ir-II** up to 24 h treatment. Similarly it

is reported that a DBCO-dye (Cy5) conjugate is also non-toxic toward cancer cells.[44] However, the longer retention time in the reverse-phase HPLC analysis of complex **Ir-II** (21.8 min) compared to the parent complex **Ir-I** (13.9 min, shown in Figure A5.1 in the **Appendix**) indicated that the addition of the DBCO group increased the lipophilicity of the resulting complex **Ir-II**, which is likely to lead to higher cellular iridium accumulation and subsequent higher cytotoxicity.[45] The carboxyl group on complex **Ir-I** will be deprotonated at (physiological) pH 7, giving a negative charge on the periphery of the complex, even though overall the complex will be neutral. In contrast, complex **Ir-II** has an overall positive charge, but no charge on the chelated bipyridyl ligand. Possible hydrolysis of these chloride complexes in the cell culture medium would also influence the speciation of the complex under screening conditions although high chloride concentrations are present (*ca.* 0.1 M) and may suppress hydrolysis, but this has yet to be studied.

5.3.4 Copper-free Click Synthesis of Ir-CP

The alkyne bond in the dibenzocyclooctyne group has been introduced as a specific reactive site in complex **Ir-II** for conjugation to the 6-azido hexanoic acid side chain of the modified cyclic peptide Azhx-c(CRWYDENAC). Synthesis of the peptide conjugate **Ir-CP** is facilitated by strain-promoted azide-alkyne cycloaddition of complex **Ir-II** to the cyclic peptide in DMF as shown in Scheme 5.3.
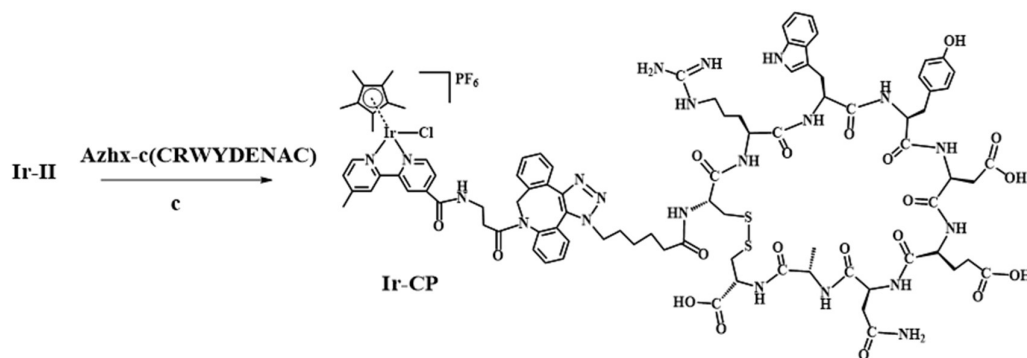
Scheme 5.3. Synthetic route for the iridium-cyclic peptide conjugate complex (**Ir-CP**) via a copper-free click method under condition (c): DMF, N$_2$, 298 K, 18 h.

The generation of **Ir-CP** by this copper-free click method was detected by HPLC analysis of the product. The Ir-Cl bonds of half-sandwich Cp* iridium chloride complexes with 2,2'-bipyridine ligands are often labile and readily hydrolyse in aqueous solution.[45] Therefore, 50 mM NaCl was added to the sample solution (acetonitrile and water, 1/9, v/v) for HPLC analysis to suppress the rapid hydrolysis of Ir-Cl bonds. The UV-vis trace of HPLC shown in Figure 5.8 exhibited new twin peaks with retention times of *ca.* 17.5 min, distinct from the free cyclic peptide (**CP**) and precursor complex **Ir-II**. These new peaks were likely to belong to the peptide conjugate **Ir-CP**. In addition, given its twin peaks were of similar shape to the those of the precursor complex **Ir-II**, **Ir-CP** also appeared to consist of diastereomers because of the diastereomeric reactant **Ir-II**. The fraction corresponding to the new twin peaks was collected and further analysed by LC-MS with unique *m/z* at 1065.54 (Figure 5.9), assignable as $[(\textbf{Ir-CP})+H^+]^{2+}$ (calcd *m/z* 1065.38), which confirmed the formation of **Ir-CP**.
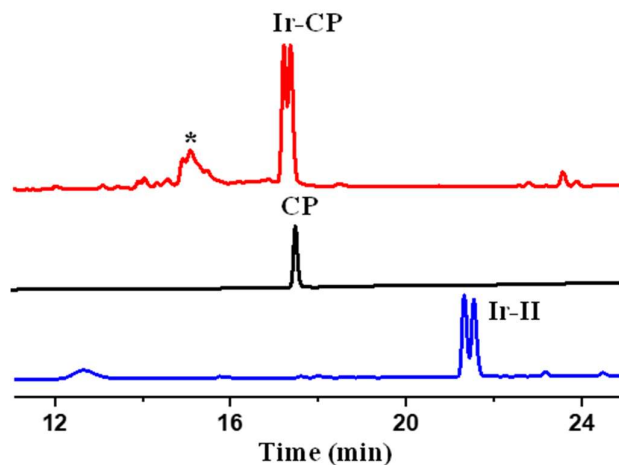
Figure 5.8. HPLC UV trace for cyclic peptide conjugate (**Ir-CP**), free peptide (**CP**) and **Ir-II** with all samples prepared in mixed 50 mM NaCl aqueous solution/acetonitrile (9/1, v/v). * denotes the aquated form of **Ir-CP**. Mobile phases: CH_3CN and H_2O, each with an additive of 0.1% v/v TFA, detection wavelength 254 nm, analysis of the free peptide 230 nm.
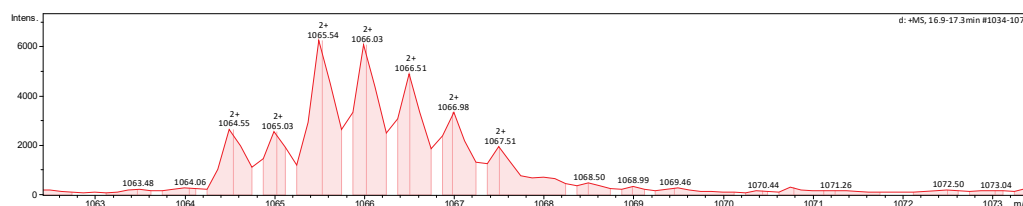
Figure 5.9. LC-MS ESI-MS detection at 17.5 min with *m/z* 1065.54, assignable as $[(\textbf{Ir-CP})+H^+]^{2+}$ (calcd *m/z* 1065.38). Mobile phases: CH_3CN and H_2O, each with an additive of 0.1% v/v TFA, detection wavelength 254 nm.

In contrast, when the sample of the **Ir-CP** used for HPLC analysis was prepared in the absence of 50 mM NaCl, the peak with retention time of 15.2 min (Figure 5.10) increased in intensity and was a major peak along with the previously mentioned peak

at 17.5 min. This peak was further analysed by high resolution ESI-MS (Figure 5.11), with m/z at 1047.8739, assignable as $[(\textbf{Ir-CP})\text{-Cl}]^{2+}$ (calcd m/z 1047.8755), and m/z at 698.9178 assignable as $[(\textbf{Ir-CP})\text{-Cl+H}]^{3+}$ (calcd m/z 698.9194). These data indicated that the peak at 15.2 min resulted from aquation of the Ir-Cl bond and the water molecule was lost under ESI-MS conditions.
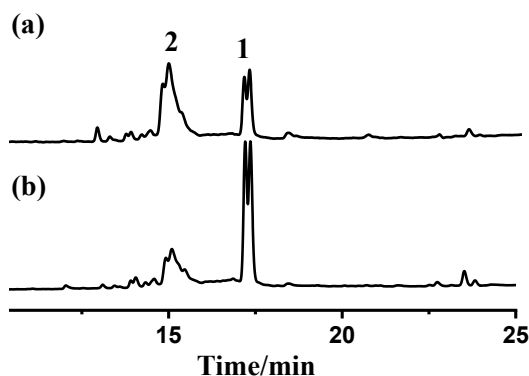
Figure 5.10. HPLC analysis of the peptide conjugate **Ir-CP** (100 µM) prepared in acetonitrile/water (1/9 v/v) (a) without NaCl; (b) with 50 mM NaCl at 298 K. Peak **1** corresponds to the peptide conjugate $[(\textbf{Ir-CP})\text{+H}^{+}]^{2+}$; peak **2** corresponds to peptide conjugate $[(\textbf{Ir-CP})\text{-Cl}]^{2+}$ resulting from aquation of the Ir-Cl bond with the water molecule lost under ESI-MS conditions. Mobile phases: CH_3CN and H_2O, each with an additive of 0.1% v/v TFA, detection wavelength 254 nm.

The solubility of **Ir-CP** is higher than that of the precursor **Ir-II** in PBS, consistent with its shorter retention time of 17.5 min (lower hydrophobicity) compared to the retention time of **Ir-II** of 21.8 min (Figure 5.8).
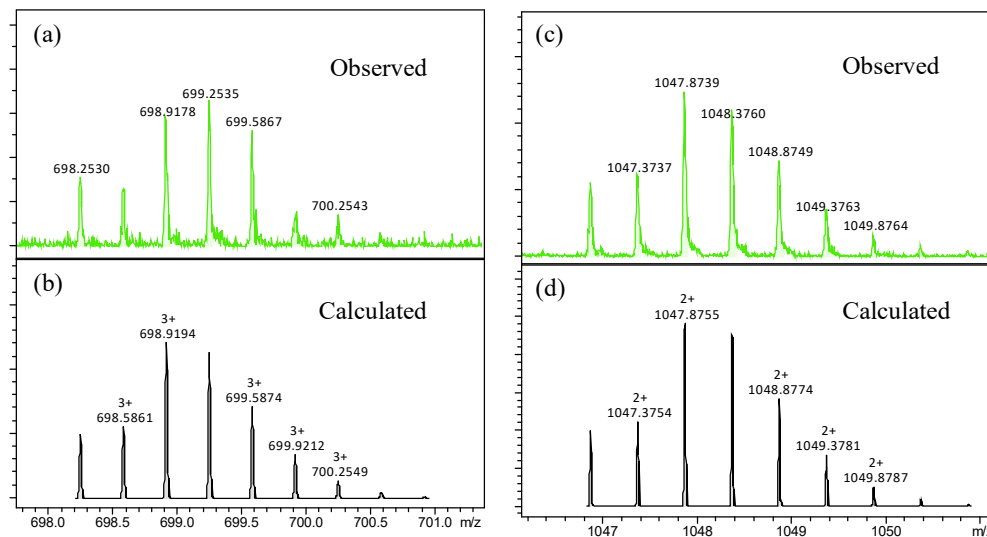
Figure 5.11. Observed and calculated high resolution mass spectra of the peptide conjugate in water/acetonitrile (9/1, v/v). (a) and (b) [(**Ir-CP**)-Cl)+H]$^{3+}$; (c) and (d) [(**Ir-CP**)-Cl]$^{2+}$.

The UV-vis absorption spectrum of **Ir-CP** was recorded in PBS at 298 K and compared with spectra of free peptide and **Ir-II**, as shown in Figure 5.12. The free peptide **CP** showed a strong absorption at 278 nm, mainly due to the tyrosine and tryptophan residues.[27] **Ir-CP** not only retained the representative absorption of the **CP** at 278 nm, but also inherited the intense absorption band from precursor complex **Ir-II** at 300-320 nm due to π*-π*/n-π* transitions, with the band at 400-430 nm assigned as metal-to-ligand charge-transfer (MLCT).[46,47] These characteristic features in the UV-vis spectrum of **Ir-CP** further illustrated the successful conjugation of the cyclic peptide to the iridium precursor.
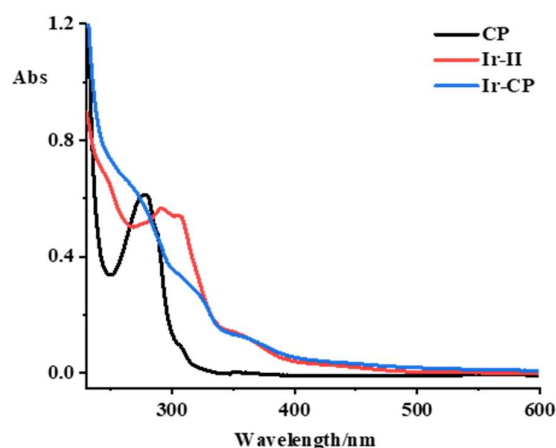
Figure 5.12. UV-vis absorption spectra of the peptide conjugate **Ir-CP**, the iridium precursor **Ir-II**, and the free cyclic peptide **CP** in PBS at 298 K.

5.4 Conclusions

Two novel half-sandwich iridium complexes **Ir-I** and the clickable analogue **Ir-II** have been synthesised and characterised by various analytical techniques, and their anticancer activity was evaluated against the human ovarian cancer cell line. Significantly, the strain-promoted copper free azide-alkyne cycloaddition strategy has been utilized successfully to conjugate the half-sandwich iridium complex **Ir-II** to a tumour-targeting vector-azide-cyclic nonapeptide c(CRWYDENAC). The characterisation of the peptide conjugate **Ir-CP** by HPLC, high resolution ESI-MS, as well as UV-vis spectroscopy has demonstrated the usefulness of this strategy for labelling organo-iridium complexes with targeting vectors. The moderate anticancer activity of the clickable complex **Ir-II** against ovarian cancer cells encourages investigation of the biological activity of the peptide conjugate in future work.

5.5 References

1   M. Hanif and C. G. Hartinger, *Future Med. Chem.*, 2018, **10**, 615-617.

2   R. G. Kenny and C. J. Marmion, *Chem. Rev.*, 2019, **119**, 1058-1137.

3   X. Wang, X. Wang, S. Jin, N. Muhammad and Z. Guo, *Chem. Rev.*, 2018, **119**, 1138-1192.

4   T. C. Johnstone, K. Suntharalingam and S. J. Lippard, *Chem. Rev.*, 2016, **116**, 3436-3486.

5   N. P. Barry and P. J. Sadler, *Chem. Commun.*, 2013, **49**, 5106-5131.

6   G. Gasser, I. Ott and N. Metzler-Nolte, *J. Med. Chem.*, 2011, **54**, 3-25.

7   N. Cutillas, G. S. Yellol, C. de Haro, C. Vicente, V. Rodríguez and J. Ruiz, *Coord. Chem. Rev.*, 2013, **257**, 2784-2797.

8   P. Zhang and P. J. Sadler, *J. Organomet. Chem.*, 2017, **839**, 5-14.

9   D.-L. Ma, D. S.-H. Chan and C.-H. Leung, *Acc. Chem. Res.*, 2014, **47**, 3614-3631.

10   Y. Geldmacher, M. Oleszak and W. S. Sheldrick, *Inorg. Chim. Acta*, 2012, **393**, 84-102.

11   Z. Liu and P. J. Sadler, *Acc. Chem. Res.*, 2014, **47**, 1174-1185.

12   S. Parveen, M. Hanif, E. Leung, K. K. Tong, A. Yang, J. Astin, G. H. De Zoysa, T. R. Steel, D. Goodman and S. Movassaghi, *Chem. Commun.*, 2019, **55**, 12016-12019.

13   A. Pontes da Costa, M. Viciano, M. Sanaú, S. Merino, J. Tejeda, E. Peris and B. Royo, *Organometallics*, 2008, **27**, 1305-1309.

14   G. Kohl, H. Pritzkow and M. Enders, *Eur. J. Inorg. Chem.*, 2008, **2008**, 4230-

4235.

15   Z. Liu, A. Habtemariam, A. M. Pizarro, S. A. Fletcher, A. Kisova, O. Vrana, L. Salassa, P. C. Bruijnincx, G. J. Clarkson and V. Brabec, *J. Med. Chem.*, 2011, **54**, 3011-3026.

16   J. J. Soldevila-Barreda and N. Metzler-Nolte, *Chem. Rev.*, 2019, **119**, 829-869.

17   J. Li, M. Tian, Z. Tian, S. Zhang, C. Yan, C. Shao and Z. Liu, *Inorg. Chem.*, 2018, **57**, 1705-1716.

18   Y. Yang, X. Ge, L. Guo, T. Zhu, Z. Tian, H. Zhang, Q. Du, H. Peng, W. Ma and Z. Liu, *Dalton Trans.*, 2019, **48**, 3193-3197.

19   L. Guo, H. Zhang, M. Tian, Z. Tian, Y. Xu, Y. Yang, H. Peng, P. Liu and Z. Liu, *New J. Chem.*, 2018, **42**, 16183-16192.

20   J. Li, L. Guo, Z. Tian, M. Tian, S. Zhang, K. Xu, Y. Qian and Z. Liu, *Dalton Trans.*, 2017, **46**, 15520-15534.

21   J. Ruiz, V. Rodríguez, N. Cutillas, K. G. Samper, M. Capdevila, Ò. Palacios and A. Espinosa, *Dalton Trans.*, 2012, **41**, 12847-12856.

22   K. Qiu, H. Zhu, T. W. Rees, L. Ji, Q. Zhang and H. Chao, *Coord. Chem. Rev.*, 2019, **398**, 113010.

23   S. C. Larnaudie, J. C. Brendel, I. Romero-Canelón, C. Sanchez-Cano, S. Catrouillet, J. Sanchis, J. P. Coverdale, J.-I. Song, A. Habtemariam and P. J. Sadler, *Biomacromolecules*, 2017, **19**, 239-247.

24   B. Albada and N. Metzler-Nolte, *Chem. Rev.*, 2016, **116**, 11797-11839.

25   S. Dissanayake, W. A. Denny, S. Gamage and V. Sarojini, *J. Controlled Release*, 2017, **250**, 62-76.

26   G. K. Feng, M. Q. Zhang, H. X. Wang, J. Cai, S. P. Chen, Q. Wang, J. Gong, K. W. Leong, J. Wang and X. Zhang, *Adv. Therap.*, 2019, **2**, 1900018.

27   H. Shi, Q. Wang, V. Venkatesh, G. Feng, L. S. Young, I. Romero-Canelón, M. Zeng and P. J. Sadler, *Dalton Trans.*, 2019, **48**, 8560-8564.

28   B. A. Krizek, B. T. Amann, V. J. Kilfoil, D. L. Merkle and J. M. Berg, *J. Am. Chem. Soc.*, 1991, **113**, 4518-4523.

29   R. Zou, Q. Wang, J. Wu, J. Wu, C. Schmuck and H. Tian, *Chem. Soc. Rev.*, 2015, **44**, 5200-5219.

30   J. Y. Axup, K. M. Bajjuri, M. Ritland, B. M. Hutchins, C. H. Kim, S. A. Kazane, R. Halder, J. S. Forsyth, A. F. Santidrian and K. Stafin, *Proc. Natl. Acad. Sci. U.S.A.*, 2012, **109**, 16101-16106.

31   A. J. De Graaf, M. Kooijman, W. E. Hennink and E. Mastrobattista, *Bioconjugate Chem.*, 2009, **20**, 1281-1295.

32   Q.-Y. Hu, F. Berti and R. Adamo, *Chem. Soc. Rev.*, 2016, **45**, 1691-1719.

33   E. M. Sletten and C. R. Bertozzi, *Angew. Chem. Int. Ed.*, 2009, **48**, 6974-6998.

34   E. Lallana, R. Riguera and E. Fernandez-Megia, *Angew. Chem. Int. Ed.*, 2011, **50**, 8794-8804.

35   P. Thirumurugan, D. Matosiuk and K. Jozwiak, *Chem. Rev.*, 2013, **113**, 4905-4979.

36   S. T. Laughlin, J. M. Baskin, S. L. Amacher and C. R. Bertozzi, *Science*, 2008, **320**, 664-667.

37   A. A. Poloukhtine, N. E. Mbua, M. A. Wolfert, G.-J. Boons and V. V. Popik, *J. Am. Chem. Soc.*, 2009, **131**, 15769-15776.

38   P. V. Chang, J. A. Prescher, E. M. Sletten, J. M. Baskin, I. A. Miller, N. J. Agard, A. Lo and C. R. Bertozzi, *Proc. Natl. Acad. Sci. U.S.A.*, 2010, **107**, 1821-1826.

39   D. G. McCafferty, B. M. Bishop, C. G. Wall, S. G. Hughes, S. L. Mecklenberg, T. J. Meyer and B. W. Erickson, *Tetrahedron*, 1995, **51**, 1093-1106.

40   W. S. Perry, S. J. Pope, C. Allain, B. J. Coe, A. M. Kenwright and S. Faulkner, *Dalton Trans.*, 2010, **39**, 10974-10983.

41   T. Cruchter, K. Harms and E. Meggers, *Chemistry–A European Journal*, 2013, **19**, 16682-16689.

42   M. Jäger, H. Görls, W. Günther and U. S. Schubert, *Chem. Eur. J.*, 2013, **19**, 2150-2157.

43   M.-T. Youinou and R. Ziessel, *J. Organomet. Chem.*, 1989, **363**, 197-208.

44   S.-W. Kang, S. Lee, J. H. Na, H. I. Yoon, D.-E. Lee, H. Koo, Y. W. Cho, S. H. Kim, S. Y. Jeong, I. C. Kwon, K. Choi and K. Kim, *Theranostics*, 2014, **4**, 420-431.

45   Z. Liu, A. Habtemariam, A. M. Pizarro, S. A. Fletcher, A. Kisova, O. Vrana, L. Salassa, P. C. A. Bruijnincx, G. J. Clarkson, V. Brabec and P. J. Sadler, *J. Med. Chem.*, 2011, **54**, 3011-3026.

46   M. Kalidasan, R. Nagarajaprakash, S. Forbes, Y. Mozharivskyj and K. M. Rao, *Z. Anorg. Allg. Chem.*, 2015, **641**, 715-723.

47   N. R. Palepu, W. Kaminsky and M. R. Kollipara, *J. Chem. Sci.*, 2017, **129**, 561-571.

Chapter 6
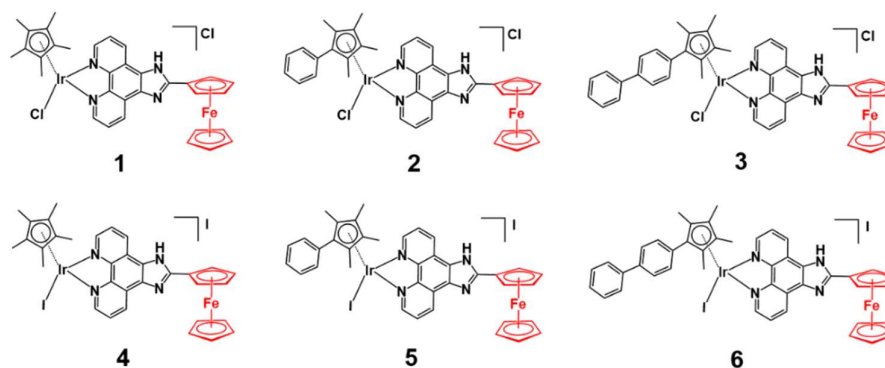
Half-sandwich Iridium Complexes Conjugated to Ferrocene and Luminescent Probes

In this Chapter, the X-ray crystal structure was solved by Dr. Guy Clarkson; confocal microscopy experiments were carried out with the help of Hannah Bridgewater; phototoxicity assays on the human nasopharyngeal carcinoma cell line were performed by Dr. Huaiyi Huang. All the other experimental data collection and analysis were carried out by the author.
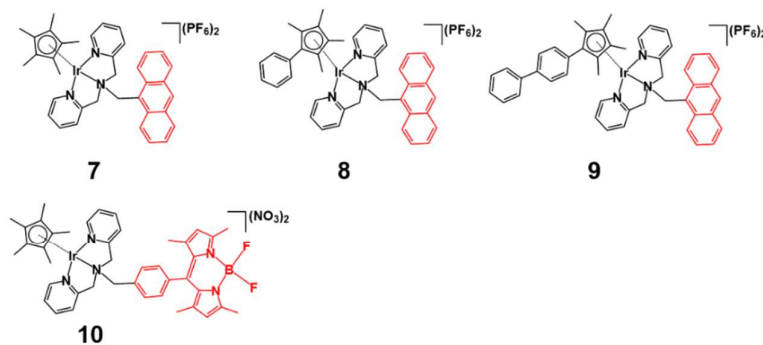
6.1 Introduction

Three classes of half-sandwich complexes are studied in this Chapter, which include (I) complexes **1-6** conjugated to ferrocene; (II) complexes **7-10** conjugated to the organic fluorophore anthracene or BODIPY; and (III) complexes **12** conjugated to the phosphorescent cyclometalated iridium fragment. The chemical structures are listed in Scheme 6.1.
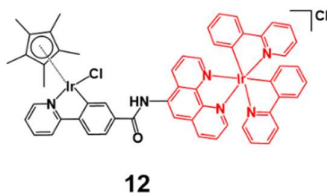

**Scheme 6.1.** Three classes of iridium complexes studied in this Chapter.

6.1.1 Ferrocene-Conjugated Iridium Complexes

Ferrocene (Fc) with the formula of $[(Cp)_2Fe]$, is the most well-known organometallic with "sandwich" structure. The stability of ferrocene in aqueous and aerobic media, the accessibility of versatile derivatives, and typically reversible redox couple of $Fc^{+/0}$ have endowed ferrocenyl compounds with wide applications in the bioorganometallic field as antimalarial, antiparasitic, and anticancer agents.[1-3] Fc itself is non-toxic and only the ferrocenium cation $[(Cp)_2Fe]^+$ exerts anticancer activity.[4] In certain cellular apartment, Fc and Fc^+ can exist in a redox equilibrium depending on the local potential of the organelles.[5] The DNA cleaving and cytotoxic activity of ferrocenium compounds have been demonstrated to arise from the generation the hydroxyl radicals ($\cdot$OH) though a Fenton mechanism.[6,7]

The Fc-conjugated derivatives has been reported as antimalarial candidate ferroquine (FQ) and the anticancer drug candidate ferrocifen (shown in Figure 6.1). The redox-active nature of FQ catalyzing $\cdot$OH formation is of great significance to its efficacy *in vivo*.[8] The Fc group acts as an intramolecular oxidation "antenna" to afford a quinone methide intermediate which is readily to be attacked by peptides or nucleobases.[9] Inspired by these two successful developments, Fc has been further incorporated into organic or other transition-metal based therapeutic agents to achieve additive or synergistic therapeutic effect. In recent years, several half-sandwich organoiridium(III) complexes bearing a Fc group have been reported.[10-14] In this Chapter, the Fc-conjugated 2-ferrocnyimidazophenanthroline ligand (**Fc-Phen**) which was reported to show phototoxicity and generate reactive oxygen species upon irradiation with visible light (400-700 nm), is incorporated into half-sandwich iridium

complexes.[15] Fc-conjugated Cp^X (Cp^*, Cp^{xph}, or Cp^{xbiph}) iridium complexes (**1-6**) containing an iodido or a chlorido monodentate ligand have been synthesised with the structures shown in Scheme 6.1. X-ray crystal structure of $[(\eta^5\text{-}Cp^*)\text{Ir}(\textbf{Fc-Phen})\text{I}]\text{I}\cdot2\text{MeOH}$ (**4·2MeOH**) has been determined. The electrochemical behavior of the Fc group in these complexes was evaluated by cyclic voltammetry. The aqueous stability in water or phosphate-buffered saline, interaction with 9-ethylguinane (9-EtG), the antiproliferative activity against human A2780 ovarian cancer cells are studied.

Ferroquine (FQ)

**Ferrocifen** (R = H)
Hydroxyferrocifen (R = OH)
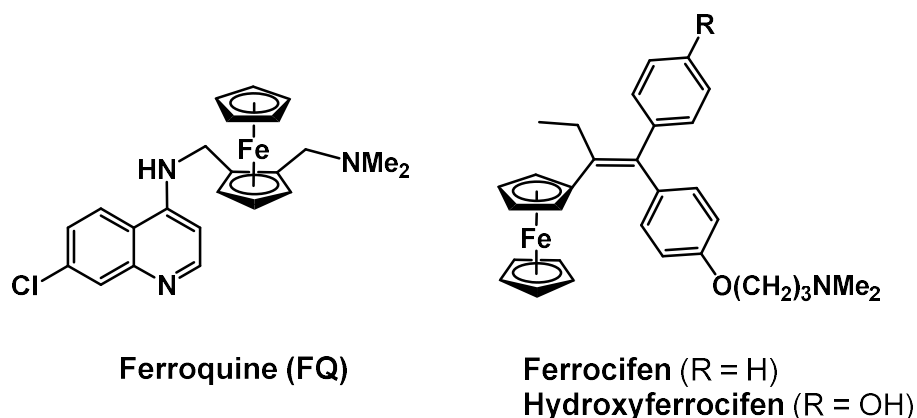
Figure 6.1. The structure of the antimalarial ferroquine which is a chloroquine derivative in phase II clinical trials and the ferrocifen-type of anticancer drug candidates.

6.1.2 Iridium Complexes Conjugated to Luminescent Probes

Photodynamic therapy (PDT) has been an effective treatment modality for cancers and certain localized diseases, which relies on light, photosensitizer and oxygen in the mechanism of action. These components work together to initiate the photochemical generation of singlet oxygen, which causes significant toxicity leading

215

to cell death via apoptosis or necrosis. For the light wavelength, the region between 600-1200 nm is often the optical window of tissue. Blue light penetrates least efficiently through tissue while red and infrared radiations penetrate more deeply. An ideal photosensitizer should have a high absorption band within 600-800 nm, as absorption at longer wavelength than 800 nm usually provides insufficient energy to facilitate the photodynamic reaction of generating singlet oxygen.[16] Boron dipyrromethene core (BODIPY) shown in Figure 6.2 shows an absorption band at 500 nm and inherent fluorescence with intense quantum yields and high photo-/chemo-stability. Halogenated BODIPY chromophores with tuned absorption bands to near infrared red (NIR) wavelengths been extensively studied as efficient photosensitizer in PDT.[17,18]

BODIPY   **[(ppy)Ir(N^N)]$^+$**
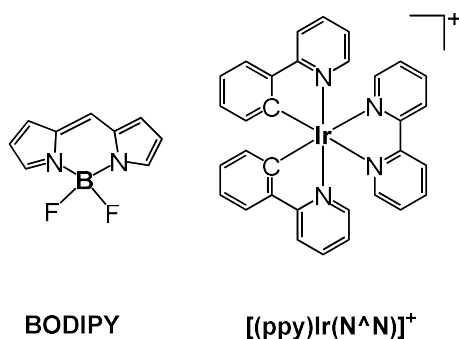
Figure 6.2. Core structures of BODIPY chromophores and bis-cyclometalated iridium (III) polypyridine complexes.

Heavy-metal iridium(III) complexes exhibit fascinating photochemistry.[19] The application of phosphorescent iridium complexes with d^6 electron configuration has attracted much attention as light-emitting diodes,[20] electrochemiluminescence,[21] photovoltaics,[22] chemical sensors[23] and bioimaging probes[24]. Especially, the

strongly-emissive bis-cyclometalated iridium (III) polypyridine complexes with core structure shown in Figure 6.2, have been used as excellent live-cell imaging regents.[25,26] Meanwhile, a wide range of such emissive Ir(III) complexes are used as PDT agents which can generate singlet oxygen as their cytotoxic components added to the overall behavior.[27]

Unlike the bis-cyclometalated Ir[III] complexes with tunable photophysical and photochemical properties, the feature of half-sandwich Cp^X iridium complexes lacking fluorescent property has led to investigation of cell accumulation and specific subcellular distribution heavily relying on the cellular fractional bioassay and subsequent instrumental ICP-MS assay or the recently developed cryo soft/hard X-ray imaging[28]. In order to get further insight into the mechanism of action and the pharmacokinetics through faster, easily accessible and cost-effective technologies, conjugating fluorescent tags to the iridium complexes is an alternative strategy allowing the real-time fluorescence imaging to track the pharmacokinetic distribution and validate the possible cellular targets. In this Chapter, aiming at designing luminescent half-sandwich iridium anticancer agents, the fluorescent anthracene/BODIPY or the bis-cyclometalated Ir[III] component is conjugated with the Cp^X iridium unit through elaborate ligand synthesis. The ligand synthesis includes two strategies: (i) conjugating the well-known fluorophore anthracene/BODIPY in the tridentate chelating ligand **An-Dpa** and **Bdp-Dpa**, respectively; (ii) conjugation of an emissive bis-cyclometalated Ir[III] unit into the multi-coordinating ligand. Half-sandwich iridium complexes conjugated to the anthracene/BODIPY/cyclometalated iridium group (shown in Scheme 6.1) have been synthesised and characterised. The

UV-vis absorption and fluorescent emission spectra of the representative complex for each type of conjugation were recorded. Their stability towards water, phosphate buffered saline (PBS), and cell culture medium RPMI-1640, as well as interaction with glutathione (GSH) and 9-EtG, hydrophobicity, the reactivities toward the reduced form of coenzyme nicotinamide adenine dinucleotide (NADH) are studied. The photocytotoxicity under blue light (463 nm) irradiation are evaluated and the cellular distribution of the luminescent iridium complexes are also studied by confocal imaging.

6.2 Experimental section

6.2.1 Materials

The ferrocene-1-carboxaldehyde, 2-phenylpyridine, 5-amino-1,10-phenanthroline ammonium acetate, and 9,10-bis(chloromethyl)anthracene, 2,2'-dipicolylamine, 4-dimethyl-1H-pyrrole, 4-(chloromethyl)benzoyl chloride, anhydrous sodium sulfate triethyl amine, (2-pyridyl)benzaldehyde and formaldehyde were purchased from Sigma-Aldrich. Glacial acetic acid and potassium iodide were purchased from Fisher Scientific. Hydrochloride acid was purchased from VWR International and boron trifluoride etherate (approx. 48% BF_3) from Acros Organics. 1,10-Phenanthroline-5,6-dione was obtained from Dr. Huaiyi Huang, University of Warwick. The preparation of the starting material $[(Cp^X)Ir(\mu\text{-Cl})Cl]_2$ and $[(Cp^X)Ir(\mu\text{-I})I]_2$ is described in Chapter 2. The chloride-bridged Ir^{III} dimer $[(ppy)_2Ir(\mu\text{-Cl})]_2$ was synthesised

by the method reported in the literature.[29] Complex [(Cp*)Ir(ppy)Cl] (ppy = 2-phenylpyridine) (**13**) was synthesised and characterised as reported.[30]

6.2.2 Synthesis

6.2.2.1 Synthesis of Ligands

2-Ferrocene-1-H-imidazole[4,5-f][1,10]-phenanthroline[31] (**Fc-Phen**), imidazole[4,5-f]1,10-phenanthroline[32] (**Im-Phen**), 9-[(2,2'-dipicolylamino)methyl]anthracene[33] (**An-Dpa**), 8-(4-chlorobenzyl)-4,4-difluro-1,3,5,7-tetramethyl-4-bora-3a,4a-diaza-s-indacene[34] (**Bdp-Dpa**) and 4-(2-pyridy)benzoic acid[35] were synthesised and characterised as reported.

N-(1,10-phenanthrolin-5-yl)-4-(2-pyridyl)benzamide (Ppy-Phen). The synthesis followed a modified procedure from the literature:[36] In a two-neck flask, 4-(2-pyridy)-benzoic acid (50 mg, 0.3 mmol) was suspended in 10 mL anhydrous DCM. Then oxalyl chloride (500 µL, 0.90 mmol) and a catalytic amount of anhydrous DMF (two drops) were added to the suspension under nitrogen atmosphere. After 10 min stirring, a catalytic amount of triethylamine (one drop) was added, and the solution became yellow immediately from colorless clear. The mixture in the flask was heated at 306 K for 3 h. The solution was dried under vacuum to obtain a yellowish solid residue. To another flask, 5-amino-1,10-phenanthroline (50 mg, 0.25 mmol) and triethylamine (125 µL) were dissolved in anhydrous DCM (5 mL) and ACN (5 mL). The residue obtained in the first step was dissolved in anhydrous DCM (10 mL) and added dropwise to the phenanthroline solution over 40 min under ice bath and nitrogen atmosphere. After stirring for 3 d at room temperature, the solution was

219

evaporated to dryness. The crude product was washed with aqueous 5% NaHCO$_3$ solution (20 mL), collected by filtration. The final product was recrystallized from ethanol (30 mL) at 353 K, then filtered after being stored at 277 K overnight. ^{1}H NMR (400 MHz, d$_6$-DMSO) δ 10.77 (s, 1H), 9.15 (d, 1H, J = 3.6 Hz), 9.10 (d, 1H, J = 4.1 Hz), 8.75 (d, 1H, J = 4.1 Hz), 8.55 (t, 2H, J = 9.8 Hz), 8.33-8.24 (m, 4H), 8.17 (s, 1H), 8.13 (d, 1H, J = 8.2 Hz), 7.98-7.93 (m, 1H), 7.84-7.77 (m, 2H), 7.46-7.42 (m, 1H).

6.2.2.2 Synthesis of Iridium Complexes

[(Cp*)Ir(Fc-Phen)Cl]Cl (1). The ligand **Fc-Phen** (20.21 mg, 0.05 mmol) was dissolved in MeOH (15 mL) to obtain a red solution and [(Cp*)Ir(μ-Cl)Cl]$_2$ (19.92 mg, 0.025 mmol) solid was added to the solution. The mixture was kept stirring for 24 h at room temperature, and the solvent was concentrated. The crude product was recrystallized with diethyl ether and filtered as reddish orange solid. Yield: 29 mg, 72%. ESI-MS Calcd for [M-Cl]$^+$ m/z 767.1, found 767.2. ^{1}H NMR (500 MHz, d$_4$-MeOD): δ 9.27-9.18 (4H, m), 8.21-8.19 (2H, m), 5.24 (2H, s), 4.61 (2H, s), 4.17 (5H, s), 1.79 (15H, s). ^{13}C{^{1}H} NMR (125 MHz, d$_4$-MeOD): δ 158.0, 151.2, 150.9, 134.4, 133.9, 128.4, 91.1, 72.2, 71.1, 68.9, 8.8. Anal. Calcd for C$_{33}$H$_{31}$Cl$_2$FeIrN$_4$: C, 49.38; H, 3.89; N, 6.98. Found: C, 48.77; H, 3.85; N, 6.89.

[(Cp*)Ir(Im-Phen)Cl]Cl (1A). Synthesis as for complex **1** using the ligand **Im-Phen** (22.0 mg, 0.1 mmol) and [(Cp*)Ir(μ-Cl)Cl]$_2$ (39.8 mg, 0.05 mmol) in 10 mL MeOH/DCM (1/1 v/v) mixed solvents. Yield: 45 mg, 73%. ESI-MS Calcd for [M-Cl]$^+$ m/z 583.1, found 583.2. ^{1}H NMR (500 MHz, d$_4$-MeOD): δ 9.30 (2H, d, J = 5.3

Hz), 9.15 (2H, d, J = 8.2 Hz), 8.67 (1H, s), 8.22 (2H, dd, J = 5.3 Hz, 8.2 Hz), 1.79 (15H, s). ^{13}C{^{1}H} NMR (125 MHz, d$_4$-MeOD): δ 151.4, 146.3, 144.6, 134.1, 128.7, 91.2, 8.8.

[(Cp^{xph})Ir(Fc-Phen)Cl]Cl (2). Synthesis as for complex **1** using the ligand **Fc-Phen** (10.10 mg, 0.025 mmol), and [(Cp^{xph})Ir(μ-Cl)Cl]$_2$ (11.51 mg, 0.0125 mmol). Yield: 19.0 mg, 88%. ESI-MS Calcd. for [M-Cl]$^+$ m/z 829.2, found 829.2. ^{1}H NMR (400 MHz, d$_4$-MeOD): δ 9.19 (2H, brs), 8.99 (2H, d, J = 4.8 Hz), 8.08 (2H, t, J= 7.0 Hz), 7.62 (2H, d, J = 7.0 Hz), 7.56-7.50 (3H, m), 5.22 (2H, s), 4.58 (2H, s), 4.15 (5H, s), 1.88 (6H, s), 1.78 (6H, s). ^{13}C{^{1}H} NMR (100 MHz, d$_4$-MeOD): δ 158.0, 131.7, 130.8, 130.6, 130.3, 128.3, 100.4, 88.7, 84.7, 73.5, 72.2, 71.1, 68.9, 10.0, 8.7. Anal. Calcd for C$_{38}$H$_{33}$Cl$_2$FeIrN$_4$: C, 52.79; H, 3.85; N, 6.48. Found: C, 52.05; H, 3.79; N, 6.51.

[(Cp^{xbiph})Ir(Fc-Phen)Cl]Cl (3). The [(Cp^{xbiph})Ir(μ-Cl)Cl]$_2$ (17.9 mg, 0.0125 mmol) was dissolved in 25 mL DCM/MeOH/CHCl$_3$ (2/2/1 v/v/v) mixed solvents at 313 K. After stirring for 1 h, the ligand **Fc-Phen** (10.1 mg, 0.025 mmol) was added to the solution. After 24 h stirring, the solvent was concentrated with product recrystallized from diethyl ether and filtered. Yield: 18 mg, 77%. ESI-MS Calcd. for [M-Cl]$^+$ m/z 905.3, found 905.3. ^{1}H NMR (500 MHz, d$_4$-MeOD): δ 9.23 (2H, brs), 9.05 (2H, d, J = 4.8 Hz), 8.13 (2H, t, J = 5.8 Hz), 7.79 (2H, d, J = 7.9 Hz), 7.73-7.70 (4H, m), 7.49 (2H, t, J = 7.3 Hz), 7.41 (1H, t, J = 7.3Hz), 5.25 (2H, s), 4.60 (2H, d, J= 14.8 Hz), 4.18 (5H, s), 1.91 (6H, s), 1.84 (6H, s). ^{13}C{^{1}H} NMR (100 MHz, d$_4$-MeOD): δ 158.2, 150.7, 143.6, 141.4, 134.6, 132.2, 130.3, 129.2, 128.4, 128.2, 100.5, 88.8, 84.2, 73.5, 72.2, 71.2, 68.9, 10.1, 7.8. Anal. Calcd for C$_{44}$H$_{37}$Cl$_2$FeIrN$_4$: C, 56.18; H, 3.96; N, 5.96. Found: C, 56.39; H, 3.93; N, 6.05.

[(Cp^xbiph^)Ir(Im-Phen)Cl]Cl (3A). Synthesis as for complex **1A** using the ligand **Im-Phen** (11.1 mg, 0.05 mmol) and [(Cp^xbiph^)Ir(μ-Cl)Cl]$_2$ (29.06 mg, 0.025 mmol) in 20 mL DCM/MeOH (1/1 v/v) mixed solvents. Yield: 35 mg, 92%. ESI-MS Calcd for [M-Cl]$^+$ *m/z* 721.3, found 721.3. ^{1}H NMR (400 MHz, d$_4$-MeOD): δ 9.14 (2H, brs), 9.08 (2H, d, *J* = 5.3 Hz), 8.71 (1H, s), 8.13 (2H, dd, *J* = 5.4 Hz, 8.1 Hz), 7.79 (2H, d, *J* = 8.5 Hz), 7.73-7.69 (5H, m), 7.49 (2H, m), 7.41 (1H, m), 1.90 (6H, s), 1.84 (6H, s). Anal. Calcd for C$_{34}$H$_{29}$Cl$_2$IrN$_4$: C, 53.96; H, 3.86; N, 7.40. Found: C, 53.34; H, 3.88; N, 7.50.

[(Cp^*^)Ir(Fc-Phen)I]I (4). Synthesis as for complex **1** using the ligand **Fc-Phen** (20.21 mg, 0.05 mmol) and [(Cp^*^)Ir(μ-I)I]$_2$ (29.06 mg, 0.025 mmol). Yield: 39.0 mg, 79%. ESI-MS Calcd for [M-Cl]$^+$ *m/z* 859.1, found 859.2. ^{1}H NMR (500 MHz, d$_4$-MeOD): δ 9.27 (2H, d, *J* = 5.1 Hz), 9.19 (2H, d, J = 8.1 Hz), 8.19-8.15 (2H, q, J = 5.1 Hz, 8.1 Hz), 5.26 (2H, s), 4.63 (2H, s), 4.20 (5H, s), 1.88 (15H, s). ^{13}C{^{1}H} NMR (125 MHz, d$_4$-MeOD): δ 158.1, 152.1, 145.5, 133.7, 128.2, 92.1, 72.2, 71.2, 68.8, 9.7. Anal. Calcd for C$_{33}$H$_{31}$I$_2$FeIrN$_4$: C, 40.22; H, 3.17; N, 5.69. Found: C, 40.04; H, 3.12; N, 5.63.

[(Cp^xph^)Ir(Fc-Phen)I]I (5). Synthesis as for complex **1** using the ligand **Fc-Phen** (16.17 mg, 0.04 mmol) and [(Cp^xph^)Ir(μ-I)I]$_2$ (25.73 mg, 0.02 mmol) in 20 mL DCM/MeOH (1/1 v/v) mixed solvents. Yield: 36.0 mg, 86%. ESI-MS Calcd for [M-Cl]$^+$ *m/z* 921.1, found 921.2. ^{1}H NMR (300 MHz, d$_4$-MeOD): δ 9.18 (2H, d, *J* = 8.3 Hz), 9.03 (2H, d, *J* = 5.3 Hz), 8.10-8.05 (2H, dd, *J* = 5.3 Hz, 8.3 Hz), 7.58-7.45 (5H, m), 5.26 (2H, t, *J* = 1.8 Hz), 4.63 (2H, t, *J* = 1.8 Hz), 4.20 (5H, s), 1.98 (6H, s), 1.94

(6H, s). Anal. Calcd for $C_{38}H_{33}I_2FeIrN_4$: C, 43.57; H, 3.18; N, 5.35. Found: C, 43.40 H, 3.13; N, 5.43.

[(Cp^{xbiph})Ir(Fc-Phen)I]I (6). Complex **3** (8.9 mg, 0.010 mmol) was dissolved in 10 mL MeOH and silver nitrate (2.4 mg, 0.015 mmol) was added to the solution. The mixture was stirred for 18 h at room temperature. Then the suspension was centrifuged, potassium iodide (31 mg, 0.2 mmol) was added to the upper layer and the mixture was stirred for 18 h at 323 K. The product was filtered and washed with diethyl ether. Yield: 7 mg, 63%. ESI-MS Calcd for [M-Cl]$^+$ *m/z* 997.2, found 997.2. ^{1}H NMR (400 MHz, d$_4$-MeOD): δ 9.19 (2H, d, *J* = 5.5 Hz), 9.08 (2H, d, *J* = 5.5 Hz), 8.10 (2H, t, J = 6.5 Hz), 7.76 (2H, d, *J* = 7.3 Hz), 7.71-7.65 (4H, m), 7.48 (2H, m), 7.39 (1H, m), 5.26 (2H, s), 4.64 (2H, s), 4.21 (5H, s), 1.99 (12H, s). Anal. Calcd for $C_{44}H_{37}FeI_2IrN_4$: C, 47.03; H, 3.32; N, 4.99. Found: C, 47.56; H, 3.29; N, 4.97.

[(Cp*)Ir(An-Dpa)](PF$_6$)$_2$ (7). The iridium dimer [(Cp*)Ir(μ-Cl)Cl]$_2$ (39.46 mg, 0.05 mmol) and silver nitrate (35.67 mg, 0.21 mmol) were dissolved in 20 mL MeOH, and stirred for 2 h at room temperature. Then the solution was centrifuged, and ligand **An-Dpa** (85.58 mg, 0.22 mmol) was added to the upper clear layer. The mixture was stirred for 48 h at room temperature, and concentrated before addition of NH$_4$PF$_6$ (163 mg, 1 mmol), which was subsequently kept at 277 K. The precipitate was filtered and washed with water, then dried under vacuum to obtain the product. Yield: 60 mg, 60%. HR-MS Calcd for [M-2PF$_6$]$^{2+}$ *m/z* 358.6342, found 358.6348; for [M-H-PF$_6$]$^{2+}$ *m/z* 716.2613, found 716.2619. ^{1}H NMR (500 MHz, d$_6$-DMSO): δ 8.99 (H, s), δ 8.77 (2H, d, *J* = 5.7 Hz), δ 8.55 (2H, d, *J* = 8.8 Hz), δ 8.30 (2H, d, *J* = 8.2 Hz), 8.00 (2H, t, *J* = 7.7 Hz), 7.74-7.67 (2H, m), 7.57 (2H, t, *J* = 6.6 Hz), 7.37 (2H, d, *J* = 7.9 Hz),

6.03 (2H, s), 5.05 (2H, d, J = 6.5 Hz), 3.92 (2H, d, J = 6.5 Hz), 1.89 (15H, s). ^{13}C{^{1}H} NMR (125 MHz, d$_6$-DMSO): δ 161.0, 151.0, 140.7, 132.4, 131.3, 131.3, 129.7, 127.7, 127.3, 125.6, 124.5, 123.4, 123.0, 91.0, 67.5, 59.9, 8.1. Anal. Calcd for C$_{37}$H$_{38}$F$_{12}$IrN$_3$P$_2$: C, 44.14; H, 3.80; N, 4.17. Found: C, 44.82; H, 3.73; N, 4.20. HPLC retention time 17.8 min.

[(Cp^{xph})Ir(An-Dpa)](PF$_6$)$_2$ (8). Synthesis as for complex **7** using the ligand **An-Dpa** (85.58 mg, 0.11 mmol) and [(Cp^{xph})Ir(μ-Cl)Cl]$_2$ (46.04 mg, 0.05 mmol). Yield: 70 mg, 65%. HR-MS Calcd. for [M-2PF$_6$]$^{2+}$ m/z 389.6422, found 389.6422; for [M-H-PF$_6$]$^+$ m/z 778.2770, found 778.2765. ^{1}H NMR (500 MHz, d$_6$-DMSO): δ 8.94 (H, s), 8.74 (2H, d, J = 5.7 Hz), 8.25 (2H, d, J = 8.2 Hz), 8.14 (2H, d, J = 8.3 Hz), 8.00 (2H, t, J = 7.7 Hz), 7.68-7.61 (9H, m), 7.55 (2H, t, J = 6.6 Hz), 7.39 (2H, d, J = 7.9 Hz), 5.71 (2H, s), 5.08 (2H, d, J = 6.4 Hz), 3.94 (2H, d, J = 6.4 Hz), 2.06 (6H, s), 1.94 (6H, s). ^{13}C{^{1}H} NMR (125 MHz, d$_6$-DMSO): δ 160.7, 151.0, 141.1, 132.1, 131.4, 131.1, 130.2, 129.8-129.7, 127.9, 127.8, 127.5, 125.5, 124.0, 123.7, 122.4, 95.0, 89.5, 68.1, 60.0, 9.0, 8.0. Anal. Calcd for C$_{42}$H$_{40}$F$_{12}$IrN$_3$P$_2$: C, 47.19; H, 3.77; N, 3.93. Found: C, 47.03; H, 3.81; N, 3.89. HPLC retention time 19.7 min.

[(Cp^{xbiph})Ir(An-Dpa)](PF$_6$)$_2$ (9). Synthesis as for complex **8** using the ligand **An-Dpa** (85.58 mg, 0.11 mmol) and [(Cp^{xbiph})Ir(μ-Cl)Cl]$_2$ (58.12 mg, 0.05 mmol). Yield: 70 mg, 61%. HR-MS Calcd. for [M-2PF$_6$]$^{2+}$ m/z 427.6579, found 427.6581; for [M-H-PF$_6$]$^+$ m/z 1000.2840, found 1000.2824. ^{1}H NMR (500 MHz, d$_6$-DMSO): δ 8.92 (H, s), 8.75 (2H, d, J = 5.7 Hz), 8.23 (4H, m), 8.00 (2H, t, J = 7.7 Hz), 7.90 (2H, d, J = 8.2 Hz), 7.76 (2H, d, J = 8.2 Hz), 7.70 (2H, d, J = 7.5 Hz), 7.65-7.60 (4H, m), 7.55 (2H, t, J = 6.5 Hz), 7.49 (2H, t, J = 7.7 Hz), 7.42 (1H, d, J = 7.3 Hz), 7.39 (2H, d, J

= 8.1 Hz), 5.78 (2H, s), 5.12 (2H, d, J = 6.6 Hz), 3.97 (2H, d, J = 6.6 Hz), 2.11 (6H, s), 1.96 (6H, s). $^{13}C\{^1H\}$ NMR (125 MHz, d_6-DMSO): δ 160.8, 151.1, 141.1, 141.1, 138.9, 132.2, 131.5, 131.3, 130.9, 129.8, 129.3, 128.3, 127.8, 127.7, 127.6, 127.1, 126.7, 125.6, 124.1, 123.7, 122.5, 94.9, 89.6, 68.2, 60.0, 10.0, 8.1. Anal. Calcd for $C_{42}H_{40}F_{12}IrN_3P_2$: C, 47.19; H, 3.77; N, 3.93. Found: C, 47.08; H, 3.85; N, 3.89. HPLC retention time 23.2 min.

[(Cp*)Ir(Bdp-Dpa)](NO₃)₂ (10). The iridium dimer [(Cp*)Ir(μ-Cl)Cl]₂ (39.46 mg, 0.05 mmol) and silver nitrate (33.97 mg, 0.2 mmol) were dissolved in 20 mL MeOH, and stirred for 2 h. The solution was centrifuged, then ligand **Bdp-Dpa** (53 mg, 0.099 mmol) was added to the upper clear layer. The mixture was stirred for 48 h at room temperature, and the product was obtained through concentration of the solvent and recrystallization from diethyl ether. Yield: 77 mg, 78%. HR-MS Calcd for [M-2NO₃]²⁺ m/z 431.6760, found 431.6753; for [M-H-2NO₃]⁺ m/z 862.3438, found 862.3447. ^{1}H NMR (400 MHz, d_4-MeOD): δ 8.76 (2H, d, J = 5.4 Hz), 8.04-7.96 (4H, m), 7.64-7.54 (6H, m), 6.13 (2H, s), 5.29 (2H, d, J = 16.6 Hz), 5.20 (2H, s), 4.36 (2H, d, J = 16.6 Hz), 2.52 (6H, s), 1.84 (15H, s), 1.50 (6H, s). HPLC retention time 20.4 min.

[(ppy)₂Ir(Ppy-Phen)]Cl. (11) A solution containing [(ppy)₂Ir(μ-Cl)]₂ (64.32 mg, 0.06 mmol) and **Ppy-Phen** ligand (51.04 mg, 0.136 mmol) in MeOH (10 mL) was refluxed in the dark under nitrogen atmosphere for 21 h at 348 K. The solvent was reduced in volume on a rotary evaporator. A yellow residue exhibiting orange fluorescence was purified through Al₂O₃ column chromatography using DCM/MeOH (50/1 v/v), or alternatively, on a Biotage Sil Zip-10g column using

225

DCM/MeOH (9/1 v/v). The component solution was reduced to dryness and the product was recrystallized from Et$_2$O/MeOH. The precipitate was collected by filtration and dried under vacuum. Yield: 90 mg, 82%. HR-MS Calcd for [M-Cl]$^+$ *m/z* 877.2240, found 877.2252. ^{1}H NMR (500 MHz, d$_6$-DMSO): δ 11.19 (1H, s), 9.00 (1H, d, *J* = 8.4 Hz), 8.92 (1H, d, *J* = 8.7 Hz), 8.75 (1H, d, *J* = 4.3 Hz), 8.64 (1H, s), 8.33 (2H, d, *J* = 8.4 Hz), 8.30-8.26 (5H, m), 8.16 (1H, d, *J* = 4.9 Hz), 8.13 (1H, d, *J* = 7.9 Hz), 8.07 (1H, dd, *J* = 5.0 Hz, 8.5 Hz), 8.04 (1H, dd, *J* = 5.1 Hz, 8.2 Hz), 7.98-7.95 (3H, m), 7.91 (2H, q, *J* = 7.3 Hz), 7.51 (2H, d, *J* = 5.7 Hz), 7.45 (1H, dd, *J* = 4.9 Hz, 7.4 Hz), 7.09-7.01 (4H, m), 6.96 (2H, t, *J* = 7.3 Hz), 6.31 (2H, t, *J* = 6.5 Hz). ^{13}C{^{1}H} NMR (125 MHz, d$_6$-DMSO): δ 166.9, 166.5, 154.9, 150.9, 150.0, 149.8, 149.7, 149.1, 146.5, 144.4, 144.1, 144.0, 142.1, 138.8, 138.5, 137.5, 135.7, 134.4, 134.0, 131.3, 130.6, 130.3, 128.7, 128.1, 127.3, 126.6, 125.1, 124.0, 123.9, 123.4, 122.6, 122.4, 120.9, 120.1, 120.0. Anal. Calcd for C$_{46}$H$_{32}$ClIrN$_6$O: C, 60.55; H, 3.54; N, 9.21. Found: C, 59.93; H, 3.60; N, 8.70. HPLC retention time 21.7 min.

[(ppy)₂Ir(Ppy-Phen)(Cp*Ir)Cl]Cl (12). The iridium dimer [(Cp*)Ir(μ-Cl)Cl]$_2$ (15.92 mg, 0.02 mmol) and silver nitrate (6.79 mg, 0.04 mmol) were dissolved in 10 mL MeOH, and sonicated for 3 min. Then complex **11** (36.50 mg, 0.04 mmol) was added to the solution, which was stirred for 4 days at room temperature. The solvent was removed on a rotary evaporator and the residue was purified on a Al$_2$O$_3$ column with MeOH/DCM (5/95 v/v) or alternatively on a Biotage Sil Zip-10g column using DCM/MeOH (4/1 v/v). Yield: 22 mg, 44%. HR-MS Calcd for [M-Cl]$^+$*m/z* 1239.2668, found 1239.2679. ^{1}H NMR (500 MHz, d$_4$-MeOD): δ 8.86-8.84 (2H, m), 8.73 (1H, d, *J* = 8.2 Hz), 8.55 (1H, d, *J* = 4.8 Hz), 8.49 (1H, s), 8.39 (1H, d, *J* = 4.7 Hz), 8.33 (1H,

d, J = 4.9 Hz), 8.14 (3H, m), 7.98-7.87 (6H, m), 7.82 (2H, t, J = 7.8 Hz), 7.76 (1H, d, J = 8.0 Hz), 7.51 (2H, t, J = 5.9 Hz), 7.37 (1H, t, J = 6.4 Hz), 7.08 (2H, t, J = 7.5 Hz), 6.97-6.93 (4H, m), 6.42 (2H, d, J = 7.4 Hz), 1.71 (15H). $^{13}C\{^1H\}$ NMR (125 MHz, d_4-MeOD): δ 171.2, 169.5, 167.3, 164.3, 153.7, 152.6, 152.0, 151.0, 150.7, 150.3, 148.9, 146.9, 145.6, 139.8, 139.7, 139.6, 136.6, 136.2, 135.9, 133.1, 132.6, 131.7, 130.2, 128.2, 127.7, 126.2, 125.4, 124.9, 124.6, 124.4, 124.3, 124.0, 123.2, 121.3, 121.2, 90.5, 9.1. Anal. Calcd for $C_{56}H_{46}Cl_2Ir_2N_6O$: C, 52.78; H, 3.64; N, 6.59. Found: C, 52.24; H, 3.57; N, 6.71. HPLC retention time 24.8 min.

6.2.3 Methods

The NMR spectroscopy, ESI-MS analysis, elemental analysis, UV-vis spectroscopy, pH measurements, HPLC, LC-MS, cyclic voltammetry, ICP-OES, ICP-MS, cell culture, and cell viability assay were carried out as described in Chapter 2.

6.2.3.1 X-ray Crystallography

The X-ray crystal structure **4**·2MeOH was solved by Dr. Guy Clarkson (Department of Chemistry, University of Warwick). Single crystals of $C_{35}H_{39}FeI_2IrN_4O_2$ (**4**·2MeOH) were grown from methanol/Et$_2$O. The details of the diffraction instrumentation are described in Chapter 2. Using Olex2,[37] the structure was solved with the ShelXS[38] structure solution program using Direct Methods and refined with the ShelXL[39] refinement package using Least Squares minimisation. The asymmetric unit contains the complex, an iodido counter ion and two solvent methanol molecules.

6.2.3.2 Catalytic NADH Oxidation

UV-vis spectroscopy was utilized to monitor the reaction between the tested complex (complexes **11**, **12**, and **13**) with NADH under various conditions at 298 K in the dark and blue light irradiation (463 nm). TON is defined as the number of moles of NADH that a mole of the tested catalyst can convert within 30 min. TOF was calculated from the linear fitting of TON vs. time (h) by Origin 2018. The concentration of NADH was obtained using the extinction coefficients $\varepsilon_{339} = 6{,}220$ M^{-1} cm^{-1}.[40]

6.2.3.3 Luminescence Spectroscopy

Luminescent emission measurements were performed on a JASCO FP-6500 spectrofluorometer. Compound **7**, **10**, **11**, or **12** (*ca.* 10 µM) in 98% (v/v) PBS was diluted from a stock solution in DMSO (1 mM). The complexes were excited at $\lambda_{ex} = 405$ nm/460 nm in a 1-cm quartz cuvette at 298 K. Experiments were performed under air at room temperature.

6.2.3.4 Log *P* Determination

The partition coefficient (log *P*) were determined for complexes **11** and **12** following the procedure: 1-octanol saturated aqueous NaCl solution and aqueous NaCl solution saturated 1-octanol were prepared by stirring the mixtures of 100 mL 1-octanol and 100 mL aqueous NaCl (15 mM) solution for 24 h and separated with a separating funnel after 3-4 h equilibration. Saturated solution of iridium complexes (3.0-4.0 mg) in 10 mL 1-octanol saturated aqueous NaCl solution were prepared by shaking the suspension on an IKA Vibrax VXC basic shaker for 5 h at the speed of 1000 r/min.

Then the suspension was filtered through a hydrophobic HPLC filter. An aliquot (2 mL) of the final filtrate was added into NaCl aqueous saturated octanol (2 mL) in triplicate. The two-layer solution was shaken on an IKA Vibrax VXC basic shaker for 15 h at the speed of 1000 r/min and subsequently equilibrated for 1.5 h. Aqueous samples before and after partitioning in octanol were diluted in the ratio (v/v) of 1: 10 and 1:5, respectively, with 3.6% (v/v) HNO_3 to the appropriate range for ICP-MS analysis. The iridium concentration was calibrated with aqueous standards in 3.6 % HNO_3 (0-700 ppb). Log P values for iridium complexes were calculated using the equation log $P_{o/w}$ = log([Ir]$_{octanol}$/[Ir]$_{aqueous}$).

6.2.3.5 *In vitro* Dark and Photocytotoxicity Assays

Phototoxicity assays on the human nasopharyngeal carcinoma cell line were performed by Dr. Huaiyi Huang (School of Pharmaceutical Science, Sun Yat-sen University). For adherent cells, 10,000 human cancer cells were seeded per well in 96-well plates and incubated in a 5% CO_2/95% air incubator at 310 K for 24 h. The stock solution of each tested compound was prepared in 0.5% DMSO (v/v) mixture with cell culture medium, followed by serial dilutions with fresh medium. Then the supernatants of each well were removed by suction and replaced with the diluted compound-containing solution and incubated in the dark for 4 h. The drug-containing supernatants were removed by suction and the cells were washed with PBS 3 times (for human nasopharyngeal carcinoma cells) and washed once with PBS (for human ovarian cancer cells), followed by adding fresh phenol-red-free cell culture medium. Then the cells were either kept in the dark or received blue light irradiation (463 nm,

light dose 11.7 J/cm^2). The cells were left to recover in the dark in the incubator for a further 44 h. The cytotoxicity against human nasopharyngeal carcinoma cells was measured by the MTT assay on a microplate spectrometer (Biorad); the cytotoxicity against human ovarian cancer cells were determined by the SRB assay on a GloMax-Multi Microplate Multimode Reader.

6.2.3.6 Confocal Microscopy

Confocal microscopy experiments were carried out with the help of Hannah E. Bridgewater (School of Life Science, University of Warwick). A2780 human ovarian cancer cells (10,000 cell/well) were seeded in 10-well plate with black side wall, and incubated at 37 °C for 24 h. The complex was incubated with the cells in the dark at 37 °C for 4 h. Then each well was washed with PBS twice. (i) Mitotracker in PBS was added to the well and incubated for 30 min at ambient temperature. After PBS wash, the cells were fixed with 4% (v/v) paraformaldehyde for 30 min at ambient temperature. After PBS wash, mounting gel were added into wells and sealed with cover slides and acetone around the edges. (ii) The cells were fixed with 4% (v/v) paraformaldehyde for 30 min at ambient temperature. After 2x PBS washes, 0.1% triton was added to each for 3-5 min. After 2x PBS washes, Alex fluor 633 Phalloidin in PBS was incubated with the cells at ambient temperature for 20 min, then the wells were washed with PBS once. Mounting gel was added and sealed with cover slides. The images were observed on a LSM880 microscope with λex/λem = 633/620–800 nm for Alex fluor 633 Phalloidin stain; 579/590–700 nm for Mitotracker Red stain.

6.3 Results

6.3.1 Synthesis of Ligands
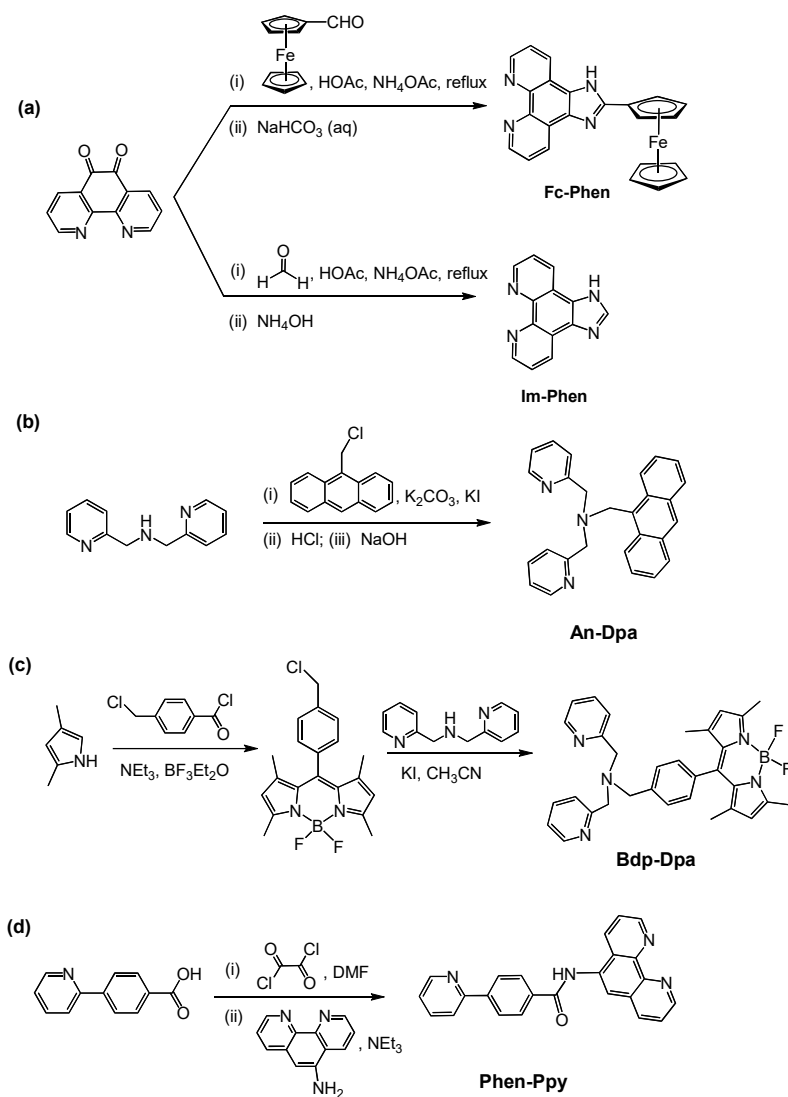
Scheme 6.2. The synthetic routes for the ligands. **Phen**: phenanthroline; **Fc**: Ferrocene; **Im**: Imidazole; **An:** Anthracene; **Bdp:** BODIPY; **Ppy**: 2-phenylpyridine.

Three classes of ligands (i) ferrocene-conjugated **Fc-Phen** and the non-ferrocene conjugated **Im-phen**; (ii) the anthracene/BODIPY-conjugated **An-Dpa**/**Bdp-DPa**;

(iii) the 2-phenylpyridine-conjugated 1,10-pehnanothraline **Ppy-Phen**, were synthesised as reported with good yields, as shown in Scheme 6.2.

6.3.2 Ferrocene-Conjugated Complexes

6.3.2.1 Synthesis and Characterisation

The synthesis of the Fc-conjugated iridium complexes **1-6** was conducted by reacting the dimer precursor $[(Cp^X)Ir(\mu-Z)Z]_2$ ($Cp^X = Cp^*$, Cp^{xph}, or Cp^{xbiph} ; $Z = Cl/I$) with the 2 mol equiv. of ferrocene conjugated ligand **Fc-Phen** as shown in Scheme 6.3 (details in **6.2.2.2** in the Experimental Section). To explore the effect of the Fc group on the property of the complexes, analogues **1A** and **3A** were also synthesised from the 2 mol equiv. of non-Fc conjugated ligand **Im-phen** reacting with the dimer precursor $[(Cp^X)Ir(\mu-Cl)Cl]_2$ as shown in Scheme 6.3. All the complexes were obtained with good yields (63%-92%), and characterised by ^1H NMR, ^{13}C NMR spectroscopy, mass spectrometry and elemental analysis. In the ^1H NMR spectra of Fc-conjugated complexes, proton signals within δ 4.1-5.3 ppm are assignable to the Fc group in three separate sets of peaks with the ratio of 2:2:5 (H_A:H_B:H_C, shown in Figure 6.3 for complex **1**). Meanwhile, the methyl protons on the Cp^X ring of complexes **1A** and **3A** exhibit the same chemical shifts as the Cp^X methyl protons in Fc-conjugated complexes **1** and **3**, respectively.
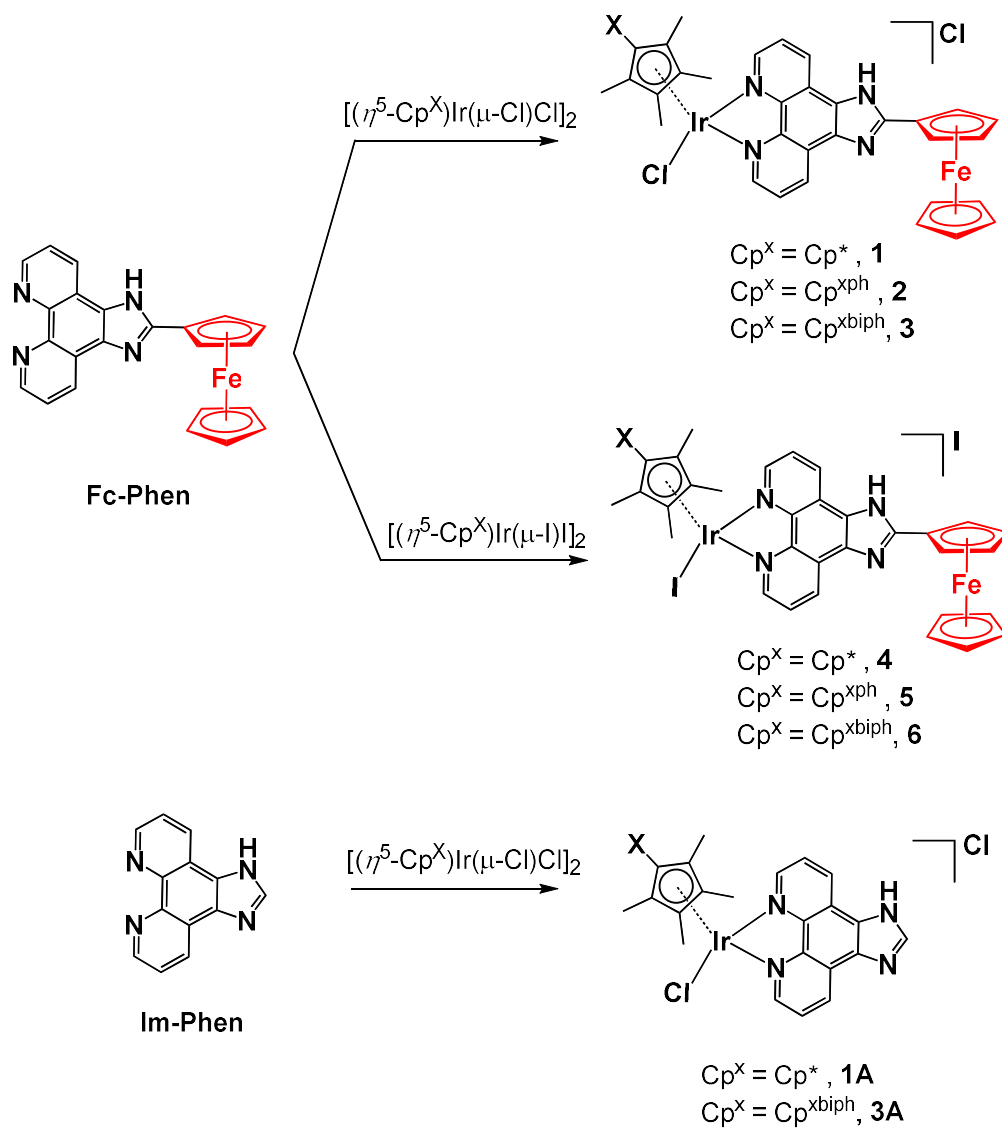
Scheme 6.3. Synthetic route for ferrocene-conjugated half-sandwich iridium complexes **1-6** from ligand **Fc-Phen** with the iridium chlorido/iodido dimer precursor; and for the non-ferrocene-conjugated analogues **1A** and **3A** prepared from the ligand **Im-Phen** with the iridium chlorido dimer precursor.
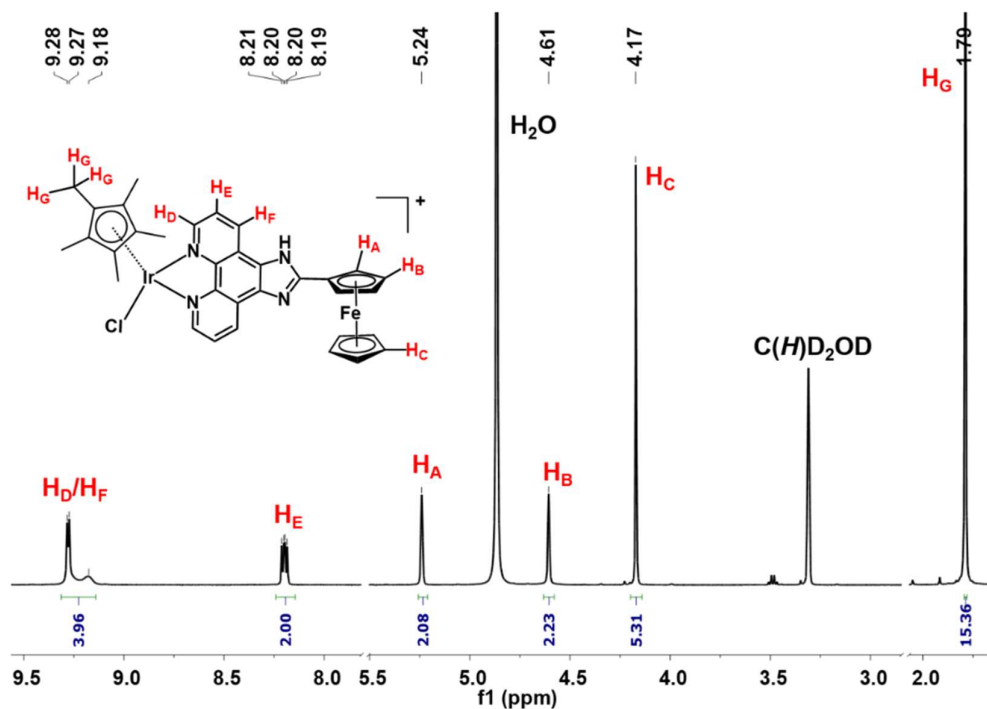
Figure 6.3. ^{1}H NMR spectrum (500 MHz, d$_4$-MeOD) of complex **1** with protons assigned.

The X-ray crystal structure [(Cp*)Ir(Fc-Phen)I]I·2MeOH (**4**·2MeOH) was determined. The crystals were grown by diffusion of diethyl ether into a methanol solution. The atom numbering scheme is shown in Figure 6.4. Crystallographic data are shown in Table 6.1 and selected bond lengths and angels are listed in Table 6.2. Around the iridium centre, the Ir-I bond of 2.6987(6) Å is the longest (Table 6.2**)**, longer than the Ir-I bond lengths (2.6799(5)-2.6851(2) Å) in the crystal structures of Cp* iridium azopyridine complexes described in Chapter 3.
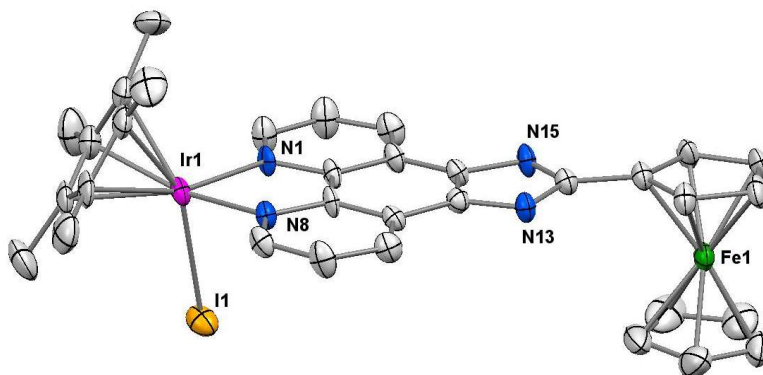
Figure 6.4. X-ray crystal structure with key atom numbering scheme for [(Cp*)Ir(Fc-Phen)I]I·2MeOH (**4**·2MeOH), drawn with thermal ellipsoids at 50% probability level. Two methanol molecules and the I⁻ counterion have been omitted for clarity.

The crystal structure confirms coordination of the ligand **Fc-phen** in a bidentate N^N fashion, forming a five-membered chelating ring with the metal centre. The Ir centre adopts the familiar three-legged "piano-stool" geometry.

In the structure, one of the cyclopentadienyl rings in Fc is in the same plane with the covalently bound imidazole[4,5-f]1,10-phenanthroline unit. The two pendant cyclopentadienyl rings are in a staggered conformation. Interestingly, the distances of the Fe1 atom from the two cyclopentadienyl rings in Figure 6.4 are different, with a distance of Fe1 from the bottom ring being 1.649 Å and the other distance of Fe1 from the upper Cp ring bound to phenanthroline though the imidazole ring being 1.634 Å (Table 6.2).

Table 6.1. Crystallographic data for **4**·2MeOH.

	4·2MeOH
Empirical formula	$C_{35}H_{39}FeI_2IrN_4O_2$
MW	1049.55
T[K]	150(2)
Crystal size/mm^3	$0.22 \times 0.08 \times 0.04$
Crystal system	monoclinic
Space group	$P2_1/n$
a [Å]	8.06829(10)
b [Å]	20.2192(2)
c [Å]	22.4102(3)
α [°]	90
β [°]	90.0234(10)
γ [°]	90
Volume [Å^3]	3655.89(8)
Z	4
ρ_{calc} [g cm^3]	1.907
μ [mm^{-1}]	23.663
F (000)	2008.0
Radiation	CuKα (λ = 1.54184)
θ range [°]	7.89 to 146.91
Index ranges	$-9 \le h \le 9$ $-25 \le k \le 25$ $-27 \le l \le 27$
Reflections collected	69862
Independent reflections	7299 [R_{int} = 0.1136]
Data/restraints/parameters	7299/31/425
Goodness of fit	1.043
Final R indexes [I>2σ(I)]	0.0358/0.0914
Final R indexes [all data]	0.0360/0.0918
Largest diff. peak/hole/eÅ^{-3}	1.31/-2.58

Table 6.2. Selected bond lengths (Å) and angles (deg) for **4**·2MeOH.

Bonds	Lengths
Ir1-C (Cp*)	2.158(7)
	2.203(6)
	2.187(7)
	2.161(8)
	2.166(8)
Ir1-Cp* (Centroid)	1.801
Ir1-N1	2.094(5)
Ir1-N8	2.095(5)
Ir1-I1	2.6987(6)
Fe1-Cp (Centroid bound with the bidentate ligand)	1.634
Fe1-Cp (Centroid)	1.649
I1-Ir1-N1	84.98(17)
I1-Ir1-N8	85.40(16)
N1-Ir-N8	77.8(2)

6.3.2.2 Electrochemical Oxidation of the Ferrocene Group

The effects that substituents could have on the redox potential of the Fc group were studied for complexes **1-4** by cyclic voltammetry in acetonitrile solutions (1 mM) using 0.1 M [Bu$_4$N]PF$_6$ as the background electrolyte. Fc was used as a standard. Free **Fc-Phen** ligand and complex **1A** were studied for comparison. The complex was subjected to two cyclic scans between 0 and 1.5 V at a scan rate of 500 mV S^{-1}. The electrochemical redox potentials are shown in Table 6.3.

Table 6.3. Redox potentials[a] (V) of complexes **1-4**, **1A** and free ligand **Fc-Phen** in comparison with ferrocene (**Fc**). E_{pa}/i_{pa} = anodic peak potential/current; E_{pc}/i_{pc} = cathodic peak potential/current; $E_{1/2}$ = half-wave potential.

Complex	E_{pa} (V)	E_{pc} (V)	$E_{1/2}$ (V)[b]	i_{pa}/i_{pc}	E_{pa} (V)
1-[(Cp*)Ir(Fc-Phen)Cl]Cl	0.217	0.181	0.199	1.047	0.736
2-[(Cp^{xph})Ir(Fc-Phen)Cl]Cl	0.213	0.176	0.195	1.169	0.808
3-[(Cp^{xbiph})Ir(Fc-Phen)Cl]Cl	0.246	0.194	0.220	1.123	0.942
4-[(Cp*)Ir(Fc-Phen)I]I	0.309	0.198	0.253	0.835	-
1A-[(Cp*)Ir(Im-Phen)Cl]Cl	-	-	-	-	0.771
Fc-Phen	0.242	0.153	0.148	1.175	-
Fc	0.101	0.000	0.051	1.042	-

[a] Measured in CH_3CN at a scan rate of 500 mV S^{-1} and referenced to Ag/Ag$^+$.

[b] $E_{1/2}$ = (E_{pa} + E_{pc})/2.

The ferrocene standard exhibits a one-electron reversible wave with I_{pa}/I_{pc} = 1.042 and $E_{1/2}$ = 0.051 V relative to the Ag/Ag$^+$ reference electrode. The analogue of complex **1**, complex **1A** exhibits a single redox anodic peak at 0.771 V for the iridium Ir^{III}/Ir^{IV}, consistent with the reported electron-transfer process for Ir^{III} → Ir^{IV}.[14] Complexes **1-4** exhibit two redox processes with the first anodic peak at 0.213-0.309 V ($E_{1/2}$ = 0.195-0.253 V) corresponding to the redox couple of Fc/Fc$^+$, which is positively-shifted compared with Fc itself ($E_{1/2}$ = 0.051 V) and the ligand Fc-Phen ($E_{1/2}$ = 0.148 V). The separation of the peaks (ΔE_p = 36-111 mV), as well as the current ratios (**i_{pa}/i_{pc}**) close to unity, revealed that the Fc/Fc$^+$ couples are reversible or

quasi-reversible one-electron redox processes for complexes **1-4**. The second anodic peak for complexes **1-3** at 0.726-0.942 V is assigned to the oxidation of iridium ion. Compared with the $E_{1/2} = 0.199V$ of Fc/Fc$^+$ in the chlorido complexes **1-3**, the $E_{1/2} = 0.253$ V for Fc/Fc$^+$ in the iodido complex **4** is shifted positively, thus the iodido ligand has made oxidation of the ferrocene group more difficult.

6.3.2.3 Aqueous Stability of Complexes 1/1A and 4

The hydrolysis of chlorido Cp* iridium complex [(Cp*)Ir(Fc-Phen)Cl]Cl (**1**) and iodido Cp* iridium complex [(Cp*)Ir(Fc-Phen)I]I (**4**) (*ca.* 2 mM) in d$_4$-MeOD/D$_2$O (1/1 v/v) at 310 K was monitored by ^{1}H NMR spectroscopy up to 24 h. The presence of methanol ensured the solubility of the complexes. The ^{1}H NMR spectra showed no additional peaks over 24 h. The final NMR solutions were subjected to ESI-MS analysis which detected the major peaks with *m/z* at 767.2 (calcd 767.1) and 859.1(calcd 859.0) corresponding to [**1**]$^+$ and [**4**]$^+$, respectively. Thus, the two complexes do not appear to hydrolyze under the NMR conditions.

The stability of complex **1** in the dark or under blue light (463 nm) exposure was studied by UV-visible spectroscopy. The UV-vis absorption of complex **1** (25 μM in PBS, pH 7.4) did not show any changes over 30 min as shown in Figure 6.5. However, when the same solution was irradiated with 463 nm light, the UV-vis absorption changed significantly with the irradiation time, shown in Figure 6.6a. The absorption band at 400-500 nm range which is the ferrocene-centred band disappeared sharply within only 5 min of light irradiation.
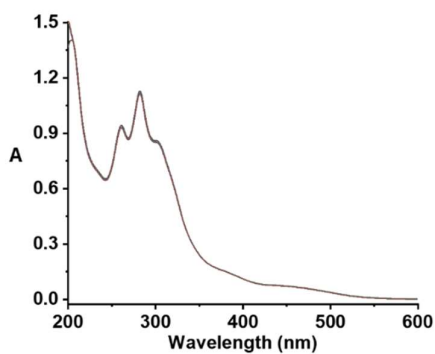
Figure 6.5. The UV-vis absorption spectra recorded every 5 min for complex **1** (25 μM) in MeOH/PBS (1/39 v/v, pH 7.4) under dark condition over 30 min.
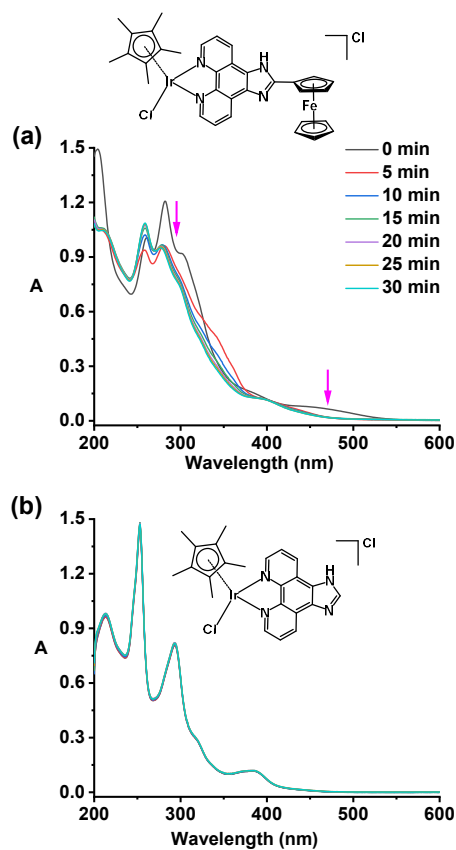
Figure 6.6. UV-vis absorption spectra recorded every 5 min for (a) complex **1** (25 μM); (b) complex **1A** (20 μM) in 2.5% MeOH/97.5% PBS buffer (v/v) upon irradiation with 463 nm light over 30 min.

240

In contrast, when solution of Cp* iridium complex **1A** (20 μM) in 2% MeOH/PBS (v/v, pH 7.4) was irradiated under the same condition, no significant changes occurred as shown in Figure 6.6b, confirming that the UV-vis changes of complex **1** were induced by the additional ferrocene moiety in ligand **Fc-Phen** under irradiation.

6.3.2.4 Anticancer Activity of Complexes 1-3

The antiproliferative activity of Fc-conjugated chlorido iridium complexes **1-3** was determined by 24 h complex treatment of A2780 human ovarian cancer cells followed with 72 h cell recovery. The Cp* complex **1** was inactive and non-toxic (IC_{50} > 100 μM), but Cp^{xph} complex **2** and Cp^{xbiph} complex **3** showed moderate antiproliferative activity (Table 6.4) compared to the clinical anticancer drug cisplatin. Meanwhile, they are less active than the analogous iridium complexes containing the 1,10-phenathroline (Phen) ligand without the ferrocene conjugation.

Table 6.4. The antiproliferative activity of complexes **1-3** against human A2780 cancer cell line, in comparison with cisplatin and the three iridium analogous complexes[41] containing 1,10-phenathroline (Phen) ligand.

Complex	IC$_{50}$ (μM)	Complex	IC$_{50}$ (μM)
1-[(Cp*)Ir(Fc-Phen)Cl]Cl	>100	[(Cp*)Ir(Phen)Cl]Cl	>100^a
2-[(Cp^{xph})Ir(Fc-Phen)Cl]Cl	17.29 ± 7.95	[(Cp^{xph})Ir(Phen)Cl]Cl	6.70 ± 0.62^a
3-[(Cp^{xbiph})Ir(Fc-Phen)Cl]Cl	7.84 ± 1.67	[(Cp^{xbiph})Ir(Phen)Cl]Cl	0.72 ± 0.01^a
Cisplatin	2.71 ± 0.36		

^{a} These values are from ref. 41.

6.3.2.5 Interaction with 9-EtG of Complexes 1 and 4

Since DNA is a potential target for half-sandwich iridium anticancer complexes,[42] nucleobase binding to 9-EtG of chlorido complex **1** and iodido complex **4** was investigated. ^{1}H NMR spectra of complex **1** with 2 mol equiv. 9-EtG in d$_4$-MeOD/D$_2$O (1/1 v/v) over 24 h were recorded. About 50% of complex **1** formed an adduct with 9-EtG after 24 h at 310 K, which was confirmed by ESI-MS peak with m/z at 910.3 assignable as [(Cp*)(Ir-9-EtG)(L1)]$^+$ (**1_9-EtG**, calcd 910.8). However, under the same conditions, ^{1}H NMR spectra recorded for complex **4** with 9-EtG showed no additional peaks, indicating no adducts formed. Thus, the iodido iridium complex **4** is unlikely to target DNA.

6.3.3 Iridium Complexes Conjugated to Luminescent Probes

6.3.3.1 Iridium Complexes Conjugated to a Fluorescent Probe

Complexes **7-10** are synthesised through the reaction between 2 mol equiv. of κ^3-(N^N'^N) ligand An-Dpa or Bdp-Dpa and the dimer precursor $[(Cp^X)Ir(\mu-Cl)Cl]_2$ ($Cp^X = Cp^*$, Cp^{xph}, or Cp^{xbiph}) as shown in Scheme 6.4. The products were obtained with good yields (60%-78%) and confirmed by HR-MS with detected m/z peak assignable to the $[M-2PF_6]^{2+}$ or $[M-2NO_3]^{2+}$ (details in Section **6.2.2.2**) and a single retention peak in the HPLC chromatograph. Only one set of signals for the Cp^X methyl and the ligand was observed in the ^1H NMR spectra, indicating the symmetric κ^3-(N^N'^N)-coordination mode in **7-10** is as shown in Scheme 6.4. Such observations are in line with the reported half-sandwich iridium complexes similarly bearing a tridentate ligand.[43]
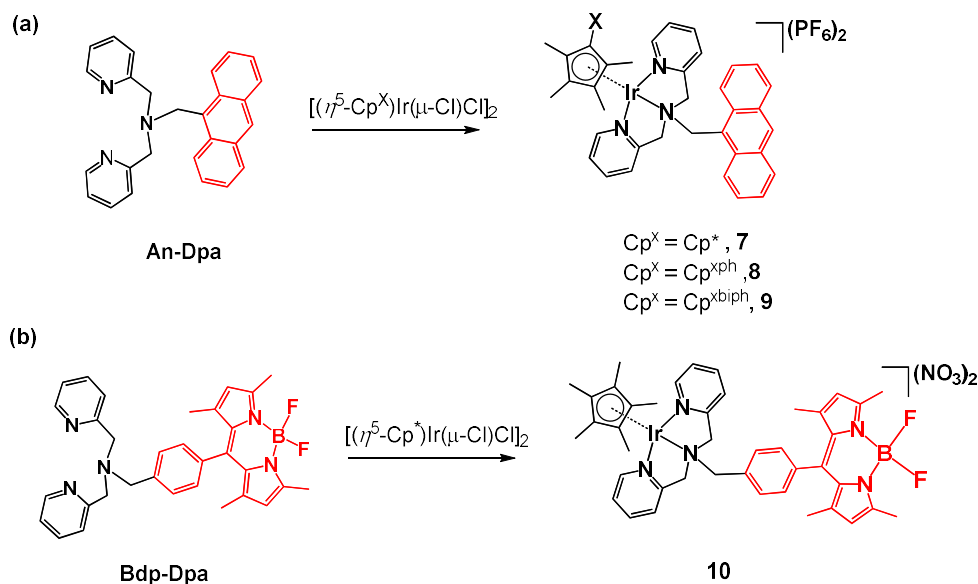
Scheme 6.4. Synthetic routes for the iridium complexes **7-10** conjugated with the fluorophore anthracenyl or BODIPY.

The aqueous stability of anthracene-conjugated iridium complexes $[(Cp^X)Ir(An-Dpa)](PF_6)_2$ (**7-9**, *ca.* 2 mM) was monitored by ^1H NMR in 35% d_6-DMSO/65% D_2O (v/v). All the complexes were stable over 24 h at 310 K. The stability of **7-9** (*ca.* 50 μM) in 5% DMSO/95% (v/v) cell culture medium (RPMI-1640 without phenol-red additive) was also investigated by UV-vis spectroscopy. The time-dependent spectra showed that the shapes and positions of the characteristic absorption peaks did not change significantly over 24 h at 310 K shown in Figure 6.7. The interaction of complex $[(Cp^*)Ir(An-Dpa)](PF_6)_2$ (**7**) with 3 mol equiv. 9-EtG or GSH was also studied by ^1H NMR spectroscopy in CD_3CN/D_2O (1/3 v/v), no changes indicating the formation of adducts were observed up to 24 h at 310 K.
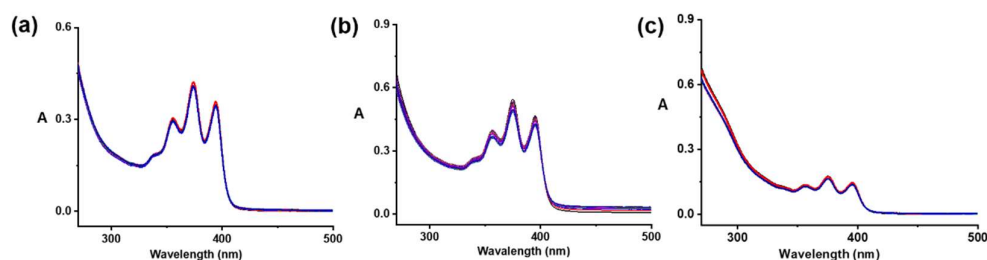
Figure 6.7. UV-vis spectra recorded every hour for (a) complex $[(Cp^*)Ir(An-Dpa)](PF_6)_2$ (**7**) (50 μM); (b) complex $[(Cp^{xph})Ir(An-Dpa)](PF_6)_2$ (**8**) (50 μM); (c) complex $[(Cp^{xbiph})Ir(An-Dpa)](PF_6)_2$ (**9**) (50 μM) in 5% DMSO/95% cell culture medium (RPMI-1640 without phenol-red additive) at 310 K over 24 h.

6.3.3.2 Iridium Complexes Conjugated to a Phosphorescent Probe

Alternatively, the conjugation of the $[Ir(C^\wedge N-ppy)_2]$ unit with the chlorido half-sandwich Cp^* iridium component to yield complex **12** was achieved by the reaction

of [Ir(ppy)₂]-coordinated complex **11** with dimer [(Cp*)Ir(μ-Cl)Cl]₂ in the aid of 2

mol equiv. silver nitrite (Scheme 6.5). Complexes **11** and **12** have been characterised

by ¹H NMR, ¹³C NMR, HR-MS, CHN elemental analysis and HPLC. Meanwhile,

the reported Cp* Ir complex **13**-[(Cp*)Ir(ppy)Cl]₂ (ppy = 2-phenylpyridine) has also

been synthesised for comparison.

The stability of complex **11** (15 µM) and **12** (11 µM) under blue light irradiation

at 463 nm (Figure 6.8) or in the dark (Figure 6.9) in acetonitrile/PBS (1/9 v/v) at 298

K was investigated by UV-vis spectroscopy. Both complexes exhibited no

photodegradation upon 463 nm light irradiation.
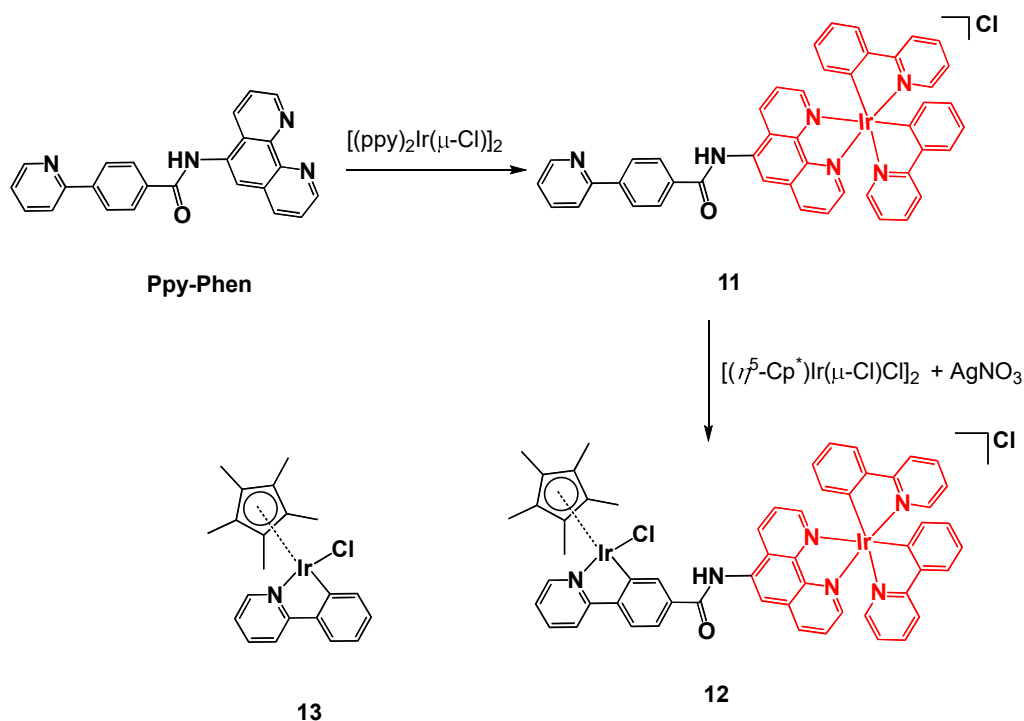
Scheme 6.5. Synthetic routes for the iridium complexes **11** and **12** and the structure

of complex **13**.
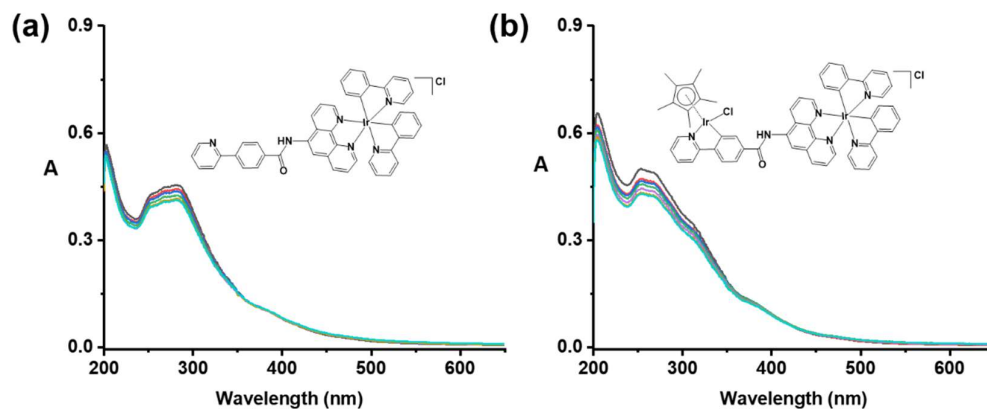
Figure 6.8. UV-vis absorption spectra recorded every 5 min for (a) complex **11** (15 µM); (b) complex **12** (11 µM) in acetonitrile/PBS (1/9 v/v) at 298 K upon irradiation with 463 nm blue light over 30 min.
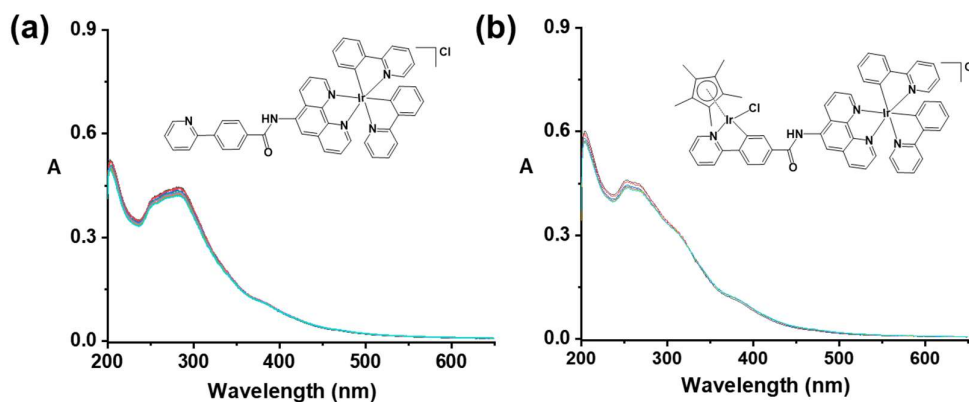
Figure 6.9. UV-vis absorption spectra recorded every 5 min for (a) complex **11** (15 µM); (b) complex **12** (11 µM) in acetonitrile/PBS (1/9 v/v) at 298 K in the dark over 30 min.

Cytotoxicity of organometallic complexes usually correlates with their lipophilicity, as complexes with high lipophilicity are highly cytotoxic.[44] The partition coefficients (log *P* values) for complexes **11** and **12** between 1-octanol layer

and the aqueous NaCl (15 mM) layer as a measurement of hydrophobicity were determined. Although both bear one positive charge, complex **12** containing one additional $[(Cp^*)IrCl]$ fragment is less hydrophobic (log P = -0.55) than complex **11** (log P = -0.09).

6.3.3.3 Photocytotoxicity

As the bis-cylcometalated iridium complexes are excellent photosensitizers in the photodynamic therapy,[27] cytotoxicity of the complexes **11** and **12** both bearing a cylcometalated iridium unit was evaluated under blue light irradiation. Complex $[(Cp^*)Ir(2-phenylpyridine)Cl]$ (**13**) and cisplatin were also studied under the same conditions. Their cytotoxicity (IC$_{50}$ values) in the dark or under light irradiation (463 nm, light dose 11.7 J/cm^2) against human nasopharyngeal carcinoma CNE-2Z cells was determined by the MTT assay, and cytotoxicity against human ovarian cancer cells determined by the sulforhodamine B (SRB) colorimetric assay as shown in Table 6.5. Phototoxicity index (PI) defined as IC$_{50(dark)}$/IC$_{50(irradiation)}$ is used to evaluate the potency of a phototherapeutic relative to its dark toxicity. Complex **11** gave a phototoxicity index of 13.2 and 16.8 towards CNE-2Z nasopharyngeal and A2780 ovarian cancer cells, respectively. For complex **12**, the PI is > 7 and > 13 towards CNE-2Z nasopharyngeal and A2780 ovarian cancer cells, respectively. In contrast, complex **13** and cisplatin are relatively non-toxic over the 4 h treatment with human nasopharyngeal carcinoma cells under irradiation or in the dark.

The anthracene-conjugated complex **7** and the BODIPY-conjugated complex **10** also exhibited phototoxicity giving the phototoxicity index of 4 and of >4, respectively, against A2780 human ovarian cancer cells.

Table 6.5. Cytotoxicity of iridium complexes and cisplatin towards human nasopharyngeal carcinoma CNE-2Z and A2780 ovarian cancer cells. IC_{50} values (µM) determined by 4 h drug treatment, 40 min irradiation (463 nm, 11.7 J/cm^2) and 44 h recovery in fresh medium; or 4 h drug treatment and 44 h recovery in the dark.

Compound	IC_{50} (µM) against CNE-2Z		IC_{50} (µM) against A2780	
	Dark	Irradiation (PI)[a]	Dark	Irradiation (PI)[a]
11-[(ppy)$_2$Ir(Ppy-Phen)]Cl	10.7	0.81 (13)	3.03 ± 0.18	0.18 ± 0.08 (17)
12-[(ppy)$_2$Ir(Ppy-Phen)(Cp*Ir)Cl]Cl	>100	13.7 (>7)	>100	7.79 ± 0.77 (>13)
13-[(Cp*)Ir(ppy)Cl]	>100	>100	ND	ND
Cisplatin	>100	>100	ND	ND
7-[(Cp*)Ir(An-Dpa)Cl](PF$_6$)$_2$	ND	ND	14.35	3.78 (4)
10-[(Cp*)Ir(Bdp-Dpa)Cl](NO$_3$)$_2$	ND	ND	>100	24.00 (>4)

[a] Phototoxicity Index = $IC_{50(dark)}/IC_{50(irradiation)}$; ND = not determined. IC_{50} values ± SD obtained from three independent experiments; IC_{50} values without SD obtained from three parallel samples in one experiment.

6.3.3.4 UV-vis Absorption and Luminescent Emission

The spectroscopic properties of complexes **7**, **10, 11** and **12** in phosphate buffered saline (PBS) containing 2% (v/v) DMSO at 298 K were studied and illustrated in Figure 6.10. These complexes showed intense UV-vis absorption bands in the range of 200-500 nm as shown in Figure 6.10a. Complex **10** exhibits an absorption maximum at 500 nm corresponding to the characteristic absorption of the BODIPY group.[45] Upon excitation at 405 nm, complex **7** exhibits an intense emission band at 425 nm corresponding to the characteristic emission of the anthracene unit,[46] and complex **11/12** exhibit maximum emission bands at 564/570 nm, respectively, Figure 6.10b. Upon excitation at 460 nm, complex **10** exhibits a maximum emission band at 514 nm (Figure 6.10b) due to the emission of the BODIPY ligand.[34]
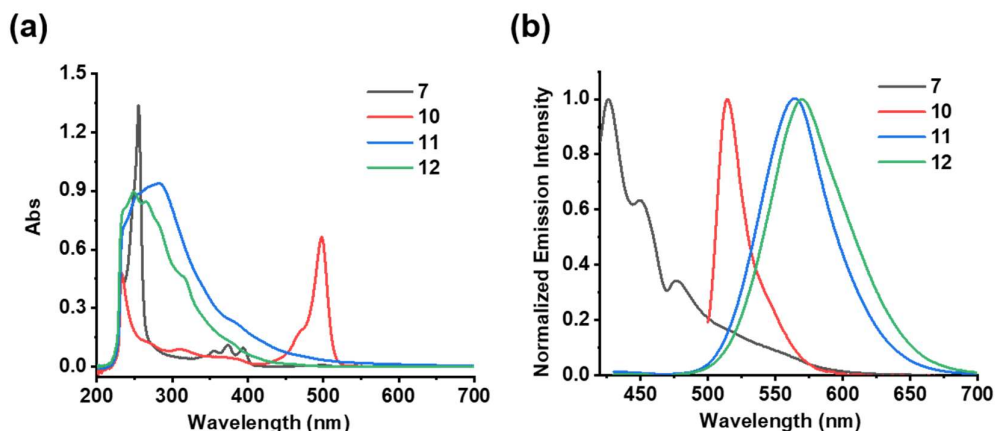
Figure 6.10. (a) UV-vis absorption spectra and (b) normalized phosphorescence emission spectra for *ca.* 10 µM complex $[(Cp^*)Ir(An-Dpa)](PF_6)_2$ (**7**), $[(Cp^*)Ir(Bdp-Dpa)](NO_3)_2$ (**10**), $[(ppy)_2Ir(Ppy-Phen)]Cl$ (**11**), or $[(ppy)_2Ir(Ppy-Phen)(Cp^*Ir)Cl]Cl$

(**12**) in DMSO/PBS (2/98 v/v, pH 7.4) at 298 K (λ_{ex} = 405 nm for **7**, **11**, and **12**; λ_{ex} = 460 nm for **10**).

6.3.3.5 Confocal Imaging Studies

To assess the imaging property of the luminescence from the iridium complexes conjugated with the luminescent probes *in vitro*, confocal microscopy was used to study their uptake and localization in the A2780 human ovarian cancer cells. Complexes [(Cp*)Ir(Bdp-Dpa)](NO$_3$)$_2$ (**10**), [(ppy)$_2$Ir(Ppy-Phen)]Cl (**11**), and [(ppy)$_2$Ir(Ppy-Phen)(Cp*Ir)Cl]Cl (**12**) with promising cytotoxicity were selected (Table 6.5). The phalloidin-iFluor 633 reagent selectively binds to actin. Actin is the monomeric subunit of two types of filaments in cells: the microfilaments are one of the three major components of the cytoskeleton; and thin filaments, part of the contractile apparatus in muscle cells. Ovarian cells were incubated with complex **10** (100 μM) for 4 h at 37 °C, then the cells were fixed with 4% (v/v) paraformaldehyde and stained with phalloidin-iFluor 633 (5 μM) at room temperature for 20 min. Alternatively, the MitoTracker red FM binding to lipids in the mitochondrial membranes, was used to stain the mitochondria. Ovarian cells were incubated with complex **10** (100 μM) for 4 h at 37 °C, then MitoTracker Red (5 μM) was added and the cells were incubated for 30 min at ambient temperature before being fixed with 4% (v/v) paraformaldehyde.

The overlapped image of the cells co-stained by complex **10** and phalloidin-iFluor 633 in Figure 6.11 indicates efficient cellular uptake of complex **10** after 4 h incubation with cancer cells. Meanwhile, it most likely targets the mitochondria from

the merged image, which is different from the reported half-sandwich iridium complexes usually found to localize in the lysozomes.[47-50] However, complexes **11** and **12** both show a large spread distribution in the human ovarian cancer cells and no specific localization from the fluorescent imaging data in Figure 6.13.
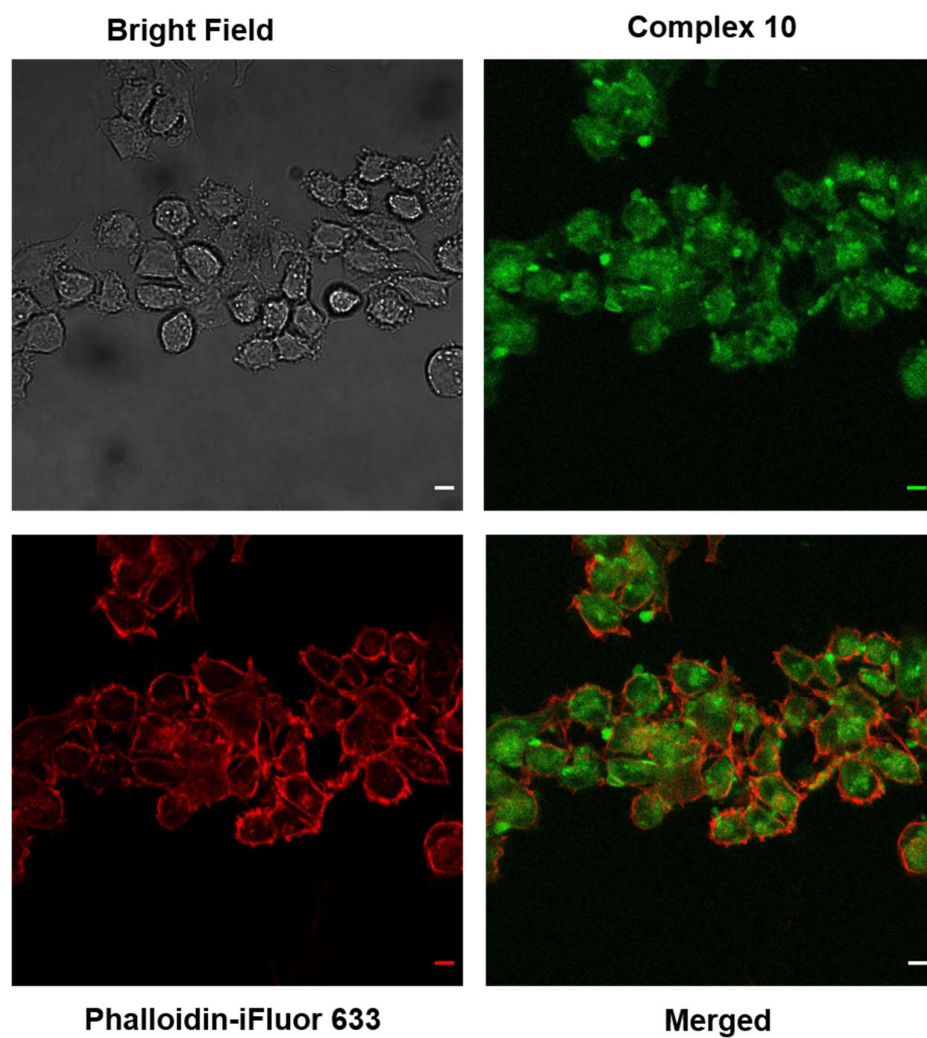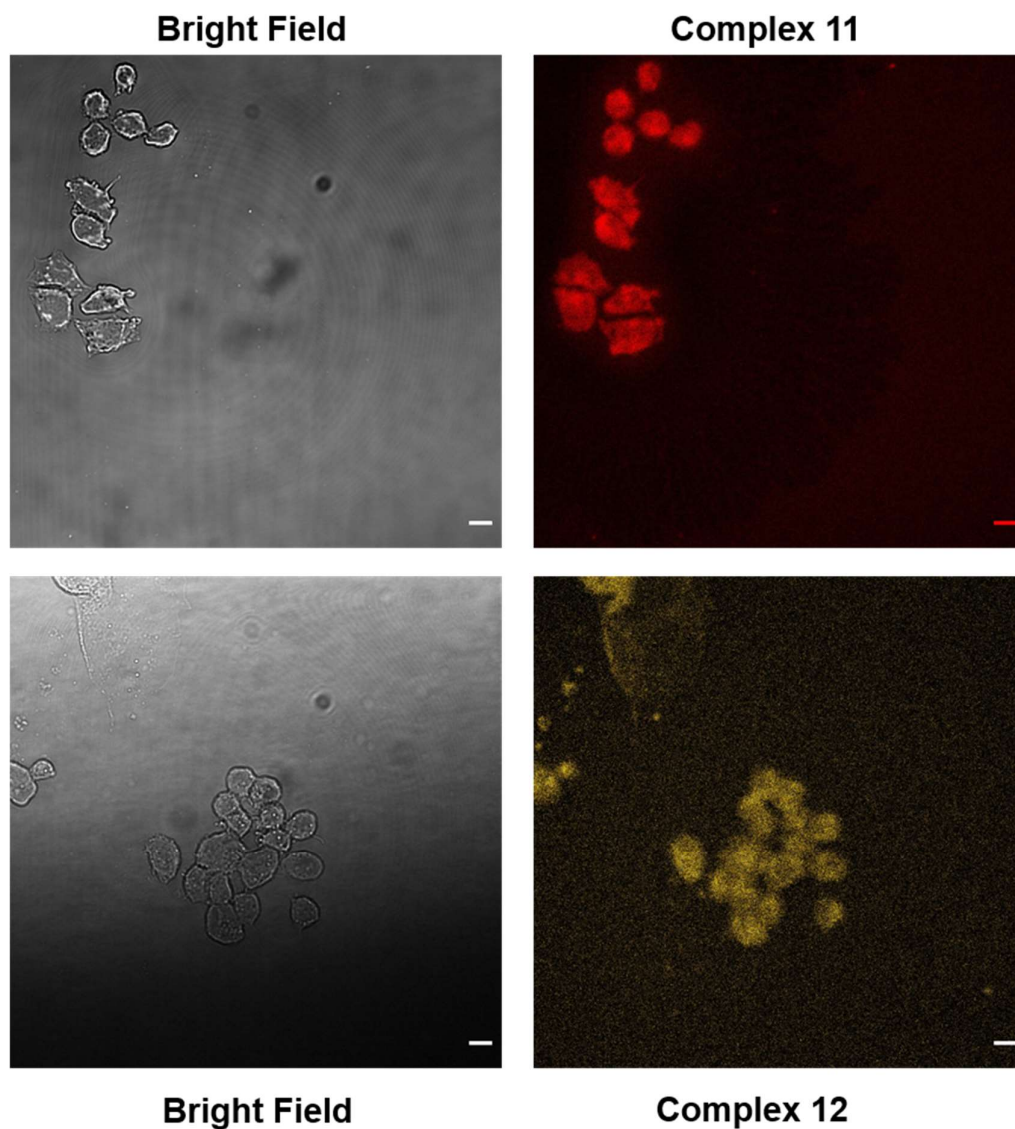

Figure 6.11. Fluorescence images of fixed A2780 ovarian cancer cells after treatment with complex [(Cp*)Ir(Bdp-Dpa)](NO_3)_2 (**10**) (100 μM, Ex/Em = 405/515 nm) in the dark for 4 h. Cells were stained by phalloidin-iFluor (5 μM, Ex/Em = 634/649 nm)

for 30 min. Scale bar = 10 μm. Phalloidin-iFluor selectively binds to actin, which is mainly localized in the cytosol.
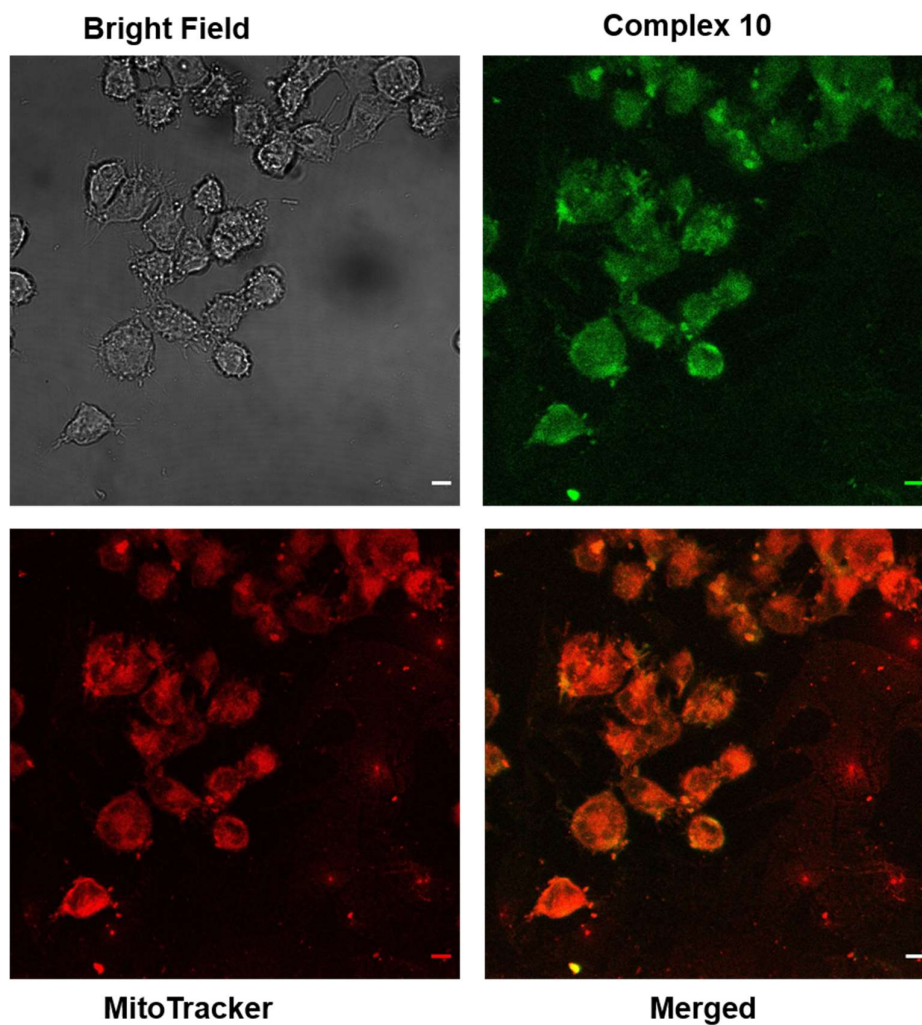
Figure 6.12. Fluorescence images of fixed A2780 ovarian cancer cells after treatment with complex [(Cp*)Ir(Bdp-Dpa)](NO$_3$)$_2$ (**10**) (100 μM, Ex/Em = 405/515 nm) in the dark for 4 h. Cells were stained by Mitotracker red (5 μM, Ex/Em = 579/599 nm) for 30 min. Scale bar = 10 μm. The fluorescence of complex **10** merges well (merged images in orange) with fluorescence of Mitotracker stain, indicating complex **10** tends to localize in the mitochondria.

Figure 6.13. Fluorescence images of fixed A2780 ovarian cancer cells after 4 h treatment with complex [(ppy)$_2$Ir(Ppy-Phen)]Cl (**11**) (2x IC$_{50}$ under dark, 6.6 μM, Ex/Em = 405/564 nm), or with complex [(ppy)$_2$Ir(Ppy-Phen)(Cp*Ir)Cl]Cl (**12**) (100 μM, Ex/Em = 405/570 nm) in the dark. Scale bar = 10 μm. Both appear to diffuse everywhere in the cell.

**6.3.3.6 Reactivity of Complexes 11-13 towards NADH Oxidation**

The intracellular coenzyme couple NADH/NAD$^+$ plays an essential role in numerous biological metabolic reactions for the survival of mammalian cells and human health.[51] An 1.8-fold increase of the NADH/NAD$^+$ ratio is reported in breast cancer cells compared to normal breast cells.[52] NADH/NAD$^+$ metabolism has been found a significant target for the metal-based catalytic chemotherapeutic agents.[53]

The photocatalytic activity toward NADH oxidation of complex [(ppy)$_2$Ir(Ppy-Phen)]Cl (**11**), [(ppy)$_2$Ir(Ppy-Phen)(Cp*Ir)Cl]Cl (**12**), and [(Cp*)Ir(2-phenylpyridine)Cl] (**13**) was examined by UV-vis spectroscopy under irradiation with blue light (463 nm) as shown in Figure 6.14. The UV absorption changes of NADH (100 μM) during the reaction with each complex (10 μM) in MeOH/phosphate buffer (5 mM, 1/9, v/v, pH 7.4) under irradiation at 298 K is shown in Figure 6.14a-c. Upon light irradiation, the characteristic absorption of NADH at 339 nm decreased significantly in the presence of the complex, contrasted with slight decreases in the dark conditions (Figure 6.14d) and negligible changes if NADH alone under the light irradiation. Meanwhile, the oxidation of NADH to produced NAD$^+$ under light irradiation by complex **12** or **13** were also confirmed by ^{1}H NMR spectra and compared with the changes in the dark (Figure 6.15).
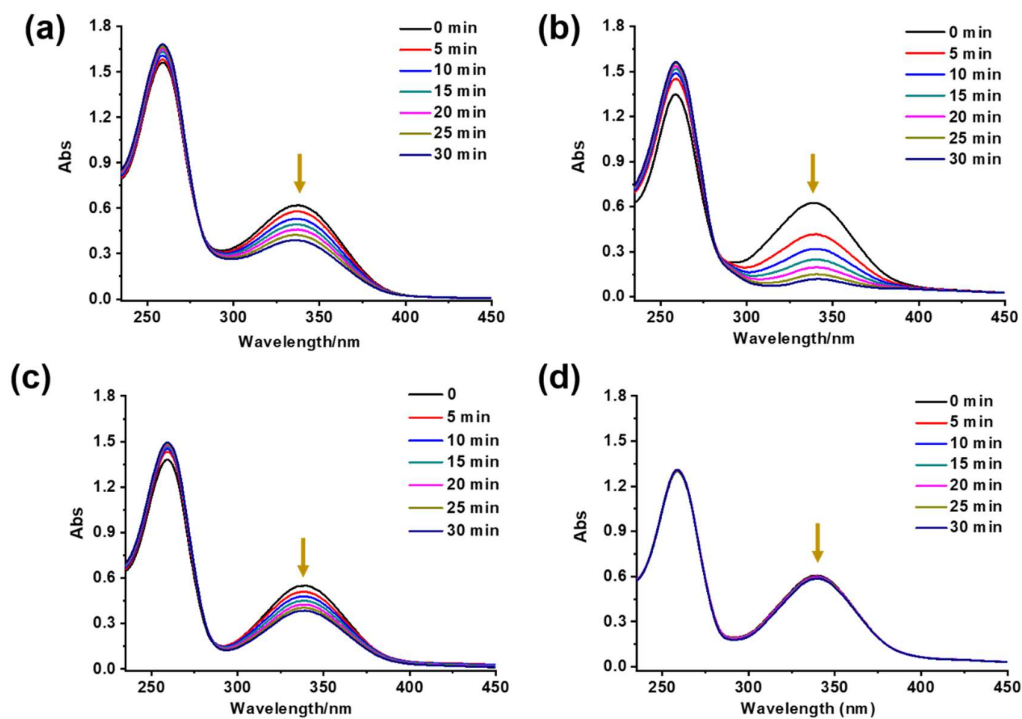
Figure 6.14. Time-dependent UV-vis spectra recorded every 5 min for 100 μM NADH reacting with 10 μM complex (a) [(ppy)$_2$Ir(Ppy-Phen)]Cl (**11**); (b) [(ppy)$_2$Ir(Ppy-Phen)(Cp*Ir)Cl]Cl (**12**); (c) [(Cp*)Ir(ppy)Cl] (**13**) under irradiation of 463 nm blue light in MeOH/phosphate buffer (5 mM, 1/9, v/v, pH 7.4); and (d) [(ppy)$_2$Ir(L5)(Cp*)IrCl]Cl (**12**) in the dark in MeOH/phosphate buffer (5 mM, 1/9, v/v, pH 7.4).
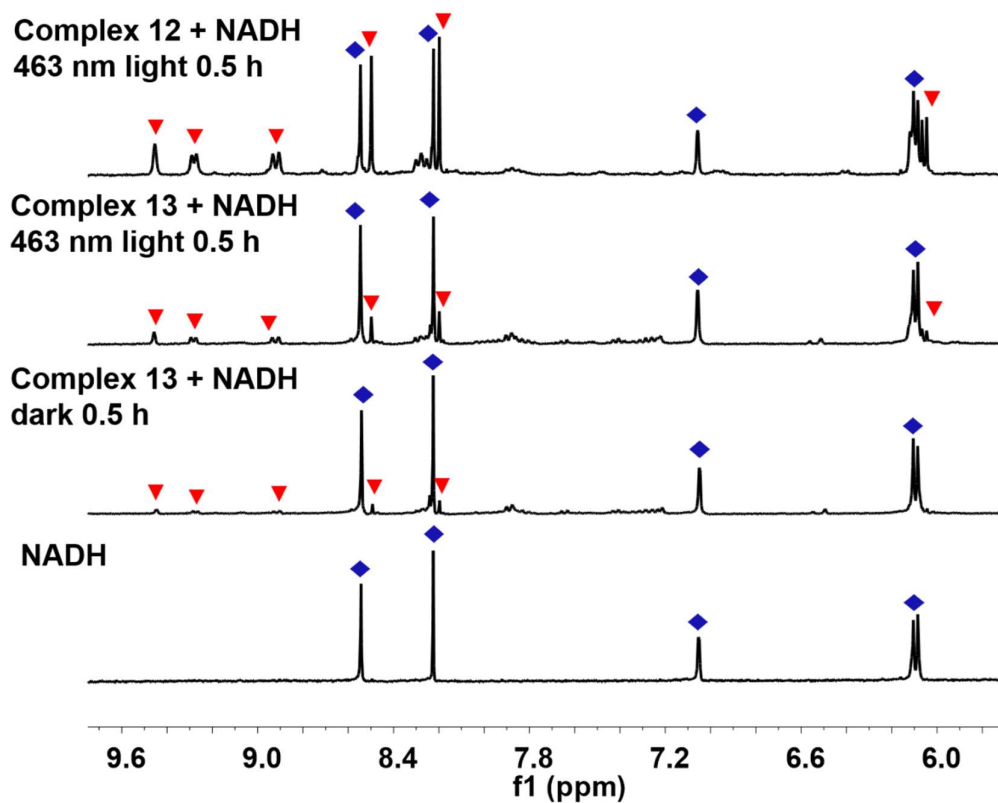
Figure 6.15. ^{1}H NMR (300 MHz, 298 K) spectra showing the photocatalytic oxidation of NADH (3 mM) by complexes **11** and **12** (*ca.* 1 mM) in D$_2$O/d$_4$-MeOD (1/1 v/v) in the dark or upon irradiation with 463 nm blue light for 30 min. Peaks labelled with blue diamonds assigned to NADH and peaks labelled with red triangles to NAD$^+$. After irradiation, the disappearance of blue diamond peaks and appearance of red triangle peaks indicates conversion of NADH to NAD$^+$.

Complex **12** showed the highest turnover frequency (TOF = 16.3 h^{-1}) under light irradiation, compared with the complex **11** (TOF = 7.4 h^{-1}) and **13** (TOF = 5.3 h^{-1}) as shown in Figure 6.16. The influence factors of turnover frequencies for complex **12** catalyzing NADH oxidation are also investigated and compared in Table 6.6. The

turnover frequency is increased upon light irradiation, or upon the increase of the [NADH]/[Ir] ratio. The use of phosphate buffer (PB) as the reaction solvent instead of phosphate buffered saline (PBS) also increases the turnover frequency.
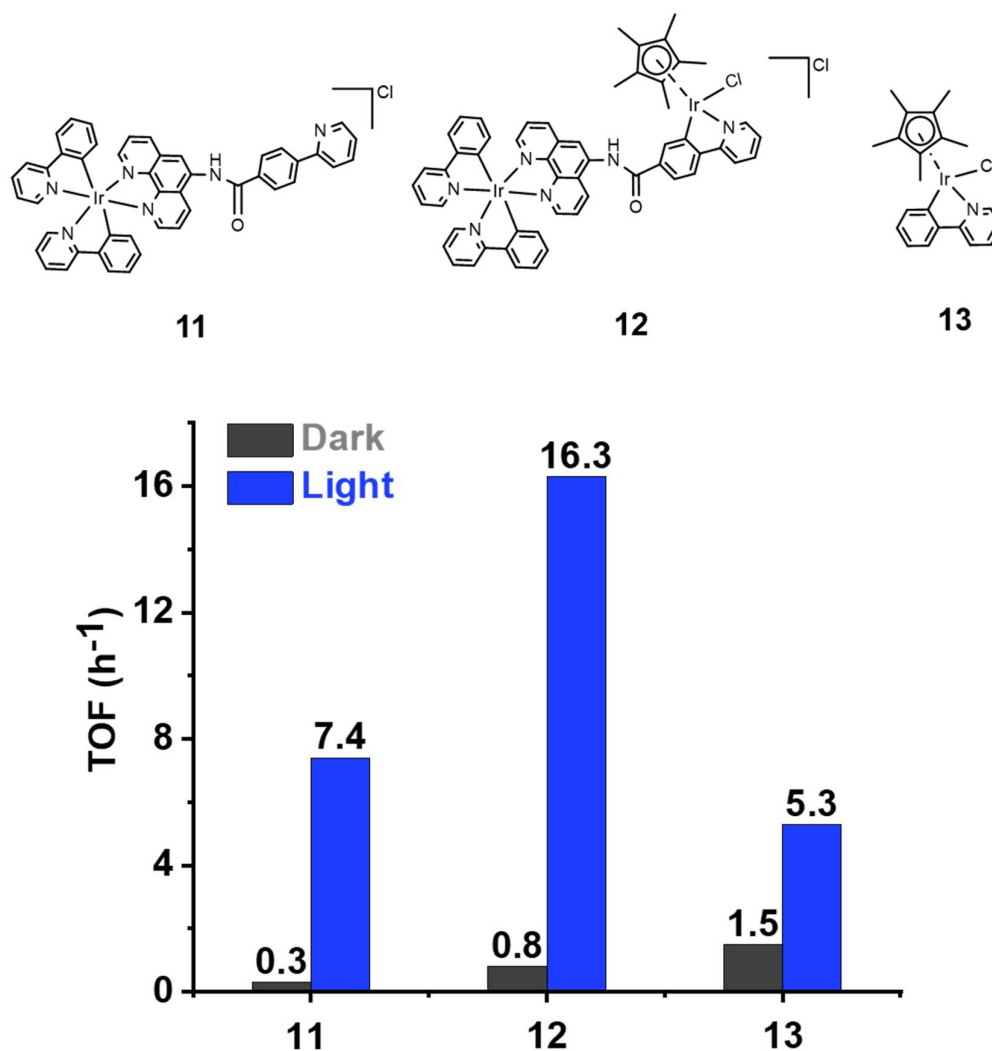
Figure 6.16. The turnover frequencies (TOFs) for reaction of 10 µM complex **11**, **12**, or **13** with 100 µM NADH in MeOH/phosphate buffer (5 mM, 1/9, v/v, pH 7.4) upon 463 nm blue light irradiation or in dark conditions at 298 K.

Table 6.6. The photocatalytic turnover TOFs of complex **12** in oxidation of NADH under various conditions at 298 K. (PB-phosphate buffer, PBS-phosphate buffered saline)

Entry	Light	Complex 12 (μM)	NADH (μM)	Solvent	TOF (h^{-1})
1	463	0	86	MeOH/PB (1/99)	0
2	Dark	0	86	MeOH/PB (1/99)	0
1	463	10	86	MeOH/PB (1/99)	13.4
2	463	10	100	MeOH/PB (1/99)	14.7
3	463	10	156	MeOH/PB (1/99)	16.9
4	463	10	210	MeOH/PB (1/99)	18.8
5	463	10	210	MeOH/PBS (1/99)	11.2
6	463	5	210	MeOH/PB (1/99)	21.9
7	Dark	5	210	MeOH/PB (1/99)	0.44
8	Dark	10	86	MeOH/PB (1/99)	0.53
9	Dark	10	100	MeOH/PB (1/99)	0.50
10	Dark	10	156	MeOH/PB (1/99)	0.75
11	Dark	10	210	MeOH/PB (1/99)	1.01
12	Dark	10	210	MeOH/PBS (1/99)	0.75

6.4 Discussion

6.4.1 Fc-Conjugated Half-sandwich Complexes

6.4.1.1 Fc-Phen Ligand Synthesis

Half-sandwich iridium complexes of the type $[(Cp^X)Ir(N^\wedge N)Cl]^+$ ($Cp^X = Cp^*$, Cp^{xph}, or Cp^{xbiph}) with various $N^\wedge N$ chelating ligands (XY) have been widely reported,[48,54] such as complexes with 1,10-phenathroline (phen), 2,2'-bypyridine, and ethylenediamine ligand.[41] In this Chapter, a redox-active ferrocene group is conjugated to the $N^\wedge N$ phenanthroline ligand (**Fc-Phen**) to synthesize iridium complexes. **Fc-Phen** was obtained from the reaction of the 1,10-phenatroline-5,6-dione with the ferrocene-1-carboxylaldehyde in the presence of ammonium acetate and glacial acetic acid under reflux conditions (Scheme 6.2a). Mechanisms of this reaction adapted from the reported pathways are shown in Figure 6.17.[55]
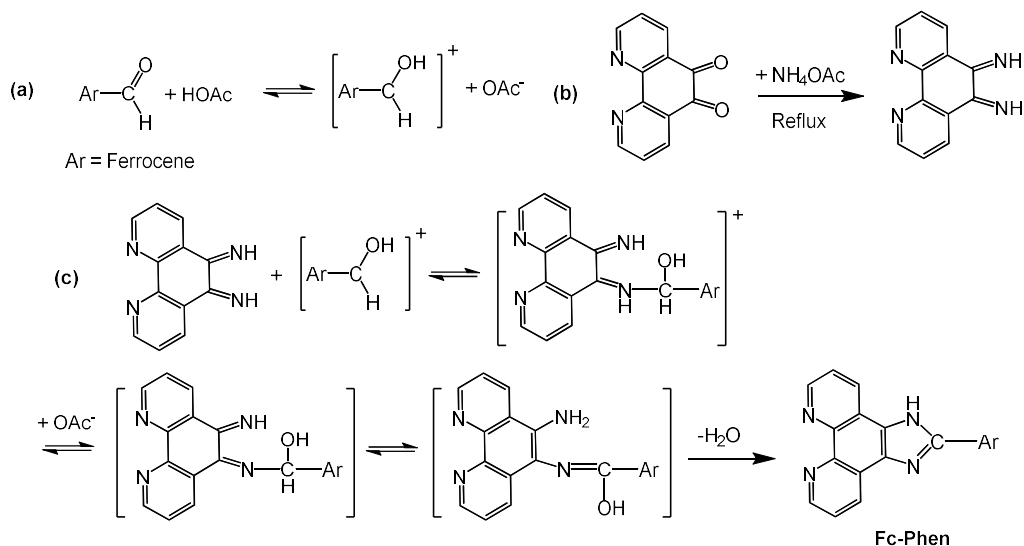
Figure 6.17. Mechanisms for reaction of 1,10-phenatroline-5,6-dione with ferrocene-1-carboxylaldehyde in the preparation of ligand **Fc-Phen**, based on ref. 55.

6.4.1.2 Ligand Effects on the Properties of Complexes

Half-sandwich iridium complexes with N^N coordinating ligand usually undergo fast hydrolysis and readily form adducts with 9-ethylguanine (9-EtG).[56] In contrast, the ferrocene-conjugated iridium complexes are stable towards hydrolysis in micromolar concentrations from ^{1}H NMR studies. Cytotoxicity of chlorido complexes **1-3** (lower IC_{50} values indicating higher cytotoxicity) was enhanced with the phenyl extension on Cp^X ring from Cp^* (inactive of **1**) < Cp^{xph} (IC_{50} = 17.29 μM of **2**) < Cp^{xbiph} (IC_{50} = 7.84 μM of **3**). However, activity of complexes $[(Cp^{xph})Ir(Fc\text{-}Phen)Cl]Cl$ (**3**) and $[(Cp^{xbiph})Ir(Fc\text{-}Phen)Cl]Cl$ (**4**) is 2.5x and 10x lower (Table 6.4) than the respective analogous complexes $[(Cp^X)Ir(1,10\text{-phenanthroline})Cl]^+$ (Cp^X = Cp^*, Cp^{xph}) against human A2780 cancer cells.[41] These observations indicate addition of an imidazole-ferrocene fragment to the phenanthroline ligand has not only inhibited the hydrolysis, but also decreased the cytotoxicity *in vitro*. However, with poorer solubility in the aqueous (phosphate buffered saline) than the chlorido analogues, the iodido complexes are expected to be more lipophilic, which might allow higher cellular iridium accumulation and higher cytotoxicity since iodido Ru/Os arene complexes are more potent than their chlorido counterparts.[57] Furthermore, half of the chlorido complex $[(Cp^*)Ir(Fc\text{-}Phen)Cl]Cl$ (**1**) formed adducts with the 9-EtG (2 mol equiv.), while the iodido complex $[(Cp^*)Ir(Fc\text{-}Phen)Cl]Cl$ (**1**) did not bind with 9-EtG. Hence, iodido complexes might have alternative targets other than DNA, such as behaving as kinase inhibitors like the unreactive half-sandwich Ru/Os complexes.[58]

The ferrocene group in the chlorido iridium complex $[(Cp^*)Ir(Fc\text{-}Phen)Cl]Cl$ (**1**) is susceptive to be oxidized upon blue light irradiation as the ferrocene-absorption

band was decreased within 5 min of irradiation. The interesting photoinitiated reaction mechanism upon visible light irradiation observed for the ferrocene-conjugated ligand has been reported in the literature,[3,59] that is, ferrocene can behave as a photo-initiator forming an unstable ferrocenium ion via the release of the unsubstituted Cp ring due to the bond cleavage between metal and Cp ring. However, the mechanisms of the structural changes on the ferrocene moiety in complex **1** upon irradiation needs further investigation.

The oxidation potential of the ferrocene group is positively shifted when the monodentate chlorido ligand in complex $[(Cp^*)Ir(Fc-Phen)Cl]Cl$ (**1**) is replaced by iodido ligand in complex $[(Cp^*)Ir(Fc-Phen)I]I$ (**4**). As previous electrochemical studies on the substituted ferrocene derivatives suggest that the presence of electron-withdrawing groups decreases the tendency of the ferrocenyl unit to be oxidized,[60] it can be speculated that the "softer" iodido ligand compared to the chlorido ligand could make the iridium centre more electron-withdrawing from the ferrocene unit. The ^{1}H NMR peaks of the ferrocene unit in iodido complex **4** are shifted to downfield compared to chlorido complex **1** ($\Delta \delta = 0.02$ ppm), which suggests a lower electron density on the ferrocene group of complex **4**. This is consistent with the positive shift of the ferrocene oxidation potential of complex **4** as the electron deficiency on the ferrocene group makes the oxidation more difficult.

6.4.2 Half-sandwich Complexes Conjugated to Anthracene/BODIPY

6.4.2.1 Tridentate An-Dpa and Bdp-Dpa Ligands

Half-sandwich Cp^X iridium complexes of the type $[Cp^X Ir(XY)Z]^{0/n+}$ as shown in Figure 6.18a are widely studied as anticancer agents, which contain a bidentate chelating ligand (XY) and a monodentate leaving group (Z). However, in this Chapter, half-sandwich iridium complexes bearing a κ^3-tridentate dipicolyamine ligand are studied with the general structure as shown in Figure 6.18b. The tridentate dipicolylamine unit is a shield for the iridium centre preventing reactions with other biomolecules, giving high stability for micromolar concentrations of complexes **7-9** in the cell culture medium, and inertness toward binding with 9-EtG and GSH were observed (Section **6.3.3.1**).
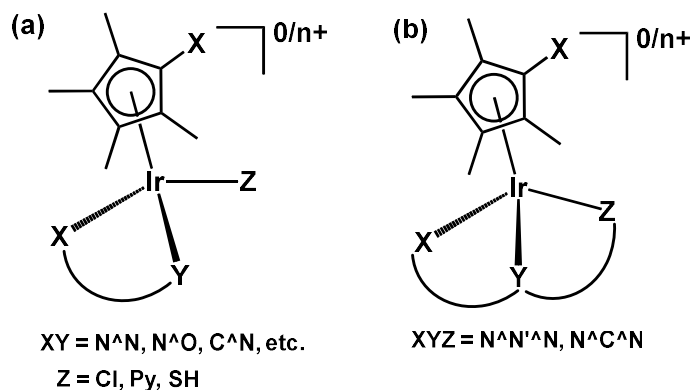
Figure 6.18. The general structures of two different classes of reported half-sandwich iridium complexes (a) bearing a bidentate chelating ligand XY, e.g. N^N, N^O, C^N etc., with a monodentate ligand such as chloride, pyridine or thiol group; (b) bearing a N^N'^N, or N^C^N tridentate ligand.

6.4.2.2 Fluorescence, Cellular Localization and Photocytotoxicity

Conjugation of the anthracene and BODIPY group to the tridentate dipicolyamine ligand have made complexes $[(Cp^*)Ir(An-Dpa)](PF_6)_2$ (**7**) and $[(Cp^*)Ir(Bpy-Dpa)](NO_3)_2$ (**10**) exhibit a respective characteristic fluorescent emission at 425 nm and 514 nm of the anthracene and BODIPY fragment, respectively. The BODIPY-conjugated complex **10** not only shows intense green fluorescence inside the human ovarian cells upon excitation at 405 nm (Figure 6.12), but also is more likely to localize in the mitochondria (Figure 6.13). The specific accumulation in the mitochondria of 2+ charged complex **10** might be driven by the negative potential in the matrix, although the free BODPY derivatives analogous to the free ligand of complex **10** have been confirmed with a mitochondria targeting property.[34]

Furthermore, complexes **7** and **10** were cytotoxic under blue light (463 nm) irradiation with photo-IC_{50} at 3.78 µM and 24.00 µM, respectively (Table 6.5). However, in the dark, complex **7** bearing an anthracenyl moiety with dark-IC_{50} of 14.35 µM also showed higher cytotoxicity than BODIPY-conjugated complex **10** with dark-$IC_{50} > 100$ µM (Table 6.5). And even at a 2x dark-IC_{50} dose treatment, the fluorescence inside human ovarian cells of complex **7** was too weak to be detectable under confocal microscopy. Anthracene is able to degrade 2-deoxyguanosine and linoleic acid peroxidation in human skin epidermal cells by producing ROS species ($^1O_2$, $O_2^{\bullet-}$, $^\bullet OH$) under sunlight irradiation.[61] Meanwhile, it can act as a DNA binder as reported for the iron(III)-based photodynamic agents.[62] The dark cytotoxicity of the anthracene-conjugated complex **7** is most possibly due to the intercalation of anthracene on the DNA bases, which does not rely on light irradiation. However,

under light irradiation, its toxicity can be enhanced because the generated ROS species could exert additional damaging to DNA or membrane lipids. But the photochemical reaction of BODIPY-modified complex **10** producing ROS species appears to be responsible for its toxicity, which renders it to be non-toxic in the dark $(IC_{50} > 100 \ \mu M)$.[45]

6.4.3 Half-sandwich Complexes Conjugated to Phosphorescent [(ppy)₂Ir]

Recent studies have shown that heteronuclear metal complexes tend to display more excellent cytotoxicity against the cancer cells compared to mononuclear metal complexes.[10] In this Chapter, a novel hetero-dinuclear iridium complex [(ppy)₂Ir(Ppy-Phen)(Cp*Ir)Cl]Cl (**12**) was prepared combining the half-sandwich [(Cp*Ir)Cl] unit with the phosphorescent cyclometalated [(ppy)₂Ir(Ppy-Phen)]Cl probe (complex **11**) into one molecule. Excitingly, **12** has high photostability stability under blue light (463 nm) irradiation and luminescent emission at 570 nm, which arises from the phosphoresce emission at 564 nm of the component [(ppy)₂Ir(C^N)]. Compared with the organic anthracene and BODIPY, complex **12** exhibits a larger Stokes shift, which is a common advantage of the octahedral cyclometalated Ir^{III} complexes by greatly reducing the interference between excitation and emission.

The half-sandwich chlorido complexes with the C^N chelated ligands (Figure 6.19a) and the octahedral iridium photosensitizer [Ir(ttpy)(pq)Cl]PF₆ (Figure 6.19b) have been reported as active catalysts for the oxidation of NADH to NAD⁺.[63,64] Herein, the photocatalytic activity of the hybrid complex **12** toward NADH oxidation was also determined since **12** contains both two catalytic components shown in

Figure 6.19. From the data in Figure 6.16, photocatalytic turnover frequency (TOF) of complex **12** is twice or triple higher than the TOF of the complex **11** or **13**, respectively, under the same reaction conditions. These results indicate integration of the two catalytic active units into one molecule can achieve synergistic photocatalytic reaction effects.
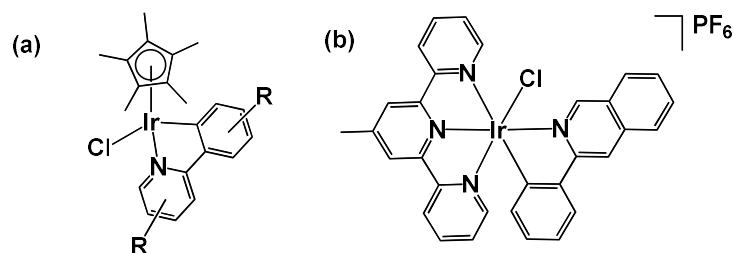
Figure 6.19. Chemical structures of (a) half-sandwich iridium complexes containing the C^N chelating ligands[63] and (b) the catalytic iridium complex [Ir(ttpy)(pq)Cl]PF$_6$,[64] which have been reported as catalysts in the oxidation of NADH.

More excitingly, complex **12** bearing two hetero-iridium components has shown 9x and 33x lower cytotoxicity than the bis-cyclometalated complex **11** in the dark towards nasopharyngeal carcinoma CNE-2Z and A2780 human ovarian cancer cell lines, respectively (Table 6.5), which can be attributed to the lower hydrophobicity of **12** (log P = -0.55) compared to **11** (log P = -0.09), leading to a lower cellular accumulation of complex **12**. However, less iridium cellular diffusion or accumulation for complex **12** might help to decrease the side effects on normal cells.

6.5 Conclusions

In summary, in this Chapter, redox-active and luminescent iridium complexes have been synthesised and characterised as anticancer agents, including three families of complexes bearing the ligand conjugated with the ferrocene moiety, the organic anthracene/BODIPY probes, or the phosphorescent bis-cyclometalated iridium unit.

Ferrocene-conjugated complexes **1-3** are stable toward hydrolysis and exhibit higher half-wave redox potentials ($E_{1/2}$ = 0.195-0.253 V) for Fc/Fc$^+$ couple, compared to free ferrocene ($E_{1/2}$ = 0.051 V). Particularly, for chlorido complexes [(Cp^{xph})Ir(Fc-Phen)Cl]Cl (**2**; IC$_{50}$ = 17.29 µM) and [(Cp^{xbiph})Ir(Fc-Phen)Cl]Cl (**3**; IC$_{50}$ =7.84 µM), conjugation of ferrocene did not render them more active than cisplatin (IC$_{50}$ = 2.71 µM), and led them to be less active compared to the analogues without ferrocene conjugation (IC$_{50}$ values at 6.70 µM for the analogue of **2** and 0.72 µM for the analogue of **3**, respectively) towards human ovarian A2780 cancer cells. These chlorido complexes can bind with 9-EtG, so DNA could be a target. Ferrocene itself is not toxic, but ferrocenium cations are cytotoxic.[10] The ferrocene group in these complexes is able to undergo oxidation upon blue light irradiation in aqueous solution, which might be a strategy of enhancing the cytotoxicity. Moreover, the iodido complexes **4-6** have also been prepared, which are promising as antiproliferative agents as they are more inert than chlorido analogues, which could reduce unwanted side reactions.

Half-sandwich complexes **7-10** are synthesised utilizing a κ^3-tridentate dipicolyamine ligand which is conjugated to an anthracene or a BODIPY group. These complexes are inert toward reactions with the biomolecules (GSH and 9-EtG)

and show the characteristic emission of the fluorescent conjugated groups. BODIPY-contained complex $[(Cp^*)Ir(Bdp-Dpa)](NO_3)_2$ (**10**) was found to mainly localize in the mitochondria in human ovarian A2780 cancer cells, while the anthracene-conjugated complex $[(Cp^*)Ir(An-Dpa)](NO_3)_2$ (**7**) showed too weak fluorescence to be detectable in cells. For complex **10**, its photocytotoxicity index (PI > 4) is higher than that of **7** (PI = 4), which makes it superior to complex **7**, both as a cellular imaging probe or a phototherapeutic agent.

Luminescent complex $[(ppy)_2Ir(Ppy-Phen)(Cp^*Ir)Cl]Cl$ (**12**) is > 33x less cytotoxic in the dark than bis-cyclometalated complex $[(ppy)_2Ir(Ppy-Phen)]Cl$ (**11**) towards human A2780 ovarian cancer cells, suggesting a greater potential of **12** to selectively kill cancer cells under area-targeted light irradiation. Meanwhile, the photocatalytic turnover frequency (TOF) in catalyzing NADH oxidation for complex **12** is 2-3x higher than that of complexes **11** and **13**. Despite the detailed photocatalytic mechanism not being clear, complex **12** provides a basis for the development of this new class of heteronuclear synergistic iridium complexes with photochemical reactivities and phototoxicity for photodynamic therapy.

6.6 References

1   M. Patra and G. Gasser, *Nat. Rev. Chem.*, 2017, **1**, 0066.

2   S. Peter and B. A. Aderibigbe, *Molecules*, 2019, **24**, 3604.

3   K. Mitra, U. Basu, I. Khan, B. Maity, P. Kondaiah and A. R. Chakravarty, *Dalton Trans.*, 2014, **43**, 751-763.

4   P. Köpf-Maier, H. Köpf and E. W. Neuse, *Angew. Chem. Int. Ed. Engl.*, 1984, **23**, 456-457.

5   E. W. Neuse and F. Kanzawa, *Appl. Organomet. Chem.*, 1990, **4**, 19-26.

6   T. Hiroshi and M. Masahiro, *Chem. Lett.*, 1997, **26**, 1177-1178.

7   D. Osella, M. Ferrali, P. Zanello, F. Laschi, M. Fontani, C. Nervi and G. Cavigiolio, *Inorg. Chim. Acta*, 2000, **306**, 42-48.

8   F. Dubar, T. J. Egan, B. Pradines, D. Kuter, K. K. Ncokazi, D. Forge, J.-F. Paul, C. Pierrot, H. Kalamou, J. Khalife, E. Buisine, C. Rogier, H. Vezin, I. Forfar, C. Slomianny, X. Trivelli, S. Kapishnikov, L. Leiserowitz, D. Dive and C. Biot, *ACS Chem. Biol.*, 2011, **6**, 275-287.

9   E. Hillard, A. Vessières, L. Thouin, G. Jaouen and C. Amatore, *Angew. Chem. Int. Ed.*, 2006, **45**, 285-290.

10   X. Ge, S. Chen, X. Liu, Q. Wang, L. Gao, C. Zhao, L. Zhang, M. Shao, X.-A. Yuan, L. Tian and Z. Liu, *Inorg. Chem.*, 2019, **58**, 14175-14184.

11   R. P. Paitandi, R. K. Gupta, R. S. Singh, G. Sharma, B. Koch and D. S. Pandey, *Eur. J. Med. Chem*, 2014, **84**, 17-29.

12   P. Govender, T. Riedel, P. J. Dyson and G. S. Smith, *Dalton Trans.*, 2016, **45**, 9529-9539.

13   L. Tabrizi and H. Chiniforoshan, *Dalton Trans.*, 2017, **46**, 2339-2349.

14   W. Nkoana, D. Nyoni, P. Chellan, T. Stringer, D. Taylor, P. J. Smith, A. T. Hutton and G. S. Smith, *J. Organomet. Chem.*, 2014, **752**, 67-75.

15   B. Maity, B. V. Chakravarthi, M. Roy, A. A. Karande and A. R. Chakravarty, *Eur. J. Inorg. Chem.*, 2011, **2011**, 1379-1386.

16   A. Juzeniene, K. P. Nielsen and J. Moan, *J Environ. Pathol. Toxicol. Oncol.*, 2006, **25**.

17   T. Yogo, Y. Urano, Y. Ishitsuka, F. Maniwa and T. Nagano, *J. Am. Chem. Soc.*, 2005, **127**, 12162-12163.

18   L. Yao, S. Xiao and F. Dan, *Journal of Chemistry*, 2013, **2013**.

19   D. M. Roundhill, *Photochemistry and Photophysics of Metal Complexes,*, Plenum Press, New York, 1994.

20   S. Lamansky, P. Djurovich, D. Murphy, F. Abdel-Razzaq, H.-E. Lee, C. Adachi, P. E. Burrows, S. R. Forrest and M. E. Thompson, *J. Am. Chem. Soc.*, 2001, **123**, 4304-4312.

21   M. Thompson, *MRS Bull.*, 2011, **32**, 694-701.

22   M. K. Nazeeruddin and M. Grätzel, in *Photofunctional Transition Metal Complexes*, Springer, 2007, pp. 113-175.

23   Q. Zhao, F. Li and C. Huang, *Chem. Soc. Rev.*, 2010, **39**, 3007-3030.

24   K. K.-W. Lo and K. Y. Zhang, *RSC Advances*, 2012, **2**, 12069-12083.

25   Q. Zhao, C. Huang and F. Li, *Chem. Soc. Rev.*, 2011, **40**, 2508-2524.

26   K. K.-W. Lo, *Acc. Chem. Res.*, 2015, **48**, 2985-2995.

27   H. Huang, S. Banerjee and P. J. Sadler, *ChemBioChem*, 2018, **19**, 1574-1589.

28   J. J. Conesa, A. C. Carrasco, V. Rodríguez-Fanjul, Y. Yang, J. L. Carrascosa, P. Cloetens, E. Pereiro and A. M. Pizarro, *Angew. Chem. Int. Ed.*, 2020, **59**, 1270-1278.

29   M. S. Lowry, W. R. Hudson, R. A. Pascal and S. Bernhard, *J. Am. Chem. Soc.*, 2004, **126**, 14129-14135.

30   L. Li, W. W. Brennessel and W. D. Jones, *J. Am. Chem. Soc.*, 2008, **130**, 12414-12419.

31   F. Otón, A. Tárraga, A. Espinosa, M. D. Velasco and P. Molina, *J. Org. Chem*, 2006, **71**, 4590-4598.

32   J.-Z. Wu, B.-H. Ye, L. Wang, L.-N. Ji, J.-Y. Zhou, R.-H. Li and Z.-Y. Zhou, *J. Chem. Soc., Dalton Trans.*, 1997, 1395-1402.

33   A. Ojida, Y. Mito-oka, M.-a. Inoue and I. Hamachi, *J. Am. Chem. Soc.*, 2002, **124**, 6256-6258.

34   Z. Li, Q.-Y. Chen, P.-D. Wang and Y. Wu, *RSC Advances*, 2013, **3**, 5524-5528.

35   A. Paul, N. Das, Y. Halpin, J. G. Vos and M. T. Pryce, *Dalton Trans.*, 2015, **44**, 10423-10430.

36   M. Kobayashi, S. Masaoka and K. Sakai, *Acta Crystallogr. Sect. Sect. E: Struct. Rep. Online*, 2008, **64**, o1979-o1979.

37   O. V. Dolomanov, L. J. Bourhis, R. J. Gildea, J. A. Howard and H. Puschmann, *J. Appl. Cryst.*, 2009, **42**, 339-341.

38   G. M. Sheldrick, *Acta Cryst.*, 2008, **A64**, 112-122.

39   G. M. Sheldrick, *Acta Cryst.*, 2015, **C71**, 3-8.

40   Z. Liu, I. Romero-Canelón, B. Qamar, J. M. Hearn, A. Habtemariam, N. P. Barry, A. M. Pizarro, G. J. Clarkson and P. J. Sadler, *Angew. Chem. Int. Ed.*, 2014, **53**, 3941-3946.

41   Z. Liu, A. Habtemariam, A. M. Pizarro, S. A. Fletcher, A. Kisova, O. Vrana, L. Salassa, P. C. Bruijnincx, G. J. Clarkson and V. Brabec, *J. Med. Chem.*, 2011, **54**, 3011-3026.

42   Z. Liu and P. J. Sadler, *Acc. Chem. Res.*, 2014, **47**, 1174-1185.

43   A. L. Müller, T. Bleith, T. Roth, H. Wadepohl and L. H. Gade, *Organometallics*, 2015, **34**, 2326-2342.

44   M. Zaki, S. Hairat and E. S. Aazam, *RSC Advances*, 2019, **9**, 3239-3278.

45   A. Kamkaew, S. H. Lim, H. B. Lee, L. V. Kiew, L. Y. Chung and K. Burgess, *Chem. Soc. Rev.*, 2013, **42**, 77-88.

46   A. Citta, E. Schuh, F. Mohr, A. Folda, M. L. Massimino, A. Bindoli, A. Casini and M. P. Rigobello, *Metallomics*, 2013, **5**, 1006-1015.

47   W. Ma, L. Guo, Z. Tian, S. Zhang, X. He, J. Li, Y. Yang and Z. Liu, *Dalton Trans.*, 2019, **48**, 4788-4793.

48   X. He, X. Liu, Y. Tang, J. Du, M. Tian, Z. Xu, X. Liu and Z. Liu, *Dyes Pigm.*, 2019, **160**, 217-226.

49   J. Li, Z. Tian, S. Zhang, Z. Xu, X. Mao, Y. Zhou and Z. Liu, *Appl. Organomet. Chem.*, 2019, **33**, e4685.

50   D. Kong, L. Guo, M. Tian, S. Zhang, Z. Tian, H. Yang, Y. Tian and Z. Liu, *Appl. Organomet. Chem.*, 2019, **33**, e4633.

51   A. A. Heikal, *Biomark Med.*, 2010, **4**, 241-263.

52   A. Chiarugi, C. Dölle, R. Felici and M. Ziegler, *Nat. Rev. Cancer*, 2012, **12**, 741-752.

53   J. J. Soldevila-Barreda and N. Metzler-Nolte, *Chem. Rev.*, 2019, **119**, 829-869.

54   W. Ma, S. Zhang, Z. Tian, Z. Xu, Y. Zhang, X. Xia, X. Chen and Z. Liu, *Eur. J. Med. Chem*, 2019, **181**, 111599.

55   E. A. Steck and A. R. Day, *J. Am. Chem. Soc.*, 1943, **65**, 452-456.

56   Z. Liu, A. Habtemariam, A. M. Pizarro, S. A. Fletcher, A. Kisova, O. Vrana, L. Salassa, P. C. A. Bruijnincx, G. J. Clarkson, V. Brabec and P. J. Sadler, *J. Med. Chem.*, 2011, **54**, 3011-3026.

57   I. Romero-Canelón, L. Salassa and P. J. Sadler, *J. Med. Chem.*, 2013, **56**, 1291-1300.

58   J. Maksimoska, D. S. Williams, G. E. Atilla-Gokcumen, K. S. M. Smalley, P. J. Carroll, R. D. Webster, P. Filippakopoulos, S. Knapp, M. Herlyn and E. Meggers, *Chem. Eur. J.*, 2008, **14**, 4816-4822.

59   Y. Yamaguchi and C. Kutal, *Macromolecules*, 2000, **33**, 1152-1156.

60   G. L. K. Hoh, W. E. McEwen and J. Kleinberg, *J. Am. Chem. Soc.*, 1961, **83**, 3949-3953.

61   S. F. Mujtaba, A. Dwivedi, M. K. R. Mudiam, D. Ali, N. Yadav and R. S. Ray, *Photochem. Photobiol.*, 2011, **87**, 1067-1076.

62   U. Basu, I. Khan, A. Hussain, P. Kondaiah and A. R. Chakravarty, *Angew. Chem. Int. Ed.*, 2012, **51**, 2658-2661.

63   A. J. Millett, A. Habtemariam, I. Romero-Canelón, G. J. Clarkson and P. J. Sadler, *Organometallics*, 2015, **34**, 2683-2694.

64   H. Huang, S. Banerjee, K. Qiu, P. Zhang, O. Blacque, T. Malcomson, M. J. Paterson, G. J. Clarkson, M. Staniforth and V. G. Stavros, *Nat. Chem.*, 2019, **11**, 1041-1048.

Chapter 7

Conclusions and Future Work

7.1 Conclusions

Since the blockbuster discovery of cisplatin as an anticancer drug for the treatment of various solid tumours about 55 years ago, organo-iridium/rhodium complexes with novel mechanisms of action have exhibited promising anticancer potency as a new generation of chemotherapeutic agents. Studies in this thesis have been focused on the synthesis and characterisation, chemical reactivity, cytotoxicity, and cellular mechanisms of action of novel series of half-sandwich Ir^{III} and Rh^{III} complexes with the formula of $[(\eta^5\text{-}Cp^X)Ir(XY)Z]^+$, where XY is a bidentate chelating ligand and Z is a monodentate chloride/iodide/pyridine ligand.

In Chapter 3, it is found that iodido Ir(III) azopyridine complexes were highly potent towards cancer cells despite being relatively inert towards aquation or nucleobase binding. Experimental data and DFT calculations suggest that reactions with the abundant intracellular tripeptide glutathione play a major role in activation of these inert complexes in cells and in generation of cytotoxic radicals (including superoxide), reduced azopyridine ligand and thiolato-bridged dinuclear complexes. The activation involves the attack of glutathione on the azo bond of the coordinated azopyridine. Reactions with GSH also give S-bound thiolato adducts which are catalysts for the oxidation of GSH to GSSG in oxygen-dependent mechanisms. These discoveries suggest that such iridium complexes have multi-targeting anticancer modes of action, which contribute to combating cisplatin resistance. The azopyridine ligand-centred reactions provide a wide scope for the design of novel organometallic chemotherapeutic compounds.

In Chapter 4, a novel library of half-sandwich rhodium complexes featuring either a monodentate pyridine or chloride ligand has been described. These complexes show greater potency than cisplatin (ca. 5-fold more active towards human A549 lung cancer cells). It was demonstrated that the chemical reactivity and cytotoxicity of such organorhodium complexes can be modulated by the nature of the monodentate ligand (chloride or pyridine). Compared to the chlorido analogues, the pyridine complexes not only show slower hydrolysis, but also weaker interactions with biomolecules (9-ethylguanine, glutathione, and catalysis of NADH oxidation). Intriguingly, the pyridine complexes exhibit higher cytotoxicity with lower cellular accumulation. They appear to act as ROS scavengers, while the chloride analogues induce ROS elevation in cancer cells.

In Chapter 5, a novel half-sandwich iridium complex **Ir-I** and its clickable analogue **Ir-II** have been synthesised and characterised. Significantly, the strain-promoted copper free azide-alkyne cycloaddition strategy has been utilized successfully to conjugate the iridium complex **Ir-II** to a tumour-targeting vector-azide-cyclic nonapeptide c(CRWYDENAC). HPLC, high resolution ESI-MS, as well as UV-vis spectroscopy were used to characterize the peptide conjugate **Ir-CP**. The moderate anticancer activity of the clickable complex **Ir-II** against ovarian cancer cells encourages investigation of the biological activity of the peptide conjugate in future work.

In Chapter 6, redox-active and luminescent half-sandwich iridium complexes are investigated as anticancer agents, including three families of complexes bearing a ferrocene group, an organic anthracene/BODIPY probe or a phosphorescent bis-

cyclometalated iridium unit. The conjugated BODIPY group in the iridium complex acts as an excellent cellular imaging probe for detecting the cellular distribution of the iridium complex. These luminescent iridium complexes are phototoxic under visible blue light irradiation. In particular, the BODIPY-conjugated and bis-cyclometalated iridium-conjugated Cp* iridium complexes are relatively non-toxic in the dark, which makes them be promising as photodynamic therapy agents. The bis-cyclometalated iridium-conjugated Cp* iridium complex also shows a synergistic photocatalytic activity in oxidizing NADH to NAD^+, which represents a new class of heteronuclear metal complexes as catalytic anticancer agents worthy of further investigation.

7.2 Future Work

7.2.1. Investigating Oxygen Effects on the Cytotoxicity

Oxygen is an indispensable requirement of eukaryotes. Healthy tissue is normoxia, also referred as physoxia, and their oxygen concentrations largely depend on the blood vessel network and metabolic activity. As shown in Figure 7.1, the oxygen concentration varies from 0%-13% in tissues from the different areas of human body.[1] While for the rapid proliferating tumour cells, oxygen is consumed within tumour vasculature, thus leading to a hypoxic microenvironment in many tumor tissues.[2] It is reported that the median oxygen levels in most hypoxic tumour tissues are within the range of 1%-2%, much lower than in healthy tissues.[2] In contrast, the oxygen concentration setting in the laboratory normoxic incubator is 20.9% O_2,[3] which makes

276

the cell culture *in vitro* actually under an oxygen-abundant condition instead of a physoxia condition as in organs.
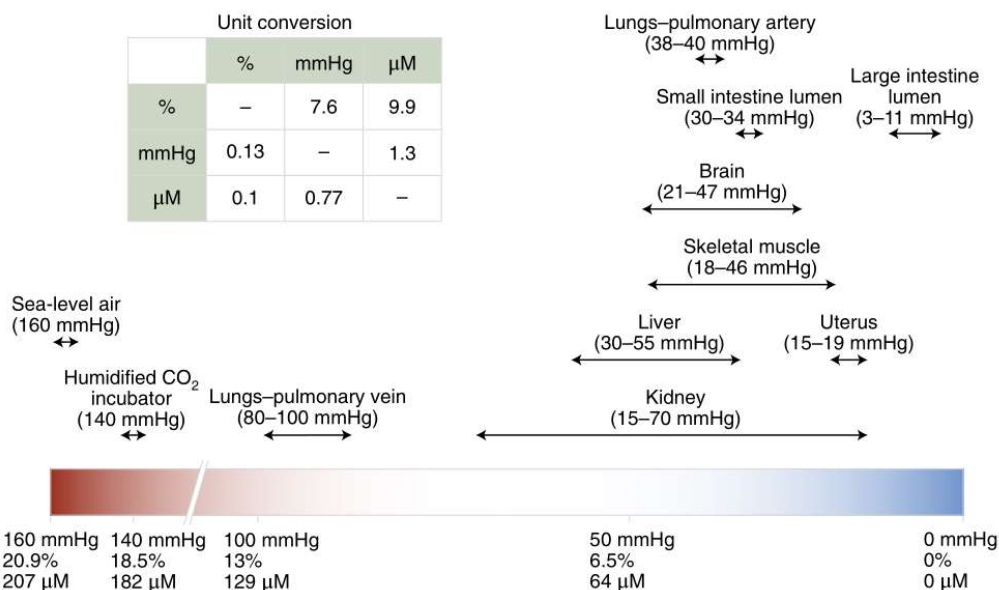
Figure 7.1. Oxygen concentrations across tissues are significantly lower than the standard cell culturing conditions. Adapted from ref. 1.

On the other side, half-sandwich iridium complexes have been reported with a redox mechanism of action mainly by elevating the levels of cellular reactive oxygen species.[4] For example, the reported complex [(Cp*)Ir(2-phenylpyridine)pyridine]PF$_6$ induced substantial increases of ROS (x1230) and superoxide (x700) levels after 1 h of treatment for human ovarian A2780 cancer cells compared to the untreated cells.[5] Its catalytic reactivity of transferring hydride from NADH to O$_2$ to produce H$_2$O$_2$ was believed to be responsible for the built-up of superoxide in cells.[5] If such chemical reactivity is the major reason to kill the cancer cells for the iridium complexes, molecular oxygen is definitely a contributory reactant in the process. As

277

aforementioned hypoxia environment is a common feature of malignant tumors, in the future work, it will be necessary to conduct the antiproliferative screening under the physiological oxygen concentration conditions to identify the possible role of oxygen in the mechanisms of action of the oxidant half-sandwich organometallic complexes. Accommodating the cell culture flasks in the airtight chambers which can be housed in standard CO_2 incubators flushed with a gas mixture would be a simple and economic way to try in the first place.[1]

7.2.2. Enhancing the Selectivity

The current chemotherapeutic drugs are mainly based on the cytotoxicity of the chemical drugs to rapidly kill the proliferating cancer cells.[6] The chemical drugs have little or no specificity towards the tumour cells, which leads to toxicity towards normal cells as well.[6] Thus, exploiting the current findings on the characteristics of cancer cells/tissues to design highly tumour-specific chemotherapeutic agents is crucial.

To improve the tumour selectivity of cytotoxic organometallic anticancer agents, an ideal solution is to develop the tumour-targeting drug delivery system which consists of a tumour-recognition moiety conjugated directly or through a suitable linker to an organometallic scaffold. Upon entering the cancer cell, the conjugate system should then release the cytotoxic component. In Chapter 5, a half-sandwich iridium complex $[(Cp^*)Ir(4-methyl-4'-carboxy-2,2'-bipyridine)Cl]PF_6$ showing moderate activity (IC_{50} = 33.7 µM) against the human ovarian cancer cells, was conjugated to a tumour-targeting cyclic peptide containing a sequence of

c(CRWYDENAC). The conjugation was made via a covalent linker between the iridium complex and the peptide by a copper-free reaction, which makes the cytotoxic iridium complex difficult to release after passage through the cell membrane. Although the cyclic peptide was reported to be cell-penetrating,[7] the iridium-peptide was found to be inactive ($IC_{50} > 100$ µM). The reasons might be the low iridium accumulation in the cells, the low cytotoxicity of the conjugated iridium complex, or the covalent binding of the iridium unit to the cyclic peptide prevent it from reaching the targets. In future work, several improvements are considered as follows.

7.2.2.1 Potent Half-sandwich Complexes as Candidates
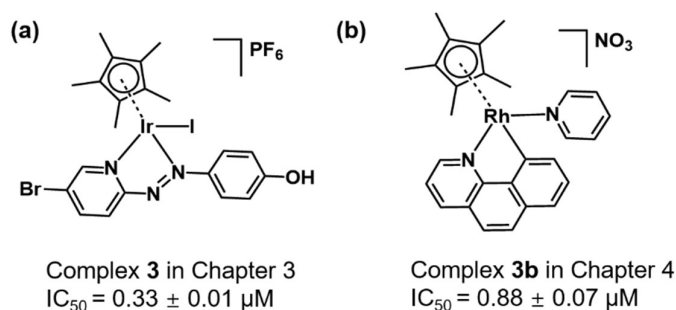
Figure 7.2. The most potent complexes screened in this thesis against human lung A549 cancer cells: (a) the half-sandwich iridium complex **3** studied in Chapter 3 with an IC_{50} value of 0.33 ± 0.01 µM; and (b) the half-sandwich iridium complex **3a** studied in Chapter 4 with an IC_{50} value of 0.88 ± 0.07 µM. Both are promising as the cytotoxic agents to conjugate with the tumour-targeting vectors.

During the studies in this thesis, the half-sandwich complexes shown in Figure 7.2 have been found to exert prominent inhibitory effects on the growth of human lung A549 cancer cells with a half-maximal inhibitory concentration (IC_{50}) of 0.33 μM (complex **3**) and 0.88 μM (complex **3b**). However, the two complexes have been found to show similar higher potency in the preliminarily screening against normal human lung fibroblasts MRC-5 with IC_{50} values of 0.13 ± 0.01 μM (complex **3**) and 0.45 ± 0.01 μM (complex **3b**).

7.2.2.2 Utilization of Stimuli-Responsive Linkers

The linkers used to connect the tumour-targeting fragments with the cytotoxic drug molecules in the drug delivery system, also play critical roles in the efficiency of the controlled release and targeted delivery.[8] Several types of linkers are shown in Table 7.1, which release the drug molecules in response to the specific endogenous stimuli in the tumour microenvironment.[9] Such as acidic pH in the extracellular environment of tumour cells, higher cellular GSH expression, dysregulation of enzymes and low oxygen levels (hypoxia) in tumour tissues in comparison with normal tissues.[10] There have been also some exogenous-sensitive such as thermo-sensitive and photo-sensitive linkers which can release the delivered cytotoxic drug.[10]

Particularly, nitroaromatic, azo-aromatic, and quinone compounds-based linkers can respond to the hypoxia-selective activation. As the expression of reducing enzymes is increased in the tumour microenvironment, the nitro group is reported to be readily reduced by the nitroreductase and the aromatic structure is degraded into several components as shown in Figure 7.3a.[10]

Table 7.1. Summary of the release mechanisms involving the linker in conjugation

chemistry. Adapted from ref. 9.

linker	release mechanism
ester	enzymatic (hydrolases, alkaline phosphatase, carboxylesterase); chemical hydrolysis (low or high pH, metal cations)
amide	enzymatic (peptidases, matrix metalloproteinase, collagenase, prostate specific membrane antigen, plasmin)
hydrazone	hydrolysis (pH 5.5−6.5)
indolequinone	hypoxia (low O_2)
Mannich base	hydrolysis (acid)
self-immolative (aminobenzyl)	enzymatic, bioreduction, hydrolysis, thiol exchange
o-nitrobenzyl, coumarinyl	light (UV, vis)
diazo	thermolysis, enzymatic reduction
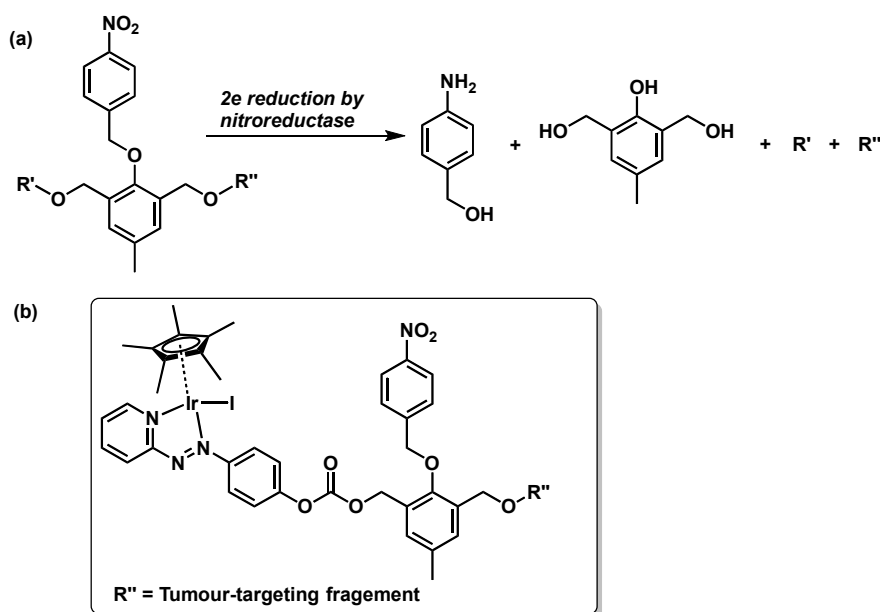
Figure 7.3. (a) Activation mechanisms for the nitroaromatic linker to release the

conjugated R' and R'' moieties upon the reduction by a nitroreductase under a

hypoxic microenvironment. Adapted from ref. 10. (b) The proposed design for the

conjugation of a Cp* iridium iodido azopyridine complex to a tumour targeting

fragment (such as the tumour-targeting cyclic peptide) via a nitroaromatic linker.

Therefore, an aromatic linker bearing the stimuli-responsive NO_2 group which is a substrate for nitroreductase under the hypoxia microenvironment of tumor cells is suggested (Figure 7.3b) for future work to enhance the tumour-selectivity of the potent half-sandwich iridium azopyridine complex.[11] Upon activation of the nitroaromatic linker, the cytotoxic half-sandwich iridium could be released from the conjugation with the tumour-targeting fragments, which assures the mechanisms of action of the complex can be displayed independently. While in the normal tissues, the conjugation would not cause severe toxic effects due to direction by the tumour-targeting moiety leading to less internalization into normal cells.

7.3 References

1 T. Ast and V. K. Mootha, *Nat. Metab.*, 2019, **1**, 858-860.

2 B. Muz, P. de la Puente, F. Azab and A. K. Azab, *Hypoxia (Auckl).* 2015, **3**, 83-92.

3 R. H. Wenger, V. Kurtcuoglu, C. C. Scholz, H. H. Marti and D. Hoogewijs, *Hypoxia (Auckl).* 2015, **3**, 35-43.

4 J. M. Hearn, G. M. Hughes, I. Romero-Canelón, A. F. Munro, B. Rubio-Ruiz, Z. Liu, N. O. Carragher and P. J. Sadler, *Metallomics*, 2018, **10**, 93-107.

5 Z. Liu, I. Romero-Canelón, B. Qamar, J. M. Hearn, A. Habtemariam, N. P. Barry, A. M. Pizarro, G. J. Clarkson and P. J. Sadler, *Angew. Chem. Int. Ed.*, 2014, **53**, 3941-3946.

6 S. Jaracz, J. Chen, L. V. Kuznetsova and I. Ojima, *Biorg. Med. Chem.*, 2005,

13, 5043-5054.

7   G. K. Feng, M. Q. Zhang, H. X. Wang, J. Cai, S. P. Chen, Q. Wang, J. Gong, K. W. Leong, J. Wang and X. Zhang, *Adv. Therap.*, 1900018.

8   P. Hassanzadeh, F. Atyabi and R. Dinarvand, *J. Controlled Release*, 2018, **270**, 260-267.

9   P. T. Wong and S. K. Choi, *Chem. Rev.*, 2015, **115**, 3388-3432.

10   M. Faal Maleki, A. Jafari, E. Mirhadi, A. Askarizadeh, B. Golichenari, F. Hadizadeh, S. M. Jalilzadeh Moghimi, R. Aryan, M. Mashreghi and M. R. Jaafari, *Int. J. Pharm.*, 2019, **572**, 118716.

11   R. Kumar, E.-J. Kim, J. Han, H. Lee, W. S. Shin, H. M. Kim, S. Bhuniya, J. S. Kim and K. S. Hong, *Biomaterials*, 2016, **104**, 119-128.

Complex List

Complexes in Chapter 3
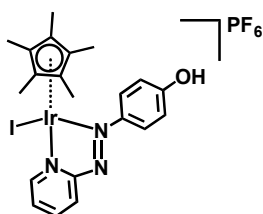
1
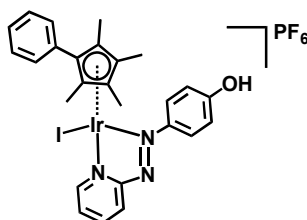
2
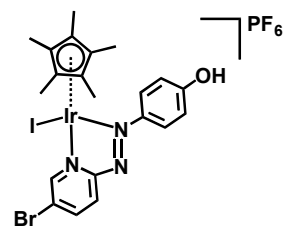
3
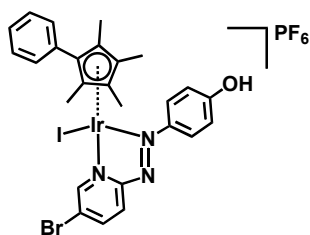
4
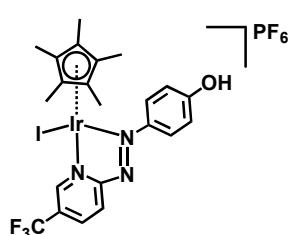
5
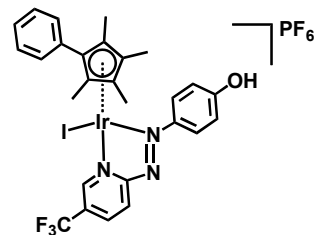
6
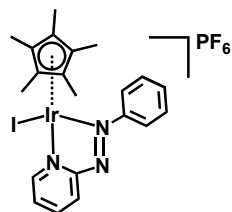
7
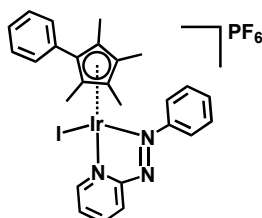
8

9

10

Complexes in Chapter 4

1a

2a

3a

1b

2b

3b
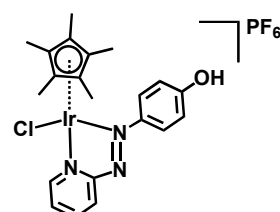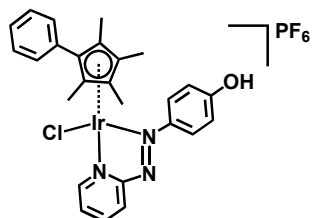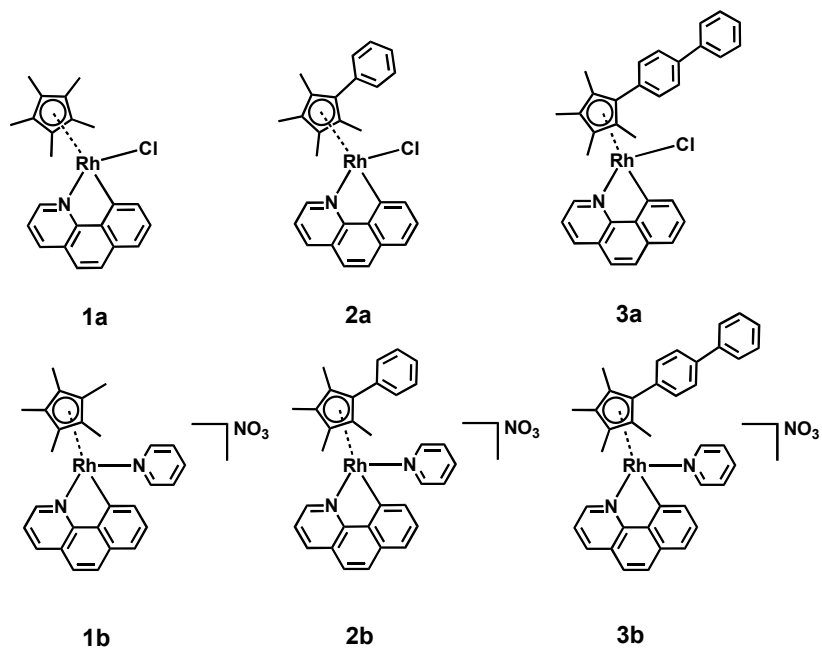
Complexes in Chapter 5

Ir-I

Ir-II

Ir-CP

1

2

3

1A

2A

4

5

6

7

8

9

10

11

12
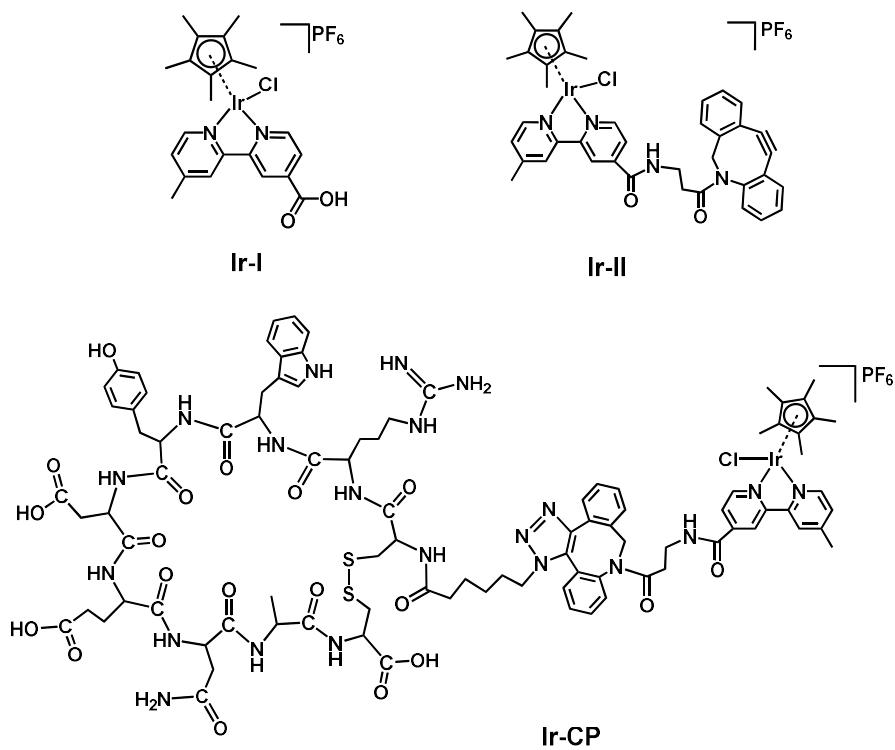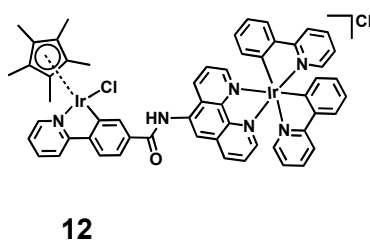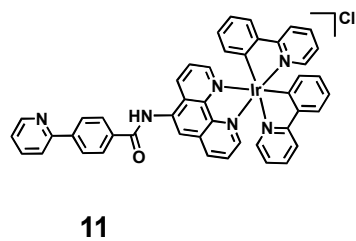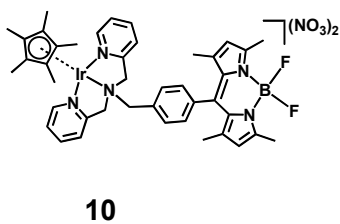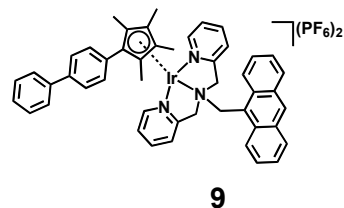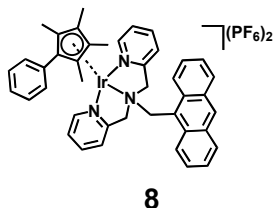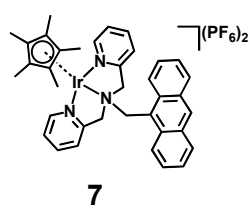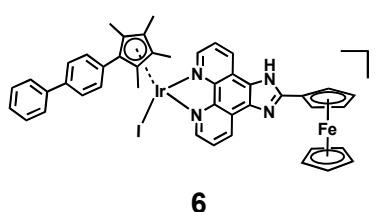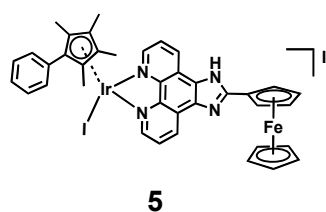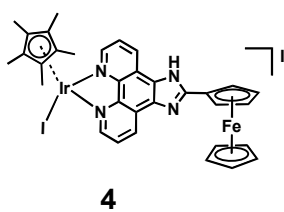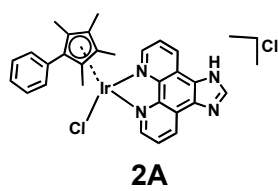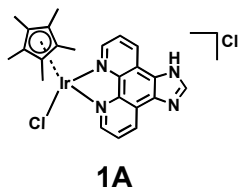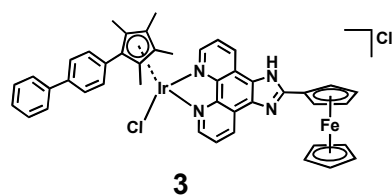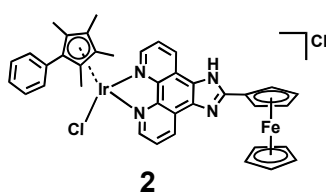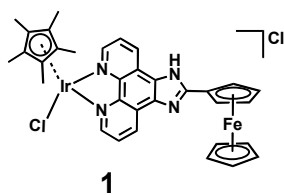
Appendix

Chapter 3

Table A3.1. Crystallographic data for complexes **1-I**, **2**, and **3**.

Parameters	1-I·MeOH	[2-H$_{0.5}$]·[PF$_6$]$_{0.5}$	3·MeOH
Empirical formula	C$_{22}$H$_{28}$I$_2$IrN$_3$O$_2$	C$_{26}$H$_{25.5}$F$_3$IIrN$_3$OP$_{0.5}$	C$_{22}$H$_{27}$BrF$_6$IIrN$_3$O$_2$P
MW	812.47	787.58	909.44
T[K]	150(2)	150(2)	150(2)
Crystal size [mm^3]	0.16 × 0.08 × 0.08	0.18 × 0.14 × 0.12	0.16 × 0.1 × 0.06
Crystal System	monoclinic	monoclinic	monoclinic
Space group	P2$_1$/n	P2/c	P2$_1$/n
a [Å]	9.29339(12)	23.1650(4)	9.61097(8)
b [Å]	13.27724(15)	7.44609(9)	20.10144(16)
c [Å]	20.1881(3)	15.7060(2)	14.45419(15)
α [°]	90	90	90
β [°]	91.3644(12)	107.2675(16)	103.4265(10)
γ [°]	90	90	90
V [Å^3]	2490.31(6)	2587.00(7)	2716.14(4)
Z	4	4	4
ρ_{calcd} [g cm^{-3}]	2.167	2.022	2.224
μ [mm^{-1}]	7.863	6.431	21.338
F(000)	1520.0	1500.0	1720.0
Radiation	MoKα (λ = 0.71073)	MoKα (λ = 0.71073)	CuKα (λ = 1.54184)
θ range [°]	4.87 - 62.262	5.192- 66.2	7.674-146.66
	-13 ≤ h ≤ 13	-34 ≤ h ≤ 35	-11 ≤ h ≤ 11
Limiting indices	-18 ≤ k ≤ 18	-11 ≤ k ≤ 11	-24 ≤ k ≤ 24
	-28 ≤ l ≤ 28	-24 ≤ l ≤ 23	-17 ≤ l ≤ 15
Collected reflns	64660	97034	29026
Unique reflns	7479 [R$_{int}$ = 0.0416]	9366 [R$_{int}$ = 0.0514]	5384 [R$_{int}$ = 0.0555]
Data/restraints/parameters	7479/0/279	9366/0/334	5384/0/379
Goodness of fit	1.093	1.050	1.121
R_1/wR_2[I>2σ(I)]	0.0208/ 0.0381	0.0231/0.0416	0.0293/ 0.0770
R_1/wR_2(all data)	0.0273/ 0.0398	0.0314/0.0439	0.0295/ 0.0772
Largest diff. peak/hole/e Å^{-3}	0.57/-0.90	0.81/-0.96	2.00/-1.81

**Table A3.2.** Crystallographic data for complexes **5**, **7-I**, and **8-I**.

| Parameters	5·MeOH	7-I	8-I
Empirical formula	$C_{23}H_{27}F_9IIrN_3O_2P$	$C_{21}H_{24}I_2IrN_3$	$C_{26}H_{26}I_2IrN_3$
MW	898.54	764.43	826.50
T[K]	296(2)	150(2)	150(2)
crystal size [mm^3]	0.24 × 0.2 × 0.08	0.18 × 0.1 × 0.02	0.2 × 0.08 × 0.02
Crystal System	monoclinic	monoclinic	monoclinic
Space group	$P2_1/n$	C2/c	$P2_1/c$
a [Å]	9.85870(10)	31.7681(4)	9.19420(10)
b [Å]	20.2807(2)	8.70230(10)	8.21580(10)
c [Å]	15.0835(2)	16.6407(2)	33.7933(3)
α [°]	90	90	90
β [°]	105.2450(10)	94.9350(10)	95.7830(10)
γ [°]	90	90	90
V [$Å^3$]	2490.31(6)	4583.36(10)	2539.68(5)
Z	4	8	4
ρ_{calcd} [g cm^{-3}]	2.051	2.216	2.162
μ [mm^{-1}]	18.514	8.531	29.401
F(000)	1712.0	2832.0	1544.0
Radiation	CuKα (λ = 1.54184)	MoKα (λ = 0.71073)	CuKα (λ = 1.54184)
θ range [°]	7.476-155.982	5.192-66.2	9.668-147.108
	-10 ≤ h ≤ 12	-34 ≤ h ≤ 35	-10 ≤ h ≤ 11
Limiting indices	-24 ≤ k ≤ 25	-11 ≤ k ≤ 11	-10 ≤ k ≤ 10
	-18 ≤ l ≤ 19	-24 ≤ l ≤ 23	-41 ≤ l ≤ 41
Collected reflns	16591	37770	43995
Unique reflns	6029 [R_{int} = 0.0469]	6241 [R_{int} = 0.0274]	5081 [R_{int} = 0.0657]
Data/restraints/parameters	6029/112/390	6241/0/249	5081/0/293
Goodness of fit	1.052	1.057	1.149
R_1/wR_2[I>2σ(I)]	0.0507/0.1375	0.0199/0.0401	0.0255/0.0610
R_1/wR_2(all data)	0.0526/0.1404	0.0257/0.0420	0.0262/0.0613
Largest diff. peak/hole/e $Å^{-3}$	1.92/-1.71	0.81/-0.96	1.26/-1.29
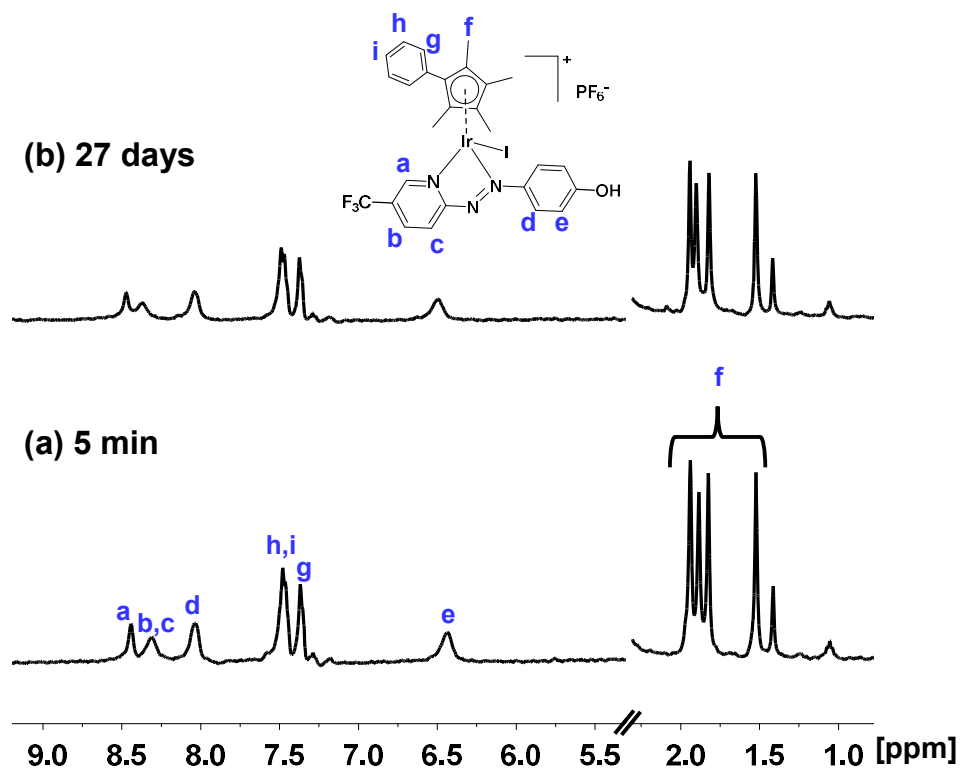
Figure A3.1. ^{1}H-NMR spectra (400 MHz, d$_6$-DMSO) of complex **6** after (a) 5 min and (b) 27 days at 298 K. No additional peaks are observed, indicating the stability of complex **6** towards DMSO.
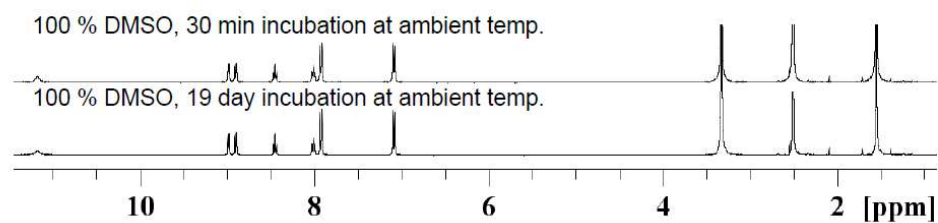
Figure A3.2. ^{1}H-NMR spectra (400 MHz, d$_6$-DMSO) of complex **9** after 30 min and 19 days at 298 K. No additional peaks are observed indicating the stability of the complex **9** towards DMSO.
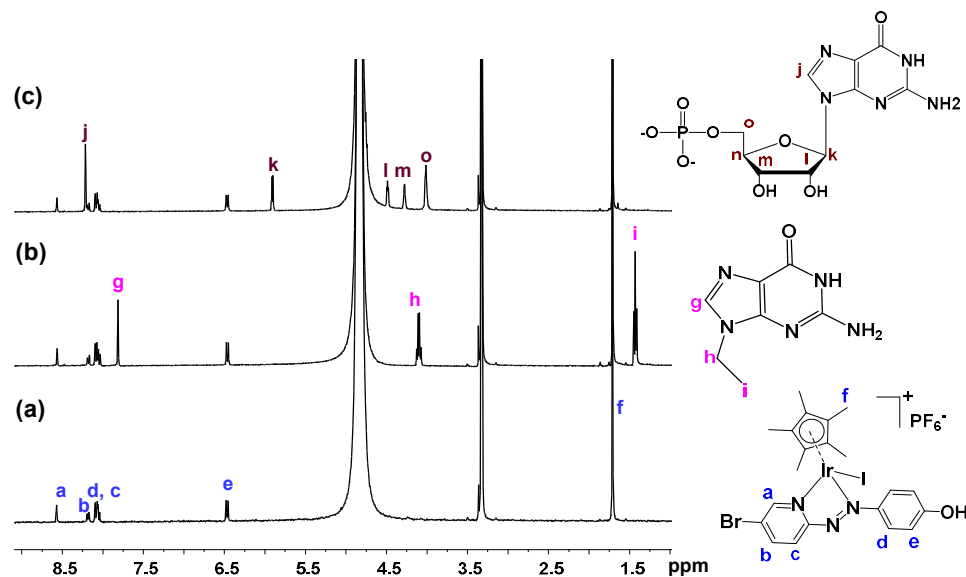
Figure A3.3. ^{1}H NMR (400 MHz, d$_4$-MeOD/D$_2$O, 1/1, v/v, pH* 7.8) of (a) **3** at 310 K after 24 h; (b) complex **3** with 3.0 mol equiv. 9-EtG at 310 K after 24 h; (c) **3** with 3.0 mol equiv. 5'-GMP at 310 K after 24 h, showing complex **3** is inert to hydrolysis or binding to nucleobases.
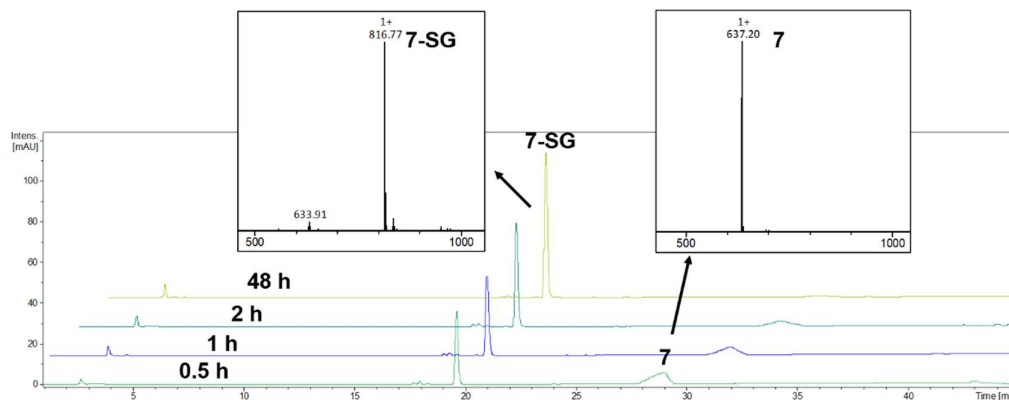
Figure A3.4. Time-dependent HPLC chromatograms (45-degree stacked) with ESI-MS peak insets for the reaction of complex **7** (100 μM) with equimolar GSH in water at 310 K. Mobile phases acetonitrile/H$_2$O (without TFA additive), with detection wavelength 254 nm.

Chapter 4

**Table A4.1.** Crystal data and refinement for complexes **2a**, **3a**, and **1b·PF$_6$**.

Parameters	2a	3a	1b·PF$_6$
Empirical formula	C$_{28}$H$_{25}$ClNRh	C$_{34}$H$_{29}$ClNRh	C$_{28}$H$_{28}$F$_6$N$_2$PRh
MW	513.85	589.94	640.40
T[K]	150(2)	100(2)	150(2)
Crystal size[mm^3]	0.2 × 0.16 × 0.12	0.4 × 0.3 × 0.12	0.18 × 0.18 × 0.1
Crystal System	monoclinic	monoclinic	monoclinic
Space group	P2$_1$	P2$_1$/n	P2$_1$/n
a [Å]	8.43680(18)	9.80373(14)	17.9087(2)
b [Å]	16.1447(3)	22.7944(3)	13.90409(15)
c [Å]	8.52368(17)	11.81996(16)	21.1305(3)
α [°]	90	90	90
β [°]	107.579(2)	102.1121(14)	98.1993(11)
γ [°]	90	90	90
Volume [Å^3]	1106.79(4)	2582.61(6)	5207.79(11)
Z	2	4	8
$\rho_{calcd.}$ [g cm^{-3}]	1.542	1.517	1.634
μ [mm^{-1}]	0.908	0.789	0.782
F (000)	524.0	1208.0	2592.0
Radiation	MoKα (λ = 0.71073)	MoKα (λ = 0.71073)	MoKα (λ = 0.71073)
θ range[°]	5.014-61.414	6.064-63.022	4.874-61.35
Index ranges	-11 ≤ h ≤ 11 -22 ≤ k ≤ 22 -12 ≤ l ≤ 12	-14 ≤ h ≤ 14 -33 ≤ k ≤ 33 -17 ≤ l ≤ 17	-24 ≤ h ≤ 25 -19 ≤ k ≤ 19 -27 ≤ l ≤ 27
Reflections Collected	27579	49882	127279
Independent reflections	6175 [R$_{int}$ = 0.0295]	8139 [R$_{int}$ = 0.0287]	14923 [R$_{int}$ = 0.0331]
Data/restraints/parameters	6175/1/285	8139/0/338	14923/75/769
Goodness of fit	1.161	1.161	1.031
Final R indexes [I>2σ(I)]	0.0249/0.0509	0.0286/0.0676	0.0377/0.0864
Final R indexes [all data]	0.0259/0.0512	0.0307/0.0685	0.0486/0.0926
Largest diff. peak/hole/e Å^{-3}	0.47/-0.56	0.68/-0.54	1.15/-0.88

Table A4.2. Selected bond length (Å) and angles (deg) for complexes **2a**, **3a**, and

1b·PF₆.

| Bond(s)	2a	3a	1b·PF₆
Rh-C (Cpˣ)	2.219(3)	2.2518(15)	2.227(2)
	2.167(3)	2.1487(15)	2.170(2)
	2.210(3)	2.1748(15)	2.240(2)
	2.137(3)	2.1753(16)	2.149(2)
	2.251(3)	2.2565(15)	2.195(2)
Rh-C (Centroid)	1.827	1.831	1.832
Rh-C(quinoline)	2.050(3)	2.0458(15)	2.058(2)
Rh-N(quinoline)	2.082(3)	2.1030(14)	2.1068(18)
Rh-Cl/N(pyridine)	2.3941(8)	2.3966(4)	2.1185(18)
C-Rh-N	79.89(12)	79.75(6)	79.39(8)
C-Rh-Cl/N(pyridine)	88.09(9)	89.59(4)	89.40(8)
N-Rh-Cl/N(pyridine)	87.88(8)	88.40(4)	86.67(7)

Table A4.3. Cell populations in flow cytometry analysis to determine the percentages of apoptotic cells, using Annexin V-FITC (detected by FL1) vs propidium iodido (detected by FL2) staining, after exposing A549 cells to complexes **3a** and **3b** at IC_{50} and 2x IC_{50} concentrations.

| Cell populations (%)	Treatment (dose)				
	Untreated	3a		3b	
		1x IC_{50}	2x IC_{50}	1x IC_{50}	2x IC_{50}
FL1-/FL2+	0.197 ± 0.015	0.427 ± 0.064	0.567 ± 0.120	0.360 ± 0.076	4.63 ± 0.82
FL1+/FL2+	0.029 ± 0.007	0.037 ± 0.012	0.008 ± 0.007	0.004 ± 0.007	0.056 ± 0.028
FL1+/FL2-	0.286 ± 0.214	0.217 ± 0.065	0.126 ± 0.132	0.021 ± 0.019	0.157 ± 0.045
FL1-/FL2-	99.55 ± 0.26	99.32 ± 0.14	99.30 ± 0.25	99.61 ± 0.09	95.15 ± 0.85
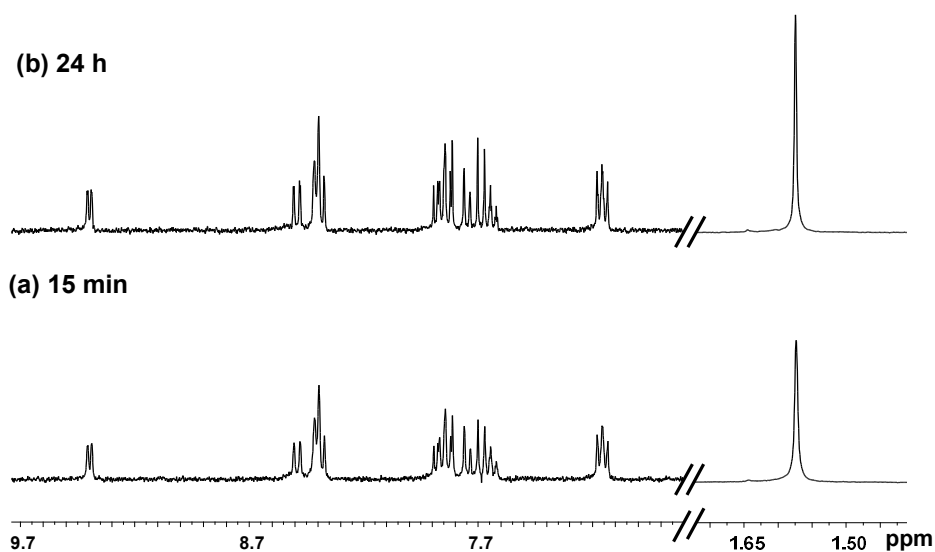
Figure A4.1. 300 MHz ^{1}H NMR spectra of complex **1b** in d_4-MeOD/D_2O (v/v 1/9) after (a) 15 min; (b) 24 h at 310 K, showing no hydrolysis.
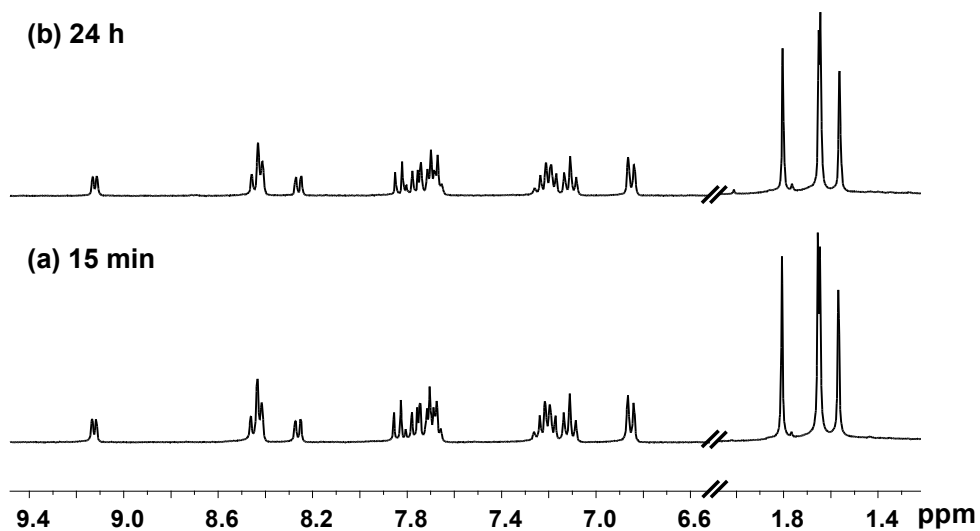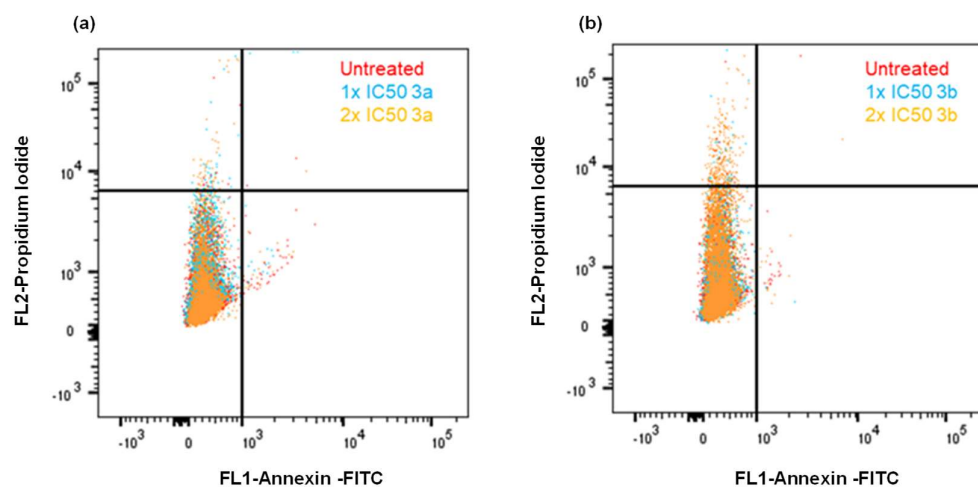
Figure A4.2. 300 MHz ^{1}H NMR spectra of complex **2b** in d$_4$-MeOD/D$_2$O (v/v 1/4) after (a) 15 min; (b) 24 h. at 310 K, showing no hydrolysis.
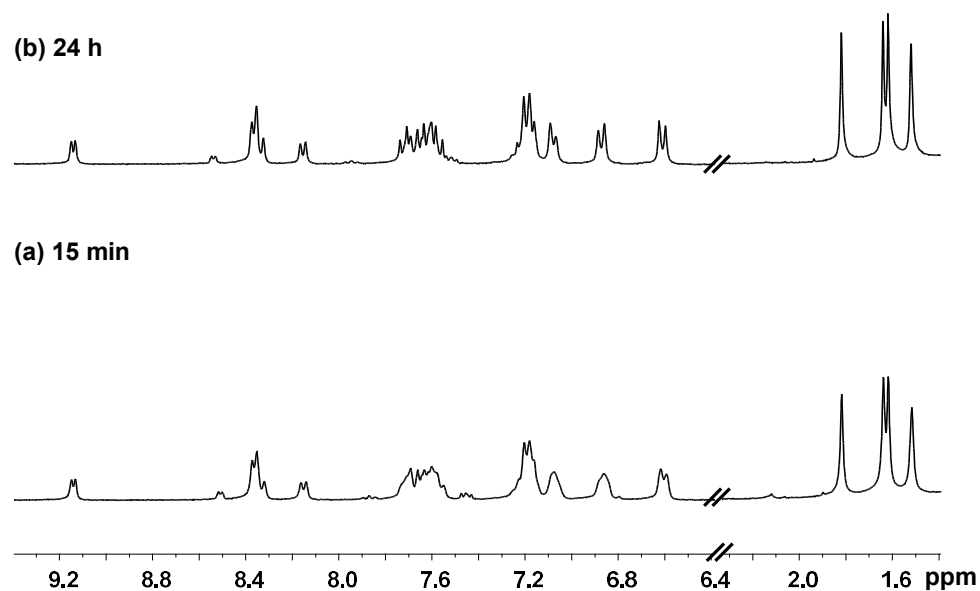
**Figure A4.3.** 300 MHz ^{1}H NMR spectra of complex **3b** in d$_4$-MeOD/D$_2$O (v/v 3/7) after (a) 15 min; (b) 24 h at 310 K, showing no hydrolysis.

Figure A4.4. Apoptosis analysis for A549 human lung cancer cells by flow cytometry after 24 h treatment with $1\times$ or $2\times$ IC$_{50}$ concentrations of complexes (**a**) **3a** and (**b**) **3b** compared with untreated A549 cells. FL1 channel detects the fluorescence of Annexin-FITC stained cells; FL2 channel detects the fluorescence propidium iodido stained cells. The horizontal and vertical axis numbers denote the fluorescence intensity.

Chapter 5
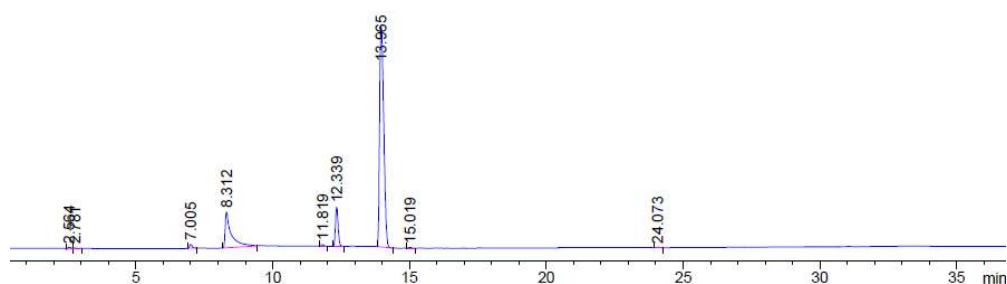
Figure A5.1. HPLC UV-vis trace for complex **Ir-I** in acetonitrile/water (1/9 v/v). The peak with retention time of 13.9 min corresponds to $[(\textbf{Ir-I})\text{-PF}_6]^+$.